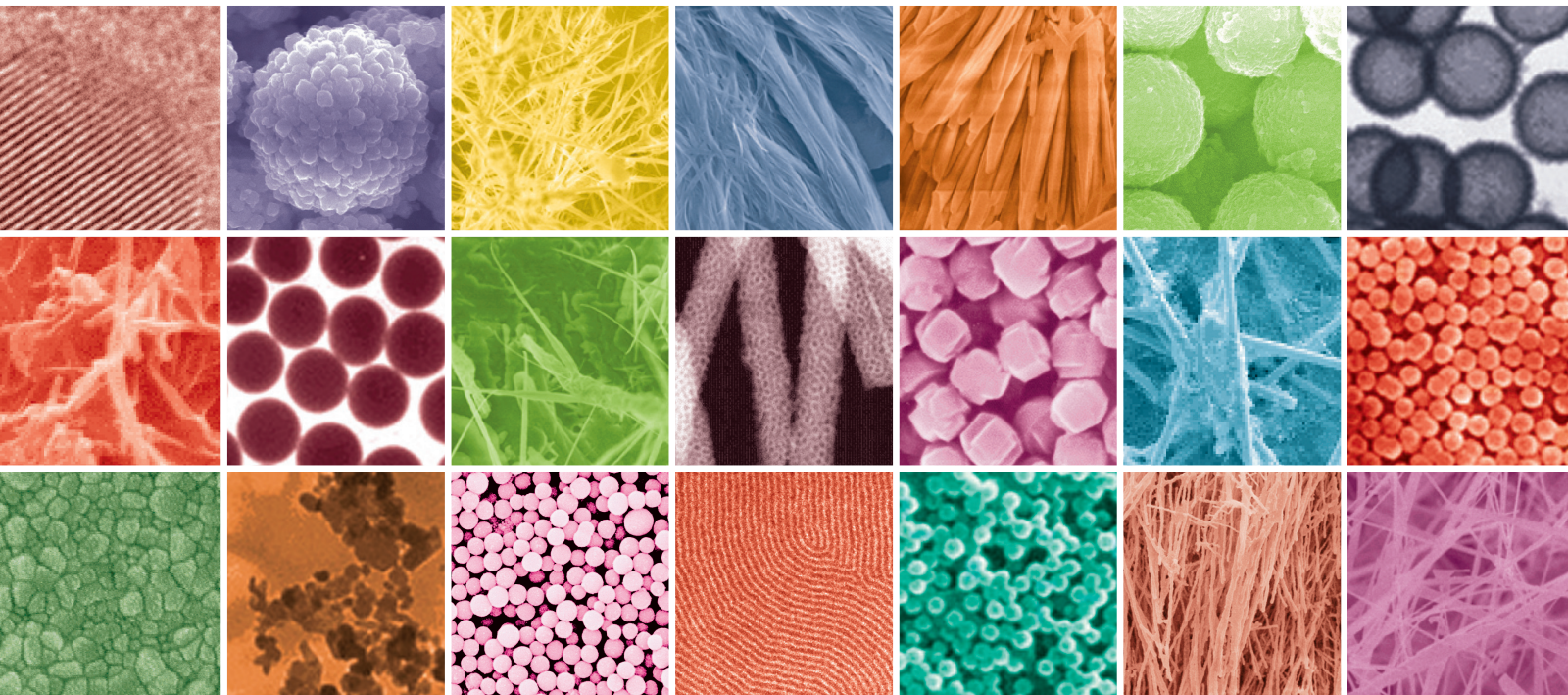


# Nanostructured Materials for Lithium-Ion Batteries

Guest Editors: Jianmin Ma, Yongzhu Fu, Bo Yu, and Jun Zhang





---

# **Nanostructured Materials for Lithium-Ion Batteries**

Journal of Nanomaterials

---

## **Nanostructured Materials for Lithium-Ion Batteries**

Guest Editors: Jianmin Ma, Yongzhu Fu, Bo Yu,  
and Jun Zhang



---

Copyright © 2013 Hindawi Publishing Corporation. All rights reserved.

This is a special issue published in "Journal of Nanomaterials." All articles are open access articles distributed under the Creative Commons Attribution License, which permits unrestricted use, distribution, and reproduction in any medium, provided the original work is properly cited.

## Editorial Board

Katerina E. Aifantis, Greece  
Nageh K. Allam, USA  
Margarida Amaral, Portugal  
Xuedong Bai, China  
Lavinia Balan, France  
Enrico Bergamaschi, Italy  
Theodorian Borca-Tasciuc, USA  
C. Jeffrey Brinker, USA  
Christian Brosseau, France  
Xuebo Cao, China  
Shafiul Chowdhury, USA  
Kwang-Leong Choy, UK  
Cui ChunXiang, China  
Miguel A. Correa-Duarte, Spain  
Shadi A. Dayeh, USA  
Claude Estourns, France  
Alan Fuchs, USA  
Lian Gao, China  
Russell E. Gorga, USA  
Hongchen Chen Gu, China  
Mustafa O. Guler, Turkey  
John Zhanhu Guo, USA  
Smrati Gupta, Germany  
Michael Harris, USA  
Zhongkui Hong, China  
Michael Z. Hu, USA  
David Hui, USA  
Y.-Keun Jeong, Republic of Korea  
Sheng-Rui Jian, Taiwan  
Wanqin Jin, China  
Rakesh K. Joshi, UK  
Zhenhui Kang, China  
Fathallah Karimzadeh, Iran  
Alireza Khataee, Iran

Do Kyung Kim, Korea  
Alan K. T. Lau, Hong Kong  
Burtrand Lee, USA  
Jun Li, Singapore  
Benxia Li, China  
Xing-Jie Liang, China  
Shijun Liao, China  
Gong Ru Lin, Taiwan  
J. -Y. Liu, USA  
Tianxi Liu, China  
Jue Lu, USA  
Songwei Lu, USA  
Daniel Lu, China  
Ed Ma, USA  
Gaurav Mago, USA  
Santanu K. Maiti, India  
Sanjay R. Mathur, Germany  
Vikas Mittal, UAE  
Weihai Ni, Germany  
Sherine Obare, USA  
Atsuto Okamoto, Japan  
Abdelwahab Omri, Canada  
Edward A. Payzant, USA  
Kui-Qing Peng, China  
Anukorn Phuruangrat, Thailand  
Suprakas Sinha Ray, South Africa  
Ugur Serincan, Turkey  
Huaiyu Shao, Japan  
Donglu Shi, USA  
Vladimir Sivakov, Germany  
Marinella Striccoli, Italy  
Bohua Sun, South Africa  
Saikat Talapatra, USA  
Nairong Tao, China

Titipun Thongtem, Thailand  
Somchai Thongtem, Thailand  
Alexander Tolmachev, Ukraine  
Valeri P. Tolstoy, Russia  
Tsung-Yen Tsai, Taiwan  
Takuya Tsuzuki, Australia  
Raquel Verdejo, Spain  
Mat U. Wahit, Malaysia  
Zhenbo Wang, China  
Ruibing Wang, Canada  
Shiren Wang, USA  
Cheng Wang, China  
Yong Wang, USA  
Jinquan Wei, China  
Ching-Ping Wong, Hong Kong  
Xingcai Wu, China  
Guodong Xia, Hong Kong  
Zhi Li Xiao, USA  
Ping Xiao, UK  
Yangchuan Xing, USA  
Shuangxi Xing, China  
N. Xu, China  
Doron Yadlovker, Israel  
Yingkui Yang, China  
Khaled Youssef, USA  
Kui Yu, Canada  
William W. Yu, USA  
Haibo Zeng, China  
Tianyou Zhai, Japan  
Renyun Zhang, Sweden  
Yanbao Zhao, China  
Lianxi Zheng, Singapore  
Chunyi Zhi, Hong Kong

# Contents

**Nanostructured Materials for Lithium-Ion Batteries**, JianminMa, Yongzhu Fu, Bo Yu, and Jun Zhang  
Volume 2013, Article ID 890197, 1 page

**Recent Advances as Materials of Functional Metal-Organic Frameworks**, Xiao-Lan Tong, Hai-Lu Lin, Jian-Hua Xin, Fen Liu, Min Li, and Xia-Ping Zhu  
Volume 2013, Article ID 616501, 11 pages

**Graphene-Based Composites as Cathode Materials for Lithium Ion Batteries**, Libao Chen, Ming Zhang, and Weifeng Wei  
Volume 2013, Article ID 940389, 8 pages

**Ag<sub>3</sub>PO<sub>4</sub> Semiconductor Photocatalyst: Possibilities and Challenges**, Gui-Fang Huang, Zhi-Li Ma, Wei-Qing Huang, Yong Tian, Chao Jiao, Zheng-Mei Yang, Zhuo Wan, and Anlian Pan  
Volume 2013, Article ID 371356, 8 pages

**A Review on the Synthesis of Manganese Oxide Nanomaterials and Their Applications on Lithium-Ion Batteries**, Xiaodi Liu, Changzhong Chen, Yiyang Zhao, and Bin Jia  
Volume 2013, Article ID 736375, 7 pages

**A Subwavelength Plasmonic Waveguide Filter with a Ring Resonator**, Xiang Zhai, Shuangchun Wen, Dong Xiang, Ling-Ling Wang, Wujiiahemaiti Rexidaiguli, Liu Wang, and Dianyuan Fan  
Volume 2013, Article ID 484207, 6 pages

**Review on the Synthesis and Applications of Fe<sub>3</sub>O<sub>4</sub> Nanomaterials**, Xiaodi Liu, Zhiguo Zhong, Yufeng Tang, and Bingyu Liang  
Volume 2013, Article ID 902538, 7 pages

**An NMR Investigation of Phase Structure and Chain Dynamics in the Polyethylene/Montmorillonite Nanocomposites**, Wei Li, Linxi Hou, and Zhongren Chen  
Volume 2013, Article ID 937210, 10 pages

**3D Self-Supported Nanoarchitected Arrays Electrodes for Lithium-Ion Batteries**, Xin Chen, Ying Du, Nai Qing Zhang, and Ke Ning Sun  
Volume 2012, Article ID 905157, 19 pages

## Editorial

# Nanostructured Materials for Lithium-Ion Batteries

Jianmin Ma,<sup>1</sup> Yongzhu Fu,<sup>2</sup> Bo Yu,<sup>3</sup> and Jun Zhang<sup>4</sup>

<sup>1</sup> Key Laboratory for Micro-Nano Optoelectronic Devices of Ministry of Education, College of Physics and Microelectronics, Hunan University, Changsha 410082, China

<sup>2</sup> Materials Science and Engineering, The University of Texas at Austin, Austin, TX 78712, USA

<sup>3</sup> Functional Nanomaterials Laboratory, Solar and Photovoltaics Engineering Research Center, King Abdullah University of Science and Technology (KAUST), Thuwal 23955-6900, Saudi Arabia

<sup>4</sup> School of Materials Science and Engineering, University of Jinan, Jinan 250022, China

Correspondence should be addressed to Jianmin Ma; [nanoelechem@hnu.edu.cn](mailto:nanoelechem@hnu.edu.cn)

Received 13 May 2013; Accepted 13 May 2013

Copyright © 2013 Jianmin Ma et al. This is an open access article distributed under the Creative Commons Attribution License, which permits unrestricted use, distribution, and reproduction in any medium, provided the original work is properly cited.

In the past decade, lithium-ion (Li-ion) batteries have been considered as one of the viable alternative technologies for applications such as electrical vehicles and grid energy storage for renewable energies (e.g., solar and wind) due to their high energy density and long cycle life. Recent nanotechnology has acted as the positive catalysts for the development of advanced electrode materials for high-performance Li-ion batteries. In this issue, some typical electrode nanomaterials have been reviewed and discussed.

The paper “*Graphene-based composites as cathode materials for lithium ion batteries*” by L. Chen et al. reviews the recent advances in graphene-based composites and their application as cathode materials for Li-ion batteries. They focus on the synthesis methods of graphene-based composites and their superior electrochemical performance in Li-ion batteries.

In the paper “*A review on the synthesis of manganese oxide nanomaterials and their applications on lithium-ion batteries*” by X. Liu et al., the authors briefly review the recent development of manganese oxide nanomaterials. They present two important viewpoints: (i) simple and effective methods should be explored for the synthesis of manganese oxide nanomaterials with high surface areas and good dispersity in the future; (ii) the electrochemical mechanism of manganese oxide nanomaterials should be deeply understood.

The paper “*3D self-supported nanoarchitected arrays electrodes for lithium-ion batteries*” by X. Chen reviews recent advances in the strategies for the fabrication, selection of the

different current collector substrates, and structural configuration of three-dimensional self-supported nanoarchitected arrays electrodes with different cathode and anode materials. It also discussed the intrinsic relationship of the unique structural characters, the conductive substrates, and electrochemical kinetic properties of three-dimensional self-supported nanoarchitected arrays electrodes. In addition, It highlights the future design trends and directions of three-dimensional self-supported nanoarchitected arrays electrodes for future advanced Li-ion batteries.

In conclusion, Li-ion batteries, as one of the most promising electrochemical energy storage technologies, will play a significant role in many applications. To further improve the energy density and cycle life, electrodes based on nanotechnologies (e.g., nanostructure, nanofabrication, and nanoframework) are believed to be the most promising strategy. To achieve these, new methods to synthesize nanomaterials need to be explored, in-depth understanding of the electrochemical phenomena in nanoscale needs to be enhanced, and new tools to characterize nanomaterials need to be developed. With the successful development of high energy density, long cycle life Li-ion batteries, our society will become efficient and sustainable.

Jianmin Ma  
Yongzhu Fu  
Bo Yu  
Jun Zhang

## Review Article

# Recent Advances as Materials of Functional Metal-Organic Frameworks

Xiao-Lan Tong,<sup>1,2</sup> Hai-Lu Lin,<sup>1</sup> Jian-Hua Xin,<sup>1</sup> Fen Liu,<sup>1</sup> Min Li,<sup>1</sup> and Xia-Ping Zhu<sup>1</sup>

<sup>1</sup> College of Biology, Chemistry and Material Science, East China Institute of Technology, Fuzhou, Jiangxi 344000, China

<sup>2</sup> Fundamental Science on Radioactive Geology and Exploration Technology Laboratory, East China Institute of Technology, NanChang, Jiangxi 330013, China

Correspondence should be addressed to Xiao-Lan Tong; [xltongecit@163.com](mailto:xltongecit@163.com)

Received 30 January 2013; Accepted 22 March 2013

Academic Editor: Jianmin Ma

Copyright © 2013 Xiao-Lan Tong et al. This is an open access article distributed under the Creative Commons Attribution License, which permits unrestricted use, distribution, and reproduction in any medium, provided the original work is properly cited.

Metal-organic frameworks (MOFs), also known as hybrid inorganic-organic materials, represent an emerging class of materials that have attracted the imagination of solid-state chemists because MOFs combine unprecedented levels of porosity with a range of other functional properties that occur through the metal moiety and/or the organic ligand. The purpose of this critical review is to give a representative and comprehensive overview of the arising developments in the field of functional metal-organic frameworks, including luminescence, magnetism, and porosity through presenting examples. This review will be of interest to researchers and synthetic chemists attempting to design multifunctional MOFs.

## 1. Introduction

Metal organic frameworks (MOFs) are a new class of crystalline materials [1], the structures of which are composed of metal-oxide units or metal ions joined by organic linkers through strong covalent bonds. It may be defined as supramolecular solids but consists of strong bonding providing robustness, linking units that are available for modification by organic synthesis, and a geometrically well-defined structure. The latter property further implies that these solids should be highly crystalline. Specifically, the chemistry of MOFs has provided an extensive class of crystalline materials with high stability, tunable metrics, organic functionality, and porosity.

An extensive body of research results [2] currently exists from the synthesis of metal-organic frameworks (MOFs), an area that has attracted widespread attention due to the facility with which well-defined molecular building blocks can be assembled into periodic frameworks and the promise that such a process holds for the logical design of materials. The synthesis of MOFs generally involves the copolymerization of organic links and metal ions in a polar solvent under mild temperatures (up to 200°C) and autogenous pressures (up to

100 atm). Since most products can be considered kinetically driven and lie on local thermodynamic minima, factors such as solubility of the organic link and metal salt, solvent polarity, ionic strength of the medium, temperature, and pressure play critical roles in determining the character of products. Indeed, slight perturbations in synthetic parameters have been the basis for the preparation of what seems to be a flood of new MOF compounds.

The designed construction of extended metal-organic frameworks from soluble molecular building blocks represent one of the most challenging issues facing synthetic chemistry today. Also metal-organic frameworks (MOFs) are widely studied because of their potential applications in many areas such as luminescence, magnetism, hydrogen storage, and gas adsorption and separation. We will give a representative and comprehensive overview of the arising developments of the functional MOFs.

## 2. Luminescent Metal-Organic Frameworks

The luminescent properties of metal-organic frameworks (MOFs) have attracted much attention for a long time,

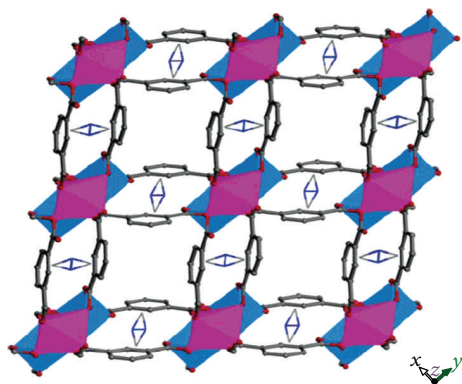


FIGURE 1: Framework of the MOF with DMF templating cations occupying the pores.

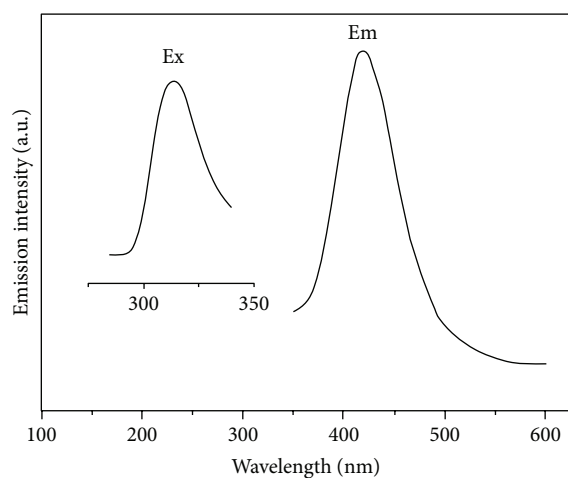


FIGURE 2: Photoluminescent spectrum of the MOF in the solid state at room temperature.

although these types of materials were frequently referred to as metal coordination polymers in the literature before the term “MOF” was widely adopted. The first report of luminescence, in which the structure was termed “MOF” that we are aware of, appeared in 2002. Since then, nearly 200 articles have appeared reporting light emission by MOFs, and a few reviews covering certain aspects of MOF luminescent properties have been published [3–10].

The hybrid nature of MOF materials, which include both an organic ligand and a metal ion, enables a wide range of emissive phenomena found in few other classes of material; the metal coordination can increase the conjugation and rigidity of the linkers. MOFs offer a unique platform for the development of solid-state luminescent materials as they have a degree of structural predictability, in addition to well-defined environments for lumophore in crystalline form. The lanthanoid (Ln) ions have spectrally narrow emission, even in solution, and nearly all of the lanthanoids exhibit photoluminescent properties [11–17].

He et al. [18] synthesized the first open-framework heterometallic MOF structure (Figure 1) based on the assembly

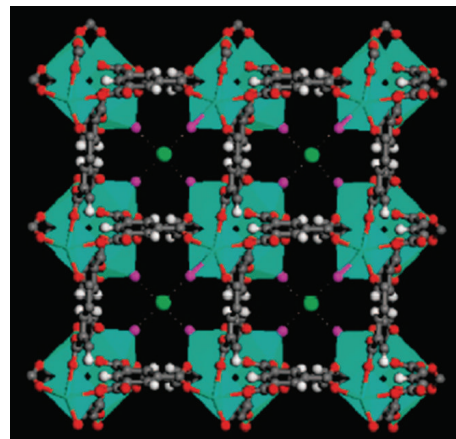


FIGURE 3: Single crystal X-ray structure of MOF-76b activated in methanol containing NaF.

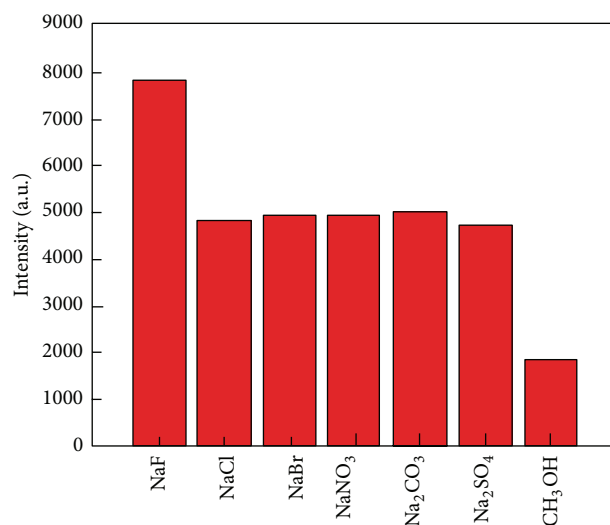


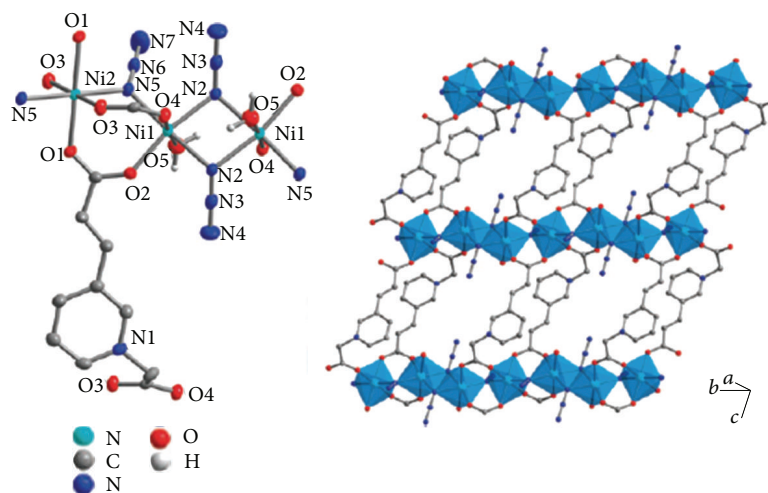
FIGURE 4:  ${}^5D_4 \rightarrow {}^7F_5$  transition intensities of MOF-76b activated in different types of 10-2 M NaX and Na<sub>2</sub>X methanol solution.

of infinite rod building units from the solvothermal reaction of zinc nitrate hexahydrate, sodium hydroxide, and 1,3-benzene-dicarboxylic (m-BDC) acid. The strong fluorescent emission (Figure 2) of the above MOF may make it a potential useful photoactive material.

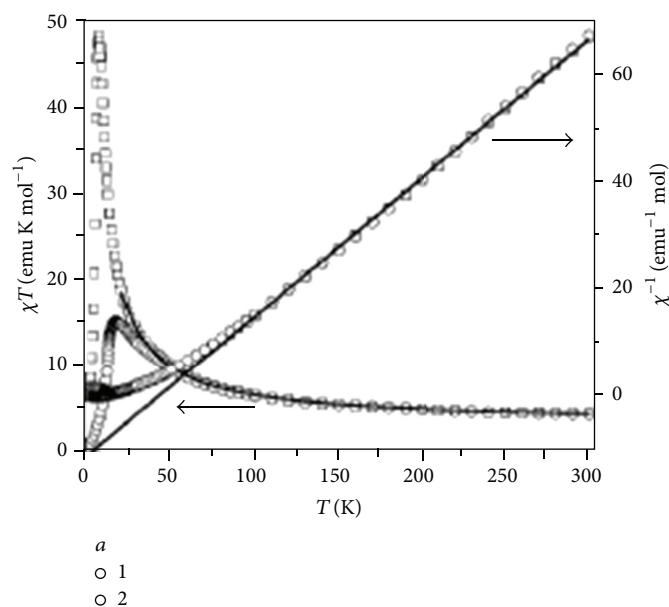
Chen et al. [19] report a prototype luminescent MOF (Figure 3), Tb (BTC)·G (MOF-76: BTC = benzene-1,3,5-tricarboxylate, G = guest solvent), for the recognition and sensing of anions, exhibiting a high-sensitivity sensing function with respect to fluoride (Figure 4). Such a recognition event can be readily transformed into an external luminescence intensity change once luminescent metal site and/or organic linkers have been incorporated into the luminescent MOFs.

### 3. Magnetic Metal-Organic Frameworks

One of the many interesting properties of metal-organic frameworks (MOF) is magnetism [20–22]. It can be implemented by incorporating magnetic moment carriers such



(a)



(b)

FIGURE 5: (a) The repeating unit (left) and the 2D layer formed by organic ligands interlinking 1D chains (right) in 1. (b) The  $\chi T$  and  $1/\chi$  versus  $\chi T$  plots at 1 kOe for 1 and 2.

as paramagnetic metals, open-shell organic ligands or both [23, 24]. Magnetic MOFs and molecular magnets reported with their designs, synthetic approaches, structures, and physical properties [25–33] are both branches of coordination chemistry where metals are bound in a solid by coordination bonds to organic linkers. There exist several reviews dealing with the different aspects of magnetism [34–38].

Lanthanoid metals are attractive as magnetic materials because of their high spin numbers and strong magnetic anisotropies on the 4f orbitals. Magnetic materials based on lanthanoid metals or lanthanoid metal oxides have extensive applications [39–42].

Sun et al. [43] have reported a novel 2D coordination polymer 1 (Figure 5(a)) consisting of ferromagnetic Ni(II)

chain with alternating double EO-azide bridges and (EO-azide)bis(carboxylate) triple bridges, and the material exhibits solvent sensitive metamagnetism; it can become 2 by dehydrating. The reversible dehydration/hydration processes are accompanied by significant changes in critical temperature, critical field and hysteresis (Figure 5(b)).

Liu et al. [44] have successfully synthesized a high nuclearity cubic cage involving 64  $\text{Fe}^{3+}$  ions (Figure 6), which displays strong antiferromagnetism (Figure 7). They also demonstrate that the combination of the small steric hindrance  $\text{HCOO}^-$  and polypodal ligands can obtain high nuclearity magnetic clusters in order to explore their novel and interesting magnetism.

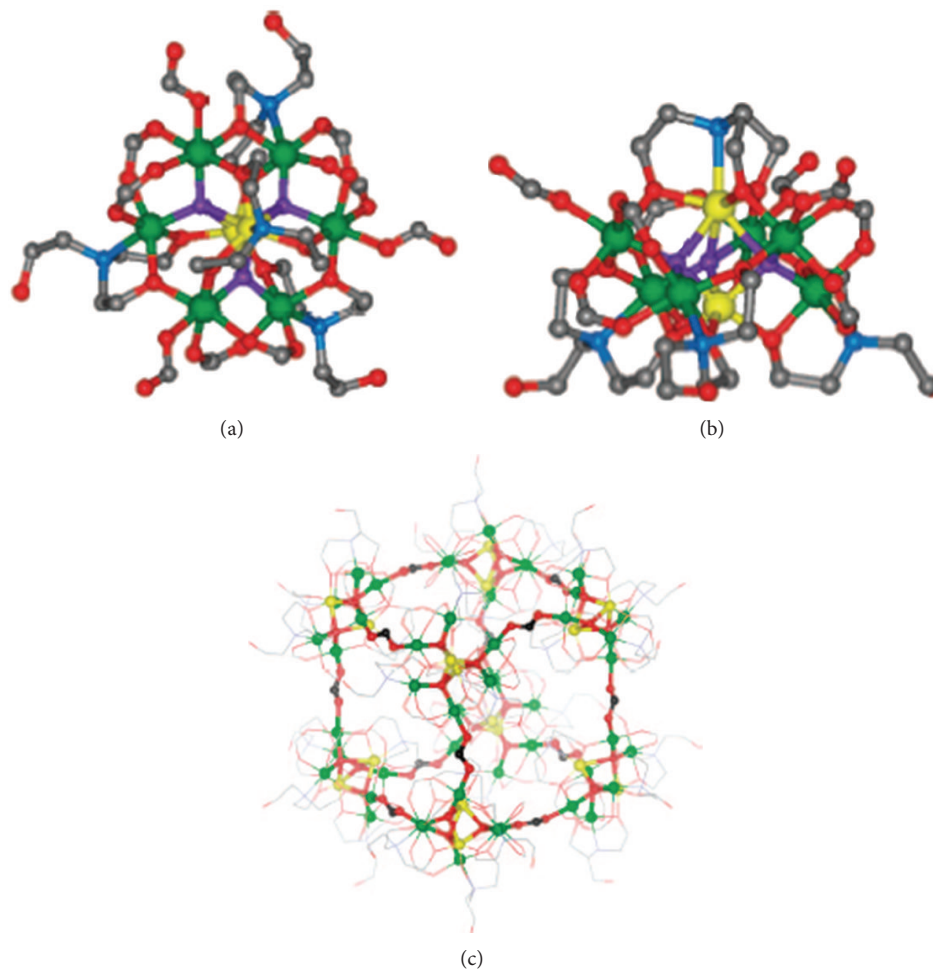


FIGURE 6: The structure of  $\text{Fe}_{64}$  cubic. ((a) and (b)) Top and side view of the  $\text{Fe}_8$  corner. (c) The cubic cage with the corner  $\text{Fe}_8\text{O}_3$  cores and  $\text{HCOO}^-$  edges highlighted.

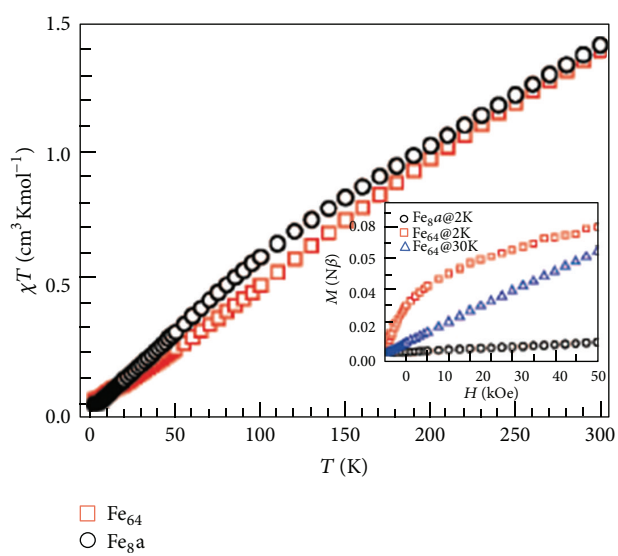


FIGURE 7:  $\chi T$  versus  $T$  plots under 1 kOe field and  $M$  versus  $H$  plot (inset) for  $\text{Fe}_{64}$  and  $\text{Fe}_{8a}$ . Data are for one  $\text{Fe}^{3+}$ .

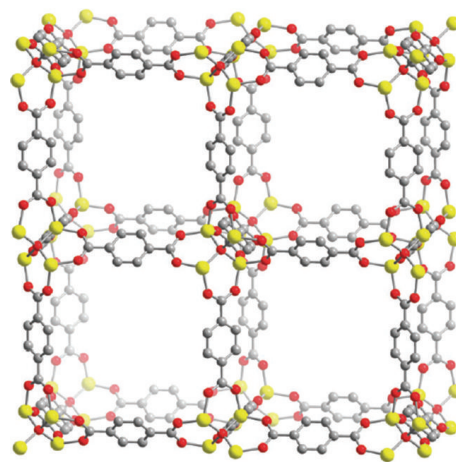


FIGURE 8: A portion of the crystal structure of  $\text{Zn}_4\text{O}(\text{BDC})_3$  (MOF-5).

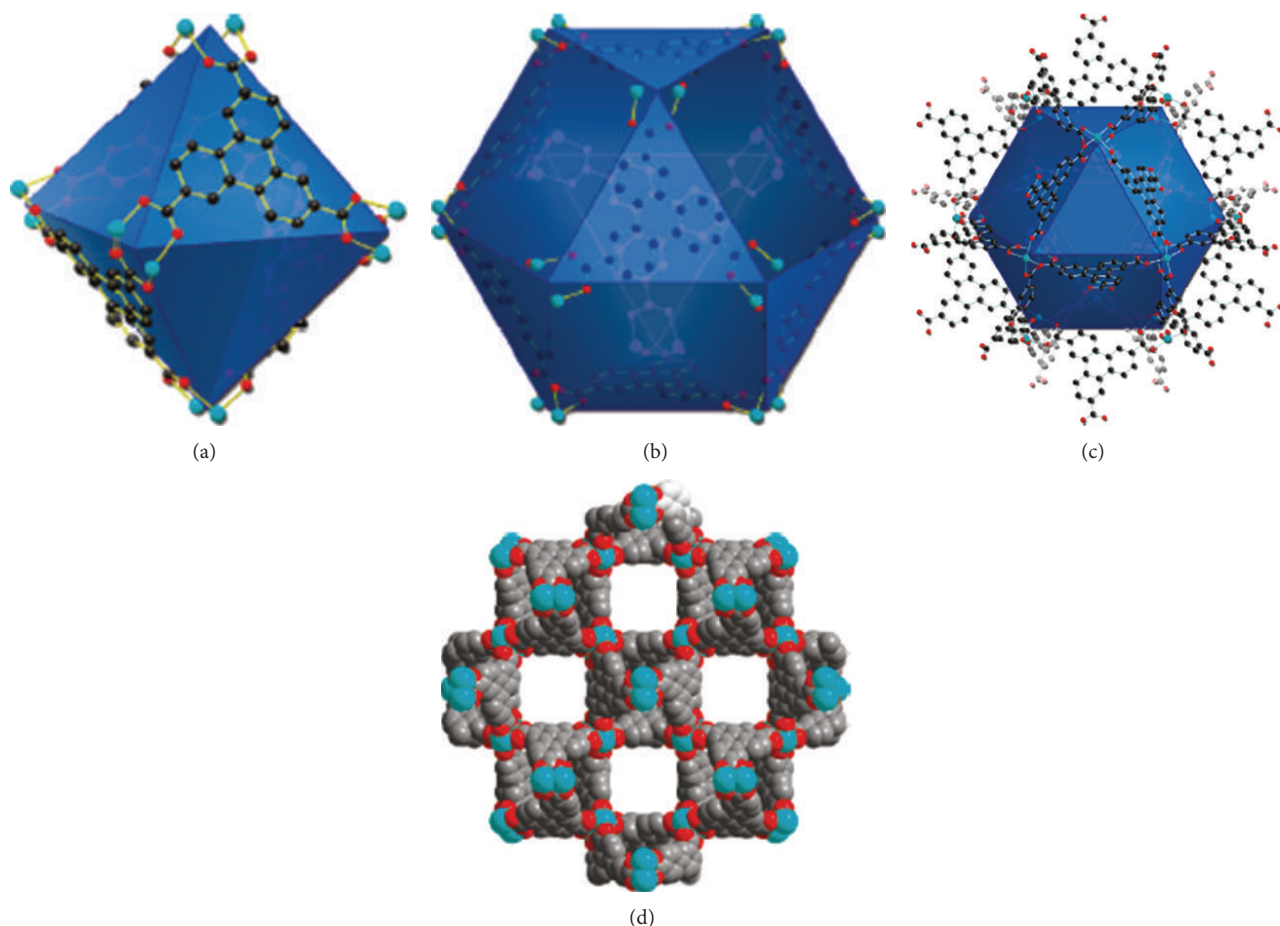


FIGURE 9: (a) Octahedral cage in PCN-20. (b) Cuboctahedral cage with alignment of the unsaturated metal center (UMCs) in PCN-20. (c) Cuboctahedral cage with open metal sites aligned orthogonally in PCN-20. (d) Square channels of PCN-20.

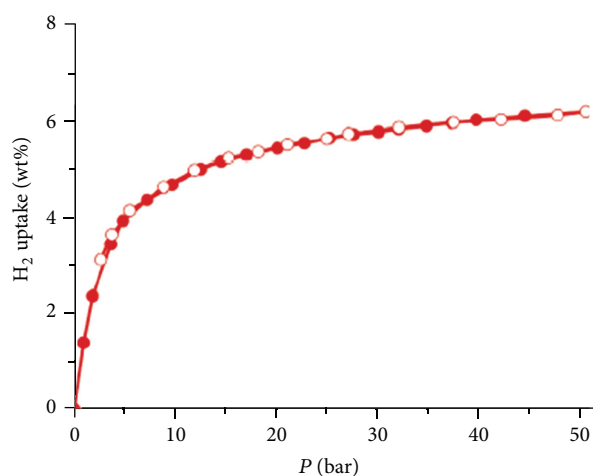


FIGURE 10: H<sub>2</sub> sorption isotherms of PCN-20 at 77 K, at high pressure.

#### 4. Porous Metal-Organic Frameworks

The designed construction of extended porous frameworks from soluble molecular building blocks represents one of the most challenging issues facing synthetic chemistry today. A large number of wonders and advances have been made possible by the synthesis of porous metal-organic frameworks (MOFs) because they have a wide array of applications, ranging from hydrogen storage to gas adsorption and separation to catalysis and so on. Thanks to several effective engineering strategies, systematic fabrication of porous MOFs can be achieved through designer assembly from judiciously selected molecular building blocks.

*4.1. Hydrogen Storage in Metal-Organic Frameworks.* New materials capable of storing hydrogen at high gravimetric and volumetric densities are required if hydrogen is to be widely employed as a clean alternative to hydrocarbon fuels in cars and other mobile applications. With exceptionally high surface areas and chemical-tunable structures, microporous metal-organic frameworks have recently emerged as some of the most promising candidate materials; they can display outstanding performance characteristics for cryogenic hydrogen storage at 77 K and pressures up to 100 bar.

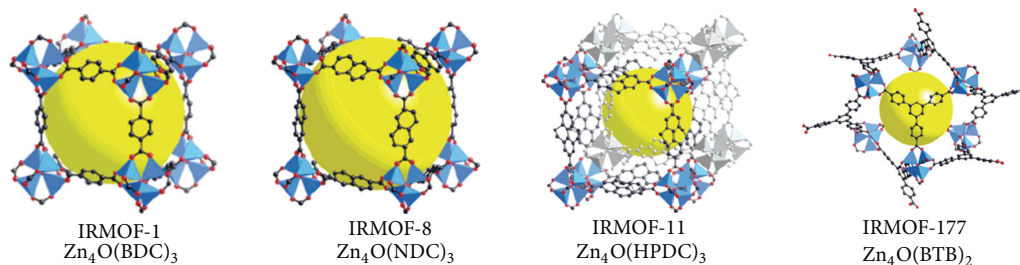


FIGURE 11: Metal-organic frameworks analyzed in this study.

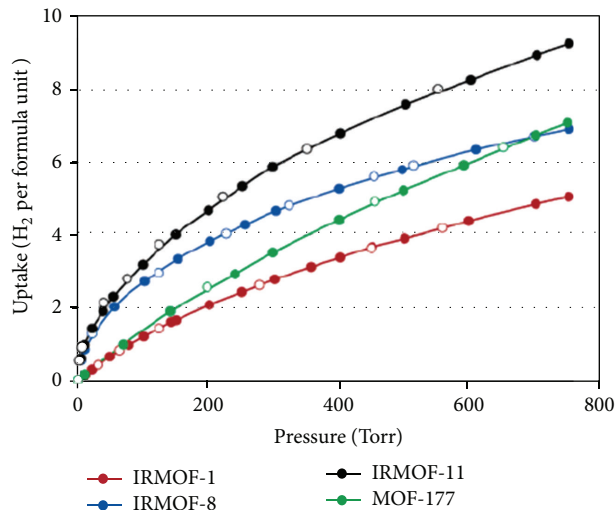


FIGURE 12: Hydrogen adsorption isotherms measured at 77 K for the MOFs analyzed in this study.

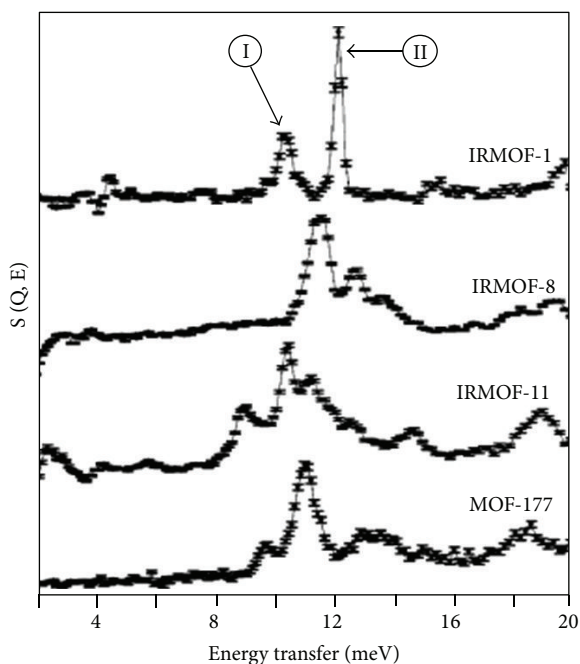


FIGURE 13: Inelastic neutron scattering spectra for each material loaded with 4  $\text{H}_2$  per formula unit.

One of the first metal-organic frameworks investigated for hydrogen storage was the cubic carboxylate-based framework  $\text{Zn}_4\text{O}(\text{BDC})_3$  (see Figure 8), and its gas storage properties were found to depend very large on the methods utilized in preparation and activation, with Langmuir surface areas ranging between  $1010$  and  $4400 \text{ m}^2 \cdot \text{g}^{-1}$  and  $\text{H}_2$  uptake capacity varying accordingly [45–49]. Inspired by the performance of compounds such as  $\text{Zn}_4\text{O}(\text{BDC})_3$ , researchers have thus far reported hydrogen storage data for over 150 other microporous metal-organic frameworks [50–55], containing carboxylate-based frameworks, heterocyclic azolate-based frameworks, mixed-ligand/functionality systems, metal cyanide frameworks, and so on.

Wang et al. [56] reported a porous MOF, PCN-20 (Figure 9) with a twisted boracite topology based on a designed planar TTCA ligand. PCN-20 possessed a large Langmuir surface area of over  $4200 \text{ m}^2 \cdot \text{g}^{-1}$  as well as demonstrated a high hydrogen uptake capacity of 6.2 wt% at 77 K and 50 bar (Figure 10).

Rowell et al. [57, 58] have obtained remarkably detailed information on the primary binding sites of hydrogen in a series of metal-organic frameworks (Figures 11, 12, and 13) composed of  $\text{Zn}_4\text{O}(\text{O}_2\text{C})_6$  secondary building units with the use of inelastic neutron scattering from the hindered rotations of the adsorbed molecule. And this paper underlines the need to explore new topologies composed of novel secondary

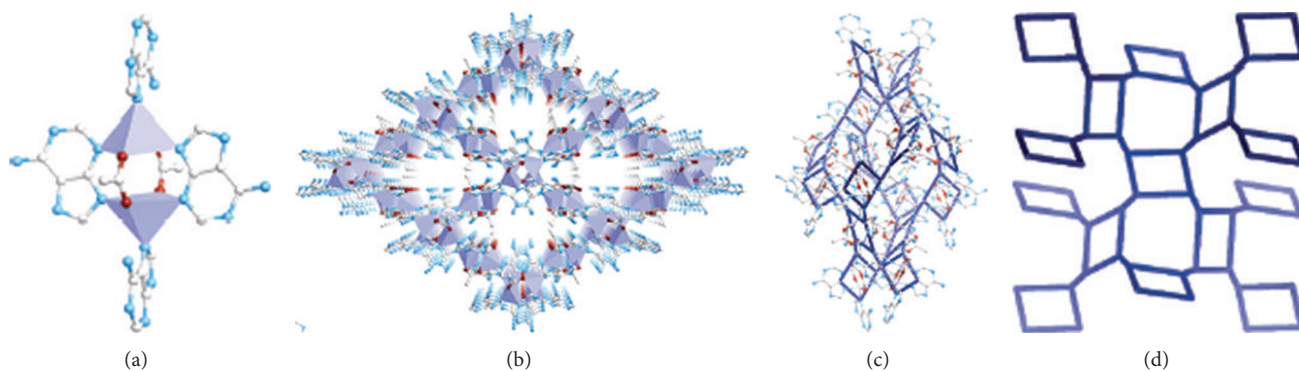
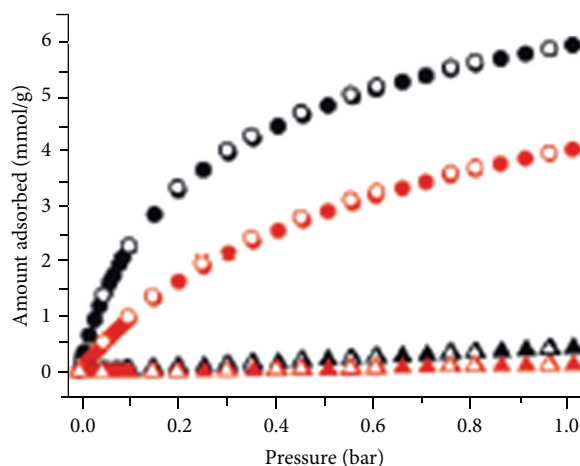


FIGURE 14: Crystal structure of bio-MOF-11.

FIGURE 15: Adsorption isotherms for CO<sub>2</sub> (circles) and N<sub>2</sub> (triangles) at 273 (black) and 298 K (red).

building units from metal cations that have received less attention to increase the building energies for H<sub>2</sub> on all sites. In particular, the use of more polarizing centers or the installment of open metal sites should enhance hydrogen physisorption by this case of materials.

However, significant further advances will be required in order to meet the US DoE targets for an onboard hydrogen system.

**4.2. Gas Adsorption and Separation.** In industry, the adsorptive separation needs efficient porous materials. Preparing as traditional porous solid material, the porous metal-organic frameworks with tailored structures and tunable surface properties are becoming promising candidates for gas adsorption and separations, also they have commendable thermal stability, in most cases, these structures are robust enough to allow the removal of the included guest species resulting in permanent porosity, so MOFs are ideal for research and practical applications, such as in gas separation and purification as adsorbents [59–63].

An et al. [64] have prepared a porous MOFs Co<sub>2</sub>(ad)<sub>2</sub>(CO<sub>2</sub>CH<sub>3</sub>)<sub>2</sub>·DMF·0.5H<sub>2</sub>O (bio-MOF-11) (Figure 14) via a solvothermal reaction between cobalt acetate tetrahydrate and adenine in DMF, which has a high heat of

adsorption for CO<sub>2</sub>, high CO<sub>2</sub> capacity, and impressive selectivity for CO<sub>2</sub> over N<sub>2</sub> (Figure 15).

In 2009, Britt et al. [65] reported that a known MOF, Mg-MOF-74 (Figures 16 and 17), with open magnesium sites, rivals competitive materials in CO<sub>2</sub> capture, with 8.9 wt.% dynamic capacity, and undergoes facile CO<sub>2</sub> release at significantly lower temperature, 80°C. Mg-MOF-74 offers an excellent balance between dynamic capacity and regeneration. These results demonstrate the potential of MOFs with open metal sites as efficient CO<sub>2</sub> capture media.

Li et al. [66] reported a novel three zeolite-like chiral guest-free MOF material (Figure 18), [Zn(dtp)] (H<sub>2</sub>dtp = 2,3-di-1H-tetrazol-5-ylpyrazine), which has high thermal stability and permanent porosity. It exhibits rare gas-adsorption selectivity for O<sub>2</sub> and CO<sub>2</sub> over N<sub>2</sub> gas (Figure 19), and could be useful in the separation of air.

Besides, MOFs also have some other properties that occur through the metal moiety and/or the organic ligand, such as catalysts [67], enantioselective catalysis [68], and applications in industry [69].

## 5. Conclusions Remarks

We exhibited the variety applications as materials of few MOFs here; in fact although a large number of MOFs have

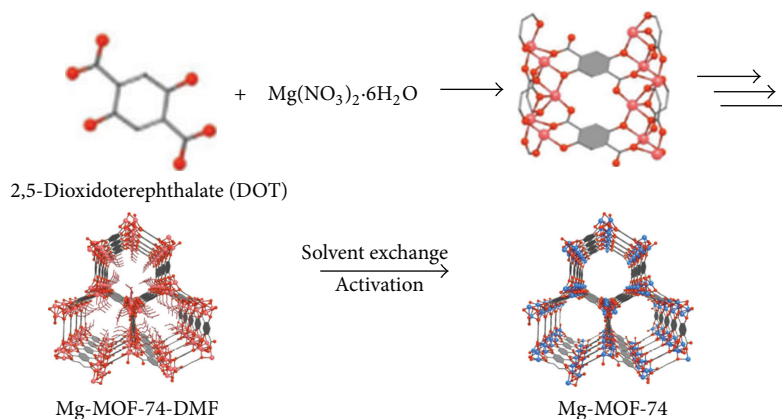
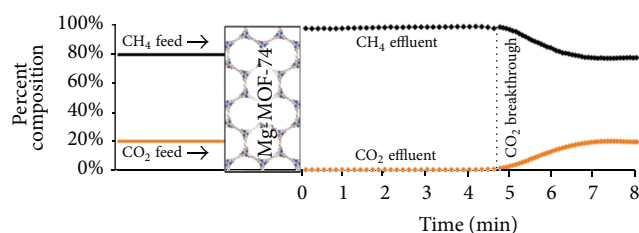
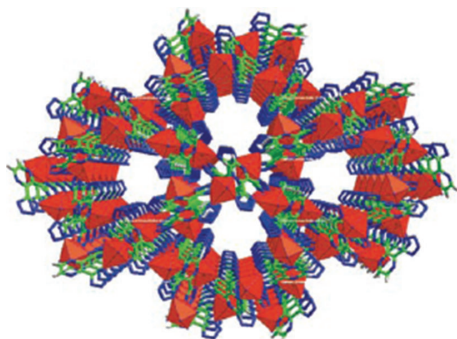


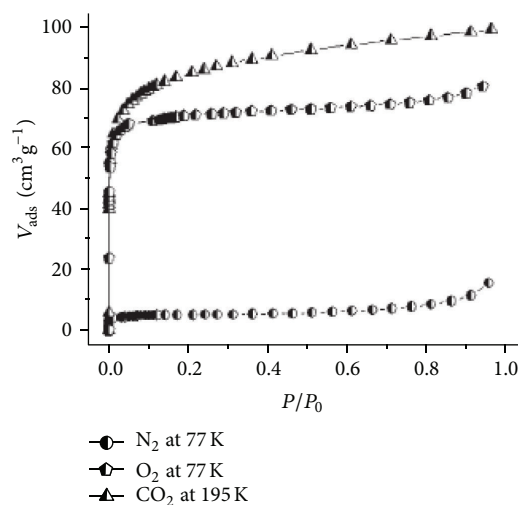
FIGURE 16: Single crystal structure of Mg-MOF-74.

FIGURE 17: A 20% mixture of  $\text{CO}_2$  in  $\text{CH}_4$  is fed into a bed of Mg-MOF-74. Effluent concentrations are shown, indicating complete retention of  $\text{CO}_2$  until saturation.  $\text{CO}_2$  breakthrough occurs at the dashed line.FIGURE 18: Structure of  $[\text{Zn}(\text{dtp})]$  showing open channel along the  $c$  axis.

been reported until now, we only have seen the tip of the iceberg with respect to the application potential of MOFs. In order to investigate more potential applications of MOFs, an extensive body of researchers should pay for further effort.

## Acknowledgments

This work was supported by Project of Jiangxi Provincial Department of Education (Grant no. GJJ12396 and no. GJJ11140), the open fund of Fundamental Science on Radioactive Geology and Exploration Technology Laboratory (REGT1212), the National Science Foundation of Jiangxi

FIGURE 19: Adsorption isotherms of  $\text{N}_2$ ,  $\text{O}_2$  and  $\text{CO}_2$  for  $[\text{Zn}(\text{dtp})]$ .

Province (no. 2010GQH0007), and the Start-up Fund of East China Institute of Technology.

## References

- [1] D. Britt, D. Tranchemontagne, and O. M. Yaghi, "Metal-organic frameworks with high capacity and selectivity for harmful gases," *Proceedings of the National Academy of Sciences of the United States of America*, vol. 105, no. 33, pp. 11623–11627, 2008.
- [2] N. L. Rosi, M. Eddaoudi, J. Kim, M. O'Keeffe, and O. M. Yaghi, "Advances in the chemistry of metal-organic frameworks," *CrystEngComm*, vol. 4, pp. 401–404, 2002.
- [3] M. D. Allendorf, C. A. Bauer, R. K. Bhakta, and R. J. T. Houk, "Luminescent metal-organic frameworks," *Chemical Society Reviews*, vol. 38, no. 5, pp. 1330–1352, 2009.
- [4] C. Janiak, "Engineering coordination polymers towards applications," *Dalton Transactions*, no. 14, pp. 2781–2804, 2003.
- [5] C. L. Cahill, D. T. de Lill, and M. Frisch, "Homo- and heterometallic coordination polymers from the f elements," *CrystEngComm*, vol. 9, no. 1, pp. 15–26, 2007.

- [6] D. MasPOCH, D. Ruiz-Molina, and J. Veciana, "Old materials with new tricks: multifunctional open-framework materials," *Chemical Society Reviews*, vol. 36, no. 5, pp. 770–818, 2007.
- [7] T. Sakamoto, A. Ojida, and I. Hamachi, "Molecular recognition, fluorescence sensing, and biological assay of phosphate anion derivatives using artificial Zn(II)-Dpa complexes," *Chemical Communications*, no. 2, pp. 141–152, 2009.
- [8] A. J. Moro, P. J. Cywinski, S. Körsten, and G. J. Mohr, "An ATP fluorescent chemosensor based on a Zn(II)-complexed dipicolylamine receptor coupled with a naphthalimide chromophore," *Chemical Communications*, no. 7, pp. 1085–1087, 2010.
- [9] H. L. Jiang, Y. Tatsu, Z. H. Lu, and Q. Xu, "Non-, micro-, and mesoporous metal-organic framework isomers: reversible transformation, fluorescence sensing, and large molecule separation," *Journal of the American Chemical Society*, vol. 132, no. 16, pp. 5586–5587, 2010.
- [10] M. Ji, X. Lan, Z. Ping, C. Hao, and J. Qiu, "Luminescent properties of metal-organic framework mof-5: relativistic time-dependent density functional theory investigations," *Inorganic Chemistry*, vol. 51, no. 22, pp. 12389–12394, 2012.
- [11] X. Q. Song, W. S. Liu, W. Don, Y. W. Wang, J. R. Zheng, and Z. P. Zang, "Structure variation and luminescence properties of lanthanide complexes incorporating a naphthalene-derived chromophore featuring salicylamide pendant arms," *European Journal of Inorganic Chemistry*, vol. 2008, no. 11, pp. 1901–1912, 2008.
- [12] N. Sabbatini, M. Guardigli, and J. M. Lehn, "Luminescent lanthanide complexes as photochemical supramolecular devices," *Coordination Chemistry Reviews*, vol. 123, no. 1-2, pp. 201–228, 1993.
- [13] F. S. Richardson, "Terbium(III) and europium(III) ions as luminescent probes and stains for biomolecular systems," *Chemical Reviews*, vol. 82, no. 5, pp. 541–552, 1982.
- [14] B. D. Chandler, J. O. Yu, D. T. Cramb, and G. K. H. Shimizu, "Series of lanthanide-alkali metal-organic frameworks exhibiting luminescence and permanent microporosity," *Chemistry of Materials*, vol. 19, no. 18, pp. 4467–4473, 2007.
- [15] P. Mahata and S. Natarajan, "A new series of three-dimensional metal-organic framework,  $[M_2(H_2O)] [C_5N_1H_3(COO)_2]_3 \cdot 2H_2O$ , M = La, Pr, and Nd: synthesis, structure, and properties," *Inorganic Chemistry*, vol. 46, no. 4, pp. 1250–1258, 2007.
- [16] P. Mahata, K. V. Ramya, and S. Natarajan, "Synthesis, structure and optical properties of rare-earth benzene carboxylates," *Dalton Transactions*, no. 36, pp. 4017–4026, 2007.
- [17] X. J. Zhang, Y. H. Xing, Z. Sun et al., "A series of two-dimensional metal-organic frameworks based on the assembly of rigid and flexible carboxylate-containing mixed ligands with lanthanide metal salts," *Crystal Growth & Design*, vol. 7, no. 10, pp. 2041–2046, 2007.
- [18] J. He, J. Yu, Y. Zhang, Q. Pan, and R. Xu, "Synthesis, structure, and luminescent property of a heterometallic metal-organic framework constructed from rod-shaped secondary building blocks," *Inorganic Chemistry*, vol. 44, no. 25, pp. 9279–9282, 2005.
- [19] B. Chen, L. Wang, F. Zapata, G. Qian, and E. B. Lobkovsky, "A luminescent microporous metal-organic framework for the recognition and sensing of anions," *Journal of the American Chemical Society*, vol. 130, no. 21, pp. 6718–6719, 2008.
- [20] P. Day and A. E. Underhill, Eds., *Metal-Organic and Organic Molecular Magnets*, vol. 252, Royal Society of Chemistry, Cambridge, UK, 2000.
- [21] C. N. R. Rao, A. K. Cheetham, and A. Thirumurugan, "Hybrid inorganic-organic materials: a new family in condensed matter physics," *Journal of Physics: Condensed Matter*, vol. 20, no. 8, Article ID 083202, 2008.
- [22] M. Kurmoo, "Magnetic metal-organic frameworks," *Chemical Society Reviews*, vol. 38, pp. 1353–1379, 2009.
- [23] S. J. Blundell and F. L. Pratt, "Organic and molecular magnets," *Journal of Physics: Condensed Matter*, vol. 16, no. 24, pp. R771–R828, 2004.
- [24] K. Itoh and M. Kinoshita, Eds., *Molecular Magnetism: New Magnetic Materials*, Gordon Breach-Kodansha, Tokyo, Japan, 2000.
- [25] B. Moulton and M. J. Zaworotko, "From molecules to crystal engineering: supramolecular isomerism and polymorphism in network solids," *Chemical Reviews*, vol. 101, no. 6, pp. 1629–1658, 2001.
- [26] M. E. Davis, "Ordered porous materials for emerging applications," *Nature*, vol. 417, no. 6891, pp. 813–821, 2002.
- [27] C. Janiak, "Engineering coordination polymers towards applications," *Dalton Transactions*, no. 14, pp. 2781–2804, 2003.
- [28] W. Lin, "Homochiral porous metal-organic frameworks: why and how?" *Journal of Solid State Chemistry*, vol. 178, no. 8, pp. 2486–2490, 2005.
- [29] C. J. Kepert, "Advanced functional properties in nanoporous coordination framework materials," *Chemical Communications*, no. 7, pp. 695–700, 2006.
- [30] D. MasPOCH, D. Ruiz-Molina, and J. Veciana, "Old materials with new tricks: multifunctional open-framework materials," *Chemical Society Reviews*, vol. 36, no. 5, pp. 770–818, 2007.
- [31] S. Chen, J. Zhang, and X. Bu, "Ionothermal synthesis of homochiral framework with acetate-pillared cobalt-camphorate architecture," *Inorganic Chemistry*, vol. 47, no. 13, pp. 5567–5569, 2008.
- [32] Z. X. Li, J. P. Zhao, E. C. Sañudo et al., "New 3D coordination polymers constructed from pillared metal-formate kagome layers exhibiting spin canting only in the Nickel(II) complex," *Inorganic Chemistry*, vol. 48, no. 24, pp. 11601–11607, 2009.
- [33] T. S. Venkatakrisnan, S. Sahoo, N. Bréfuel et al., "Enhanced ion anisotropy by nonconventional coordination geometry: single-chain magnet behavior for a  $[Fe^{II}L]_2\{Nb^{IV}(CN)_8\}$  helical chain compound designed with heptacoordinate  $Fe^{II}$ ," *Journal of the American Chemical Society*, vol. 132, no. 17, pp. 6047–6056, 2010.
- [34] X. Y. Wang, Z. M. Wang, and S. Gao, "Constructing magnetic molecular solids by employing three-atom ligands as bridges," *Chemical Communications*, no. 3, pp. 281–294, 2008.
- [35] N. Guillou, C. Livage, and G. Férey, "Cobalt and nickel oxide architectures in metal carboxylate frameworks: from coordination polymers to 3D inorganic skeletons," *European Journal of Inorganic Chemistry*, vol. 2006, no. 24, pp. 4963–4978, 2006.
- [36] L. M. C. Beltran and J. R. Long, "Directed assembly of metal-cyanide cluster magnets," *Accounts of Chemical Research*, vol. 38, no. 4, pp. 325–334, 2005.
- [37] E. Coronado, C. Martí-Gastaldo, J. R. Galán-Mascarós, and M. Cavallini, "Polymetallic oxalate-based 2D magnets: soluble molecular precursors for the nanostructuring of magnetic oxides," *Journal of the American Chemical Society*, vol. 132, no. 15, pp. 5456–5468, 2010.

- [38] D. Sarma, P. Mahata, S. Natarajan, P. Panissod, G. Rogez, and M. Drillon, "Synthesis, structure, and magnetic properties of a new eight-connected metal-organic framework (MOF) based on  $\text{Co}_4$  clusters," *Inorganic Chemistry*, vol. 51, no. 8, pp. 4495–4501, 2012.
- [39] K. Nakabayashi and S. Ohkoshi, "Monometallic lanthanoid assembly showing ferromagnetism with a Curie temperature of 11 K," *Inorganic Chemistry*, vol. 48, no. 18, pp. 8647–8649, 2009.
- [40] X. Feng, L. Y. Wang, J. S. Zhao et al., "Series of anion-directed lanthanide-rigid-flexible frameworks: syntheses, structures, luminescence and magnetic properties," *CrystEngComm*, vol. 12, no. 3, pp. 774–783, 2010.
- [41] Y. Wang, X. L. Li, T. W. Wang, Y. Song, and X. Z. You, "Slow relaxation processes and single-ion magnetic behaviors in dysprosium-containing complexes," *Inorganic Chemistry*, vol. 49, no. 3, pp. 969–976, 2010.
- [42] D. P. Li, T. W. Wang, C. H. Li, D. S. Liu, Y. Z. Li, and X. Z. You, "Single-ion magnets based on mononuclear lanthanide complexes with chiral Schiff base ligands  $[\text{Ln}(\text{FTA})_3\text{L}]$  ( $\text{Ln} = \text{Sm}, \text{Eu}, \text{Gd}, \text{Tb}$  and  $\text{Dy}$ )," *Chemical Communications*, vol. 46, no. 17, pp. 2929–2931, 2010.
- [43] W. W. Sun, C. Y. Tian, X. H. Jing, Y. Q. Wang, and E. Q. Gao, "Solvent-modulated metamagnetism in a nickel(II) coordination polymer with mixed azide and carboxylate bridges," *Chemical Communications*, no. 31, pp. 4741–4743, 2009.
- [44] T. Liu, J. Zhang, Z. M. Wang, and S. Gao, "A 64-nuclear cubic cage incorporating propeller-like  $\text{FeIII}$  apices and  $\text{HCOO}$ -edges," *Journal of the American Chemical Society*, vol. 130, no. 32, pp. 10500–10501, 2008.
- [45] R. Q. Zhong, R. Q. Zou, M. Du et al., "Metal-organic frameworks of manganese(II) 4,4'-biphenyldicarboxylates: crystal structures, hydrogen adsorption, and magnetism properties," *CrystEngComm*, vol. 12, no. 3, pp. 677–681, 2010.
- [46] S. S. Kaye, A. Dailly, O. M. Yaghi, and J. R. Long, "Impact of preparation and handling on the hydrogen storage properties of  $\text{Zn}_4\text{O}(\text{1,4-benzenedicarboxylate})_3$  (MOF-5)," *Journal of the American Chemical Society*, vol. 129, no. 46, pp. 14176–14177, 2007.
- [47] D. N. Dybtsev, H. Chun, and K. Kim, "Rigid and flexible: a highly porous metal-organic framework with unusual guest-dependent dynamic behavior," *Angewandte Chemie International Edition*, vol. 43, no. 38, pp. 5033–5036, 2004.
- [48] B. Panella and M. Hirscher, "Hydrogen physisorption in metal-organic porous crystals," *Advanced Materials*, vol. 17, no. 5, pp. 538–541, 2005.
- [49] L. J. Murray, M. Dincă, and J. R. Long, "Hydrogen storage in metal-organic frameworks," *Chemical Society Reviews*, vol. 38, no. 5, pp. 1294–1314, 2009.
- [50] S. S. Kaye and J. R. Long, "Hydrogen storage in the dehydrated prussian blue analogues  $\text{M}_3[\text{Co}(\text{CN})_6]_2$  ( $\text{M} = \text{Mn}, \text{Fe}, \text{Co}, \text{Ni}, \text{Cu}, \text{Zn}$ )," *Journal of the American Chemical Society*, vol. 127, no. 18, pp. 6506–6507, 2005.
- [51] F. Nouar, J. F. Eubank, T. Bousquet, L. Wojtas, M. J. Zaworotko, and M. Eddaoudi, "Supermolecular building blocks (SBBs) for the design and synthesis of highly porous metal-organic frameworks," *Journal of the American Chemical Society*, vol. 130, no. 6, pp. 1833–1835, 2008.
- [52] I. Senkovska and S. Kaskel, "Solvent-Induced pore-size adjustment in the metal-organic framework  $[\text{Mg}_3(\text{ndc})_3(\text{dmf})_4]$  ( $\text{ndc} = \text{naphthalenedicarboxylate}$ )," *European Journal of Inorganic Chemistry*, vol. 2006, no. 22, pp. 4564–4569, 2006.
- [53] M. Dincă and J. R. Long, "High-enthalpy hydrogen adsorption in cation-exchanged variants of the microporous metal-organic framework  $\text{Mn}_3[(\text{Mn}_4\text{Cl})_3(\text{BTT})_8(\text{CH}_3\text{OH})_{10}]_2$ ," *Journal of the American Chemical Society*, vol. 129, no. 36, pp. 11172–11176, 2007.
- [54] D. Sun, S. Ma, Y. ke, D. J. Collins, and H. C. Zhou, "An Interweaving MOF with high hydrogen uptake," *Journal of the American Chemical Society*, vol. 128, no. 12, pp. 3896–3897, 2006.
- [55] R. Zou, A. I. Abdel-Fattah, H. Xu, Y. Zhao, and D. D. Hickmott, "Storage and separation applications of nanoporous metal-organic frameworks," *CrystEngComm*, vol. 12, no. 5, pp. 1337–1353, 2010.
- [56] X. S. Wang, S. Ma, D. Yuan et al., "A large-surface-area boracite-network-topology porous MOF constructed from a conjugated ligand exhibiting a high hydrogen uptake capacity," *Inorganic Chemistry*, vol. 48, no. 16, pp. 7519–7521, 2009.
- [57] J. L. C. Rowsell, J. Eckert, and O. M. Yaghi, "Characterization of  $\text{H}_2$  binding sites in prototypical metal-organic frameworks by inelastic neutron scattering," *Journal of the American Chemical Society*, vol. 127, no. 42, pp. 14904–14910, 2005.
- [58] J. L. C. Rowsell, A. R. Millward, K. S. Park, and O. M. Yaghi, "Hydrogen sorption in functionalized metal-organic frameworks," *Journal of the American Chemical Society*, vol. 126, no. 18, pp. 5666–5667, 2004.
- [59] U. Mueller, M. Schubert, F. Teich, H. Puetter, K. Schierle-Arndt, and J. Pastré, "Metal-organic frameworks—prospective industrial applications," *Journal of Materials Chemistry*, vol. 16, no. 7, pp. 626–636, 2006.
- [60] D. Britt, D. Tranchemontagne, and O. M. Yaghi, "Metal-organic frameworks with high capacity and selectivity for harmful gases," *Proceedings of the National Academy of Sciences of the United States of America*, vol. 105, no. 33, pp. 11623–11627, 2008.
- [61] L. H. Xie, J. B. Lin, X. M. Liu et al., "Porous coordination polymer with flexibility imparted by coordinatively changeable lithium ions on the pore surface," *Inorganic Chemistry*, vol. 49, no. 3, pp. 1158–1165, 2010.
- [62] A. U. Czaja, N. Trukhan, and U. Mueller, "Industrial applications of metal-organic frameworks," *Chemical Society Reviews*, vol. 38, no. 5, pp. 1284–1293, 2009.
- [63] S. J. Yang, T. Kim, J. H. Im et al., "MOF-derived hierarchically porous carbon with exceptional porosity and hydrogen storage capacity," *Chemistry of Materials*, vol. 24, no. 3, pp. 464–470, 2012.
- [64] J. An, S. J. Geib, and N. L. Rosi, "High and selective  $\text{CO}_2$  uptake in a cobalt adeninate metal-organic framework exhibiting pyrimidine- and amino-decorated pores," *Journal of the American Chemical Society*, vol. 132, no. 1, pp. 38–39, 2010.
- [65] D. Britt, H. Furukawa, B. Wang, T. G. Glover, and O. M. Yaghi, "Highly efficient separation of carbon dioxide by a metal-organic framework replete with open metal sites," *Proceedings of the National Academy of Sciences of the United States of America*, vol. 106, no. 49, pp. 20637–20640, 2009.
- [66] J. R. Li, Y. Tao, Q. Yu, X. H. Bu, H. Sakamoto, and S. Kitagawa, "Selective gas adsorption and unique structural topology of a highly stable guest-free zeolite-type MOF material with N-rich chiral open channels," *Chemistry—A European Journal*, vol. 14, no. 9, pp. 2771–2776, 2008.
- [67] J. Lee, O. K. Farha, J. Roberts, K. A. Scheidt, S. T. Nguyen, and J. T. Hupp, "Metal-organic framework materials as catalysts," *Chemical Society Reviews*, vol. 38, no. 5, pp. 1450–1459, 2009.

- [68] L. Ma, C. Abney, and W. Lin, "Enantioselective catalysis with homochiral metal-organic frameworks," *Chemical Society Reviews*, vol. 38, no. 5, pp. 1248–1256, 2009.
- [69] A. U. Czaja, N. Trukhan, and U. Müller, "Industrial applications of metal-organic frameworks," *Chemical Society Reviews*, vol. 38, no. 5, pp. 1284–1293, 2009.

## Review Article

# Graphene-Based Composites as Cathode Materials for Lithium Ion Batteries

Libao Chen,<sup>1,2</sup> Ming Zhang,<sup>2</sup> and Weifeng Wei<sup>1</sup>

<sup>1</sup> State Key Laboratory for Powder Metallurgy, Central South University, Changsha 410083, China

<sup>2</sup> Key Laboratory for Micro-Nano Optoelectronic Devices of Ministry of Education and State Key Laboratory for Chemo/Biosensing and Chemometrics, Hunan University, Changsha 410082, China

Correspondence should be addressed to Weifeng Wei; weifengmit@gmail.com

Received 30 January 2013; Accepted 27 March 2013

Academic Editor: Yongzhu Fu

Copyright © 2013 Libao Chen et al. This is an open access article distributed under the Creative Commons Attribution License, which permits unrestricted use, distribution, and reproduction in any medium, provided the original work is properly cited.

Owing to the superior mechanical, thermal, and electrical properties, graphene was a perfect candidate to improve the performance of lithium ion batteries. Herein, we review the recent advances in graphene-based composites and their application as cathode materials for lithium ion batteries. We focus on the synthesis methods of graphene-based composites and the superior electrochemical performance of graphene-based composites as cathode materials for lithium ion batteries.

## 1. Introduction

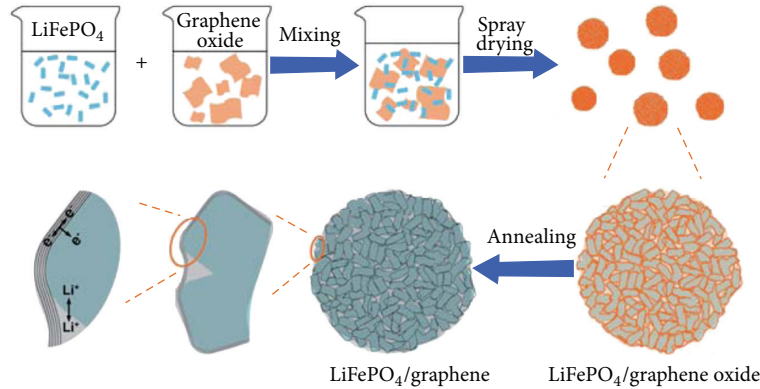
Graphene is a free-standing 2D crystal with one-atom thickness of carbon atom. Those carbon atoms are  $sp^2$ -hybridized atoms arranged in six-membered rings in a honeycombed network which is also considered as the fundamental foundation for fullerenes, carbon nanotubes, and graphite [1]. Graphene was discovered by Novoselov and coworkers in 2004 [2]. Owing to their great contribution for the study of graphene, Geim and Novoselov were awarded the Nobel Prize which was the third Nobel Prize in the field of carbon materials. As a kind of carbon materials, graphene has attracted increasing attention in a variety of fields because of its large specific surface area, good flexibility, superior chemical/thermal stability, and extraordinary electrical, and thermal, mechanical properties. With so many advantages, it is desirable to utilize the unique properties of graphene in composites through the incorporation with all kinds of functional materials [3–11]. One of the most important applications of graphene-based composites is electrode material for lithium ion batteries [12–15]. In this review, we focus on the synthesis methods and electrochemical performance of graphene-based composites as cathode materials for lithium ion batteries.

## 2. $LiMPO_4$ (M = Fe, Co, Mn, V)-Graphene Composites as Cathode Materials for LIBs

$LiFePO_4$  has been extensively investigated as cathode materials for LIBs because of low-cost, low toxicity, and relatively high theoretical specific capacity of 170 mA h/g. A significant restriction for  $LiFePO_4$  is its poor electronic conductivity (as low as  $10^{-9}$  S  $cm^{-1}$ ) which exerts negative effects on the performance of LIBs. A concept of establishing a conducting network formed by carbonaceous materials has been proposed to improve the rate performance of electrode materials [16]. Graphene possessing high conductivity, chemical stability, and mechanical performance has been demonstrated to be excellent additive to improve the electrochemical performance of  $LiFePO_4$  as cathodes for LIBs. With the help of graphene, the electrons could be transferred easily between current collectors and the  $LiFePO_4$  particles, reducing the internal resistance of the batteries and enhancing the output power. On the other hand, the excellent mechanical properties of graphene sheets are of benefit for the structure stability of electrode materials, resulting in an improved cyclic stability. Therefore, graphene sheets are beneficial to improve the properties of  $LiFePO_4$ . The first publication about  $LiFePO_4$ -graphene composites was finished by Ding and coworkers

TABLE 1: Electrochemical performance of 3D LiFePO<sub>4</sub>-graphene composites in publications.

Methods	Cycling stability	Rate capacity at 10C (mA h/g)		References
		Composites	Without graphene	
Sol-gel	140% after 100 cycles	60	45	[21]
Mechanical mixing	—	109	75	[22]
Spray drying	70% after 1000 cycles at 10C	130	110	[23]

FIGURE 1: Illustration of the synthesis procedures and the microstructure of LiFePO<sub>4</sub>-graphene composites [23].

in 2010 [17]. The composites were prepared by a coprecipitation method, which delivered a specific capacity of 160 mA h/g while there was only 113 mA h/g for bare LiFePO<sub>4</sub>. A research carried out by Su and coworkers demonstrated that graphene sheets were powerful planar conductive additive to enhance the electrochemical performance of LiFePO<sub>4</sub> [18]. The results showed that with a much lower fraction of graphene additive than those of commercial carbon-based agents, LiFePO<sub>4</sub> displayed better charge/discharge performance than commercial cases. In a later study, LiFePO<sub>4</sub>-graphene composites were prepared through a facile hydrothermal route followed by heat treatment [19]. Except the liquid reaction, a solid-state route also was used to prepare LiFePO<sub>4</sub>-graphene composites [20]. The composites with a structure of scattering graphene sheets among LiFePO<sub>4</sub> delivered a specific capacity of 161 and 70 mA h/g at 0.1C and 50C.

To improve the electronic conductivity and transformation rate of Li<sup>+</sup>, 3D porous LiFePO<sub>4</sub>-graphene composites were fabricated [21–23]. A case in point is that 3D hierarchical self-assembled LiFePO<sub>4</sub>-graphene composites were prepared by a facile template-free sol-gel method [21]. Another way to 3D LiFePO<sub>4</sub>-graphene composites included the synthesis of 3D graphene networks by CVD and following mechanical mixing of graphene networks and LiFePO<sub>4</sub> nanoparticles [22]. The electrochemical performance of the above two composites is shown in Table 1.

A more effective method to prepare LiFePO<sub>4</sub>-graphene composites with excellent performance was a spray-drying route [23]. This method is illustrated in Figure 1. LiFePO<sub>4</sub> nanoparticles were wrapped by homogeneously and loosely graphene 3D networks to form LiFePO<sub>4</sub>-graphene composites with a microsized spherical secondary structure. The spherical secondary structure was of benefit for Li<sup>+</sup> diffusion,

resulting in a high-specific capacity of 70 mA h/g at 60C discharge rate.

The electrochemical performance of LiFePO<sub>4</sub> could be further improved by modifying it with both graphene sheets and carbon layers [36–40]. For example, LiFePO<sub>4</sub>@graphene composites were prepared by a solvothermal route firstly. Then, the mixture of the above LiFePO<sub>4</sub>-graphene and citric acid was annealed at 873 K in Ar/H<sub>2</sub> to form LiFePO<sub>4</sub>@C-graphene composites [36]. Another similar route was employed to synthesis LiFePO<sub>4</sub>@C-graphene composites by using sucrose instead of citric acid [37]. Both of the above composites showed the specific capacity of 110 mA h/g at a rate of 5C. LiFePO<sub>4</sub>-graphene-C nanofibers also were fabricated by using a combination of electrospun and sol-gel techniques [38]. As cathode materials for LIBs, the composites possess high capacity, good cycling performances, and high rate capacity. A microwave-assisted hydrothermal method also was developed to synthesize LiFePO<sub>4</sub>/C/graphene composites with high efficiency and low cost [39].

FePO<sub>4</sub> as a cathode material for LIBs also has drawn much attention recently. It can be prepared at low temperature and by a facile route. Besides, amorphous FePO<sub>4</sub> exhibited continuous charge/discharge voltage profile. However, its conductance is unexpectedly lower than that of LiFePO<sub>4</sub>, resulting in its poor properties. To enhance the electrochemical performance of FePO<sub>4</sub>, FePO<sub>4</sub>-graphene composites were synthesized from an easy and simple chemical method [41]. The composites delivered a specific capacity of 156 mA h/g after 100 cycles with a coulombic efficiency of nearly 100%. At a large current density of 2.5 A/g, the capacity could retain at 100 mA h/g. In a later study, FePO<sub>4</sub>-graphene composites with hollow nanospheres were prepared by a hydrothermal method [42]. Those composites exhibited high rate capability and good cycle stability arising from the thin wall of

the hollow nanospheres and fast electron transport through the graphene networks.

Compared to  $\text{LiFePO}_4$ ,  $\text{Li}_3\text{V}_2(\text{PO}_4)_3$  is an attractive cathode material for LIBs, because its average extraction/reinsertion voltage is about 4.0 V, and its theoretical capacity is 197 mA h/g. Its intrinsic low electronic conductivity (240 nS/cm at room temperature) limits its rate capacity. Although some approaches, such as doping by metal ions and carbon coating, have been employed to enhance its performance [43], graphene sheets seemed to be a more effective additive to improve its electrochemical performance. Liu and coworkers prepared  $\text{Li}_3\text{V}_2(\text{PO}_4)_3$ -graphene composites and investigated their electrochemical performances [44, 45]. The composites prepared by a sol-gel route showed excellent rate capacity and cycling stability. The research also discovered that graphene was a more efficient carbon coating compared with the conventional carbon, which showed the advantages of graphene to improve the properties of  $\text{Li}_3\text{V}_2(\text{PO}_4)_3$ . Therefore, the rate capacities of  $\text{Li}_3\text{V}_2(\text{PO}_4)_3$ -graphene composites were much higher than those of bare  $\text{Li}_3\text{V}_2(\text{PO}_4)_3$  and the hybrids of  $\text{Li}_3\text{V}_2(\text{PO}_4)_3$  and conventional carbon.  $\text{Li}_3\text{V}_2(\text{PO}_4)_3$ /graphene composites with 3D structure were synthesized by a spray-drying process [46]. The properties of  $\text{Li}_3\text{V}_2(\text{PO}_4)_3$  could be improved further by coating the  $\text{Li}_3\text{V}_2(\text{PO}_4)_3$  with a carbon layer. The composites could deliver a capacity of 131 mA h/g at 10C after 100 cycles [47].

Compared to  $\text{LiFePO}_4$ ,  $\text{LiMnPO}_4$  is another attractive cathode for LIBs due to its higher  $\text{Li}^+$  intercalation potential of 4.1 V, resulting in about 20% higher energy density than that of  $\text{LiFePO}_4$ . However, the electrical conductivity of  $\text{LiMnPO}_4$  is ultra low (lower than  $\text{LiFePO}_4$  by five orders of magnitude). Fe-doping of  $\text{LiMnPO}_4$  has been demonstrated to be an effective method to improve its performance [48]. But its performance still lies behind the demand of consumers. Therefore,  $\text{LiMn}_{1-x}\text{Fe}_x\text{PO}_4$ -graphene composites were prepared to improve the electrochemical performances [49, 50].  $\text{LiMn}_{0.75}\text{Fe}_{0.25}\text{PO}_4$ -graphene composites with high electrical conductivity and low ionic resistance led to excellent rate properties for the otherwise extremely insulating  $\text{LiMn}_{0.75}\text{Fe}_{0.25}\text{PO}_4$  cathodes. A further investigation showed that the interaction between  $\text{LiMn}_{0.75}\text{Fe}_{0.25}\text{PO}_4$  nanorods and graphene via charge redistribution not only anchored the nanorods onto the graphene sheets but also modified their surface chemistry, resulting in an ultra-high rate capacity as cathodes for LIBs [50].

The fundamental of using graphene to improve the properties of phosphate could be indexed to follow aspects. Firstly, graphene with high conductivity could enhance the conductance of electrode materials compared to unmodified phosphate. Secondly, the good mechanical property of graphene could maintain the microstructure of phosphate and improve the cyclic stability.

### 3. Lithium Metal (Mn, Co, Ni) Oxide-Graphene Composites as Cathode Materials for LIBs

$\text{LiMn}_2\text{O}_4$  with advantages of low cost, environmental friendliness, and high abundance has drawn much attention in

recent years [51]. Its low electrical conductivity resulted in a low-rate capacity. Published papers have demonstrated that graphene sheets were effective agents to improve their conductivity and rate capacity.  $\text{LiMn}_2\text{O}_4$ -graphene composites with high rate capacity were synthesized by a microwave-assisted hydrothermal method [52]. The composites exhibited reversible capacities of 117 and 101 mA h/g at 50C and 100C. In another study,  $\text{LiMn}_2\text{O}_4$ -graphene composites were synthesized by self-assembly approach combined with a solid-state lithiation method [53]. The enhancement in electrochemical properties could be attributed to the superior  $\text{Li}^+$  diffusion kinetics and improved stability across a wide voltage window in crystalline  $\text{LiMn}_2\text{O}_4$ -graphene composites. Especially, their capacities approached the theoretical value, and the cycling stability was enhanced.

$\text{LiNi}_{1/3}\text{Mn}_{1/3}\text{Co}_{1/3}\text{O}_2$  as a promising candidate for  $\text{LiCoO}_2$  has attracted a lot of interest [54]. It shows a high energy density, good stability, enhanced safety, and low cost. However, the cation disorder occurred during calcination results in the deterioration in the kinetic property. To enhance its electrochemical performance,  $\text{LiNi}_{1/3}\text{Mn}_{1/3}\text{Co}_{1/3}\text{O}_2$ -graphene composites were prepared as cathodes for LIBs. It was reported by Jiang and coworkers that  $\text{LiNi}_{1/3}\text{Mn}_{1/3}\text{Co}_{1/3}\text{O}_2$ -graphene composites prepared by mechanical mixing could deliver a capacity of 115 mA h/g at 6C [55].  $\text{LiNi}_{1/3}\text{Mn}_{1/3}\text{Co}_{1/3}\text{O}_2$ -graphene composites prepared by microemulsion and ball-milling route could deliver a reversible capacity of 150 mA h/g at a rate of 5C, much higher than that of bare  $\text{LiNi}_{1/3}\text{Mn}_{1/3}\text{Co}_{1/3}\text{O}_2$  [56]. The improved performance was attributed to the grain connectivity and high electronic conductivity.  $\text{LiNi}_{0.8}\text{Co}_{0.15}\text{Al}_{0.05}\text{O}_2$ -graphene also was prepared by a high mechanical ball-milling method. They exhibited the high capacity of 180 mA h/g with good cycle stability [57].

### 4. Sulfur-Graphene Composites as Cathode Materials for LIBs

The lower specific capacities of cathode materials (about 150 mA h/g for layered oxides and 170 mA h/g for  $\text{LiFePO}_4$ ) compared to those of anodes (370 mA h/g for graphene and 993 mA h/g for tin) have been a limiting factor to improve the energy density of LIBs. As a cathode for LIBs, sulfur possesses a theoretical specific capacity of 1675 mA h/g which is about five times higher than those of traditional cathode materials [58]. Its disadvantages of the low electrical conductivity and dissolution of polysulfides in electrolyte also are obvious. Sulfur-graphene composite has been demonstrated to be one way to improve the electrochemical performance of sulfur in LIBs.

The first report about S-graphene composite as cathode for LIBs was available online in October of 2010, which was completed by Wang and coworkers [24]. The composites, prepared by the heat treatment of the mixture of graphene sheets and elemental sulfur, exhibited a specific capacity of 600 mA h/g after 40 cycles at a current density of 50 mA/g. An improved method of preparing S-graphene

TABLE 2: Electrochemical performance of S-graphene composites in the literatures.

Structure	Method	Capacity	References
Graphene coated by S particles	Heat mixing	400 mA h/g after 40 cycles	[24]
Sandwich-type	Solution-mixing	505 mA h/g after 100 cycles	[25]
S particles wrapped by graphene	Self-assembly	600 mA h/g after 100 cycles	[26]
S particles in graphene	Oil/water system	620 mA h/g after 60 cycles at 1C	[27]
—	Deposition from $\text{Na}_2\text{S}_x$	950 mA h/g after 55 cycles	[28]
Wrinkled laminar structure	Deposition from $\text{Na}_2\text{S}_2\text{O}_3$	667 mA h/g after 200 cycles	[29]
S particles in graphene sheets	Deposition from $\text{Na}_2\text{S}_2\text{O}_3$	830 mA h/g after 50 cycles	[30]
S in the pores of activated graphene	Melt-diffusion	1000 mA h/g after 60 cycles at 0.2C	[31]
S particles on graphene	Melting diffusion	957 mA h/g after 50 cycles	[32]
Ternary composites	In situ polymerization	560 mA h/g after 100 cycles	[33]
Sandwich-type	Heat mixing	800 mA h/g after 100 cycles	[34]
S in the porous graphene	Melt-diffusion	755 mA h/g at 0.1C	[35]

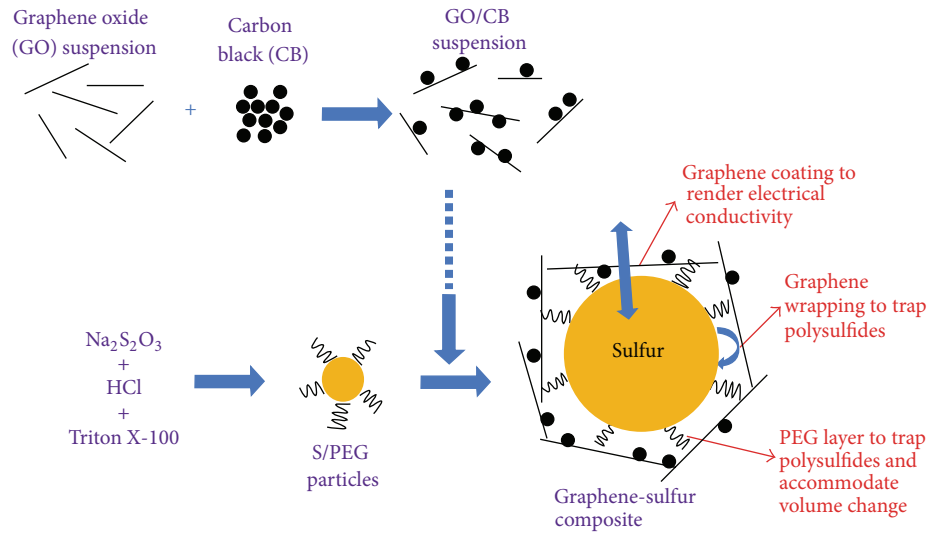


FIGURE 2: Illustration of the synthesis procedures for S-graphene composites and a proposed schematic structure of the composite [26].

by mixing graphene with the solution of sulfur was developed by Cao and coworkers [25]. The composites with a sandwich structure could deliver a specific capacity of 750 mA h/g after 50 cycles at a current density of 168 mA/g. To further improve the electrochemical performance, S-graphene composites with a wrapped structure were synthesized [26]. Improved performance was achieved by the graphene-wrapped composites which could be attributed to sulfur particles of well coated and confined by graphene sheets and meanwhile integrated polymeric cushions in composites. The synthesis method and the microstructure of composites were illustrated in Figure 2. An oil/water system also could be employed to prepare sulfur/graphene with a core/shell structure [27].

To modify the interface between graphene and sulfur, sulfur was anchored on graphene sheets by using  $\text{Na}_2\text{S}_x$  as sulfur sources [28]. Graphene sheets were coated by a uniform and thin sulfur to form S-graphene composites. A similar method by employing  $\text{Na}_2\text{S}_2\text{O}_3$  as sulfur source also was used to prepare S-graphene composites [29]. To improve

the electrochemical performance of S-graphene composites, graphene was treated by HF to eliminate impurities and create active sites for the nucleation of sulfur particles on graphene sheets [30]. The composites showed a specific capacity of 830 mA h/g after 50 cycles at a current density of 168 mA/g, much higher than that of S-carbon composites. Another active method for graphene is based on the thermal process with KOH [31].

S-graphene composites with a layer-by-layer structure were synthesized by melt-diffusion strategy [32]. A dwindled over-discharged phenomenon and excellent rate capability were achieved by the composites. To avoid the dissolution of polysulfides and improve the performance of composites, polyacrylonitrile-sulfur-graphene composites were prepared by an in situ polymerization approach [33]. Table 2 shows some results about S-graphene composites as cathodes for LIBs. The improved performance of S-graphene composites could be ascribed to graphene sheets, which acted as conductive agent to enhance conductivity and protective layer to block the diffusion of polysulfides.

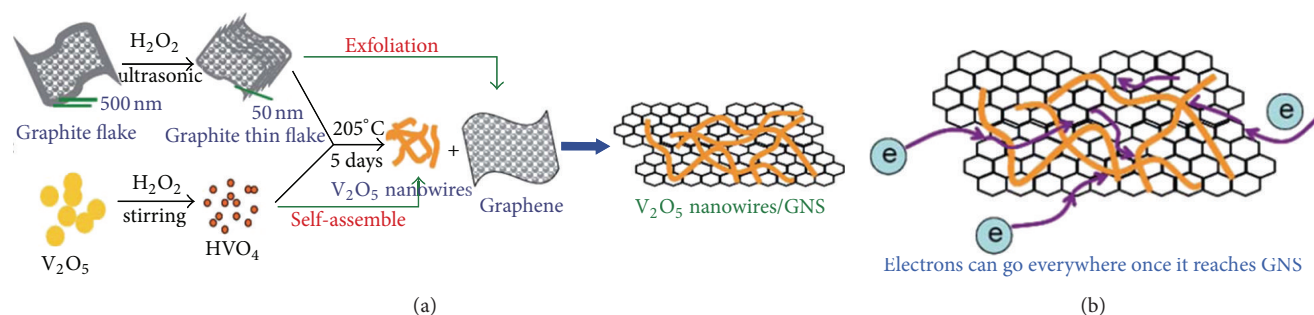


FIGURE 3: (a) Illustration of the synthesis route of  $V_2O_5$ -graphene composites. (b) Ideal electron transfer pathway for  $V_2O_5$ -graphene composites [60].

The enhancement of S-graphene as cathodes for LIBs could be ascribed to the following reasons. Firstly, graphene sheets as good electronic conductors could enhance the conductance of sulfur-based materials. Secondly, the layered graphene sheets with good sealability could prevent the loss of polysulfides.

## 5. Metal Oxide-Graphene Composites as Cathode Materials for LIBs

$V_2O_5$  is one of the most promising candidates for cathodes for LIBs because of its intercalation structure, low-cost, and high energy density [59]. However, the practical application of  $V_2O_5$  is limited by sluggish kinetics of electron and  $Li^+$  transport, resulting in low specific capacities at high rates and poor cyclability. Carbon has been introduced as a composite component to enhance electrical conductivity and prevent the vanadium dissolution. As a kind of carbon materials, graphene has attracted much attention in the field of LIBs. Especially,  $V_2O_5$ -graphene composites were investigated as cathodes for LIBs.

$V_2O_5 \cdot nH_2O$  synthesized via a simple hydrothermal route was mechanically mixed with graphene sheets to form  $V_2O_5 \cdot nH_2O$ -graphene composites [61]. The composites with a structure of  $V_2O_5 \cdot nH_2O$  ribbons on graphene sheets could deliver a reversible capacity of 190 mA h/g after 50 cycles. The graphene-based composites involved a metastable monoclinic polymorph of  $VO_2$  also were prepared by a hydrothermal method, which delivered a high capacity of 450 mA h/g [62]. Thermal decomposition also was used to prepare  $V_2O_5$ -graphene composites by employing  $(NH_4)_2V_2O_6$ -graphene as precursors [63]. The composites showed a specific capacity of 178 mA h/g after 50 cycles at a current density of 0.3 A/g. The improved performance was ascribed to the conductive network built by graphene sheets.  $V_2O_5$ -graphene composites with a discharge capacity of 202 mA h/g after 50 cycles were synthesized by a hydrothermal route based on the hydrolysis of  $VO(OiPr)_3$  [64]. A modified hydrothermal method of using graphite as precursors were developed to prepare  $V_2O_5$ -graphene composites, as shown in Figure 3 [60]. The composites with structure of  $V_2O_5$  ribbons on graphene sheets were obtained. Due to the improved conductance,  $V_2O_5$ -graphene composites showed a specific capacity

of 190 mA h/g after 50 cycles.  $V_2O_5$  with extremely stable cycling was achieved by preparing  $V_2O_5$ /graphene composites using a facile vacuum filtration method [65]. They could deliver the capacity of 0.1 A h/g after 100,000 cycles at a current density of 10 A/g. The improvement could be ascribed to the graphene sheets which are excellent electronic conductor and could reduce the polarization of LIBs.

$MnO_2$ -graphene composites could be used as anodes for LIBs. They could be used as cathodes as well.  $MnO_2$ -graphene composites were synthesized by immersing graphene sheets into a  $KMnO_4$  aqueous solution [66]. A reversible capacity of 230 mA h/g after 150 cycles was obtained by employing sodium alginate as a binder. When PVDF was used as a binder, a bad performance of 115 mA h/g after 150 cycles was achieved.

## 6. Other Graphene-Based Composites as Cathode Materials for LIBs

Except above composites, there are a few graphene-based composites which could be used as cathodes for LIBs. A case in point is that  $Ag_2V_4O_{11}$ -graphene composites were prepared for LIBs [67]. The composites were fabricated by mechanical mixing of carbon fluoride,  $Ag_2V_4O_{11}$ , and graphene. The ternary composites showed a specific capacity of 480 mA h/g at a rate of 5C. The impedance analysis demonstrated that the charge transfer resistance of composites is very low, accounting for excellent rate capability.  $FeF_3$  has drawn much attention owing to its high capacity and electrical insulating. Its property could be improved by modifying it with graphene. The composites could deliver a capacity of 200 mA h/g after 80 cycles [68]. The properties of iron fluoride-graphene composites could be improved further by preparing  $LiF/Fe/graphene$  composites [69]. The composites showed a high reversible capacity of 150 mA h/g after 180 cycles.

## 7. Perspectives and Challenges

Herein, we have reviewed the preparation and application of graphene-based composites as cathode materials for LIBs. In those graphene-based composites, emphasis is given to the synthesis methods and the synergistic effects between

graphene and cathode materials. A variety of published papers are the evidences that graphene sheets are desirable candidates for enhancing the performance of cathode materials for LIBs to meet the demands of consumers.

Graphene-based cathode materials are of so many advantages. However, more effort should be made to overcome the following challenges for the commercial application of graphene-based cathode materials. (1) The effect of graphene precursor (GO) on the morphology of cathode materials are not very clear at this moment. There are some oxygen-containing groups on GO. Published papers have demonstrated that those groups affect the crystal growth of cathode materials. However, the detailed mechanism is not clear. (2) Rational design and controllable synthesis of cathode materials are of great significance for commercial application. (3) Developing the synthesis methods of graphene-based cathode materials, with low cost and environmentally-friendly, is very necessary for the industrial production. Although the precursor of graphene (graphite) is abundant on the earth, the common precursor of graphene is GO, needing many steps and reagents to transfer from graphite. The traditional approach for the synthesis of GO needs so many chemicals, leading to a high cost and potential damage to the environment. So many interesting results have been achieved from the investigation of graphene-based cathode materials. With continuous investigation of worldwide scientists, it is believed that graphene-based cathode materials for LIBs will be used in many fields, such as personal movable tools and hybrid electric vehicles.

## Acknowledgments

This project was supported by The Postdoctoral Science Foundation of Central South University and National Natural Science Foundation of China (21103046).

## References

- [1] A. K. Geim and K. S. Novoselov, "The rise of graphene," *Nature Materials*, vol. 6, no. 3, pp. 183–191, 2007.
- [2] K. S. Novoselov, A. K. Geim, S. V. Morozov et al., "Electric field in atomically thin carbon films," *Science*, vol. 306, no. 5696, pp. 666–669, 2004.
- [3] I. Meric, M. Y. Han, A. F. Young, B. Ozyilmaz, P. Kim, and K. L. Shepard, "Current saturation in zero-bandgap, top-gated graphene field-effect transistors," *Nature Nanotechnology*, vol. 3, no. 11, pp. 654–659, 2008.
- [4] Y. M. Lin, K. A. Jenkins, V. G. Alberto, J. P. Small, D. B. Farmer, and P. Avouris, "Operation of graphene transistors at gigahertz frequencies," *Nano Letters*, vol. 9, no. 1, pp. 422–426, 2009.
- [5] Y. M. Lin, C. Dimitrakopoulos, K. A. Jenkins et al., "100-GHz transistors from wafer-scale epitaxial graphene," *Science*, vol. 327, no. 5966, p. 662, 2010.
- [6] Y. Dan, Y. Lu, N. J. Kybert, Z. Luo, and A. T. C. Johnson, "Intrinsic response of graphene vapor sensors," *Nano Letters*, vol. 9, no. 4, pp. 1472–1475, 2009.
- [7] G. Lu, L. E. Ocola, and J. Chen, "Reduced graphene oxide for room-temperature gas sensors," *Nanotechnology*, vol. 20, no. 22, Article ID 445502, 2009.
- [8] S. Guo and S. Dong, "Graphene nanosheet: synthesis, molecular engineering, thin film, hybrids, and energy and analytical applications," *Chemical Society Reviews*, vol. 40, pp. 2644–2672, 2011.
- [9] N. G. Shang, P. Papakonstantinou, M. McMullan et al., "Catalyst-free efficient growth, orientation and biosensing properties of multilayer graphene nanoflake films with sharp edge planes," *Advanced Functional Materials*, vol. 18, no. 21, pp. 3506–3514, 2008.
- [10] C. Liu, Z. Yu, D. Neff, A. Zhamu, and B. Z. Jang, "Graphene-based supercapacitor with an ultrahigh energy density," *Nano Letters*, vol. 10, no. 12, pp. 4863–4868, 2010.
- [11] E. J. Yoo, J. Kim, E. Hosono, H. S. Zhou, T. Kudo, and I. Honma, "Large reversible Li storage of graphene nanosheet families for use in rechargeable lithium ion batteries," *Nano Letters*, vol. 8, no. 8, pp. 2277–2282, 2008.
- [12] S. M. Paek, E. Yoo, and I. Honma, "Enhanced cyclic performance and lithium storage capacity of SnO<sub>2</sub>/graphene nanoporous electrodes with three-dimensionally delaminated flexible structure," *Nano Letters*, vol. 9, no. 1, pp. 72–75, 2009.
- [13] M. Zhang, D. Lei, X. Yin et al., "Magnetite/graphene composites: microwave irradiation synthesis and enhanced cycling and rate performances for lithium ion batteries," *Journal of Materials Chemistry*, vol. 20, no. 26, pp. 5538–5543, 2010.
- [14] Z. S. Wu, W. Ren, L. Wen et al., "Graphene anchored with Co<sub>3</sub>O<sub>4</sub> nanoparticles as anode of lithium ion batteries with enhanced reversible capacity and cyclic performance," *ACS Nano*, vol. 4, no. 6, pp. 3187–3194, 2010.
- [15] Y. J. Mai, D. Zhang, Y. Q. Qiao, C. D. Gu, X. L. Wang, and J. P. Tu, "MnO/reduced graphene oxide sheet hybrid as an anode for Li-ion batteries with enhanced lithium storage performance," *Journal of Power Sources*, vol. 216, pp. 201–207, 2012.
- [16] Y. Wang, Y. Wang, E. Hosono, K. Wang, and H. Zhou, "The design of a LiFePO<sub>4</sub>/carbon nanocomposite with a core-shell structure and its synthesis by an in situ polymerization restriction method," *Angewandte Chemie*, vol. 47, no. 39, pp. 7461–7465, 2008.
- [17] Y. Ding, Y. Jiang, F. Xu et al., "Preparation of nano-structured LiFePO<sub>4</sub>/graphene composites by co-precipitation method," *Electrochemistry Communications*, vol. 12, no. 1, pp. 10–13, 2010.
- [18] F. Y. Su, C. You, Y. B. He et al., "Flexible and planar graphene conductive additives for lithium-ion batteries," *Journal of Materials Chemistry*, vol. 20, pp. 9644–9650, 2010.
- [19] L. Wang, H. Wang, Z. Liu et al., "A facile method of preparing mixed conducting LiFePO<sub>4</sub>/graphene composites for lithium-ion batteries," *Solid State Ionics*, vol. 181, no. 37–38, pp. 1685–1689, 2010.
- [20] Y. Wang, Z. S. Feng, J. J. Chen, and C. Zhang, "Synthesis and electrochemical performance of LiFePO<sub>4</sub>/graphene composites by solid-state reaction," *Materials Letters*, vol. 71, pp. 54–56, 2012.
- [21] J. Yang, J. Wang, D. Wang et al., "3D porous LiFePO<sub>4</sub>/graphene hybrid cathodes with enhanced performance for Li-ion batteries," *Journal of Power Sources*, vol. 208, pp. 340–344, 2012.
- [22] Y. Tang, F. Huang, H. Bi, Z. Liu, and D. Wan, "Highly conductive three-dimensional graphene for enhancing the rate performance of LiFePO<sub>4</sub> cathode," *Journal of Power Sources*, vol. 203, pp. 130–134, 2012.
- [23] X. Zhou, F. Wang, Y. Zhu, and Z. Liu, "Graphene modified LiFePO<sub>4</sub> cathode materials for high power lithium ion batteries," *Journal of Materials Chemistry*, vol. 21, pp. 3353–3358, 2011.

- [24] J. Z. Wang, L. Lu, M. Choucair, J. A. Stride, X. Xu, and H. K. Liu, "Sulfur-graphene composite for rechargeable lithium batteries," *Journal of Power Sources*, vol. 196, no. 16, pp. 7030–7034, 2011.
- [25] Y. Cao, X. Li, I. A. Aksay et al., "Sandwich-type functionalized graphene sheet-sulfur nanocomposite for rechargeable lithium batteries," *Physical Chemistry Chemical Physics*, vol. 13, no. 17, pp. 7660–7665, 2011.
- [26] H. Wang, Y. Yang, Y. Liang et al., "Graphene-wrapped sulfur particles as a rechargeable lithium-sulfur battery cathode material with high capacity and cycling stability," *Nano Letters*, vol. 11, pp. 2644–2647, 2011.
- [27] F. Zhang, X. Zhang, Y. Dong, and L. Wang, "Facile and effective synthesis of reduced graphene oxide encapsulated sulfur *via* oil/water system for high performance lithium sulfur cells," *Journal of Materials Chemistry*, vol. 22, pp. 11452–11454, 2012.
- [28] L. Ji, M. Rao, H. Zheng et al., "Graphene oxide as a sulfur immobilizer in high performance lithium/sulfur cells," *Journal of the American Chemical Society*, vol. 133, pp. 18522–18525, 2011.
- [29] N. Li, M. Zheng, H. Lu et al., "High-rate lithium-sulfur batteries promoted by reduced graphene oxide coating," *Chemical Communications*, vol. 48, pp. 4106–4108, 2012.
- [30] M. S. Park, J. S. Yu, K. J. Kim et al., "One-step synthesis of a sulfur-impregnated graphene cathode for lithium-sulfur batteries," *Physical Chemistry Chemical Physics*, vol. 14, pp. 6796–6804, 2012.
- [31] B. Ding, C. Yuang, L. Shen et al., "Chemically tailoring the nanostructure of graphene nanosheets to confine sulfur for high-performance lithium-sulfur batteries," *Journal of Materials Chemistry A*, vol. 1, pp. 1096–1101, 2013.
- [32] Y. X. Wang, L. Huang, L. C. Sun et al., "Facile synthesis of a interleaved expanded graphite-embedded sulphur nanocomposite as cathode of Li-S batteries with excellent lithium storage performance," *Journal of Materials Chemistry*, vol. 22, pp. 4744–4750, 2012.
- [33] L. Yin, J. Wang, F. Lin, J. Yang, and Y. Nuli, "Polyacrylonitrile/graphene composite as a precursor to a sulfur-based cathode material for high-rate rechargeable Li-S batteries," *Energy & Environmental Science*, vol. 5, pp. 6966–6972, 2012.
- [34] B. Wang, K. Li, D. Su, H. Ahn, and G. Wang, "Superior electrochemical performance of sulfur/graphene nanocomposite material for high-capacity lithium-sulfur batteries," *Chemistry*, vol. 7, pp. 1637–1643, 2012.
- [35] J. Q. Huang, X. F. Liu, Q. Zhang et al., "Entrapment of sulfur in hierarchical porous graphene for lithium-sulfur batteries with high rate performance from  $-40$  to  $60^{\circ}\text{C}$ ," *Nano Energy*, vol. 2, no. 2, pp. 314–321, 2013.
- [36] C. Su, X. Bu, L. Xu, J. Liu, and C. Zhang, "A novel  $\text{LiFePO}_4$ /graphene/carbon composite as a performance-improved cathode material for lithium-ion batteries," *Electrochimica Acta*, vol. 64, pp. 190–195, 2012.
- [37] Y. Zhang, W. Wang, P. Li, Y. Fu, and X. Ma, "A simple solvothermal route to synthesize graphene-modified  $\text{LiFePO}_4$  cathode for high power lithium ion batteries," *Journal of Power Sources*, vol. 210, pp. 47–53, 2012.
- [38] O. Toprakci, H. A. K. Toprakci, L. Ji, Z. Lin, R. Gu, and X. J. Zhang, " $\text{LiFePO}_4$  nanoparticles encapsulated in graphene-containing carbon nanofibers for use as energy storage materials," *Renewable Sustainable Energy*, vol. 4, Article ID 013121, 10 pages, 2012.
- [39] Y. Shi, S. L. Chou, J. Z. Wang et al., "Graphene wrapped  $\text{LiFePO}_4$ /C composites as cathode materials for Li-ion batteries with enhanced rate capability," *Journal of Materials Chemistry*, vol. 22, no. 32, pp. 16465–16470, 2012.
- [40] H. Bi, F. Huang, Y. Tang et al., "Study of  $\text{LiFePO}_4$  cathode modified by graphene sheets for high-performance lithium ion batteries," *Electrochimica Acta*, vol. 88, pp. 414–420, 2013.
- [41] H. Kim, S. W. Kim, J. Hong et al., "Graphene-based hybrid electrode material for high-power lithium-ion batteries," *Journal of the Electrochemical Society*, vol. 158, pp. A930–A935, 2011.
- [42] Y. Yin, Y. Hu, P. Wu, H. Zhang, and C. Cai, "A graphene-amorphous  $\text{FePO}_4$  hollow nanosphere hybrid as a cathode material for lithium ion batteries," *Chemical Communications*, vol. 48, no. 15, pp. 2137–2139, 2012.
- [43] M. M. Ren, Z. Zhou, X. P. Gao, W. X. Peng, and J. P. Wei, "Core-shell  $\text{Li}_3\text{V}_2(\text{PO}_4)_3$ @C composites as cathode materials for lithium-ion batteries," *The Journal of Physical Chemistry C*, vol. 112, pp. 5689–5693, 2008.
- [44] H. Liu, P. Gao, J. Fang, and G. Yang, " $\text{Li}_3\text{V}_2(\text{PO}_4)_3$ /graphene nanocomposites as cathode material for lithium ion batteries," *Chemical Communications*, vol. 47, no. 32, pp. 9110–9112, 2011.
- [45] H. Liu, G. Yang, X. Zhang et al., "Kinetics of conventional carbon coated- $\text{Li}_3\text{V}_2(\text{PO}_4)_3$  and nanocomposite  $\text{Li}_3\text{V}_2(\text{PO}_4)_3$ /graphene as cathode materials for lithium ion batteries," *Journal of Materials Chemistry*, vol. 22, pp. 11039–11047, 2012.
- [46] Y. Jiang, W. Xu, D. Chen et al., "Graphene modified  $\text{Li}_3\text{V}_2(\text{PO}_4)_3$  as a high-performance cathode material for lithium ion batteries," *Electrochimica Acta*, vol. 85, pp. 377–383, 2012.
- [47] L. Zhang, S. Wang, D. Cai et al., " $\text{Li}_3\text{V}_2(\text{PO}_4)_3$ /C/graphene composite with improved cycling performance as cathode material for lithium-ion batteries," *Electrochimica Acta*, vol. 91, pp. 108–113, 2013.
- [48] G. R. Gardiner and M. S. Islam, "Anti-site defects and ion migration in the  $\text{LiFe}_{0.5}\text{Mn}_{0.5}\text{PO}_4$  mixed-metal cathode material," *Chemistry of Materials*, vol. 22, no. 3, pp. 1242–1248, 2010.
- [49] H. Wang, Y. Yang, Y. Liang et al., " $\text{LiMn}_{1-x}\text{Fe}_x\text{PO}_4$  nanorods grown on graphene sheets for ultrahigh-rate-performance lithium ion batteries," *Angewandte Chemie*, vol. 50, no. 32, pp. 7364–7368, 2011.
- [50] J. Zhou, J. Wang, L. Zuin et al., "Spectroscopic understanding of ultra-high rate performance for  $\text{LiMn}_{0.75}\text{Fe}_{0.25}\text{PO}_4$  nanorods-graphene hybrid in lithium ion battery," *Physical Chemistry Chemical Physics*, vol. 14, pp. 9578–9581, 2012.
- [51] V. Manev, B. Banov, A. Momchilov, and A. Nassalevska, " $\text{LiMn}_2\text{O}_4$  for 4 V lithium-ion batteries," *Journal of Power Sources*, vol. 57, no. 1-2, pp. 99–103, 1995.
- [52] S. M. Bak, K. W. Nam, C. W. Lee et al., "Spinel  $\text{LiMn}_2\text{O}_4$ /reduced graphene oxide hybrid for high rate lithium ion batteries," *Journal of Materials Chemistry*, vol. 21, pp. 17309–17315, 2011.
- [53] X. Zhao, C. M. Hayner, and H. H. Hung, "Self-assembled lithium manganese oxide nanoparticles on carbon nanotube or graphene as high-performance cathode material for lithium-ion batteries," *Journal of Materials Chemistry*, vol. 21, pp. 17297–17303, 2011.
- [54] H. S. Kim, S. I. Kim, and W. S. Kim, "A study on electrochemical characteristics of  $\text{LiCoO}_2/\text{LiNi}_{1/3}\text{Mn}_{1/3}\text{Co}_{1/3}\text{O}_2$  mixed cathode for Li secondary battery," *Electrochimica Acta*, vol. 52, pp. 1457–1461, 2006.
- [55] K. C. Jiang, S. Xin, J. S. Lee, J. Kim, X. L. Xiao, and Y. G. Guo, "Improved kinetics of  $\text{LiNi}_{1/3}\text{Mn}_{1/3}\text{Co}_{1/3}\text{O}_2$  cathode material through reduced graphene oxide networks," *Physical Chemistry Chemical Physics*, vol. 14, pp. 2934–2939, 2012.

- [56] C. V. Rao, A. L. M. Reddy, Y. Ishikawa, and P. M. Ajayan, "LiNi<sub>1/3</sub>Co<sub>1/3</sub>Mn<sub>1/3</sub>O<sub>2</sub>-graphene composite as a promising cathode for lithium-ion batteries," *ACS Applied Materials & Interfaces*, vol. 3, pp. 2966–2972, 2011.
- [57] S. Yoon, K. N. Jung, S. H. Yeon, C. S. Jin, and K. H. Shin, "Electrochemical properties of LiNi<sub>0.8</sub>Co<sub>0.15</sub>Al<sub>0.05</sub>O<sub>2</sub>-graphene composite as cathode materials for lithium-ion batteries," *Journal of Electroanalytical Chemistry*, vol. 683, pp. 88–93, 2012.
- [58] X. Ji, K. T. Lee, and L. F. Nazar, "A highly ordered nanostructured carbon-sulphur cathode for lithium-sulphur batteries," *Nature Materials*, vol. 8, pp. 500–506, 2009.
- [59] D. Yu, C. Chen, S. Xie et al., "Mesoporous vanadium pentoxide nanofibers with significantly enhanced Li-ion storage properties by electrospinning," *Energy & Environmental Science*, vol. 4, pp. 858–861, 2011.
- [60] H. Liu and W. Yang, "Ultralong single crystalline V<sub>2</sub>O<sub>5</sub> nanowire/graphene composite fabricated by a facile green approach and its lithium storage behavior," *Energy & Environmental Science*, vol. 4, pp. 4000–4008, 2011.
- [61] G. Du, K. H. Seng, Z. Guo et al., "Graphene-V<sub>2</sub>O<sub>5</sub>·nH<sub>2</sub>O xerogel composite cathodes for lithium ion batteries," *RSC Advances*, vol. 1, pp. 690–697, 2011.
- [62] C. Nethravathi, B. Viswanath, J. Michael, and M. Rajamath, "Hydrothermal synthesis of a monoclinic VO<sub>2</sub> nanotube-graphene hybrid for use as cathode material in lithium ion batteries," *Carbon*, vol. 50, pp. 4839–4846, 2012.
- [63] Z. L. Wang, D. Xu, Y. Huang, Z. Wu, L. M. Wang, and X. B. Zhang, "Facile, mild and fast thermal-decomposition reduction of graphene oxide in air and its application in high-performance lithium batteries," *Chemical Communications*, vol. 48, pp. 976–978, 2012.
- [64] X. Rui, J. Zhu, D. Sim et al., "Reduced graphene oxide supported highly porous V<sub>2</sub>O<sub>5</sub> spheres as a high-power cathode material for lithium ion batteries," *Nanoscale*, vol. 3, pp. 4752–4758, 2011.
- [65] J. W. Lee, S. Y. Lim, H. M. Jeong, T. H. Hwang, and J. K. Kang, "Extremely stable cycling of ultra-thin V<sub>2</sub>O<sub>5</sub> nanowire-graphene electrodes for lithium rechargeable battery cathodes," *Energy & Environmental Science*, vol. 5, pp. 9889–9894, 2012.
- [66] J. Li, Y. Zhao, N. Wang, Y. Ding, and L. Guan, "Enhanced performance of a MnO<sub>2</sub>-graphene sheet cathode for lithium ion batteries using sodium alginate as a binder," *Journal of Materials Chemistry*, vol. 22, pp. 13002–13004, 2012.
- [67] P. Meduri, H. Chen, X. Chen et al., "Hybrid CF<sub>x</sub>-Ag<sub>2</sub>V<sub>4</sub>O<sub>11</sub> as a high-energy, power density cathode for application in an underwater acoustic microtransmitter," *Electrochemical Communications*, vol. 13, pp. 1344–1348, 2011.
- [68] X. Zhao, C. M. Hayner, M. C. Kung, and K. Kung, "Photothermal-assisted fabrication of iron fluoride-graphene composite paper cathodes for high-energy lithium-ion batteries," *Chemical Communications*, vol. 48, pp. 9909–9911, 2012.
- [69] R. Ma, Y. Dong, L. Xi, S. Yang, Z. Lu, and C. Chung, "Fabrication of LiF/Fe/Graphene nanocomposites as cathode material for lithium-ion batteries," *ACS Applied Materials & Interfaces*, vol. 5, no. 3, pp. 892–897, 2013.

## Review Article

# Ag<sub>3</sub>PO<sub>4</sub> Semiconductor Photocatalyst: Possibilities and Challenges

Gui-Fang Huang, Zhi-Li Ma, Wei-Qing Huang, Yong Tian, Chao Jiao, Zheng-Mei Yang, Zhuo Wan, and Anlian Pan

Department of Applied Physics, Key Laboratory for Micro-Nano Physics and Technology of Hunan Province, Hunan University, Changsha 410082, China

Correspondence should be addressed to Wei-Qing Huang; wqhuang@hnu.edu.cn

Received 30 January 2013; Accepted 8 March 2013

Academic Editor: Yongzhu Fu

Copyright © 2013 Gui-Fang Huang et al. This is an open access article distributed under the Creative Commons Attribution License, which permits unrestricted use, distribution, and reproduction in any medium, provided the original work is properly cited.

Ag<sub>3</sub>PO<sub>4</sub> as a photocatalyst has attracted enormous attention in recent years due to its great potential in harvesting solar energy for environmental purification and fuel production. The photocatalytic performance of Ag<sub>3</sub>PO<sub>4</sub> strongly depends on its morphology, exposed facets, and particle size. The effects of morphology and orientation of Ag<sub>3</sub>PO<sub>4</sub> on the catalytic performance and the efforts on the stability improvement of Ag<sub>3</sub>PO<sub>4</sub> are reviewed here. This paper also discusses the current theoretical understanding of photocatalytic mechanism of Ag<sub>3</sub>PO<sub>4</sub>, together with the recent progress towards developing Ag<sub>3</sub>PO<sub>4</sub> composite photocatalysts. The crucial issues that should be addressed in future research activities are finally highlighted.

## 1. Introduction

The development of efficient photocatalysts is very important and desirable in environmental pollution mediation and solar energy conversion [1–6]. Over the past decades, fundamental progress has been made in developing novel photocatalysts, particularly visible light response catalysts for the efficient utilization of solar energy. A great deal of photocatalysts, including inorganic, molecular, and hybrid organic/inorganic materials, have been explored to meet specific requirements such as a light-absorbing wavelength modification, photoinduced charge separation, and a faster photocatalytic reaction. Among the various photocatalysts developed, TiO<sub>2</sub> is undoubtedly the most popular and widely used photocatalyst since it is of low cost, high photocatalytic activity, chemical and photochemical stability [7, 8]. However, TiO<sub>2</sub> is not ideal for all purposes and performs rather poorly in processes associated with solar photocatalysis due to its wide band gap (3–3.2 eV), thus making impractical overall technological process based on TiO<sub>2</sub>. To design visible-light-driven photocatalysts, two strategies have been proposed. One is to modify the wide band gap photocatalysts (such as TiO<sub>2</sub>, ZnS) by doping or by producing

hetero-junctions between them and other materials [4, 7–12], and the other involves exploration of novel semiconductor materials capable of absorbing visible light. Various compounds, such as BiVO<sub>4</sub> [13], Bi<sub>2</sub>WO<sub>6</sub> [1, 14], CaBi<sub>2</sub>O<sub>4</sub> [15], PbBi<sub>2</sub>Nb<sub>2</sub>O<sub>9</sub> [16], Bi<sub>4</sub>Ti<sub>3</sub>O<sub>12</sub> [17], and Ag@AgCl [18], and others have been reported to be promising photocatalysts under visible light irradiation [19–22]. Despite many of these photocatalysts being effective for the degradation of organic pollutants and water splitting, up to date, the present achievements are still far from the ideal goal.

Yi and his coworkers [23] have recently presented the pioneering work on exploring the photocatalytic properties of Ag<sub>3</sub>PO<sub>4</sub> that exhibit extremely high photooxidative capabilities for the O<sub>2</sub> evolution from water and the decomposition of organic dyes under visible-light irradiation. Actually, the photodegradation rate of organic dyes over Ag<sub>3</sub>PO<sub>4</sub> is dozens of times faster than the rate over BiVO<sub>4</sub> and commercial TiO<sub>2-x</sub>N<sub>x</sub> [23, 24]. Moreover, the most interesting is that this novel photocatalyst can achieve a quantum efficiency of up to 90% at wavelengths greater than 420 nm, which is significantly higher than the previous reported values. This finding potentially opens an avenue for solving current energy crisis and environment problems with abundant solar light, and the

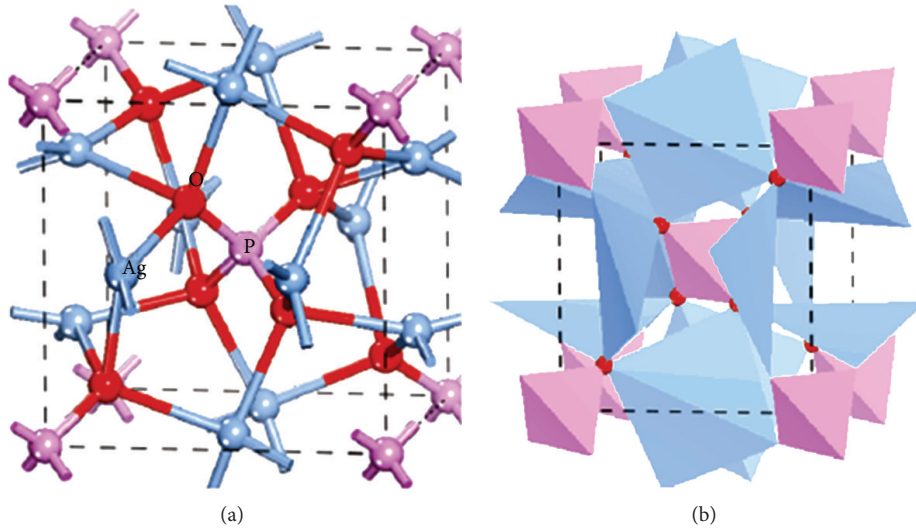


FIGURE 1: Unit-cell structure of cubic  $\text{Ag}_3\text{PO}_4$ , showing (a) ball and stick and (b) polyhedron configurations. Red, purple, and blue spheres represent O, P, and Ag atoms, respectively [24].

research of  $\text{Ag}_3\text{PO}_4$  is thus attracting considerable interest. Since then, many efforts have been devoted to further improving and optimizing their photoelectric and photocatalytic properties. Despite the fact that  $\text{Ag}_3\text{PO}_4$  is a promising candidate for environmental remediation and renewable energy, the consumption of a large amount of noble metal and the low structural stability of pure  $\text{Ag}_3\text{PO}_4$  strongly limits its practical environmental applications. Therefore, it is a highly crucial task to improve the photocatalytic stability of  $\text{Ag}_3\text{PO}_4$  while maintaining its high photocatalytic activity. In this paper, the effects of morphology and orientation of  $\text{Ag}_3\text{PO}_4$  on the catalytic performance and the current theoretical understanding of key aspects of  $\text{Ag}_3\text{PO}_4$  photocatalysts are presented. Also reviewed is the effort on the photocatalytic stability of  $\text{Ag}_3\text{PO}_4$  and  $\text{Ag}_3\text{PO}_4$  composite photocatalyst.

## 2. The Structure of $\text{Ag}_3\text{PO}_4$

$\text{Ag}_3\text{PO}_4$  is of body-centred cubic structure type with space group  $P4-3n$  and a lattice parameter of  $\sim 6.004 \text{ \AA}$ . The structure consists of isolated, regular  $\text{PO}_4$  tetrahedra (P–O distance of  $\sim 1.539 \text{ \AA}$ ) forming a body-centred-cubic lattice. The six  $\text{Ag}^+$  ions are distributed among twelve sites of twofold symmetry [25]. This indicates that each Ag atom at  $(0.25, 0, 0.50)$  actually occupies one of the two sites at  $(x, 0, 0.50)$  and  $(0.5 - x, 0, 0.50)$  on the 2-fold axis. The unit-cell structure of cubic  $\text{Ag}_3\text{PO}_4$  is shown in Figure 1, in which the Ag atom experiences 4-fold coordination by four O atoms [24]. The P atoms have 4-fold coordination surrounded by four O atoms, while the O atoms have 4-fold coordination surrounded by three Ag atoms and one P atom.

## 3. Morphology Control and Catalytic Properties of $\text{Ag}_3\text{PO}_4$

Since  $\text{Ag}_3\text{PO}_4$  was first reported as visible light response photocatalyst by Yi and his coworkers [23], much research

has been devoted to investigate this active photocatalyst [26–29], and different methods have been developed to synthesize various  $\text{Ag}_3\text{PO}_4$  and its composites [28, 30–32]. The investigation of photocatalytic activity shows that all of the prepared  $\text{Ag}_3\text{PO}_4$  exhibit excellent photocatalytic activity under UV light irradiation or visible-light illumination, which is much more excellent than that of commercial P25  $\text{TiO}_2$  [33, 34] or N-doped  $\text{TiO}_2$  [30, 35, 36] as shown in Figure 2.

It is well known that the morphology of materials is closely related to the exposed facets of the crystals, which directly affect the properties of the catalysts. Various  $\text{Ag}_3\text{PO}_4$  nanostructures including spherical morphology [33, 34], rhombic dodecahedrons [30], concave trisoctahedrons [37], cubes [26, 30], and tetrapods [38] with controlling particle size [39] have been designed and synthesized to further improve or optimize the photocatalytic properties. The investigations revealed that the rhombic dodecahedrons exhibit much higher photocatalytic activity in comparison with spheres and cubes for the degradation of organic contaminants [23, 30], and the enhanced photocatalytic activity of  $\text{Ag}_3\text{PO}_4$  rhombic dodecahedrons is primarily ascribed to the higher surface energy of  $\{110\}$  facets ( $1.31 \text{ J/m}^2$ ). The highly exposed  $\{110\}$  facets also lead to the higher visible light activity of  $\text{Ag}_3\text{PO}_4$  tetrapods than that of the polyhedrons for the degradation of toxic organic compounds [38]. The concave trisoctahedral  $\text{Ag}_3\text{PO}_4$  microcrystals with high-index facets have also been reported to show much higher photocatalytic properties than cubic  $\text{Ag}_3\text{PO}_4$  and commercial N-doped  $\text{TiO}_2$  [37].

The synthetic parameters, such as reaction component, temperature, and reaction time, usually serve as effective routes for tailoring the morphology and structure of  $\text{Ag}_3\text{PO}_4$  crystals. By directly reacting  $\text{AgNO}_3$  and  $\text{Na}_2\text{HPO}_4$ , only  $\text{Ag}_3\text{PO}_4$  particles with irregular spherical structures can be obtained, while the single crystalline  $\text{Ag}_3\text{PO}_4$  submicrocubes with sharp corners, edges, and smooth surfaces can be

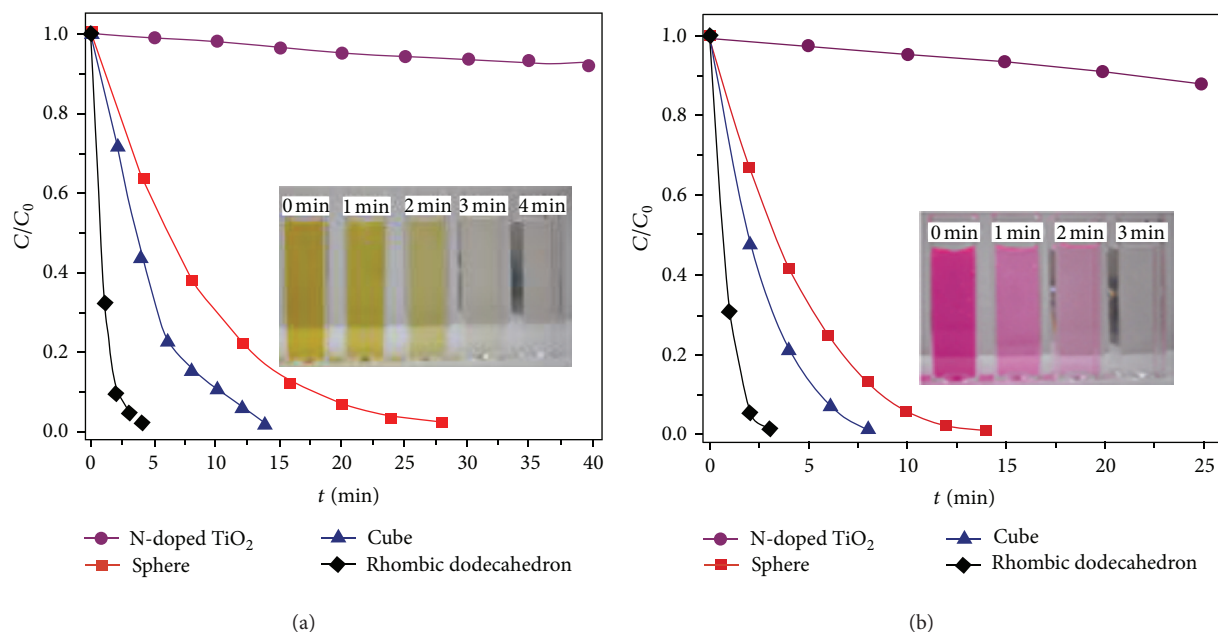


FIGURE 2: Photocatalytic activities of  $\text{Ag}_3\text{PO}_4$  rhombic dodecahedrons, cubes, and spheres and N-doped  $\text{TiO}_2$  for (a) MO and (b) RhB degradation under visible-light irradiation ( $\lambda > 420 \text{ nm}$ ) [30].

fabricated with  $[\text{Ag}(\text{NH}_3)_2]^+$  as precursors under the same conditions, which therefore exhibit higher photocatalytic activity than spherical nanoparticles [35]. Moreover, the morphologies and structures of the as-prepared  $\text{Ag}_3\text{PO}_4$  crystals could be further tailored by changing the aging time of the  $[\text{Ag}(\text{NH}_3)_2]^+$  complex due to the ammonia volatility. For example, when  $[\text{Ag}(\text{NH}_3)_2]^+$  complex solution was aged at room temperature for 1 h, the as-prepared  $\text{Ag}_3\text{PO}_4$  crystals possess irregular cubic morphology and six rhombic planes. Upon further increasing the aging time up to 2 h, the  $\text{Ag}_3\text{PO}_4$  crystals transform into irregular structure with concave surfaces. Interestingly, when the aging time has been prolonged to 4 h, the corresponding  $\text{Ag}_3\text{PO}_4$  products with four symmetrically arrowheaded morphologies have been fabricated (shown in Figure 3), and no cubes have been observed. The variation of morphologies and structures of the as-prepared  $\text{Ag}_3\text{PO}_4$  crystals leads to the variation of optical properties (Figure 3(d)). Similar morphology variation of  $\text{Ag}_3\text{PO}_4$  particles prepared by a pyridine-assisted hydrothermal method is found to change regularly from spherical to particles with the corners and edges then to rhombic dodecahedrons with an increase in pyridine concentration [27].

#### 4. Theoretical Study of the Electronic Structure and Photocatalytic Performance

To elucidate its mechanism of the extremely high photooxidative under visible light irradiation of  $\text{Ag}_3\text{PO}_4$ , theoretical works have been carried out by using first-principle method. Photocatalysis reactions are determined primarily by three processes: (1) the photoexcitation of electron-hole pairs due to light harvesting, (2) the transfer of carriers to the surface,

and (3) chemical reactions on the surface. So far, theoretical investigations are mainly focused on the first process, which is relevant to energy band configuration because photoexcited carriers are generated only when the incident photon energy is higher than the bandgap of the photocatalyst. Alignment between the band edges and the redox potentials of the target molecules is also crucial, considering that photoexcited carriers can only be transferred to the adsorbed molecules when there is a sufficiently large negative offset of the conduction band minimum (CBM) and a sufficiently large positive offset of the valence band maximum (VBM) with respect to the redox potentials. Ma et al. investigated the electronic properties and photocatalytic activation of  $\text{Ag}_3\text{PO}_4$  using first principles density functional theory (DFT) incorporating the local density approximation (LDA) + U formalism [24]. It is found that one  $\text{PO}_4$  tetrahedron and three tetrahedral  $\text{AgO}_4$  are combined with each other through the corner oxygen. The tetrahedral  $\text{AgO}_4$  is heavily distorted to have a dipole moment of 2.2 D (D = debye), which should be closely attributed to a specific nonmetal salt of the oxyacid structure of  $\text{Ag}_3\text{PO}_4$ . In addition,  $\text{PO}_4^{3-}$  ions have a large negative charge which maintains a large dipole in the  $\text{Ag}_3\text{PO}_4$ , resulting in the distortion of tetrahedral  $\text{AgO}_4$ . As a consequence, a correlation between the photocatalytic activity and the distortion of  $\text{AgO}_4$  tetrahedron is true for a specific phosphate structure. Meanwhile,  $\text{PO}_4^{3-}$  possessing a large electron cloud overlapping prefers to attract holes and repel electrons, which helps the  $e^-/h^+$  separation. The calculated results show that  $\text{Ag}_3\text{PO}_4$  is an indirect band gap semiconductor; the direct band gap is 2.61 eV and the indirect band gap is 2.43 eV having the character of  $\sigma$  or  $\pi$  bonding states in the VB and the corresponding  $\sigma^*$  or  $\pi^*$  antibonding states in the CB. The effective mass of electrons is far smaller

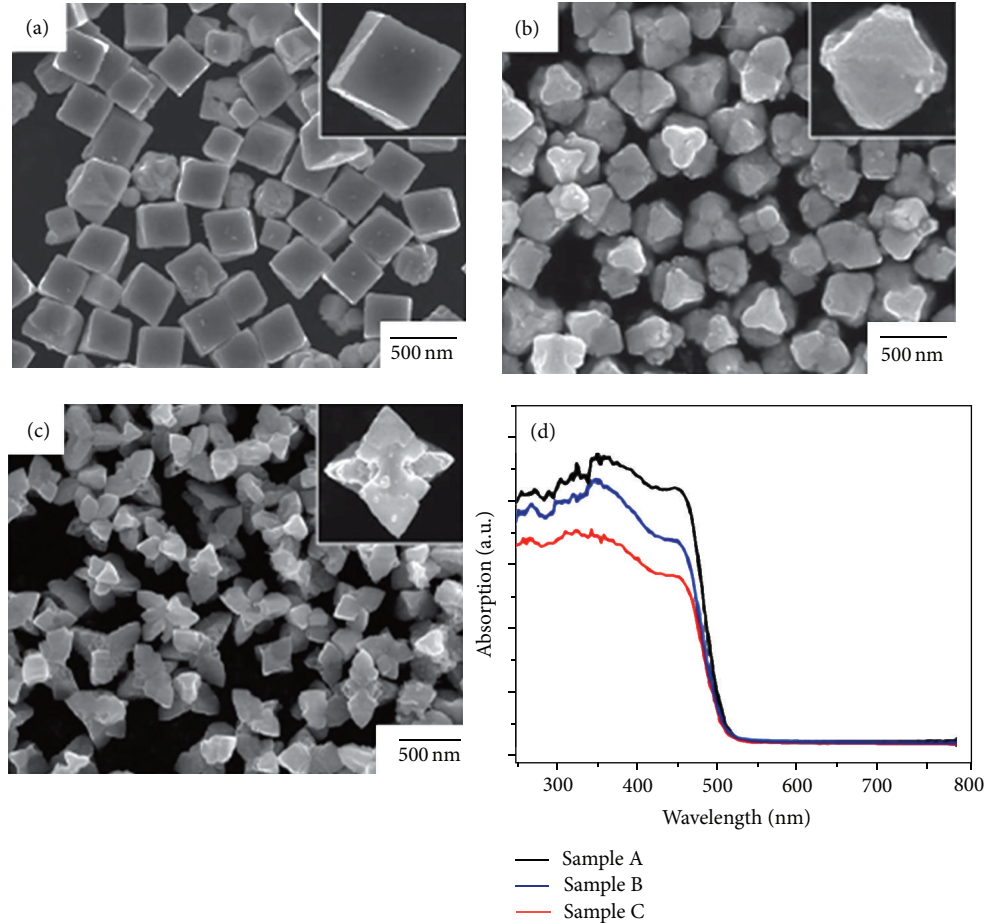


FIGURE 3: SEM images of  $\text{Ag}_3\text{PO}_4$  products prepared with different aging time: (a) 1 h, (b) 2 h, and (c) 4 h; (d) their ultraviolet-visible diffusive absorption spectrums [35].

than that of holes, which consequently results in a striking difference of the mobility between photoexcited electrons and holes. This is beneficial for decreasing the recombination of electron-hole pairs in  $\text{Ag}_3\text{PO}_4$ . In addition, Ag vacancies in  $\text{Ag}_3\text{PO}_4$  with high concentration have a significant effect on the separation of electron-hole pairs and optical absorbance in the visible-light region. To explore the mechanism of the high performance of  $\text{Ag}_3\text{PO}_4$ , Umezawa et al. have conducted a comparative study of the electronic structures of  $\text{Ag}_3\text{PO}_4$ ,  $\text{Ag}_2\text{O}$ , and  $\text{AgNbO}_3$  by first principles calculations [32]. The CBM consisting of Ag s states in  $\text{Ag}_3\text{PO}_4$  and Ag d states in  $\text{Ag}_2\text{O}$  is the main difference between  $\text{Ag}_3\text{PO}_4$  and  $\text{Ag}_2\text{O}$ , which is due to the rigid  $\text{PO}_4$  tetrahedral unit; partial charge density originating from O sp and P sp derived bonding states is evident in the local density of states (DOS). This increases the ionic character of  $\text{Ag}^+$  and  $(\text{PO}_4)^{3-}$ , making the covalent Ag–O bonds weaker. Thus, the hybridization of Ag d and O p states is negligible in  $\text{Ag}_3\text{PO}_4$ , rendering fully occupied d states at the VBM. On the contrary, covalent Ag–O bonds, that is, antibonding states of Ag d–O p lying at the CBM are formed in  $\text{Ag}_2\text{O}$ . In  $\text{AgNbO}_3$ , the majority of the CBM is composed of Nb d states and the nature of the Ag–O bonding does not significantly affect the characteristics of the CBM.

In Figure 4, the band structures of  $\text{Ag}_3\text{PO}_4$ ,  $\text{Ag}_2\text{O}$ , and  $\text{AgNbO}_3$  are illustrated, accompanied by the wave function corresponding to the CBM. In  $\text{Ag}_3\text{PO}_4$ , the wave function at the CBM is dramatically delocalized due to mainly consisting of Ag s states. In contrast, the CBM of  $\text{Ag}_2\text{O}$  possesses the character of Ag d–O p antibonding states, which are unfavorable for electron transfer due to their localization. In  $\text{Ag}_3\text{PO}_4$ , a large amount of hybridization between Ag s states on adjacent atoms leads to a dispersive band structure at the CBM without the “contamination” of d states, resulting in a decreased effective electron mass. In  $\text{AgNbO}_3$ , the CBM mainly composes of  $d_{xz}$  and  $d_{yz}$  states, causing an anisotropic charge distribution (Figure 4(c)) and allowing electron transfer only along the z-direction. This anisotropy can also be found in the band structure, where the dispersion of the CBM is very dispersive along X-S-Y and flat along S- $\Gamma$  indicating the high dependence of the directions. This is undesirable for photocatalysis process because the limited directionality of the electron transfer leads to higher probability of carrier recombination. The CBM of  $\text{Ag}_3\text{PO}_4$  has, on the contrary, a very isotropic distribution and is hence favorable for electron transfer (Figure 4(a)). The effective mass of the electron is relatively small in every direction in  $\text{Ag}_3\text{PO}_4$ , which is

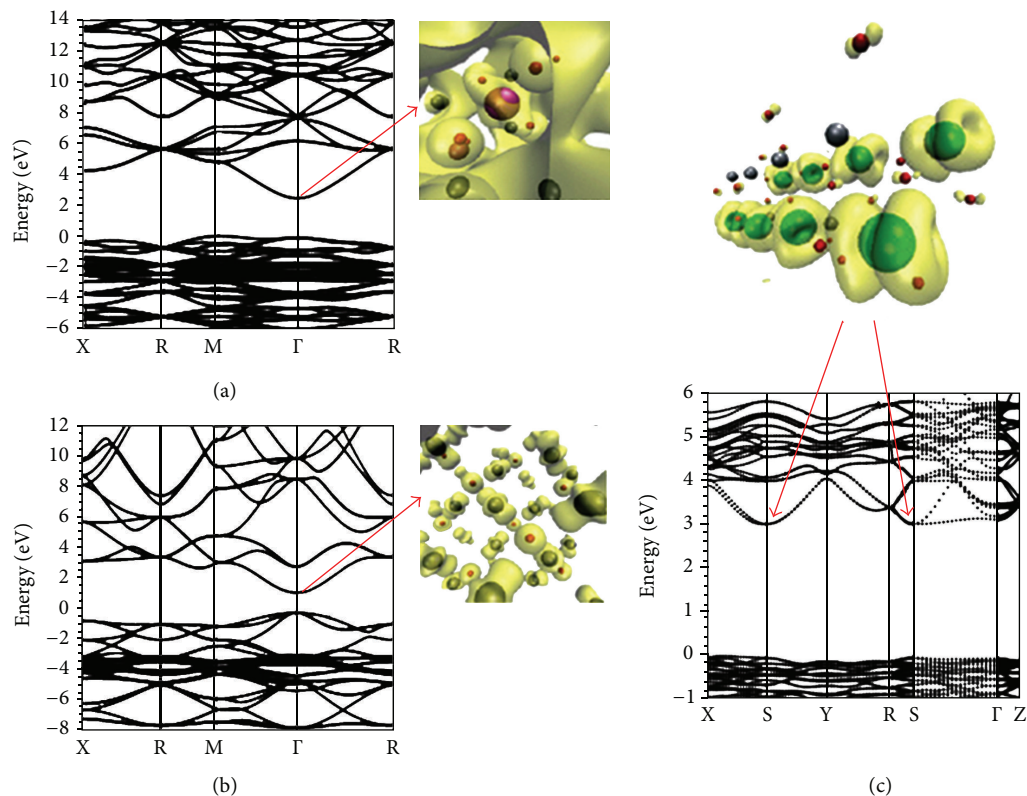


FIGURE 4: (Color) band structures for (a)  $\text{Ag}_3\text{PO}_4$ , (b)  $\text{Ag}_2\text{O}$ , and (c)  $\text{AgNbO}_3$ . The square of the wave function (yellow surface) corresponding to the CBM is also shown in each case, where silver, red, mauve, and green particles represent the positions of Ag, O, P, and Nb atoms, respectively. The isosurfaces are at  $0.01 e/\text{\AA}^3$  [32].

also advantageous for electron transfer. Thus, the excellent photocatalytic performance of  $\text{Ag}_3\text{PO}_4$  is partly due to the highly dispersive band structure at the CBM, which results from Ag s–Ag s hybridization without localized d states.

Using the local density approximation (LDA) and LDA+U approaches, the calculated band gaps of 0.36 and 1.30 eV are far less than the experimental value of 2.45 eV due to the missing discontinuity in the exchange–correlation potential and the self-interaction error within the LDA. To effectively remedy the drawbacks of LDA and understand the photocatalytic mechanism, hybrid density functional theory (DFT) using PBE0 formalism, was used to calculate the band structure, density of state (DOS), and optical properties of  $\text{Ag}_3\text{PO}_4$  [40]. The hybrid-DFT method gives a direct band gap,  $E_{\text{gdir}} = 2.61$  eV, and an indirect one,  $E_{\text{gindir}} = 2.43$  eV, which agrees well with the experimental value (2.45 eV). Compared with the top of valence band (VB), the bottom of conduction band (CB) is well dispersive, which indicates that the photogenerated electrons possess smaller effective mass and, therefore, higher migration ability. The redox ability of  $\text{Ag}_3\text{PO}_4$  is evaluated by determining the energy positions of valence and conduction bands using Mulliken electronegativity and the band gap value calculated accurately. Figure 5 renders the valence and conduction band edge potentials of  $\text{Ag}_3\text{PO}_4$ . The VBM potential of  $\text{Ag}_3\text{PO}_4$  is 2.67 V, more positive than  $\text{O}_2/\text{H}_2\text{O}$  (1.23 V), indicating that  $\text{Ag}_3\text{PO}_4$  has the ability to oxidize  $\text{H}_2\text{O}$  to produce  $\text{O}_2$  or

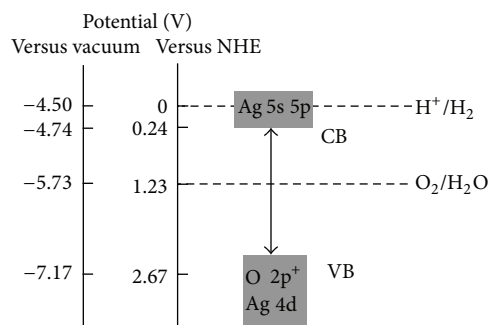


FIGURE 5: Calculated VBM and CBM potentials of  $\text{Ag}_3\text{PO}_4$  [40].

oxidation pollutants. Whereas the CBM potential of  $\text{Ag}_3\text{PO}_4$  is 0.24 V, which is lesser than  $\text{H}^+/\text{H}_2$  (0 V) and cannot reduce  $\text{H}^+$  to  $\text{H}_2$  [40]. More recently, Ma et al. investigated the electronic and photocatalytic properties of  $\text{Ag}_3\text{PC}_4$  ( $\text{C} = \text{O}, \text{S}, \text{Se}$ ) by the hybrid density functional method. Similar results for  $\text{Ag}_3\text{PO}_4$  are obtained [41].

## 5. Visible Light Response $\text{Ag}_3\text{PO}_4$ Based Composite Photocatalyst

To harvest photons in visible region, many narrow bandgap metal oxides or chalcogenides have been coupled with  $\text{TiO}_2$

to fabricate visible-light photocatalysts, which exhibit visible-light photocatalytic activity to a certain extent. Such a strategy is also applied to modify  $\text{Ag}_3\text{PO}_4$  photocatalyst to enhance its photocatalytic activity and/or improve its stability. The previous investigations showed that the photocatalytic activity of  $\text{Ag}_3\text{PO}_4$  can be enhanced as Ag nanoparticles deposited on  $\text{Ag}_3\text{PO}_4$  because the  $\text{Ag}_3\text{PO}_4$  decomposition could capture the photogenerated electrons and thus prevent the recombination of electron-hole pairs within the  $\text{Ag}_3\text{PO}_4$  samples at the initial stage of photocatalytic reactions. However, the photoactivity decreases with increasing Ag contents due to the formation of Ag layers on the surface of  $\text{Ag}_3\text{PO}_4$  that shield light absorption, inhibit the transfer of holes from the valence band of  $\text{Ag}_3\text{PO}_4$  to the interface between photocatalyst, and solution and also hinder the contact of dye molecules with  $\text{Ag}_3\text{PO}_4$ , and, accordingly, the photocatalytic activity deteriorates gradually [34]. This deterioration of the  $\text{Ag}_3\text{PO}_4$  photocatalytic activity due to photocorrosion largely limits its practical application as a recyclable highly efficient photocatalyst. It is found that the Ag/ $\text{Ag}_3\text{PO}_4$  heterocubes synthesized by reacting  $\text{Ag}_3\text{PO}_4$  cubes with glucose in an aqueous ammonia solution exhibit higher photocatalytic activities than pure  $\text{Ag}_3\text{PO}_4$  cubes for the organic contaminants degradation under visible-light irradiation [26]. The stability improvement of  $\text{Ag}_3\text{PO}_4$  by covering  $\text{Ag}^0$  nanoparticles on the surface of  $\text{Ag}_3\text{PO}_4$  is attributed to the localized surface plasmon resonance (LSPR) effects of silver nanoparticles and a large negative charge of  $\text{PO}_4^{3-}$  ions [2, 27], which effectively inhibit the reducibility of  $\text{Ag}^+$  ions in the  $\text{Ag}_3\text{PO}_4$  lattice.  $\text{Ag}_3\text{PO}_4$  can also be rejuvenated from weak photocatalytically active Ag as a recyclable highly efficient photocatalyst by oxidizing Ag with  $\text{H}_2\text{O}_2$  under a  $\text{PO}_4^{3-}$  ion atmosphere [29]. However, these strategies are not ideal from the practical application perspective. Thus, the fabrication of  $\text{Ag}_3\text{PO}_4$  based composite photocatalysts with high photocatalytic activity and excellent stability as well as lower Ag usage for their large scale applications is desirable.

Yao et al. synthesized  $\text{Ag}_3\text{PO}_4/\text{TiO}_2$  visible light photocatalyst by depositing of  $\text{Ag}_3\text{PO}_4$  nanoparticles onto the  $\text{TiO}_2$  (P25) surface photocatalyst [42]. Their results show that the  $\text{Ag}_3\text{PO}_4/\text{TiO}_2$  heterostructured photocatalyst shows enhanced activity and is much more stable than unsupported  $\text{Ag}_3\text{PO}_4$ . The enhanced activity is attributed to the electron-hole effective separation and the larger surface area of the  $\text{Ag}_3\text{PO}_4/\text{TiO}_2$  composite, while the enhanced stability is ascribed to the chemical adsorption of  $\text{Ag}^+$  cations in  $\text{Ag}_3\text{PO}_4$  and  $\text{O}^-$  anions in  $\text{TiO}_2$ . Moreover, the silver weight percentage of the photocatalyst decreases from 77% to 47%, significantly reducing the cost of  $\text{Ag}_3\text{PO}_4$  based photocatalysts for the  $\text{Ag}_3\text{PO}_4/\text{TiO}_2$  composite [42].

The UV photocatalytic activity of  $\text{Ag}_3\text{PO}_4/\text{TiO}_2$  composite heterostructures was comparable to that of  $\text{Ag}_3\text{PO}_4$  nanoparticles surfaces. While the stability and hence reusability of the  $\text{Ag}_3\text{PO}_4/\text{TiO}_2$  heterostructure catalysts was substantially enhanced as compared with that of  $\text{Ag}_3\text{PO}_4$  nanoparticles or  $\text{TiO}_2$  nanobelts alone. These results were attributed to the improved charge separation of the photogenerated electrons and holes under UV light at the

$\text{Ag}_3\text{PO}_4/\text{TiO}_2$  interface and/or surfactant-like function of the nanobelts in stabilizing the  $\text{Ag}_3\text{PO}_4$  nanoparticles.  $\text{Ag}_3\text{PO}_4/\text{TiO}_2$  composite heterostructures appear to be more desirable in long-term applications because of their photocatalytic activity as well as the enhanced chemical stability [33].

Considering that the VB level of  $\text{Ag}_3\text{PO}_4$  is appreciably lower than that of  $\text{TiO}_2$  with +2.7 V (versus NHE) and  $\text{Ag}_3\text{PO}_4$  can be severed as an appropriate sensitizer for  $\text{TiO}_2$ , Lee et al. fabricated the novel heterojunction structures of  $\text{Ag}_3\text{PO}_4$ -core/ $\text{TiO}_2$ -shell by covering the  $\text{Ag}_3\text{PO}_4$  nanoparticles with polycrystalline  $\text{TiO}_2$  by sol-gel method. The prepared  $\text{Ag}_3\text{PO}_4/\text{TiO}_2$  composites show notably enhanced photocatalytic activity in decomposing gaseous 2-propanol and evolving  $\text{CO}_2$  compared to bare  $\text{Ag}_3\text{PO}_4$  and  $\text{TiO}_2$ . It is inferred that the unusually high visible-light photocatalytic activity of  $\text{Ag}_3\text{PO}_4/\text{TiO}_2$  composite originates from the unique relative band positions of the two semiconductors [43].

Besides  $\text{Ag}_3\text{PO}_4/\text{TiO}_2$  composite heterostructures,  $\text{AgX}/\text{Ag}_3\text{PO}_4$  (X=Cl, Br, I) heterocrystals have also attracted much attention due to the excellent photocatalytic activity. Bi and coworkers [44] have reported that the  $\text{AgX}/\text{Ag}_3\text{PO}_4$  (X=Cl, Br, I) heterocrystals prepared by in situ ionexchange method embodied some advantages compared to the single  $\text{Ag}_3\text{PO}_4$ , and it is a more promising and fascinating visible-light-driven photocatalyst than pure  $\text{Ag}_3\text{PO}_4$  [45]. The  $\text{AgBr}/\text{Ag}_3\text{PO}_4$  hybrid synthesized using an in situ anion-exchange method displayed much higher photocatalytic activity than single  $\text{AgBr}$  or  $\text{Ag}_3\text{PO}_4$ , as well as high stability under visible light irradiation. The high stability was attributed to the formed  $\text{Ag}@\text{AgBr}/\text{Ag}_3\text{PO}_4@/\text{Ag}$  plasmonic system, which effectively retains its activity due to the efficient transfer of photoinduced electrons [45].

## 6. Conclusion and Perspectives

In this paper, we have summarized the survey of efforts on  $\text{Ag}_3\text{PO}_4$  photocatalysts. As a quintessence, for example,  $\text{Ag}_3\text{PO}_4$  photocatalysts have excellent photocatalytic activity and yield a high quantum yield of nearly 90% under visible light ( $\lambda = 420$  nm) found for the evolution of  $\text{O}_2$  in water photolysis [23]. All of the developments show that  $\text{Ag}_3\text{PO}_4$  and/or its heterogeneous composites have the potential as excellent visible-light-active candidates with high photocatalytic activity. However, to comply with the challenging requirements of economically viable industrial production, many issues are still yet to be addressed, including long-term stability of  $\text{Ag}_3\text{PO}_4$  in photocatalytic processes. New methods for fabrication  $\text{Ag}_3\text{PO}_4$  with exposed high-energy facets and novel heterogeneous  $\text{Ag}_3\text{PO}_4$  cocatalysts are highly desirable. To date, there have been relatively few quantitative studies in the charge carrier dynamics in  $\text{Ag}_3\text{PO}_4$  and/or its cocatalysts systems, how these dynamics are related to material design, and how they impact the photocatalytic processes. In heterogeneous systems, a particular challenge is that electron-hole recombination is a bimolecular process, which its dynamics often depend nonlinearly on the charge carrier density and so cannot be described using a single time constant. Therefore, obtaining a substantial

breakthrough in efficiency requires an exact understanding of the surface/interface processes at the atomic scale. A true picture of photocatalyst surfaces in action, including such recombination dynamics, needs to be studied by in situ observations using transient optical spectroscopy techniques. A further challenge is translating laboratory-scale academic research into scalable, manufacturable technologies to meet the demands of the efficient utilization of solar energy in the areas of renewable energy and environmental purification.

## Acknowledgments

This work is supported by the Hunan Provincial Natural Science Foundation of China (Grant no. 12JJ3009), the Science and Technology Plan Projects of Hunan Province (2012ZK3021).

## References

- [1] L. W. Zhang, Y. Man, and Y. F. Zhu, "Effects of Mo replacement on the structure and visible-light-induced photocatalytic performances of  $\text{Bi}_2\text{WO}_6$  photocatalyst," *ACS Catalysis*, vol. 1, no. 8, pp. 841–848, 2011.
- [2] Y. P. Liu, L. Fang, H. D. Lu, L. J. Liu, H. Wang, and C. Z. Hu, "Highly efficient and stable  $\text{Ag}/\text{Ag}_3\text{PO}_4$  plasmonic photocatalyst in visible light," *Catalysis Communications*, vol. 17, pp. 200–204, 2012.
- [3] R. Asahi, T. Morikawa, T. Ohwaki et al., "Photocatalysts sensitive to visible light," *Science*, vol. 295, no. 5555, pp. 626–627, 2002.
- [4] G. S. Wu, J. L. Wen, S. Nigro, and A. C. Chen, "One-step synthesis of N- and F-codoped mesoporous  $\text{TiO}_2$  photocatalysts with high visible light activity," *Nanotechnology*, vol. 21, no. 8, Article ID 085701, 2010.
- [5] Y. Tian, G. F. Huang, L. J. Tang, M. G. Xia, W. Q. Huang, and Z. L. Ma, "Size-controllable synthesis and enhanced photocatalytic activity of porous ZnS nanospheres," *Materials Letters*, vol. 83, pp. 104–107, 2012.
- [6] Y. Chen, G. F. Huang, W. Q. Huang, B. S. Zou, and A. L. Pan, "Enhanced visible-light photoactivity of La-doped ZnS thin films," *Applied Physics A*, vol. 108, no. 4, pp. 895–900, 2012.
- [7] V. Etacheri, M. K. Seery, S. J. Hinder, and S. C. Pillai, "Highly visible light active  $\text{TiO}_{2-x}\text{N}_x$  heterojunction photocatalysts," *Chemistry of Materials*, vol. 22, no. 13, pp. 3843–3853, 2010.
- [8] L. Feng, K. F. He, and W. P. Chen, "Study on stability of  $\text{AgI}/\text{TiO}_2$  visible light photocatalysts in solutions of various pH values," *New Materials, Applications and Processes*, vol. 399–401, pp. 1272–1275, 2012.
- [9] J. J. Yuan, H. D. Li, S. Y. Gao, Y. H. Lin, and H. Y. Li, "A facile route to n-type  $\text{TiO}_2$ -nanotube/p-type boron-doped-diamond heterojunction for highly efficient photocatalysts," *Chemical Communications*, vol. 46, no. 18, pp. 3119–3121, 2010.
- [10] J. Q. Li, D. F. Wang, Z. Y. Guo, and Z. F. Zhu, "Preparation, characterization and visible-light-driven photocatalytic activity of Fe-incorporated  $\text{TiO}_2$  microspheres photocatalysts," *Applied Surface Science*, vol. 263, pp. 382–388, 2012.
- [11] Y. Komai, K. Okitsu, R. Nishimura et al., "Visible light response of nitrogen and sulfur co-doped  $\text{TiO}_2$  photocatalysts fabricated by anodic oxidation," *Catalysis Today*, vol. 164, no. 1, pp. 399–403, 2011.
- [12] X. M. Fang, Z. G. Zhang, and Q. L. Chen, "Nitrogen doped  $\text{TiO}_2$  photocatalysts with visible-light activity," *Progress in Chemistry*, vol. 19, no. 9, pp. 1282–1290, 2007.
- [13] Y. Hu, D. Z. Li, Y. Zheng et al., " $\text{BiVO}_4/\text{TiO}_2$  nanocrystalline heterostructure: a wide spectrum responsive photocatalyst towards the highly efficient decomposition of gaseous benzene," *Applied Catalysis B*, vol. 104, no. 1–2, pp. 30–36, 2011.
- [14] Y. J. Chen, Y. Q. Zhang, C. Liu, A. M. Lu, and W. H. Zhang, "Photodegradation of malachite green by nanostructured  $\text{Bi}_2\text{WO}_6$  visible light-induced photocatalyst," *International Journal of Photoenergy*, vol. 2012, Article ID 510158, 6 pages, 2012.
- [15] J. W. Tang, Z. G. Zou, and J. H. Ye, "Efficient photocatalytic decomposition of organic contaminants over  $\text{CaBi}_2\text{O}_4$  under visible-light irradiation," *Angewandte Chemie*, vol. 43, no. 34, pp. 4463–4466, 2004.
- [16] H. G. Kim, P. H. Borse, J. S. Jang, E. D. Jeong, and J. S. Lee, "Enhanced photochemical properties of electron rich W-doped  $\text{PbBi}_2\text{Nb}_2\text{O}_9$  layered perovskite material under visible-light irradiation," *Materials Letters*, vol. 62, no. 8–9, pp. 1427–1430, 2008.
- [17] T. P. Cao, Y. J. Li, C. H. Wang et al., " $\text{Bi}_4\text{Ti}_3\text{O}_{12}$  nanosheets/ $\text{TiO}_2$  submicron fibers heterostructures: in situ fabrication and high visible light photocatalytic activity," *Journal of Materials Chemistry*, vol. 21, no. 19, pp. 6922–6927, 2011.
- [18] D. L. Chen, S. H. Yoo, Q. S. Huang, G. Ali, and S. O. Cho, "Sonochemical synthesis of  $\text{Ag}/\text{AgCl}$  nanocubes and their efficient visible-light-driven photocatalytic performance," *Chemistry A*, vol. 18, no. 17, pp. 5192–5200, 2012.
- [19] M. Kitano, M. Matsuoka, M. Ueshima, and M. Anpo, "Recent developments in titanium oxide-based photocatalysts," *Applied Catalysis A*, vol. 325, no. 1, pp. 1–14, 2007.
- [20] L. Xu, C. Li, W. Shi, J. Guan, and Z. Sun, "Visible light-response  $\text{NaTa}_{1-x}\text{Cu}_x\text{O}_3$  photocatalysts for hydrogen production from methanol aqueous solution," *Journal of Molecular Catalysis A*, vol. 360, pp. 42–47, 2012.
- [21] R. Niishiro, H. Kato, and A. Kudo, "Nickel and either tantalum or niobium-codoped  $\text{TiO}_2$  and  $\text{SrTiO}_3$  photocatalysts with visible-light response for  $\text{H}_2$  or  $\text{O}_2$  evolution from aqueous solutions," *Physical Chemistry Chemical Physics*, vol. 7, no. 10, pp. 2241–2245, 2005.
- [22] W. Xiong, Q. D. Zhao, X. Y. Li, and D. K. Zhang, "One-step synthesis of flower-like  $\text{Ag}/\text{AgCl}/\text{BiOCl}$  composite with enhanced visible-light photocatalytic activity," *Catalysis Communications*, vol. 16, no. 1, pp. 229–233, 2011.
- [23] Z. G. Yi, J. H. Ye, N. Kikugawa et al., "An orthophosphate semiconductor with photooxidation properties under visible-light irradiation," *Nature Materials*, vol. 9, no. 7, pp. 559–564, 2010.
- [24] X. G. Ma, B. Lu, D. Li, R. Shi, C. S. Pan, and Y. F. Zhu, "Origin of photocatalytic activation of silver orthophosphate from first-principles," *Journal of Physical Chemistry C*, vol. 115, no. 11, pp. 4680–4687, 2011.
- [25] H. N. Ng, C. Calvo, and R. Faggiani, "A new investigation of the structure of silver orthophosphate," *Acta Crystallographica B*, vol. 34, no. 3, pp. 898–899, 1978.
- [26] Y. P. Bi, H. Y. Hu, S. X. Ouyang, Z. B. Jiao, G. X. Lu, and J. H. Ye, "Selective growth of metallic Ag nanocrystals on  $\text{Ag}_3\text{PO}_4$  submicro-cubes for photocatalytic applications," *Chemistry A*, vol. 18, no. 45, pp. 14272–14275, 2012.
- [27] Y. P. Liu, L. Fang, H. D. Lu, Y. W. Li, C. Z. Hu, and H. G. Yu, "One-pot pyridine-assisted synthesis of visible-light-driven

- photocatalyst  $\text{Ag}/\text{Ag}_3\text{PO}_4$ ,” *Applied Catalysis B*, vol. 115–116, pp. 245–252, 2012.
- [28] G. P. Li and L. Q. Mao, “Magnetically separable  $\text{Fe}_3\text{O}_4$ - $\text{Ag}_3\text{PO}_4$  sub-micrometre composite: facile synthesis, high visible light-driven photocatalytic efficiency, and good recyclability,” *RSC Advances*, vol. 2, no. 12, pp. 5108–5111, 2012.
- [29] H. Wang, Y. S. Bai, J. T. Yang, X. F. Lang, J. H. Li, and L. Guo, “A facile way to rejuvenate  $\text{Ag}_3\text{PO}_4$  as a recyclable highly efficient photocatalyst,” *Chemistry A*, vol. 18, no. 18, pp. 5524–5529, 2012.
- [30] Y. Bi, S. Ouyang, N. Umezawa, J. Cao, and J. Ye, “Facet effect of single-crystalline  $\text{Ag}_3\text{PO}_4$  sub-microcrystals on photocatalytic properties,” *Journal of the American Chemical Society*, vol. 133, no. 17, pp. 6490–6492, 2011.
- [31] H. C. Zhang, H. Huang, H. Ming et al., “Carbon quantum dots/ $\text{Ag}_3\text{PO}_4$  complex photocatalysts with enhanced photocatalytic activity and stability under visible light,” *Journal of Materials Chemistry*, vol. 22, no. 21, pp. 10501–10506, 2012.
- [32] N. Umezawa, O. Y. Shuxin, and J. H. Ye, “Theoretical study of high photocatalytic performance of  $\text{Ag}_3\text{PO}_4$ ,” *Physical Review B*, vol. 83, no. 3, Article ID 035202, 2011.
- [33] R. Y. Liu, P. G. Hu, and S. W. Chen, “Photocatalytic activity of  $\text{Ag}_3\text{PO}_4$  nanoparticle/ $\text{TiO}_2$  nanobelt heterostructures,” *Applied Surface Science*, vol. 258, no. 24, pp. 9805–9809, 2012.
- [34] W. G. Wang, B. Cheng, J. G. Yu, G. Liu, and W. H. Fan, “Visible-light photocatalytic activity and deactivation mechanism of  $\text{Ag}_3\text{PO}_4$  spherical particles,” *Chemistry*, vol. 7, no. 8, pp. 1902–1908, 2012.
- [35] Y. P. Bi, H. Y. Hu, S. X. Ouyang, G. X. Lu, J. Y. Cao, and J. H. Ye, “Photocatalytic and photoelectric properties of cubic  $\text{Ag}_3\text{PO}_4$  sub-microcrystals with sharp corners and edges,” *Chemical Communications*, vol. 48, no. 31, pp. 3748–3750, 2012.
- [36] M. Ge, N. Zhu, Y. P. Zhao, J. Li, and L. Liu, “Sunlight-assisted degradation of dye pollutants in  $\text{Ag}_3\text{PO}_4$  suspension,” *Industrial & Engineering Chemistry Research*, vol. 51, no. 14, pp. 5167–5173, 2012.
- [37] Z. B. Jiao, Y. Zhang, H. C. Yu, G. X. Lu, J. H. Ye, and Y. P. Bi, “Concave trisoctahedral  $\text{Ag}_3\text{PO}_4$  microcrystals with high-index facets and enhanced photocatalytic properties,” *Chemical Communications*, vol. 49, no. 6, pp. 636–638, 2013.
- [38] J. Wang, F. Teng, M. D. Chen, J. J. Xu, Y. Q. Song, and X. L. Zhou, “Facile synthesis of novel  $\text{Ag}_3\text{PO}_4$  tetrapods and the {110} facets-dominated photocatalytic activity,” *Crystengcomm*, vol. 15, no. 1, pp. 39–42, 2013.
- [39] C. T. Dinh, T. D. Nguyen, F. Kleitz, and T. O. Do, “Large-scale synthesis of uniform silver orthophosphate colloidal nanocrystals exhibiting high visible light photocatalytic activity,” *Chemical Communications*, vol. 47, no. 27, pp. 7797–7799, 2011.
- [40] J. J. Liu, X. L. Fu, S. F. Chen, and Y. F. Zhu, “Electronic structure and optical properties of  $\text{Ag}_3\text{PO}_4$  photocatalyst calculated by hybrid density functional method,” *Applied Physics Letters*, vol. 99, Article ID 191903, 3 pages, 2011.
- [41] Z. J. Ma, Z. G. Yi, J. Sun, and K. C. Wu, “Electronic and photocatalytic properties of  $\text{Ag}_3\text{PC}_4\text{VI}$  (C = O, S, Se): a systemic hybrid DFT study,” *The Journal of Physical Chemistry C*, vol. 116, no. 47, pp. 25074–25080, 2012.
- [42] W. F. Yao, B. Zhang, C. P. Huang, C. Ma, X. L. Song, and Q. J. Xu, “Synthesis and characterization of high efficiency and stable  $\text{Ag}_3\text{PO}_4/\text{TiO}_2$  visible light photocatalyst for the degradation of methylene blue and rhodamine B solutions,” *Journal of Materials Chemistry*, vol. 22, no. 9, pp. 4050–4055, 2012.
- [43] S. B. Rawal, S. D. Sung, and W. I. Lee, “Novel  $\text{Ag}_3\text{PO}_4/\text{TiO}_2$  composites for efficient decomposition of gaseous 2-propanol under visible-light irradiation,” *Catalysis Communications*, vol. 17, pp. 131–135, 2012.
- [44] Y. P. Bi, S. X. Ouyang, J. Y. Cao, and J. H. Ye, “Facile synthesis of rhombic dodecahedral  $\text{AgX}/\text{Ag}_3\text{PO}_4$  (X = Cl, Br, I) heterocrystals with enhanced photocatalytic properties and stabilities,” *Physical Chemistry Chemical Physics*, vol. 13, no. 21, pp. 10071–10075, 2011.
- [45] J. Cao, B. D. Luo, H. L. Lin, B. Y. Xu, and S. F. Chen, “Visible light photocatalytic activity enhancement and mechanism of  $\text{AgBr}/\text{Ag}_3\text{PO}_4$  hybrids for degradation of methyl orange,” *Journal of Hazardous Materials*, vol. 217, pp. 107–115, 2012.

## Review Article

# A Review on the Synthesis of Manganese Oxide Nanomaterials and Their Applications on Lithium-Ion Batteries

Xiaodi Liu, Changzhong Chen, Yiyang Zhao, and Bin Jia

College of Chemistry and Pharmaceutical Engineering, Nanyang Normal University, Nanyang, Henan 473061, China

Correspondence should be addressed to Xiaodi Liu; liuxd1983@yahoo.com.cn

Received 21 January 2013; Accepted 22 February 2013

Academic Editor: Bo Yu

Copyright © 2013 Xiaodi Liu et al. This is an open access article distributed under the Creative Commons Attribution License, which permits unrestricted use, distribution, and reproduction in any medium, provided the original work is properly cited.

Most recently, manganese oxides nanomaterials, including MnO and MnO<sub>2</sub>, have attracted great interest as anode materials in lithium-ion batteries (LIBs) for their high theoretical capacity, environmental benignity, low cost, and special properties. Up to now, manganese oxides nanostructures with excellent properties and various morphologies have been successfully synthesized. Herein, we provide an in-depth discussion of recent development of the synthesis of manganese oxides nanomaterials and their application in the field of LIBs.

## 1. Introduction

Nanomaterials, having a length scale less than 100 nm, have received increasing interest owing not only to their fundamental scientific significance but also to the potential applications that derive from their fascinating electrical, magnetic, and catalytic properties [1]. Compared to bulk active electrode materials, the corresponding nanomaterials possess more excellent electrochemical activity, such as higher capacities, larger surface areas, and lower current densities, thereby, nanomaterials have widely potential application in electrochemistry field. Manganese oxides, including MnO, MnO<sub>2</sub>, and Mn<sub>3</sub>O<sub>4</sub>, are intriguing composites and have been used in wastewater treatment, catalysis, sensors, supercapacitors, and alkaline and rechargeable batteries [2–6]. Particularly, MnO and MnO<sub>2</sub> nanomaterials have attracted great interest as anode materials in lithium-ion batteries (LIBs) for their high theoretical capacity, low cost, environmental benignity, and special properties [7–9].

It is known that the phases, sizes, and morphologies of nanomaterials have great influence on the properties and applications; therefore, many research efforts have focused on rational control of phase, shape, size, and dimensionality of nanomaterials [14]. Several novel and effective routes have been devoted to prepare manganese oxides nanomaterials with various shapes and excellent properties, such as hydrothermal method [15–18], sol-gel synthesis [19], wet

chemical route [12, 20, 21], pulsed laser deposition method [22], and precursor technique [23]. Moreover, lots of successes on the properties and applications of manganese oxides nanomaterials have been reported in the last few years, for example, a hydrothermal method has been used to synthesize sea urchin shaped  $\alpha$ -MnO<sub>2</sub> [24]; Wu et al. have prepared  $\gamma$ -MnO<sub>2</sub> hexagon-based layer-cake-like and intertexture-like nanoarchitectures *via* a hydrothermal route [25]; Liu and coworkers have found MnO<sub>2</sub> nanoparticle-enriched poly(3,4-ethylenedioxythiophene) nanowires that could maintain high specific capacitance at high charge-discharge rates [26]. Thus, it is necessary to review the development of manganese oxides nanomaterials to keep the readers abreast of the rapid development. In this paper, we review the synthesis of manganese oxides nanomaterials with various morphologies and their application on LIBs; furthermore, the future prospects have also been discussed.

## 2. Synthesis of Manganese Oxide Nanomaterials

**2.1. Synthesis of MnO<sub>2</sub> Nanomaterials.** It is known that MnO<sub>2</sub> can exist in different structural forms,  $\alpha$ -,  $\beta$ -,  $\gamma$ -,  $\delta$ -,  $\epsilon$ - and  $\lambda$ -types and so forth, when the basic structural unit ([MnO<sub>6</sub>] octahedron) is linked in different ways. Based on the different [MnO<sub>6</sub>] links, MnO<sub>2</sub> can be divided into three

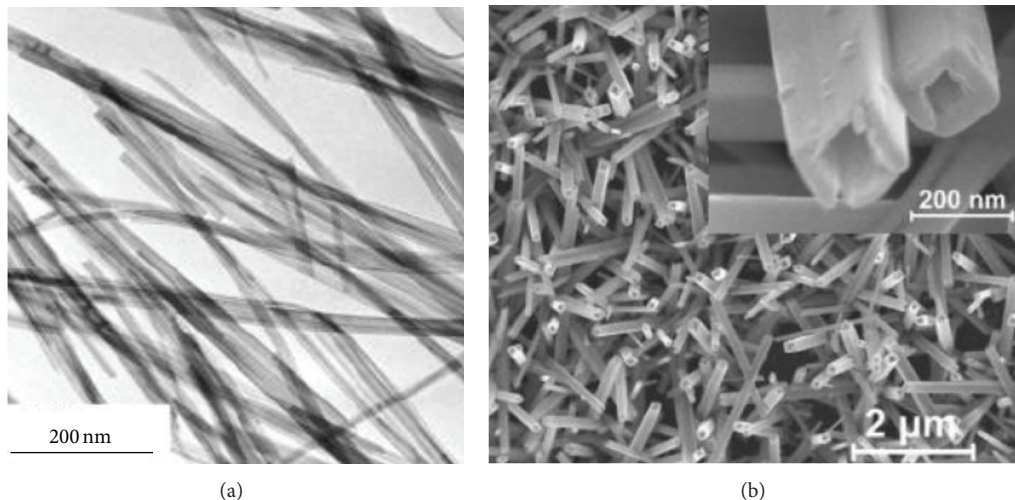


FIGURE 1: (a) TEM image of  $\alpha$ - $\text{MnO}_2$  nanowires and (b) SEM image of  $\alpha$ - $\text{MnO}_2$  nanotubes [10, 11].

categories: the chain-like tunnel structure such as  $\alpha$ -,  $\beta$ -, and  $\gamma$ -types, the sheet or layered structure such as  $\delta$ - $\text{MnO}_2$ , and the 3D structure such as  $\lambda$ -type [27]. The properties of  $\text{MnO}_2$  are significantly affected by their phases and morphologies; moreover, the operating properties of LIBs also depend on the phase of  $\text{MnO}_2$ . In this regard, a great effort has been directed toward the preparation of  $\text{MnO}_2$  with different phases and various shapes [28]. Generally,  $\text{MnO}_2$  nanostructures could be synthesized through the oxidation of  $\text{Mn}^{2+}$ , reduction of  $\text{MnO}_4^-$ , redox reactions between  $\text{Mn}^{2+}$  and  $\text{MnO}_4^-$ , or direct phase transformation from other manganese oxides.

1D  $\text{MnO}_2$  may provide the possibility of detecting the theoretical operating limits of LIBs, so various 1D  $\text{MnO}_2$  nanomaterials have been synthesized [29, 30]. Chen et al. have synthesized  $\text{MnO}_2$  with different crystal structures ( $\alpha$ -,  $\gamma$ -) and morphologies *via* quick precipitation of  $\text{Mn}^{2+}$  and  $\text{Mn}^{7+}$  in water isopropanol without using templates or surfactants [31]. In a typical synthesis,  $\text{MnCl}_2$  (0.18 g) mixed with isopropanol (50 mL) was heated to  $83^\circ\text{C}$  in a refluxing process, and then  $\text{KMnO}_4$  (0.10 g) dissolved in DI water (5 mL) was added to the solution. Finally,  $\text{MnO}_2$  nanoneedles were obtained. Singly-crystal nanowires of  $\alpha$ - and  $\beta$ - $\text{MnO}_2$  have been prepared in a hydrothermal procedures employing  $\text{Mn}^{2+}$  with oxidizing reagents such as  $(\text{NH}_4)_2\text{S}_2\text{O}_8$  or  $\text{KMnO}_4$  [28, 32]. Ma group have used a hydrothermal method for  $\text{MnO}_2$  nanobelts, which have narrow size dispersions and can be self-assembled into bundles [6]. In a typical procedure,  $\text{Mn}_2\text{O}_3$  powders (2 g) were dispersed in  $\text{NaOH}$  aqueous solution ( $10 \text{ mol}\cdot\text{dm}^{-3}$ ), and then the solution was sealed and heated at  $170^\circ\text{C}$  for 12 h to 1 week. Sui et al. have synthesized  $\alpha$ - $\text{MnO}_2$  nanowires and  $\beta$ - $\text{MnO}_2$  nanorods *via* molten salt method [10]. In the synthesis,  $\text{KNO}_3$ ,  $\text{NaNO}_3$ , and  $\text{LiNO}_3$  are applied as the reaction media.  $\alpha$ - $\text{MnO}_2$  is a  $(2 \times 2)$  and  $(1 \times 1)$  tunnel structure, and large ions ( $\text{K}^+$ ) are needed to support the framework; thus,  $\text{KNO}_3$  is used as molten salt to prepare  $\alpha$ - $\text{MnO}_2$  nanomaterials (Figure 1(a)).  $\beta$ - $\text{MnO}_2$  is a  $(1 \times 1)$  tunnel structure, so a mixture of  $\text{NaNO}_3$  and

$\text{LiNO}_3$  with smaller cation is selected. Zheng et al. have prepared  $\beta$ - $\text{MnO}_2$  nanotubes using  $\text{MnSO}_4$  as reagent, PVP as morphology directing agent and  $\text{NaClO}_3$  as oxidant [33].  $\alpha$ - $\text{MnO}_2$  nanotubes have been synthesized by a hydrothermal treatment of  $\text{KMnO}_4$  in  $\text{HCl}$  solution [11]. As shown in Figure 1(b), the obtained nanotubes have an average outer diameter of 100 nm and the wall thickness of 30 nm, and the length is up to several microns. It is found that the nanotubes are formed *via* solid nanorods involving in chemical etching process.

Other special shapes, such as nanowalls [34], nanodisks [35], urchin-like nanoballs [27], multipods [36], and nanosheets [37], have been fabricated. Some successes discussed above can be summarized in Table 1.

Compared to 1D/2D nanostructures, 3D  $\text{MnO}_2$  hierarchical structures often produce more active sites or possess more interesting properties, so great interests have been given to well-defined  $\text{MnO}_2$  architectures with controlled crystal structures [38]. Six-branched  $\epsilon$ - $\text{MnO}_2$  architectures have been synthesized *via* an aqueous chemical route without any organic templates (Figure 2(a)). The growth rate along the six-fold  $c$ -axis is faster than along the other axes for the crystal structure of  $\epsilon$ - $\text{MnO}_2$ , which results in the elongated twinned pyramidal shape of the crystals. Consequently, the edges of the adjacent facets of the pyramid become the nucleation sites, and the sprouted branches form the central core [13]. Jana et al. have used a green method for the synthesis of hierarchical flower-like Ag-doped  $\beta$ - $\text{MnO}_2$  nanostructures at 300 K. As displayed in Figure 2(b), the flowery nanostructures are composed of tiny nanopetals (500 nm in diameter and  $1.25 \mu\text{m}$  in length) [12]. Fei group have reported a controlled synthesis of hollow microspheres and microcubes of hierarchical  $\text{MnO}_2$  superstructures using  $\text{MnCO}_3$  crystals as the templates [39].  $\text{MnCO}_3$  microspheres and microcubes are synthesized by the reaction of  $\text{MnSO}_4$  and  $\text{NH}_4\text{HCO}_3$ , and  $\text{MnO}_2$  hollow microspheres and microcubes are prepared by mixing  $\text{KMnO}_4$  and the solid  $\text{MnCO}_3$  crystals. In

TABLE I: Synthesis of MnO<sub>2</sub> with different morphologies.

Method	Morphology	Size	Year
Molten salt route	Nanowires	Length of several microns and diameter of 15–30 nm	2009 [10]
	Nanorods	Length of 500 nm–2 μm and diameter of 20–40 nm	
Hydrothermal method	Urchin-like nanoballs	Diameter of 1 μm	2010 [27]
Microemulsion method	Nanodisks	Size of 1–2 μm and thickness of 50–100 nm	2007 [35]
Hydrothermal method	Nanotubes	Outer diameter of 100 nm, wall thickness of 30 nm, and length of several microns	2008 [11]
Hydrothermal method	Multipods	The legs of the multipods are 200–600 nm in width and several microns in length	2006 [36]

the synthesis, a microscale Kirkendall effect is used for the synthesis of hollow microstructures. Other hierarchical architectures with novel morphologies have also been prepared [20, 40–44], such as λ-MnO<sub>2</sub> nanodisks assembled from nanoparticles *via* a novel wet chemical route [20] and MnO<sub>2</sub> microspheres composed of nanodisks [41].

**2.2. Synthesis of MnO Nanomaterials.** MnO, a simple binary metal oxide, has an *Fm-3m* rock-salt structure with a lattice constant of 4.445 Å at 300 K and has attracted strong interest for its application as catalysts [45], contrast enhancement for magnetic resonance imaging (MRI) [46], and LIBs materials [47]. Currently, several methods have been developed for the fabrication of MnO nanostructures with well-controlled shapes, such as nanocrystals [48], nanofibers [49], and nanosheets [50]. Monodisperse MnO nanocrystals have been synthesized by thermal decomposition of manganese oleate using the hot-injection method or thermal decomposition of manganese acetate in the presence of oleic acid [51, 52]. Park et al. have prepared MnO nanospheres (sizes of 5–40 nm) and nanorods (diameters of 7–10 nm and lengths of 30–140 nm) by the thermal decomposition of Mn-surfactant complexes [53]. Nanoscale MnO octahedrons have been prepared by decomposing manganese oleate in octadecene and S at high temperature [54]. Xie and coworkers have fabricated supercrystals (SCs) assembled of octahedral MnO nanocrystals (NCs) [55]. In the synthesis, octahedral MnO NCs are synthesized by thermal deposition of Mn(OOC<sub>2</sub>H<sub>5</sub>)<sub>2</sub> assisted by a mixed solvent of TOA and OA, and then microscale cubic SCs built by NCs are created *via* direct crystallization in ethanol (Figures 3(a) and 3(b)). Other unusual shapes, such as nanoclusters, nanocube, and nanoflake, have also been fabricated [56–59]. Besides rock-salt structure, MnO has another crystal structure, which is hexagonal wurtzite. Nam et al. have reported the synthesis of wurtzite MnO on a carbon template, which may offer an extra degree of freedom in the design of sensors and energy storage devices (Figure 3(c)) [60, 61].

Hybrid nanostructures consisting of two or more different functional units possess novel and enriched properties for magnetic, optical, and catalytic applications. As to MnO, several hybrid nanomaterials have been fabricated, such as porous C-MnO disks, MnO/C nanotubes, MnO/SiO<sub>2</sub> core-shell nanoparticles, and MnO/C core-shell nanoplates [16, 62–64].

### 3. Applications of Manganese Oxide Nanomaterials on Lithium-Ion Batteries (LIBs)

Lithium-ion batteries (LIBs) are regarded as a promising rechargeable power sources for hybrid electric vehicles (HEVs) and portable electronic devices for their high specific capacity, long cycle life, and lack of memory [65]. Electrode materials play an important role in the performance of LIBs. It was found that transition metal oxides nanomaterials are very appealing anode materials owing to their higher theoretical capacities than that of commercial graphite (372 mA·h·g<sup>-1</sup>) [66]. Among them, nanoscale MnO and MnO<sub>2</sub> have attracted more and more attention due to the high theoretical capacities, environmentally benign, low cost, and special properties.

Zhao et al. have synthesized nanoporous γ-MnO<sub>2</sub> hollow microspheres and nanocubes with high initial capacities and excellent cycle performance in LIBs. The γ-MnO<sub>2</sub> architectures provide more possibility to serve as an ideal host material for the insertion and extraction of lithium ions for the nanoporous structure. After 20 cycles, the capacities of the γ-MnO<sub>2</sub> microspheres and nanocubes are 602.1 and 656.5 mA·h·g<sup>-1</sup> [67]. Interconnected porous MnO nanoflakes have been prepared on Ni foam. The obtained nanoflakes retain a capacity of 708.4 mA·h·g<sup>-1</sup> at the 200th charge-discharge cycle after cycling with different current densities up to 2460 mA·g<sup>-1</sup> and deliver a capacity of 376.4 mA·h·g<sup>-1</sup> at 2460 mA·g<sup>-1</sup>. The special morphology of the porous MnO nanoflake affected its electrochemical property: (I) the nanomaterials have a large specific area and offer a large material/electrolyte contact area; (II) the structure can supply enough space to buffer the volume change caused by the electrochemical reaction; (III) the nanosize of flakes leads to a shortened electronic and ionic transport length [59]. In addition, Chen et al. have reported the best cycle performance of MnO anode material, which deliver a capacity of 650 mA·h·g<sup>-1</sup> after 150 cycles at 35.5 mA·g<sup>-1</sup> [68].

Despite the above successes, there are still many challenges in using MnO<sub>2</sub> and MnO as anode materials for LIBs, such as poor cycling performance and poor electrical conductivity. It has been demonstrated that electrode materials with a deliberately designed nanostructure can partly accommodate the strains of Li<sup>+</sup> intercalation and deintercalation [62]. The electrical conductivity of manganese oxide can be enhanced by mixing them with electrolytes

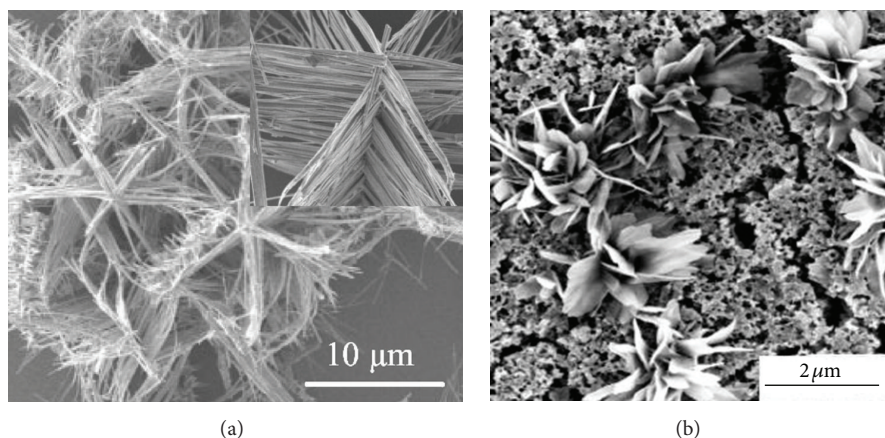


FIGURE 2: (a) SEM image of hierarchical  $\epsilon$ -MnO<sub>2</sub> architectures, the inset is high-magnification SEM image of one architecture, and (b) SEM image of hierarchical flower-like Ag-doped MnO<sub>2</sub> nanostructures [12, 13].

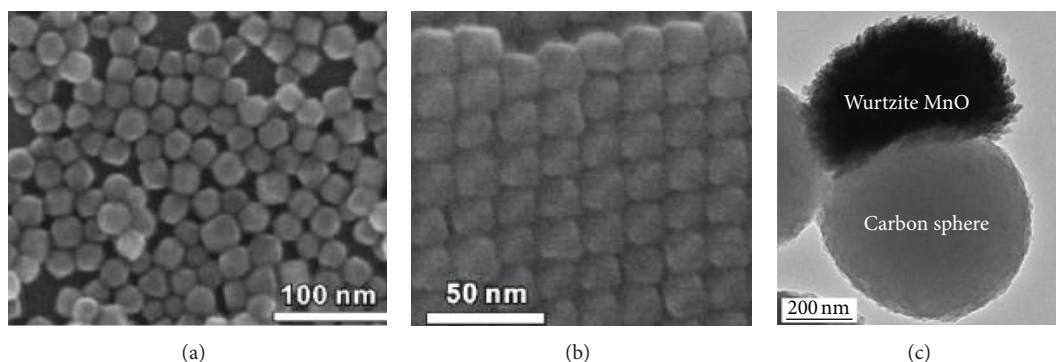


FIGURE 3: (a) SEM image of disperse MnO octahedral NCs, (b) SEM image of well-oriented MnO SCs, and (c) TEM image of hexagonal wurtzite MnO on the carbon sphere template [55, 61].

[69]. For instance, amorphous MnO<sub>2</sub> in a mild KCl aqueous electrolyte has been proved to be an excellent electrode for the faradaic electrochemical capacitor [70]. More importantly, a common strategy for improving the poor electrical conductivity is combining them with carbon to form composites. After Raymundo-Piñero et al. have studied the electrical conductivity and the capacity of the manganese oxide/C nanotubes composites for the first time, several groups have researched the electrical conductivity of different MnO/C composites [71]. For example, MnO/C core-shell nanoplates with a C-shell thickness of about 8.1 nm display a high reversible capacity of 770 mA·h·g<sup>-1</sup> at 200 mA·g<sup>-1</sup> [60]. C-MnO disks exhibit a capacity of 534.6 mA·h·g<sup>-1</sup> after 250 cycles at a relatively high current density of 1000 mA·g<sup>-1</sup>. The high capacity and excellent cycling stability can be attributed to the assembled nanoarchitecture including 3D interconnected nanopores, carbon modification, and the small particle sizes of MnO nanocrystals [64]. Porous MnO/C nanotubes can deliver a reversible capacity as high as 763.3 mA·h·g<sup>-1</sup> after 100 cycles at a charge/discharge current

density of 100 mA·g<sup>-1</sup>. The superior cyclability and rate capability are attributed to the hollow interior, porous structure, 1D structure, and the uniformly dispersed carbon in the porous MnO/C nanotubes [16]. MnO/C nanoparticles have a reversible capacity of 470 mA·h·g<sup>-1</sup> after the 50th cycle, when tested at 75 mA·g<sup>-1</sup> [72]. Additionally, it has been found that nanopainting metal oxides with a thin layer of conducting polymers can improve their lithium storage capabilities. Xiao et al. have synthesized porous spheres assembled from polythiophene-coated MnO<sub>2</sub> nanosheets. The electrochemical measurements show that the obtained nanocomposites can deliver a capacity of 500 mA·h·g<sup>-1</sup> after 100 cycles at a current density of 500 mA·g<sup>-1</sup>. The high-rate lithium storage capability of the nanocomposites might be explained by the special structure: (I) the ultrathin nanosheets entail a high effective electrolyte/electrode contact area and a short solid-state diffusion length of Li<sup>+</sup> ions; (II) the mesopores enable fast ionic transport throughout the electrode; (III) the hierarchical structure is beneficial for the stability of the electrode; (IV) the polythiophene “nanopaint” not only enhances the electrical conductivity but also acts as a buffer

layer for the large volume change and drastic structural or textural alterations during charge/discharge cycling [73].

#### 4. Conclusions

In summary, we have briefly reviewed the recent development of manganese oxide nanomaterials. In the near future, we will face some challenges in spite of the successes discussed above. For instance (I) manganese oxide nanomaterials have recently been synthesized in the labs, and they should be applied in industry. Therefore, we should explore simple and effective methods for the synthesis of manganese oxide nanomaterials with high surface areas and good dispersity, and (II) the application of manganese oxide in the field of electrochemistry is still in its infancy; moreover, some data and conclusions are controversial. Thus, the electrochemical mechanism of manganese oxide nanomaterials should be deeply understood. In short, we hope that this paper will not only show the development of manganese oxide nanomaterials but also give the readers some inspiration to explore novel routes for the synthesis of manganese oxide nanomaterials.

#### Acknowledgments

This work is financially supported by the Natural Science Foundation of Henan Department of Science & Technology (no. 112300410224), Natural Science Foundation of Henan Department of Education (no. 13A150813) and the Natural Science Foundation of Nanyang Normal University (no. 2X2010014).

#### References

- [1] C. Burda, X. B. Chen, R. Narayanan, and M. A. El-Sayed, "Chemistry and properties of nanocrystals of different shapes," *Chemical Reviews*, vol. 105, no. 4, pp. 1025–1102, 2005.
- [2] J. Cao, Q. H. Mao, L. Shi, and Y. T. Qian, "Fabrication of  $\gamma$ -MnO<sub>2</sub>/ $\alpha$ -MnO<sub>2</sub>/ hollow core/shell structures and their application to water treatment," *Journal of Materials Chemistry*, vol. 21, pp. 16210–16215, 2011.
- [3] D. Yan, S. Cheng, R. F. Zhuo et al., "Nanoparticles and 3D sponge-like porous networks of manganese oxides and their microwave absorption properties," *Nanotechnology*, vol. 20, no. 10, Article ID 105706, 2009.
- [4] Y. W. Tan, L. R. Meng, Q. Peng, and Y. D. Li, "One-dimensional single-crystalline Mn<sub>3</sub>O<sub>4</sub> nanostructures with tunable length and magnetic properties of Mn<sub>3</sub>O<sub>4</sub> nanowires," *Chemical Communications*, vol. 47, no. 4, pp. 1172–1174, 2011.
- [5] X. Zhang, Z. Xing, Y. Yu et al., "Synthesis of Mn<sub>3</sub>O<sub>4</sub> nanowires and their transformation to LiMn<sub>2</sub>O<sub>4</sub> polyhedrons, application of LiMn<sub>2</sub>O<sub>4</sub> as a cathode in a lithium-ion battery," *CrystEngComm*, vol. 14, no. 4, pp. 1485–1489, 2012.
- [6] R. Ma, Y. Bando, L. Zhang, and T. Sasaki, "Layered MnO<sub>2</sub> nanobelts: hydrothermal synthesis and electrochemical measurement," *Advanced Materials*, vol. 16, no. 11, pp. 918–922, 2004.
- [7] F. Y. Cheng, J. Z. Zhao, W. Song et al., "Facile controlled synthesis of MnO<sub>2</sub> nanostructures of novel shapes and their application in batteries," *Inorganic Chemistry*, vol. 45, no. 5, pp. 2038–2044, 2006.
- [8] F. Y. Cheng, J. A. Shen, B. Peng, Y. D. Pan, Z. L. Tao, and J. Chen, "Rapid room-temperature synthesis of nanocrystalline spinels as oxygen reduction and evolution electrocatalysts," *Nature Chemistry*, vol. 3, pp. 79–84, 2011.
- [9] B. Sun, Z. X. Chen, H. S. Kim, H. Ahn, and G. X. Wang, "MnO/C core-shell nanorods as high capacity anode materials for lithium-ion batteries," *Journal of Power Sources*, vol. 196, no. 6, pp. 3346–3349, 2011.
- [10] N. Sui, Y. Duan, X. Jiao, and D. Chen, "Large-scale preparation and catalytic properties of one-dimensional  $\alpha/\beta$ -mno<sub>2</sub> nanostructures," *Journal of Physical Chemistry C*, vol. 113, no. 20, pp. 8560–8565, 2009.
- [11] J. Luo, H. T. Zhu, H. M. Fan et al., "Synthesis of single-crystal tetragonal  $\alpha$ -MnO<sub>2</sub> nanotubes," *Journal of Physical Chemistry C*, vol. 112, no. 33, pp. 12594–12598, 2008.
- [12] S. Jana, S. Pande, A. K. Sinha et al., "A green chemistry approach for the synthesis of flower-like Ag-doped MnO<sub>2</sub> nanostructures probed by surface-enhanced raman spectroscopy," *Journal of Physical Chemistry C*, vol. 113, no. 4, pp. 1386–1392, 2009.
- [13] Y. S. Ding, X. F. Shen, S. Gomez, H. Luo, M. Aindow, and S. L. Sui, "Hydrothermal growth of manganese dioxide into three-dimensional hierarchical nanoarchitectures," *Advanced Functional Materials*, vol. 16, no. 4, pp. 549–555, 2006.
- [14] C. N. R. Rao, S. R. C. Vivekchand, K. Biswas, and A. Govindaraja, "Synthesis of inorganic nanomaterials," *Dalton Transactions*, no. 34, pp. 3728–3749, 2007.
- [15] W. Xiao, D. Wang, and X. W. Lou, "Shape-controlled synthesis of MnO<sub>2</sub> nanostructures with enhanced electrocatalytic activity for oxygen reduction," *The Journal of Physical Chemistry C*, vol. 114, pp. 1694–1700, 2010.
- [16] G. L. Xu, Y. F. Xu, H. Sun et al., "Facile synthesis of porous MnO/C nanotubes as a high capacity anode material for lithium ion batteries," *Chemical Communications*, vol. 48, pp. 8502–8504, 2012.
- [17] D. Yan, P. X. Yan, G. H. Yue et al., "Self-assembled flower-like hierarchical spheres and nanobelts of manganese oxide by hydrothermal method and morphology control of them," *Chemical Physics Letters*, vol. 440, no. 1–3, pp. 134–138, 2007.
- [18] X. Wang and Y. Li, "Synthesis and formation mechanism of manganese dioxide nanowires/nanorods," *Chemistry*, vol. 9, pp. 300–306, 2003.
- [19] S. Ching, E. J. Welch, S. M. Hughes, A. B. F. Bahadoor, and S. L. Suib, "Nonaqueous sol-gel syntheses of microporous manganese oxides," *Chemistry of Materials*, vol. 14, no. 3, pp. 1292–1299, 2002.
- [20] N. Wang, X. Cao, L. He et al., "One-Pot synthesis of highly crystalline  $\lambda$ -MnO<sub>2</sub> nanodisks assembled from nanoparticles: morphology evolutions and phase transitions," *The Journal of Physical Chemistry C*, vol. 112, no. 2, pp. 365–369, 2008.
- [21] Y. Oaki and H. Imai, "One-pot synthesis of manganese oxide nanosheets in aqueous solution: chelation-mediated parallel control of reaction and morphology," *Angewandte Chemie*, vol. 119, no. 26, pp. 5039–5043, 2007.
- [22] X. Yu, Y. He, J. Sun et al., "Nanocrystalline MnO thin film anode for lithium ion batteries with low overpotential," *Electrochemical Communications*, vol. 11, no. 4, pp. 791–794, 2009.
- [23] T. Ahmad, K. V. Ramanujachary, S. E. Lofland, and A. K. Ganguli, "Nanorods of manganese oxalate: a single source precursor to different manganese oxide nanoparticles (MnO, Mn<sub>2</sub>O<sub>3</sub>, Mn<sub>3</sub>O<sub>4</sub>)," *Journal of Materials Chemistry*, vol. 14, no. 23, pp. 3406–3410, 2004.

- [24] P. Yu, X. Zhang, D. Wang, L. Wang, and Y. Ma, "Shape-controlled synthesis of 3D hierarchical MnO<sub>2</sub> nanostructures for electrochemical supercapacitors," *Crystal Growth & Design*, vol. 9, no. 1, pp. 528–533, 2009.
- [25] C. Wu, W. Xie, M. Zhang, L. Bai, J. Yang, and Y. Xie, "Environmentally friendly  $\gamma$ -MnO<sub>2</sub> hexagon-based nanoarchitectures: structural understanding and their energy-saving applications," *Chemistry*, vol. 15, no. 2, pp. 492–500, 2009.
- [26] R. Liu, J. Duay, and S. B. Lee, "Redox exchange induced MnO<sub>2</sub> nanoparticle enrichment in poly(3,4-ethylenedioxythiophene) nanowires for electrochemical energy storage," *ACS Nano*, vol. 4, no. 7, pp. 4299–4307, 2010.
- [27] Y. Chen, Y. Hong, Y. Ma, and J. Li, "Synthesis and formation mechanism of urchin-like nano/micro-hybrid  $\alpha$ -MnO<sub>2</sub>," *Journal of Alloys and Compounds*, vol. 490, pp. 331–335, 2010.
- [28] X. Wang and Y. Li, "Selected-control hydrothermal synthesis of  $\alpha$ - and  $\beta$ -MnO<sub>2</sub> single crystal nanowires," *Journal of the American Chemical Society*, vol. 124, no. 12, pp. 2880–2881, 2002.
- [29] N. Kijima, H. Yasuda, T. Sato, and Y. Yoshimura, "Preparation and characterization of open tunnel oxide  $\alpha$ -MnO<sub>2</sub> precipitated by ozone oxidation," *Journal of Solid State Chemistry*, vol. 159, no. 1, pp. 94–102, 2001.
- [30] M. H. Huang, S. Mao, H. Feick et al., "Room-temperature ultraviolet nanowire nanolasers," *Science*, vol. 292, no. 5523, pp. 1897–1899, 2001.
- [31] S. Chen, J. Zhu, Q. Han, Z. Zheng, Y. Yang, and X. Wang, "Shape-controlled synthesis of one-dimensional MnO<sub>2</sub> via a facile quick-precipitation procedure and its electrochemical properties," *Crystal Growth & Design*, vol. 9, no. 10, pp. 4356–4361, 2009.
- [32] X. Wang and Y. Li, "Rational synthesis of  $\alpha$ -MnO<sub>2</sub> single-crystal nanorods," *Chemical Communications*, no. 7, pp. 764–765, 2002.
- [33] D. Zheng, S. Sun, W. Fan et al., "One-step preparation of single-crystalline  $\beta$ -MnO<sub>2</sub> nanotubes," *Journal of Physical Chemistry B*, vol. 109, no. 34, pp. 16439–16443, 2005.
- [34] H. T. Zhu, J. Luo, H. X. Yang et al., "Birnessite-type MnO<sub>2</sub> nanowalls and their magnetic properties," *Journal of Physical Chemistry C*, vol. 112, no. 44, pp. 17089–17094, 2008.
- [35] N. Wang, X. Cao, L. Guo, and S. Yang, " $\lambda$ -MnO<sub>2</sub> nanodisks and their magnetic properties," *Nanotechnology*, vol. 18, no. 47, Article ID 475605, 2007.
- [36] D. Zheng, Z. Yin, W. Zhang, X. Tan, and S. Sun, "Novel branched  $\gamma$ -MnOOH and  $\beta$ -MnO<sub>2</sub> multipod nanostructures," *Crystal Growth & Design*, vol. 6, no. 8, pp. 1733–1735, 2006.
- [37] X. Yang, Y. Makita, Z. H. Liu, K. Sakane, and K. Ooi, "Structural characterization of self-assembled MnO<sub>2</sub> nanosheets from birnessite manganese oxide single crystals," *Chemistry of Materials*, vol. 16, no. 26, pp. 5581–5588, 2004.
- [38] Z. Li, Y. Ding, Y. Xiong, Q. Yang, and Y. Xie, "One-step solution-based catalytic route to fabricate novel  $\alpha$ -MnO<sub>2</sub> hierarchical structures on a large scale," *Chemical Communications*, no. 7, pp. 918–920, 2005.
- [39] J. Fei, Y. Cui, X. Yan et al., "Controlled preparation of MnO<sub>2</sub> hierarchical hollow nanostructures and their application in water treatment," *Advanced Materials*, vol. 20, no. 3, pp. 452–456, 2008.
- [40] B. Li, G. Rong, Y. Xie, L. Huang, and C. Feng, "Low-temperature synthesis of  $\alpha$ -MnO<sub>2</sub> hollow urchins and their application in rechargeable Li<sup>+</sup> batteries," *Inorganic Chemistry*, vol. 45, no. 16, pp. 6404–6410, 2006.
- [41] C. Xia, W. Ning, and G. Lin, "Facile synthesis of novel MnO<sub>2</sub> hierarchical nanostructures and their application to nitrite sensing," *Sensors and Actuators B*, vol. 137, no. 2, pp. 710–714, 2009.
- [42] X. Fu, J. Feng, H. Wang, and K. M. Ng, "Room temperature synthesis of a novel  $\gamma$ -MnO<sub>2</sub> hollow structure for aerobic oxidation of benzyl alcohol," *Nanotechnology*, vol. 20, no. 37, Article ID 375601, 2009.
- [43] X. C. Song, Y. Zhao, and Y. F. Zheng, "Synthesis of MnO<sub>2</sub> nanostructures with sea urchin shapes by a sodium dodecyl sulfate-assisted hydrothermal process," *Crystal Growth & Design*, vol. 7, no. 1, pp. 159–162, 2007.
- [44] H. Chen and J. He, "Self-assembly of birnessite manganese dioxide into monodisperse honeycomb and hollow nanospheres," *Chemistry Letters*, vol. 36, pp. 174–175, 2007.
- [45] Q. C. Sun, X. Xu, S. N. Baker, A. D. Christianson, and J. L. Musfeldt, "Experimental determination of ionicity in MnO nanoparticles," *Chemistry of Materials*, vol. 23, no. 11, pp. 2956–2960, 2011.
- [46] M. Baldi, E. Finocchio, F. Milella, and G. Busca, "Catalytic combustion of C3 hydrocarbons and oxygenates over Mn<sub>3</sub>O<sub>4</sub>," *Applied Catalysis B*, vol. 16, no. 1, pp. 43–51, 1998.
- [47] L. Ji and X. Zhang, "Manganese oxide nanoparticle-loaded porous carbon nanofibers as anode materials for high-performance lithium-ion batteries," *Electrochemistry Communications*, vol. 11, no. 4, pp. 795–798, 2009.
- [48] S. L. Brock, M. Sanabria, S. L. Suib, V. Urban, P. Thiyagarajan, and D. I. Potter, "Particle size control and self-assembly processes in novel colloids of nanocrystalline manganese oxide," *Journal of Physical Chemistry B*, vol. 103, no. 35, pp. 7416–7428, 1999.
- [49] Z. Tian, Q. Feng, N. Sumida, Y. Makita, and K. Ooi, "Synthesis of manganese oxide nanofibers by self-assembling hydrothermal process," *Chemistry Letters*, vol. 33, no. 8, pp. 952–953, 2004.
- [50] Y. Oaki and H. Imai, "One-pot synthesis of manganese oxide nanosheets in aqueous solution: chelation-mediated parallel control of reaction and morphology," *Angewandte Chemie*, vol. 46, pp. 4951–4955, 2007.
- [51] Q. Li, J. Wang, Y. He, W. Liu, and X. Qiu, "Growth of nearly monodisperse MnO nanocrystals in a two-size distribution system," *Crystal Growth & Design*, vol. 9, no. 7, pp. 3100–3103, 2009.
- [52] M. Yin and S. O'Brien, "Synthesis of monodisperse nanocrystals of manganese oxides," *Journal of the American Chemical Society*, vol. 125, no. 34, pp. 10180–10181, 2005.
- [53] J. Park, E. Kang, C. J. Bae et al., "Synthesis, characterization, and magnetic properties of uniform-sized MnO nanospheres and nanorods," *Journal of Physical Chemistry B*, vol. 108, no. 36, pp. 13594–13598, 2004.
- [54] A. Puglisi, S. Mondini, S. Cenedese, A. M. Ferretti, N. Santo, and A. Ponti, "Monodisperse octahedral  $\alpha$ -MnS and MnO nanoparticles by the decomposition of manganese oleate in the presence of sulfur," *Chemistry of Materials*, vol. 22, no. 9, pp. 2804–2813, 2010.
- [55] S. Xie, X. Zhou, X. Han et al., "Supercrystals from crystallization of octahedral MnO nanocrystals," *Journal of Physical Chemistry C*, vol. 113, no. 44, pp. 19107–19111, 2009.
- [56] R. Xing, G. Liu, Q. Quan et al., "Functional MnO nanoclusters for efficient siRNA delivery," *Chemical Communications*, vol. 47, pp. 12152–12154, 2011.

- [57] T. Ould-Ely, D. Prieto-Centurion, A. Kumar et al., "Manganese(II) oxide nanohexapods: insight into controlling the form of nanocrystals," *Chemistry of Materials*, vol. 18, no. 7, pp. 1821–1829, 2006.
- [58] I. Rusakova, T. Ould-Ely, C. Hofmann et al., "Nanoparticle shape conservation in the conversion of MnO nanocrosses into Mn<sub>3</sub>O<sub>4</sub>," *Chemistry of Materials*, vol. 19, no. 6, pp. 1369–1375, 2007.
- [59] X. Li, D. Li, L. Qiao et al., "Interconnected porous MnO nanoflakes for high-performance lithium ion battery anodes," *Journal of Materials Chemistry*, vol. 22, pp. 9189–9194, 2012.
- [60] H. Ohno, "Making nonmagnetic semiconductors ferromagnetic," *Science*, vol. 281, no. 5379, pp. 951–956, 1998.
- [61] K. M. Nam, Y. Kim, Y. Jo et al., "New crystal structure: synthesis and characterization of hexagonal wurtzite MnO," *Journal of the American Chemical Society*, vol. 134, pp. 8392–8395, 2012.
- [62] X. Zhang, Z. Xing, L. Wang et al., "Synthesis of MnO@C core-shell nanoplates with controllable shell thickness and their electrochemical performance for lithium-ion batteries," *Journal of Materials Chemistry*, vol. 22, no. 34, pp. 17864–17869, 2012.
- [63] T. D. Schladt, K. Koll, S. Prüfer et al., "Multifunctional superparamagnetic MnO@SiO<sub>2</sub> core/shell nanoparticles and their application for optical and magnetic resonance imaging," *Journal of Materials Chemistry*, vol. 22, pp. 9253–9262, 2012.
- [64] Y. Sun, X. Hu, W. Luo, and Y. Huang, "Porous carbon-modified MnO disks prepared by a microwave-polyol process and their superior lithium-ion storage properties," *Journal of Materials Chemistry*, vol. 22, pp. 19190–19195, 2012.
- [65] M. Armand and J. M. Tarascon, "Building better batteries," *Nature*, vol. 451, no. 7179, pp. 652–657, 2008.
- [66] X. Sun, X. Wang, L. Qiao et al., "Electrochemical behaviors of porous SnO<sub>2</sub>-Sn/C composites derived from pyrolysis of SnO<sub>2</sub>/poly(vinylidene fluoride)," *Electrochimica Acta*, vol. 66, pp. 204–209, 2012.
- [67] J. Zhao, Z. Tao, J. Liang, and J. Chen, "Facile synthesis of nanoporous  $\gamma$ -MnO<sub>2</sub> structures and their application in rechargeable li-Ion batteries," *Crystal Growth & Design*, vol. 8, pp. 2799–2805, 2008.
- [68] K. Zhong, X. Xia, B. Zhang, H. Li, Z. Wang, and L. Chen, "MnO powder as anode active materials for lithium ion batteries," *Journal of Power Sources*, vol. 195, no. 10, pp. 3300–3308, 2010.
- [69] Y. U. Jeong and A. Manthiram, "Nanocrystalline manganese oxides for electrochemical capacitors with neutral electrolytes," *Journal of the Electrochemical Society*, vol. 149, no. 11, pp. A1419–A1422, 2002.
- [70] H. Y. Lee and J. B. Goodenough, "Supercapacitor behavior with KCl electrolyte," *Journal of Solid State Chemistry*, vol. 144, no. 1, pp. 220–223, 1999.
- [71] E. Raymundo-Piñero, V. Khomenko, E. Frackowiak, and F. Béguin, "Performance of manganese oxide/CNTs composites as electrode materials for electrochemical capacitors," *Journal of the Electrochemical Society*, vol. 152, no. 1, pp. A229–A235, 2005.
- [72] J. Liu and Q. M. Pan, "MnO/C nanocomposites as high capacity anode materials for li-Ion batteries," *Electrochemical and Solid-State Letters*, vol. 13, no. 10, pp. A139–A142, 2010.
- [73] W. Xiao, J. S. Chen, Q. Lu, and X. W. Lou, "Porous spheres assembled from polythiophene (PTh)-coated ultrathin MnO<sub>2</sub> nanosheets with enhanced lithium storage capabilities," *The Journal of Physical Chemistry C*, vol. 114, no. 27, pp. 12048–12051, 2010.

## Research Article

# A Subwavelength Plasmonic Waveguide Filter with a Ring Resonator

Xiang Zhai,<sup>1,2</sup> Shuangchun Wen,<sup>1,2</sup> Dong Xiang,<sup>2,3</sup> Ling-Ling Wang,<sup>2</sup> Wujiaihemaiti Rexidaiguli,<sup>2</sup> Liu Wang,<sup>2</sup> and Dianyun Fan<sup>1,2</sup>

<sup>1</sup> Key Laboratory for Micro/Nano Optoelectronic Devices of Ministry of Education, School of Information Science and Engineering, Hunan University, Changsha 410082, China

<sup>2</sup> School of Physics and Microelectronics, Hunan University, Changsha 410082, China

<sup>3</sup> School of Nuclear Science and Technology, University of South China, Hengyang 421001, China

Correspondence should be addressed to Shuangchun Wen; [scwen@hnu.edu.cn](mailto:scwen@hnu.edu.cn) and Dong Xiang; [xiangdong007@163.com](mailto:xiangdong007@163.com)

Received 29 January 2013; Accepted 20 February 2013

Academic Editor: Bo Yu

Copyright © 2013 Xiang Zhai et al. This is an open access article distributed under the Creative Commons Attribution License, which permits unrestricted use, distribution, and reproduction in any medium, provided the original work is properly cited.

The transmission characteristics of the electromagnetic wave are numerically investigated in two-dimensional compound plasmonic structures composed of two straight subwavelength metal-insulator-metal (MIM) waveguides and a ring resonator. The two straight MIM waveguides situate on both sides of the ring resonator, and the MIM waveguide of the outgoing side has a positional angular deviation  $\theta$  relative to the MIM waveguide of the incoming side. The results show that the filtering performances of the asymmetric structures ( $\theta \neq 0^\circ$ ) are greatly improved in comparison with the symmetric structure ( $\theta = 0^\circ$ ). For most of the asymmetric structures, there is a transmission minimum at the slightly bigger wavelength than one at which the transmission peak appears for the symmetric structures, and there is still a transmission peak at the wavelength of the transmission peak of the symmetric structures. Moreover, the difference between the transmission peak and valley is increased, and the breadth of the transmission peak becomes narrow.

## 1. Introduction

Surface plasmon polaritons (SPPs) are *p*-polarized optical surface waves that propagate along a metal-dielectric interface with fields that peak at the interface and decay exponentially away into both sides [1]. However, the single metal-dielectric interface SPP, characterized by high attenuation and low confinement, limits the scope for applications. To date, one of the most practical ways of enhancing the SPP confinement is to use a metal-insulator-metal (MIM) subwavelength waveguide structure, along which a symmetrically coupled-SPP mode can propagate. This provides us an avenue to concentrate and channel light with subwavelength structures and develop practical nanophotonic devices for future information technologies. Thus, some novel plasmonic elements based on MIM waveguide structures have been proposed, such as bends and splitters [2], Y-shaped combiners [3], Mach-Zehnder interferometers [4, 5], Bragg reflectors [6,

7], directional couplers [8, 9], and tooth-shaped plasmonic waveguide filters [10].

Recently, Wang and his coworkers [11] have investigated two-dimensional (2D) compound plasmonic structures composed of two straight MIM waveguides with a ring resonator. Their result shows that some transmission resonance peaks appear at some specific wavelengths which meet the resonance conditions in the ring. However, the discussed compound structure in their work is symmetric; that is, both of the two MIM straight waveguides are located symmetrically at both sides of the ring resonator. This suggests that even if the resonance condition has not been satisfied, optical wave will still have not low transmission. Therefore, if the symmetrical distribution is broken, the properties of the optical transmission through this kind of asymmetric structure can present more novel features, and then the filtering performance will be greatly improved. In this work, we will mainly discuss the transmission characteristics of

the asymmetric structure based on MIM plasmonic waveguides with a ring resonator.

## 2. Model and Method

Figure 1 shows schematically a 2D subwavelength plasmonic waveguide filter composed of two straight MIM waveguides and a ring resonator. The two MIM waveguides situate on both sides of the ring resonator, and the MIM waveguide of the outgoing side (waveguide II) has a positional angular deviation  $\theta$  relative to the MIM waveguide of the incoming side (waveguide I). All the widths of the slits in the two MIM waveguides and the width of the ring are  $w = 50$  nm. The radius of the ring is  $r$ , which is the average of the inner radius  $r_i$  and the outer radius  $r_a$ ,  $r = (r_a + r_i)/2$ . The medium of the the slits and the ring (white area) is assumed to be air whose relative permittivity  $\epsilon_d$  is set to be 1. The metal (gray area) is chosen to be silver, whose frequency-dependent relative permittivity obeys the Drude model as  $\epsilon_m(\omega) = \epsilon_\infty - \omega_p^2/(\omega^2 + i\gamma\omega)$ . Here  $\epsilon_\infty = 4.2$  is the high-frequency bulk permittivity,  $\omega_p = 1.346 \times 10^{16}$  rad/s is the bulk plasmon frequency,  $\gamma = 9.617 \times 10^{13}$  rad/s is the damping factor, and  $\omega$  is the angular frequency of the incident electromagnetic radiation [12].

The 2D finite-difference time-domain (FDTD) method [13] is employed to simulate and calculate the optical transmission through these gratings. In our simulation, the spatial mesh steps are set  $\Delta x = \Delta z = 5$  nm and the time step is set  $\Delta t = \Delta x/2c$  ( $c$  is the velocity of light in the air), and the calculated region is truncated by using Mur boundary condition on all the boundaries. Only normally incident  $p$ -polarized waves are considered here, implying that the magnetic field ( $H$ ) is along the  $y$  direction. Two power monitors are set at the locations Port-1 and Port-2, far from the ring 150 nm, to detect the incident and the transmission fields for calculating the incident power of  $P_{in}$  and the transmitted power of  $P_{out}$ , respectively. The transmittance is defined to be  $T = P_{out}/P_{in}$ .

## 3. Simulation Results and Discussion

Firstly, we initialized the radius of the ring  $r = 155$  nm and studied the effect of the positional angular deviation  $\theta$  on transmission spectrum of the structure. Figure 2 displays the calculated transmission spectra of the structure with different  $\theta$  ( $0^\circ$ ,  $30^\circ$ ,  $45^\circ$ ,  $60^\circ$ , and  $90^\circ$ ) at the range from 400 nm to 1800 nm, respectively. In Figure 2, one can find the following main features. First, the transmission spectra of the asymmetric structures ( $\theta \neq 0^\circ$ ) are almost the symmetric structure ( $\theta = 0^\circ$ ), and the transmittances of symmetrical structure are approximately maxima at all the wavelength range. Second, when  $\theta = 0^\circ$ , there are three transmission maxima corresponding to 457 nm, 665 nm, 1235 nm and two minima located at 523 nm and 861 nm. However, these transmission minima are still relatively high and greater than 0.5, even the difference between the transmission peak and valley is only about 0.4. Third, for the most of the asymmetric structures ( $\theta \neq 0^\circ$ ), a transmission minimum appears at the slightly bigger wavelength than one at which the transmission peak

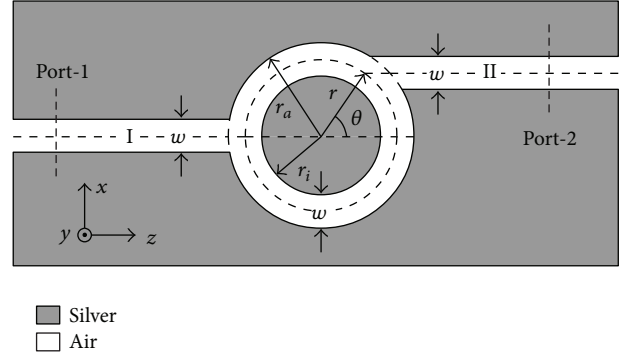


FIGURE 1: Schematic of the MIM plasmonic waveguide with a ring resonator.

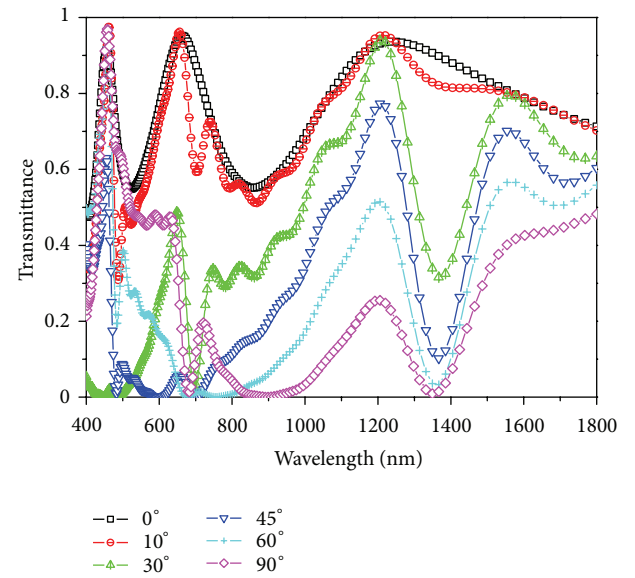


FIGURE 2: (Color Online) Transmission spectra of the MIM plasmonic waveguide with a ring resonator and different  $\theta$  for  $r = 155$  nm.

appears for the symmetric structure ( $\theta = 0^\circ$ ), and some of these transmission minima are almost reduced to zero. For example, the transmission minima are almost zero at wavelengths 488 nm and 697 nm for  $\theta = 30^\circ$ , 483 nm and 702 nm for  $\theta = 45^\circ$ , 478 nm and 1367 nm for  $\theta = 60^\circ$ , and 683 nm and 1332 nm for  $\theta = 90^\circ$ . Fourth, for the most of the asymmetric structures ( $\theta \neq 0^\circ$ ), there is still a transmission peak at the peak wavelength of the symmetric structure ( $\theta = 0^\circ$ ), but the transmittance becomes smaller. Here, it should be pointed out that the transmittance at wavelength about 1200 nm decreases gradually as the positional angular deviation  $\theta$  increases from  $0^\circ$  to  $90^\circ$ . Finally, just because of the above two, when  $\theta \neq 0^\circ$ , the breadth of the transmission peak becomes narrow and the difference between the transmission peak and valley is increased apparently. For example, when  $\theta = 45^\circ$ , transmission maximum at wavelength 1206 nm is about 0.77, while the transmission minima at wavelengths 702 nm and 1367 nm are about 0.002 and 0.1, respectively, so the difference

between the transmission peak and valley increases to about 0.7.

It is very clear that the transmission characteristics of these above MIM plasmonic waveguide structures with a ring resonator mainly depend on two kinds of factors: one is electromagnetic wave resonance effect of the ring cavity, and the other is the relative positions of two MIM waveguides I and II on both sides of the ring. It is known that the resonating wavelength of a ring resonator can be obtained theoretically by the following equation:

$$n_{\text{eff}} \cdot 2\pi r = N \cdot \frac{\lambda}{2}, \quad (1)$$

where  $n_{\text{eff}}$  is the effective index of the coupled-SPP mode in the ring,  $\lambda$  is vacuum wavelength of the incident wave, and  $N$  is mode number. Because the light channel in the ring can be approximated as arc-shaped MIM waveguide, for  $p$ -polarized case,  $n_{\text{eff}}$  can be approximately calculated by the following [14]:

$$\frac{\varepsilon_d \sqrt{n_{\text{eff}}^2 - \varepsilon_m}}{\varepsilon_m \sqrt{n_{\text{eff}}^2 - \varepsilon_d}} = \frac{1 - \exp\left(w \sqrt{n_{\text{eff}}^2 - \varepsilon_d}\right)}{1 + \exp\left(w \sqrt{n_{\text{eff}}^2 - \varepsilon_d}\right)}. \quad (2)$$

Secondly, in order to show electromagnetic wave resonance effect of ring cavity, we calculated the electromagnetic field distribution of the three transmission maxima and two minima of the symmetric structure ( $\theta = 0^\circ$ ). Figures 3(a) and 3(c) depict the contour profiles of fields  $|H_y|$  for transmission maxima at 1235 nm and 665 nm, respectively. According to (1) and (2), transmission maxima at wavelength 1235 nm and 665 nm correspond to the even order resonant mode of  $N = 2$  and 4, respectively. At the same time, joints between the ring cavity and two straight MIM waveguides are antinodes, and there is a higher magnetic field intensity in two straight MIM waveguides. It indicates that even-order waveguide resonances in the ring can lead to efficient coupling of the incident electromagnetic wave from MIM waveguide I through the ring cavity into MIM waveguide II. On the contrast, in Figures 3(b) and 3(d), the magnetic field distributions of transmission minima at 861 nm and 523 nm in the ring also produced a typical standing wave pattern, but the resonant mode numbers inside the ring are odd, such as  $N = 3$  and 5. Because the MIM waveguide I and II symmetrically locate on both sides of the ring, the magnetic field distribution at joints of ring resonator with two straight MIM waveguide will be different: one is a node, and another is an antinode. Therefore, in such odd-order resonance condition, the incident electromagnetic wave from MIM waveguide I is strongly reflected back by the ring cavity, and the electromagnetic energy flow coupled into the ring cavity is relatively low. However, because the structure is symmetric, resulting in equivalent optical path in the ring, a certain optical transmission can be still maintained. Between the wavelength range of the maximum and minimum transmissions as the above mentioned, we can speculate that electromagnetic wave in the ring will not form a stable resonance (including even-order and odd-order resonance), and the optical transmission will vary between the maximum and minimum transmission.

Thirdly, we investigated the reason why there is a transmission minimum for most of the asymmetric structures ( $\theta \neq 0^\circ$ ) at the slightly bigger peak wavelength than one at which the transmission peak appears for the symmetric structure ( $\theta = 0^\circ$ ). In addition, we also calculated the electromagnetic field distribution corresponding to the transmission minima. Figures 4(a)–4(c) depict the field distributions of  $|H_y|$  for the asymmetric structure with  $\theta = 45^\circ$  at the transmission minimum wavelengths 1367 nm, 702 nm, and 483 nm, respectively. In Figure 4, one can find that the typical standing wave patterns formed in the ring and the antinode number inside the ring are even, which suggests that these wavelengths, respectively, correspond to the resonant modes for  $N = 2, 4,$  and  $6$ . However, the two straight MIM waveguides are asymmetric to the ring cavity, so the magnetic field distribution is different at the two joints. The joint with the waveguide I locates in the range of the magnetic antinode of standing wave in the ring resonator (not strictly on the location of the maximum of the magnetic intensity), so the magnetic field intensity at the joint is relatively strong. On the contrary, the magnetic field intensity at the joint with the waveguide II is weaker, just because the joint is the magnetic nodes of the standing wave. Therefore, only little electromagnetic wave of that joint can enter into the straight MIM waveguide II, resulting in a very low transmission. According to the relation between the positional deviation angle  $\theta$  and the position of the magnetic nodes of the standing wave, it is not hard to forecast that the transmittance of the asymmetric structure with  $\theta = 45^\circ$  for the  $N = 4$  resonance mode could be close to zero, because the joint of the waveguide II and the ring may be locate at the magnetic nodes of the standing wave. Figures 2 and 4(b) can further confirm this point.

Fourthly, we also calculated the electromagnetic field distribution corresponding to the transmission maxima of the asymmetric structures ( $\theta \neq 0^\circ$ ). Figures 5(a)–5(c) show the contour profiles of magnetic field intensity  $|H_y|$  at wavelengths 1206 nm ( $N = 2$  mode) for  $\theta = 45^\circ$ , 648 nm ( $N = 4$  mode) for  $\theta = 30^\circ$ , and 457 nm ( $N = 6$  mode) for  $\theta = 90^\circ$ , respectively. In these pictures, one can see that magnetic field distribution of these transmission maxima has the same characteristic that the magnetic field intensities in the joints of the ring cavity with two straight MIM waveguides are relatively strong. All the joints are nearby antinodes of standing wave in the ring, which indicates that more electromagnetic wave from straight MIM waveguide I can couple into the ring cavity and enter into the straight MIM waveguide II.

Finally, we studied the influence of the radius of the ring on the wavelengths of the resonant mode. Figure 6 shows the transmission spectra corresponding to the rings with radii  $r = 135$  nm, 155 nm, and 175 nm for the symmetric structure ( $\theta = 0^\circ$ ), respectively. As shown in Figure 6, the transmission peaks exhibit red shift as the radius increases. This result can be explained in terms of (1) and (2). According to (2), when  $\varepsilon_d$  and  $w$  are fixed,  $n_{\text{eff}}$  changes little as  $\lambda$  increases in the considered wavelength region. Consequently,  $\lambda$  will increase as  $r$  increases in terms of (1). In addition, we also calculated the transmission spectra of the MIM plasmonic waveguide with a ring resonator of different radius for different  $\theta$ .

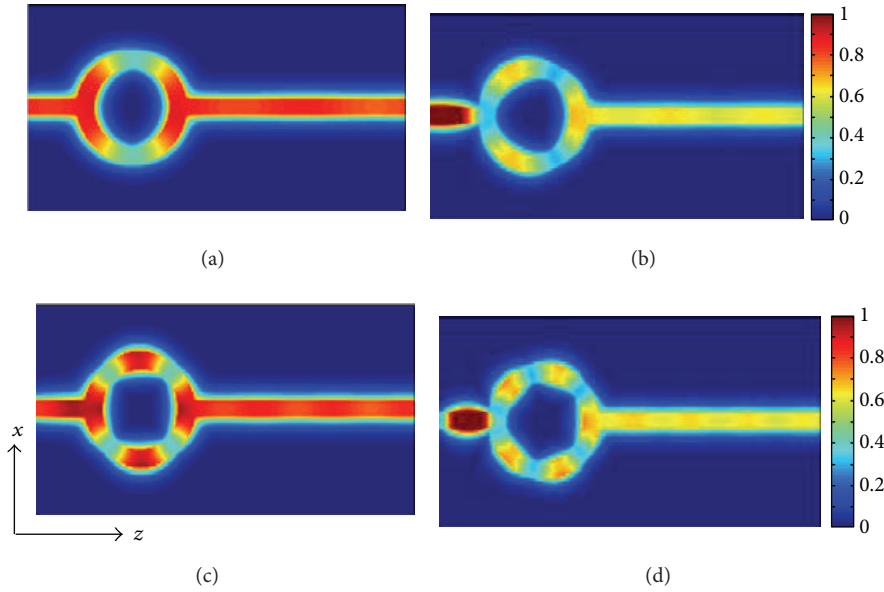


FIGURE 3: (Color Online) The contour profiles of magnetic field intensity  $|H_y|$  at maximum and minimum wavelengths for the symmetric structure ( $\theta = 0^\circ$ ). (a) and (c) are at maximum wavelengths 1235 nm and 665 nm, respectively. (b) and (d) are at minimum wavelengths 861 nm and 523 nm, respectively.

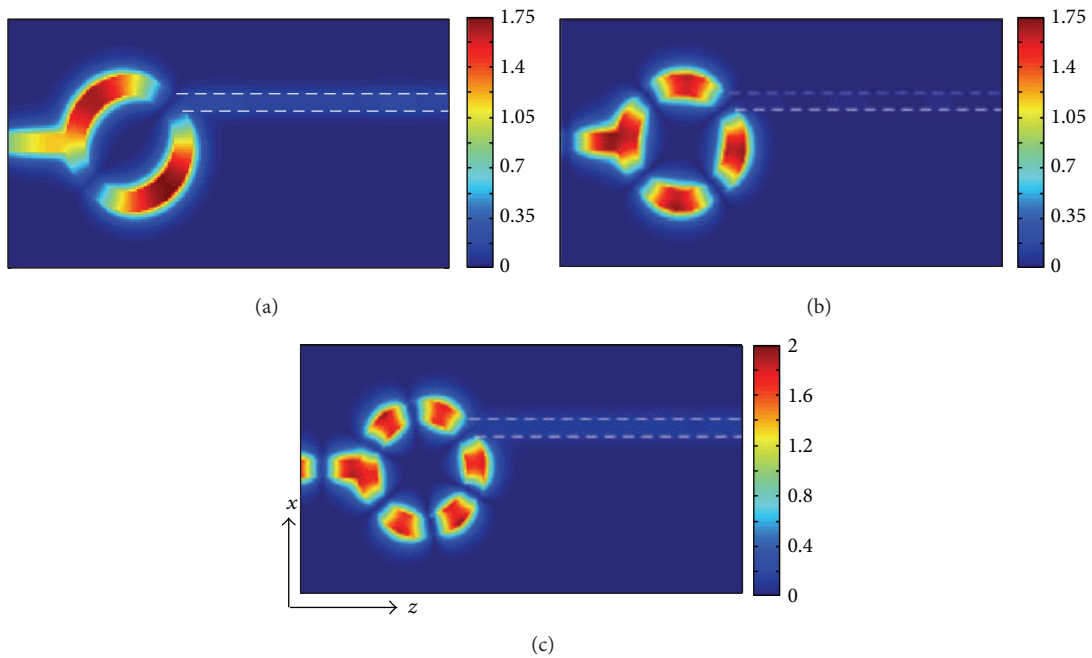


FIGURE 4: (Color Online) The contour profiles of magnetic field intensity  $|H_y|$  at minimum wavelengths for the asymmetric structure with  $\theta = 45^\circ$ . (a), (b), and (c) are at wavelengths 1367 nm, 702 nm, and 483 nm, respectively.

The result shows the transmission characteristic in these spectra is completely the same as that in Figure 2. Therefore, if we change the ring cavity radius, the wavelength of the maximum and minimum transmission discussed above will vary with the change of the radius of the ring resonator. This means that we can filter any wavelength by setting the geometric parameters of the structure.

#### 4. Summary

In conclusion, the transmission characteristics of the electromagnetic wave are investigated in two-dimensional compound plasmonic structures composed of two straight sub-wavelength MIM waveguides and a ring resonator by using FDTD method. The results show that the filtering

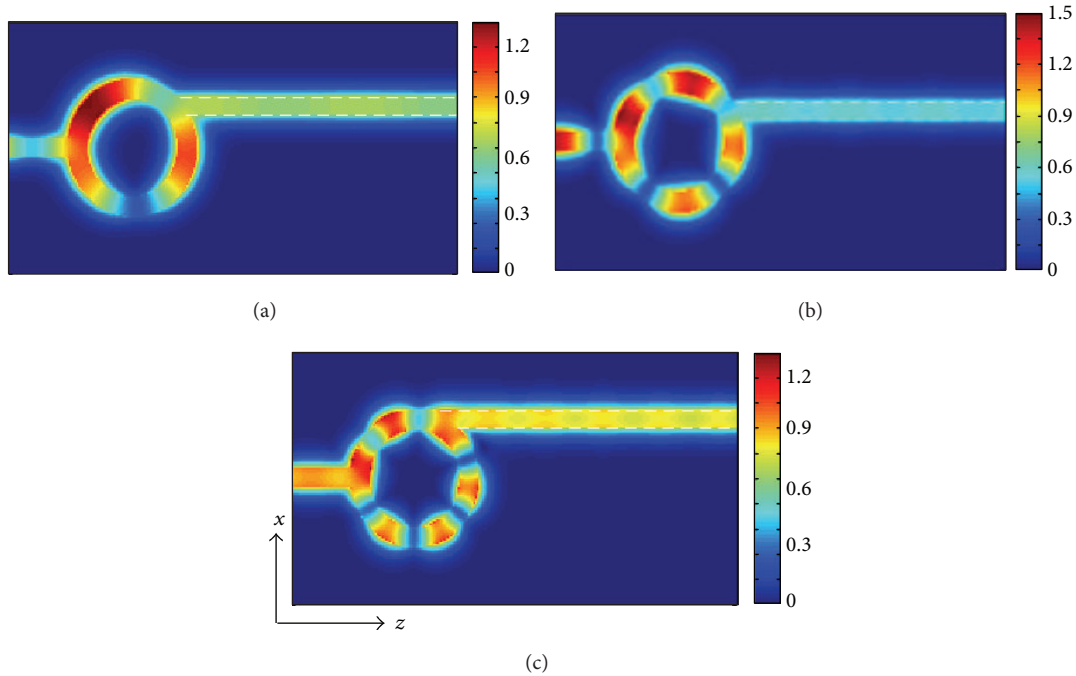


FIGURE 5: (Color Online) The contour profiles of magnetic field intensity  $|H_y|$  at maximum wavelengths for the asymmetric structure. (a), (b), and (c) are at wavelengths 1206 nm for  $\theta = 45^\circ$ , 648 nm for  $\theta = 30^\circ$ , and 457 nm for  $\theta = 90^\circ$ , respectively.

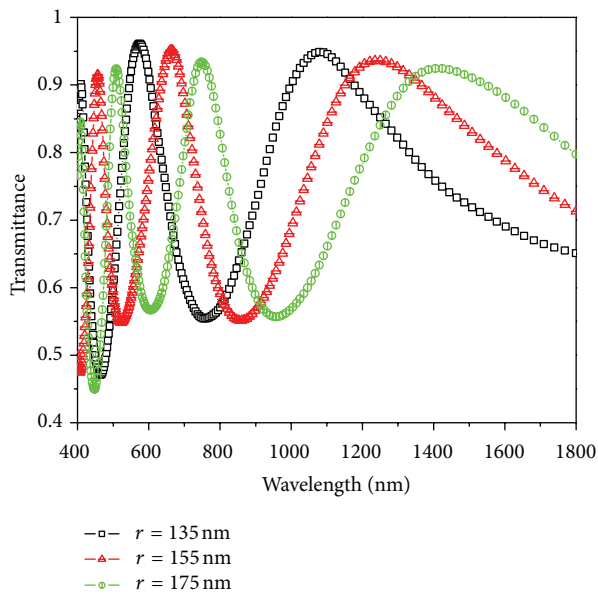


FIGURE 6: (Color Online) Transmission spectra of the MIM plasmonic waveguide with a different radius' ring resonator for  $\theta = 0^\circ$ .

performances of the asymmetric structures (positional angular deviation  $\theta \neq 0^\circ$ ) are greatly improved in comparison with the symmetric structure ( $\theta = 0^\circ$ ). For the most of the asymmetric structures, there is a transmission minimum at the slightly bigger wavelength than that at which the transmission peak appears for the symmetric structures, and there is still a transmission peak at the wavelength of the

transmission peak of the symmetric structures. And then the difference between the transmission peak and valley is increased, the breadth of the transmission peak becomes narrow. For these transmission minima of the asymmetric structures, it is found that the parts of coupling the MIM waveguide of the outgoing side with the ring resonator locate at the magnetic nodes of the standing waves in the ring resonator.

## Acknowledgments

This work was supported by the National Natural Science Foundation of China (Grant nos. 11074069 and 61176116), the Specialized Research Fund for the Doctoral Program of Higher Education of China (Grant no. 20120161130003), the Hunan Provincial Natural Science Foundation of China (Grant no. 12JJ4009), the Hunan Provincial Science and Technology Project of China (Grant no. 2012FJ4121), and Aid program for Science and Technology Innovative Research Team in Higher Educational Institutions of Hunan Province.

## References

- [1] P. Berini, "Long-range surface plasmon polaritons," *Advances in Optics and Photonics*, vol. 1, no. 3, pp. 484–588, 2009.
- [2] G. Veronis and S. Fan, "Bends and splitters in metal-dielectric-metal subwavelength plasmonic waveguides," *Applied Physics Letters*, vol. 87, no. 13, Article ID 131102, pp. 1–3, 2005.
- [3] H. Gao, H. Shi, C. Wang et al., "Surface plasmon polariton propagation and combination in Y-shaped metallic channels," *Optics Express*, vol. 13, no. 26, pp. 10795–10800, 2005.

- [4] B. Wang and G. P. Wang, "Surface plasmon polariton propagation in nanoscale metal gap waveguides," *Optics Letters*, vol. 29, no. 17, pp. 1992–1994, 2004.
- [5] Z. Han, L. Liu, and E. Forsberg, "Ultra-compact directional couplers and Mach-Zehnder interferometers employing surface plasmon polaritons," *Optics Communications*, vol. 259, no. 2, pp. 690–695, 2006.
- [6] A. Hosseini and Y. Massoud, "A low-loss metal-insulator-metal plasmonic bragg reflector," *Optics Express*, vol. 14, no. 23, pp. 11318–11323, 2006.
- [7] J. Q. Liu, L. L. Wang, M. D. He et al., "A wide bandgap plasmonic Bragg reflector," *Optics Express*, vol. 16, no. 7, pp. 4888–4894, 2008.
- [8] T. Nikolajsen, K. Leosson, and S. I. Bozhevolnyi, "Surface plasmon polariton based modulators and switches operating at telecom wavelengths," *Applied Physics Letters*, vol. 85, no. 24, pp. 5833–5835, 2004.
- [9] H. Zhao, X. G. Guang, and J. Huang, "Novel optical directional coupler based on surface plasmon polaritons," *Physica E*, vol. 40, no. 10, pp. 3025–3029, 2008.
- [10] X. S. Lin and X. G. Huang, "Tooth-shaped plasmonic waveguide filters with nanometeric sizes," *Optics Letters*, vol. 33, no. 23, pp. 2874–2876, 2008.
- [11] T. B. Wang, X. W. Wen, C. P. Yin, and H. Z. Wang, "The transmission characteristics of surface plasmon polaritons in ring resonator," *Optics Express*, vol. 17, no. 26, pp. 24096–24101, 2009.
- [12] D. Xiang, L. L. Wang, L. Wang et al., "Optical transmission through double-layer compound metallic gratings with sub-wavelength slits," *Journal of Modern Optics*, vol. 59, no. 15, pp. 1342–1348, 2012.
- [13] A. Taflove and S. C. Hagness, *Computational Electrodynamics: The Finite-Difference Time-Domain Method*, Artech House, Norwood, Mass, USA, 2nd edition, 2000.
- [14] D. Xiang, L. L. Wang, X. F. Li et al., "Transmission resonances of compound metallic gratings with two subwavelength slits in each period," *Optics Express*, vol. 19, no. 3, pp. 2187–2192, 2011.

## Review Article

# Review on the Synthesis and Applications of $\text{Fe}_3\text{O}_4$ Nanomaterials

Xiaodi Liu,<sup>1</sup> Zhiguo Zhong,<sup>2</sup> Yufeng Tang,<sup>1</sup> and Bingyu Liang<sup>1</sup>

<sup>1</sup> College of Chemistry and Pharmaceutical Engineering, Nanyang Normal University, Nanyang, Henan 473061, China

<sup>2</sup> Center of Analysis and Testing, Nanyang Normal University, Nanyang, Henan 473061, China

Correspondence should be addressed to Xiaodi Liu; liuxd1983@yahoo.com.cn

Received 17 January 2013; Accepted 16 February 2013

Academic Editor: Jianmin Ma

Copyright © 2013 Xiaodi Liu et al. This is an open access article distributed under the Creative Commons Attribution License, which permits unrestricted use, distribution, and reproduction in any medium, provided the original work is properly cited.

Recently,  $\text{Fe}_3\text{O}_4$  nanomaterials have attracted tremendous attention because of their favorable electric and magnetic properties.  $\text{Fe}_3\text{O}_4$  nanostructures with various morphologies have been successfully synthesized and have been used in many fields such as lithium-ion batteries (LIBs), wastewater treatment, and magnetic resonance imaging (MRI) contrast agents. In this paper, we provide an in-depth discussion of recent development of  $\text{Fe}_3\text{O}_4$  nanomaterials, including their effective synthetic methods and potential applications.

## 1. Introduction

Nanomaterials have been attracting great attention owing to their excellent electrical, optical, magnetic, and catalytic properties. It is well known that the phases, sizes, and morphologies of nanomaterials have great influence on their properties and potential applications; thereby, the controlled synthesis of nanostructured materials with novel morphologies has recently received much attention [1–3]. As a kind of conventional magnetic material,  $\text{Fe}_3\text{O}_4$  nanomaterials have been used in many fields because of their unique electric and magnetic properties [4, 5]. Several novel and effective methods have been developed to synthesize  $\text{Fe}_3\text{O}_4$  nanomaterials with various shapes, such as nanorods, nanotubes, and hierarchical superstructures [6–10].  $\text{Fe}_3\text{O}_4$  nanomaterials have superior properties and great potential applications in the fields of lithium-ion batteries, wastewater treatment, and drug delivery [11–15].

Until now, several overviews of the literature on the  $\text{Fe}_3\text{O}_4$  nanomaterials have been reported to keep the readers abreast of the rapid development. For example, a review by Yang's group has focused on the synthesis, growth mechanism, and applications of  $\text{Fe}_3\text{O}_4$  nanomaterials [16]. Nevertheless, many successes on the synthesis, properties, and applications

of  $\text{Fe}_3\text{O}_4$  nanomaterials have been continually reported in the last few years; thereby, it seems timely to review the development of  $\text{Fe}_3\text{O}_4$  nanostructures.

Herein, we provide an update on currently available methods for the synthesis of  $\text{Fe}_3\text{O}_4$  nanomaterials with various morphologies; in spite of that, some important and original findings reported earlier are also included. The unique properties, potential applications, and future prospects of  $\text{Fe}_3\text{O}_4$  nanostructures have also been discussed.

## 2. Synthesis of $\text{Fe}_3\text{O}_4$ Nanomaterials

Generally, the intrinsic shape of nanocrystal is dominated by the crystalline structure of initial seed, and the final shape is governed by the subsequent growth stage through delicate control of external factors (e.g., kinetic energy barrier and templates) [17].  $\text{Fe}_3\text{O}_4$  has a cubic inverse spinel structure based on  $Fd-3m$  space group [18]. The lattice constant is  $a = 0.839$ . In the unit cell, as shown in Figure 1, the oxygen ions form an fcc closed packing, and the iron ions occupy interstitial tetrahedral sites and octahedral sites, symbolized as  $[\text{Fe}^{3+}]_A-[\text{Fe}^{2+}\text{Fe}^{3+}]_B\text{O}_4$ , in which  $A$  (tetrahedral positions) is occupied by  $\text{Fe}^{3+}$  ions and  $B$  (octahedral sites) is occupied by eight  $\text{Fe}^{2+}$  ions and eight  $\text{Fe}^{3+}$  ions.

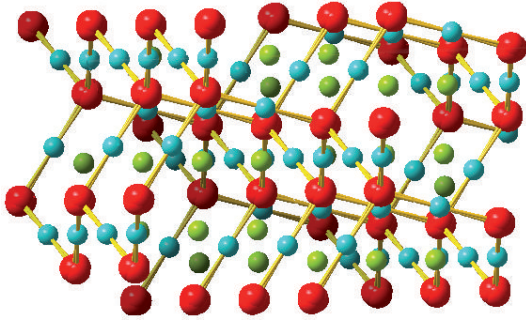


FIGURE 1: Crystal structure of cubic inverse spinel  $\text{Fe}_3\text{O}_4$  ((green ball)  $\text{Fe}^{3+}$  (blue ball)  $\text{Fe}^{2+}$  (red ball) O).

**2.1. 0D  $\text{Fe}_3\text{O}_4$  Nanomaterials.** 0D  $\text{Fe}_3\text{O}_4$  nanomaterials have been widely studied due to their current and promising applications. It is known that the physicochemical properties and potential applications of  $\text{Fe}_3\text{O}_4$  nanomaterials are strongly influenced by their sizes; moreover,  $\text{Fe}_3\text{O}_4$  nanomaterials tend to aggregate because of the strong magnetic dipole-dipole attractions between the crystals and the large surface energy [24]. Thus, many efforts have been devoted to prepare  $\text{Fe}_3\text{O}_4$  nanomaterials with controlled size and well-defined surface property [25].

After the Sugimoto group have fabricated monodisperse  $\text{Fe}_3\text{O}_4$  nanoparticles in 1980, various methods have been developed for the synthesis of  $\text{Fe}_3\text{O}_4$  nanoparticles with narrow size distribution and good dispersity. Sun and Zeng have synthesized 4 nm  $\text{Fe}_3\text{O}_4$  nanoparticles *via* the high-temperature reaction of  $\text{Fe}(\text{acac})_3$  in the phenyl ether with 1,2-hexadecanediol, oleic acid, and oleylamine. “Seed-mediated” growth method is used to make larger nanoparticles, and  $\text{Fe}_3\text{O}_4$  nanoparticles (3–20 nm) can be obtained by changing the quantity of seeds [26]. The Gao’s group have used a solvothermal method to synthesize  $\text{Fe}_3\text{O}_4$  nanoparticles with a mean diameter of 25 nm [27]. In the synthesis,  $[\text{Zn}(\text{CO}_3)_2(\text{OH})_6]$ , accepting  $\text{Fe}^{2+}$  precipitates through  $-\text{OH}$ , can prevent the agglomeration of  $\text{Fe}^{2+}$  precipitates, and superparamagnetic  $\text{Fe}_3\text{O}_4$  nanoparticles can be sequentially obtained. Compared to other successes [11, 28], the as-synthesized  $\text{Fe}_3\text{O}_4$  nanoparticles with good dispersity have not been coated by other substances (e.g., silica and polymer) and can keep their naturally properties. Other routes, including coprecipitation method, reverse micelle method, and high temperature liquid phase method, have also been explored to fabricate  $\text{Fe}_3\text{O}_4$  nanoparticles with different diameters [29–32].

Besides spherical nanoparticles, 0D  $\text{Fe}_3\text{O}_4$  nanomaterials with other morphologies have been prepared, such as octahedron [19, 33, 34], dodecahedron [6], and cube [35–37]. Based on the literature [38], the shape of the particle is closely related to the crystallographic surfaces that enclose the particle. As to  $\text{Fe}_3\text{O}_4$ , the relative surface energies are in the order of  $\gamma_{111} < \gamma_{100} < \gamma_{110}$  owing to the distances between these three faces and coordination number with neighboring atoms [39, 40]. Therefore, the growth rate of (111) plane is quicker than that of other planes, and the octahedral shapes would

be the thermodynamically favored morphology according to the Wulff theorem. For example, Zhang et al. have presented a simple method for octahedral  $\text{Fe}_3\text{O}_4$  nanoparticles, in which tetracosane is the reaction media, oleylamine is the surfactant and the reducing agent, and  $\text{Fe}(\text{OA})_3$  is the precursor [19]. As shown in Figure 2(a), the octahedrons have a size of  $21 \pm 2$  nm. The octahedrons can also self-assemble into oriented superstructures due to their anisotropic shapes (Figure 2(b)). As discussed above, the (110) facet has the highest surface energy, so there is much difficulty to fabricate magnetite nanocrystals enclosed by (110) plane. Nevertheless, Li and coworkers have prepared rhombic dodecahedral (RD)  $\text{Fe}_3\text{O}_4$  nanocrystals *via* a microwave-assisted route in the presence of ionic liquid (IL)  $[\text{C}_{12}\text{Py}]^+[\text{ClO}_4]^-$  [6]. In the synthesis, ILs change the surface condition of the  $\text{Fe}_3\text{O}_4$  nanocrystals, and HMT/phenol adsorbed on (110) planes is beneficial for the crystal growth along [100] direction; thus, RD  $\text{Fe}_3\text{O}_4$  nanocrystals enclosed by twelve (110) flakes can be obtained. Moreover, if the nuclei are bounded by (100) planes, cubic  $\text{Fe}_3\text{O}_4$  nanomaterials can be formed [36].

**2.2. 1D and 2D  $\text{Fe}_3\text{O}_4$  Nanomaterials.** Although it is difficult to prepare anisotropic  $\text{Fe}_3\text{O}_4$  nanocrystal because of its cubic spinel structure, anisotropic nanocrystals can be obtained by using templates or surfactants to control the growth rate on different crystal planes. More recently, 1D magnetic nanomaterials, such as nanotubes, nanorods, and nanowires, have become a pressing need for their potential applications in lithium-ion batteries and field emission displays [41]. Particularly, tubular  $\text{Fe}_3\text{O}_4$  nanostructures have stimulated extensive efforts owing to their well-defined magnetic states. It was reported that some conventional methods (i.e., template-assisted method) are not beneficial for the formation of single-crystalline nanotubes; thereby, some novel methods have been explored [9, 42–44]. Geng et al. have applied proteins from egg albumin as nanoreactors for the fabrication of single-crystalline  $\text{Fe}_3\text{O}_4$  nanotubes. A flake structure is prepared with the assistance of egg albumin, and then  $\text{Fe}_3\text{O}_4$  nanotubes are prepared from the flake-like precursors based on a “rolling-up” mechanism. Additionally, nanorods and nanowires have been successfully synthesized [43, 45–48]. For example, Zhang and coworkers have prepared single-crystalline  $\text{Fe}_3\text{O}_4$  nanowires with large aspect ratio by a one-step sol-gel process; Wang et al. have reduced  $\alpha\text{-Fe}_2\text{O}_3$  nanowires to  $\text{Fe}_3\text{O}_4$  nanowires under  $\text{H}_2$  and  $\text{Ar}_2$  at 400–900°C *via* a V-S process; chemical vapor deposition (CVD) method has also been used to synthesize 1D  $\text{Fe}_3\text{O}_4$  nanomaterials.

2D  $\text{Fe}_3\text{O}_4$  nanomaterials, such as nanorings and nanoflakes, have also attracted much attention to their special properties. Jia et al. have synthesized  $\text{Fe}_3\text{O}_4$  nanorings by the reduction of hematite in the presence of phosphate and sulfate [49]. In the synthesis, compared with (001) plane,  $\text{PO}_4^{3-}$  and  $\text{SO}_4^{2-}$  have stronger adhesion to the (110) and (100) planes; therefore, the capsule crystals have a tendency to grow along the [001] direction and the following dissolution process also takes place along the [001] direction. Finally,  $\text{Fe}_3\text{O}_4$  nanorings can be formed. Zhu group have prepared  $\text{Fe}_3\text{O}_4$  nanosheets

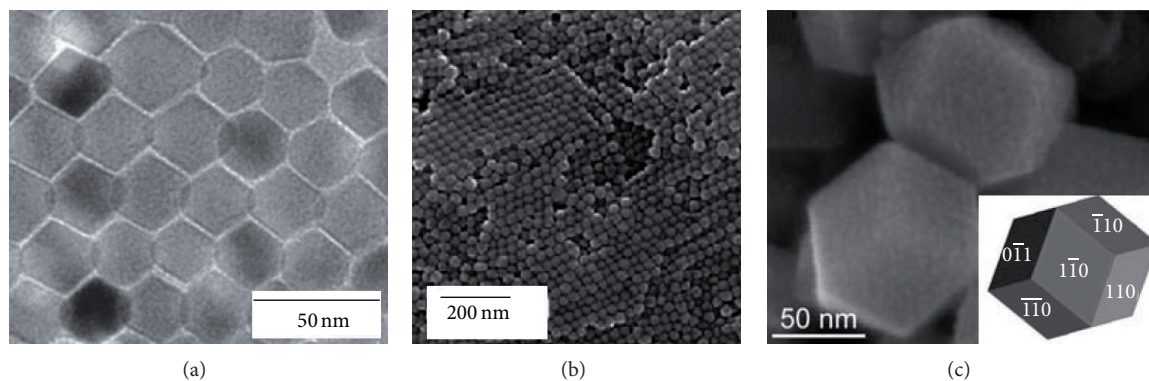


FIGURE 2: (a) TEM image of self-assembled monolayer  $\text{Fe}_3\text{O}_4$  nanocrystals; (b) SEM image of assembled multilayer  $\text{Fe}_3\text{O}_4$  nanocrystals; (c) SEM image of RD  $\text{Fe}_3\text{O}_4$  nanocrystals; the inset is model of RD enclosed by twelve  $\{110\}$  planes [6, 19].

by oxidizing Fe substrates in acidic solution in a hot plate at  $70^\circ\text{C}$  [50].  $\text{Fe}_3\text{O}_4$  nanoplates have been synthesized by reducing  $\gamma\text{-Fe}_2\text{O}_3$  nanoplates in the presence of PVP. In the experiment, PVP can selectively coordinate with  $\{111\}$  facet of  $\gamma\text{-Fe}_2\text{O}_3$ , which reduces the growth rate along the  $[111]$  direction, resulting in nanoplates bounded by the  $\{111\}$  planes. Finally,  $\gamma\text{-Fe}_2\text{O}_3$  nanoplates could be transformed to  $\text{Fe}_3\text{O}_4$  with the shape and size being unchanged. Other strategies (i.e., hydrothermal and solvothermal methods) have been developed to fabricate  $\text{Fe}_3\text{O}_4$  nanoprisms [15, 51, 52].

**2.3.  $\text{Fe}_3\text{O}_4$  Hierarchical Superstructures.** Recently, many research efforts in nanoscience have been devoted to the self-assembly of nanoscale building blocks into 2D and 3D hierarchical superstructures, which could prevent the agglomeration of nanomaterials and supply more tunable and unique properties [53]. In addition, the “superparamagnetic limit,” that is, the conflict between reducing the magnetic energy barrier and decreasing the size, restrains the development of  $\text{Fe}_3\text{O}_4$  nanomaterials [9]. To some extent,  $\text{Fe}_3\text{O}_4$  hierarchical superstructures could overcome this limit, and some researchers concerned about the synthesis of self-assembled  $\text{Fe}_3\text{O}_4$  superstructures.

As shown in Figure 3(a), 1D chainlike arrays of hollow  $\text{Fe}_3\text{O}_4$  nanospheres have been prepared by aging preassembled Fe nanoparticles in aqueous solution [20]. The formation mechanism is proposed based on the nanoscale Kirkendall effect: Fe nanoparticles are firstly self-assembled into chainlike structure and solid Fe spheres are then gradually oxidized into  $\text{Fe}_3\text{O}_4$  hollow nanospheres. Other self-assembled  $\text{Fe}_3\text{O}_4$  chains have also been synthesized [10, 54].

The Wang group have successfully synthesized a hierarchical and porous structure of  $\text{Fe}_3\text{O}_4$  hollow submicrospheres with  $\text{Fe}_3\text{O}_4$  nanoparticles *via* a solvothermal method [21]. As displayed in Figure 3(b),  $\text{Fe}_3\text{O}_4$  submicrospheres are built from  $\text{Fe}_3\text{O}_4$  nanoparticles with diameters of 20–30 nm. The formation mechanism can be attributed to reduction and Ostwald ripening:  $\text{Fe}_2\text{O}_3$  submicrospheres are firstly synthesized; hematite is then reduced to magnetite and an incomplete layer consisted of  $\text{Fe}_3\text{O}_4$  nuclei is formed on the solid  $\text{Fe}_2\text{O}_3$  surfaces; a  $\text{Fe}_2\text{O}_3\text{-Fe}_3\text{O}_4$  core-shell structure is

formed in the presence of 1,6-hexanediol; finally,  $\text{Fe}_3\text{O}_4$  hollow submicrospheres are obtained through Ostwald ripening process.

Hierarchical flower-like  $\text{Fe}_3\text{O}_4$  superstructures have been widely researched [22, 55–57]. Zhong et al. have reported the synthesis of flower-like  $\text{Fe}_3\text{O}_4$  superstructures by an ethylene-glycol-(EG-)mediated self-assembly process. Han and coworkers have prepared flower-like  $\text{Fe}_3\text{O}_4$  under  $80^\circ\text{C}$  in the absent of any surfactant or organic solvent (Figure 3(c)). Ultrasound-assisted hydrothermal route has also been used to fabricate  $\text{Fe}_3\text{O}_4$  hierarchical flower-like microspheres.

Many other  $\text{Fe}_3\text{O}_4$  hierarchical superstructures with special morphologies have been synthesized. For example,  $\text{Fe}_3\text{O}_4$  microspheres assembled by tetrahedral nanocrystals [58], porous hollow  $\text{Fe}_3\text{O}_4$  beads constructed with rodlike nanoparticles [59], and nanoparticles-assembled  $\text{Fe}_3\text{O}_4$  dendritic patterns [60].

### 3. Potential Applications of $\text{Fe}_3\text{O}_4$ Nanomaterials

**3.1. Lithium-Ion Batteries (LIBs).** Lithium-ion batteries are regarded as the most promising rechargeable energy storage technology due to the increasing applications of portable electronic devices and transportations. In order to obtain high power and energy density,  $\text{Fe}_3\text{O}_4$  nanomaterials have been extensively explored as LIB anode materials for their high theoretical capacity ( $900\text{--}1000\text{ mA}\cdot\text{h}\cdot\text{g}^{-1}$ ), low cost, environmental benignity, and special properties [59, 61]. For example, single-crystalline mesoporous  $\text{Fe}_3\text{O}_4$  nanorod exhibits a high reversible capacity of  $843.5\text{ mA}\cdot\text{h}\cdot\text{g}^{-1}$  after 50th cycle at 0.1 C; furthermore, the nanorods have superior electron transport ability, which makes them highly attractive for the potential application as LIB anode materials [46]. However, the high surface area of nanomaterials may cause secondary reactions such as electrolyte decomposition between electrode and electrolyte and form thick solid electrolyte interphase (SEI) films on the electrode surface [62]. Fortunately, it was found that surface modifications could partly solve these problems [23]. Carbon-coated  $\text{Fe}_3\text{O}_4$

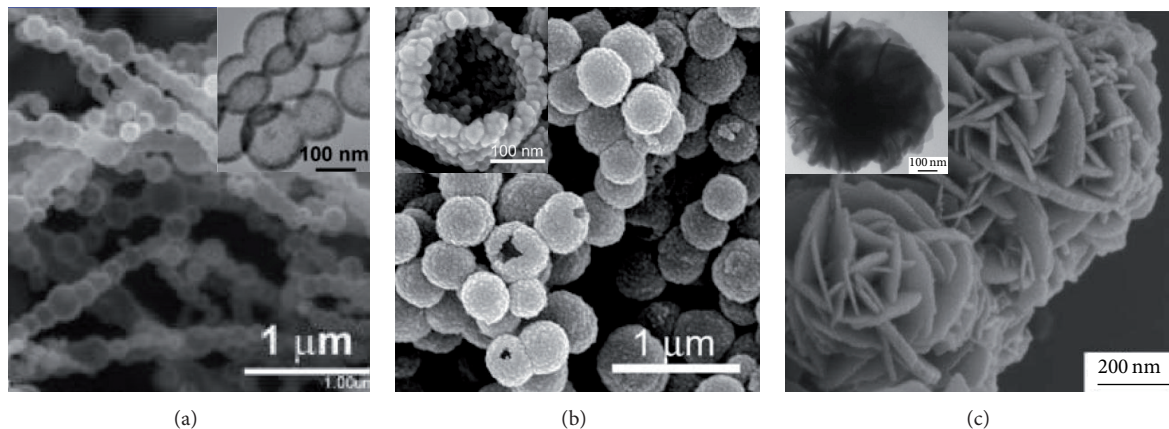


FIGURE 3: (a) TEM images of the chainlike arrays of Fe<sub>3</sub>O<sub>4</sub> hollow nanospheres; (b) SEM image of the hierarchical porous Fe<sub>3</sub>O<sub>4</sub> hollow submicrospheres; (c) SEM and TEM images of the flower-like Fe<sub>3</sub>O<sub>4</sub> superstructures [20–22].

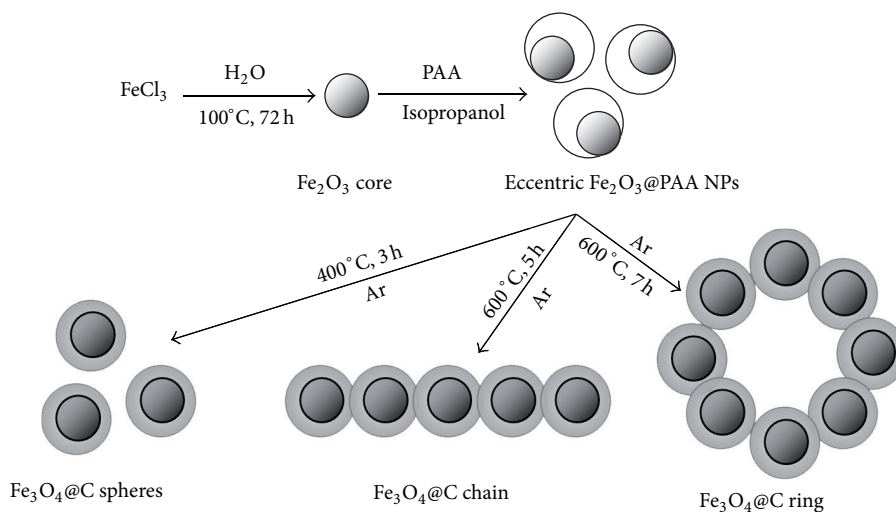


FIGURE 4: Schematic illustration of the synthesis of Fe<sub>3</sub>O<sub>4</sub>/C core-shell spheres, chains, and rings [23].

nanospindles can increase the electronic conductivity of electrodes leading to thin and uniform SEI films, but also stabilize the obtained SEI films; thereafter, the Fe<sub>3</sub>O<sub>4</sub>-C composites are excellent anode materials for highly efficient LIBs with high reversible capacity, high rate capability, and enhanced cycling performance. Li group have reported monodisperse Fe<sub>3</sub>O<sub>4</sub>/C core-shell spheres, chains, and rings with tunable magnetic properties based on structural evolution from eccentric Fe<sub>2</sub>O<sub>3</sub>/poly(acrylic acid) core-shell nanoparticles [63]. The possible formation mechanism is shown in Figure 4. Compared with the Fe<sub>3</sub>O<sub>4</sub>/C core-shell spheres, the chains and rings exhibit higher reversible capacity and better cycling stability. Several other ways have been used to form Fe<sub>3</sub>O<sub>4</sub>-C composites [30, 64, 65]. For instance, porous carbons or mixing graphene layers are impregnated with Fe<sub>3</sub>O<sub>4</sub> precursor; Fe<sub>3</sub>O<sub>4</sub> NPs and carbon are simultaneously formed from a precursor with high surface area and porosity.

**3.2. Wastewater Treatment.** In recent years, wastewater treatment has attracted considerable attention because clean water is vital to the human and because of a variety of key industries [66]. The development of nanoscience opens a novel and effective way for the wastewater treatment. Many groups have used Fe<sub>3</sub>O<sub>4</sub> nanomaterials to treat heavy metal ions and organic pollution. Nanostructured Fe<sub>3</sub>O<sub>4</sub> microspheres (NFMSs) with a large specific surface area (135.9 m<sup>2</sup>·g<sup>-1</sup>) can remove toxic Cr<sup>6+</sup> from polluted water, and it is found that 1 g NFMSs remove 43.48 mg Cr<sup>6+</sup> ions at room temperature [67]. Fe<sub>3</sub>O<sub>4</sub> nanomaterials have also been successfully used as catalysts to remove organic pollutions, such as xylene orange, phenol, and aniline, from wastewater [68–70].

**3.3. Other Applications.** Fe<sub>3</sub>O<sub>4</sub> nanomaterials have been applied in many other fields, including metal chemosensor [71], magnetorheological elastomer [72], SERS spectroscopy

[57], magnetic resonance contrast agent [73], catalyst [74, 75], drug delivery [76], and magnetic resonance imaging (MRI) contrast agents [77].

#### 4. Conclusions

In conclusions, recent synthetic efforts have led to the formation of  $\text{Fe}_3\text{O}_4$  nanomaterials with various morphologies. In spite of the exciting new development, the application of  $\text{Fe}_3\text{O}_4$  nanomaterials in industry is still in its infancy. However, with the progress in the fundamental understanding of the physics and chemistry in the  $\text{Fe}_3\text{O}_4$  nanomaterials, we foresee that novel properties and applications will be demonstrated in the not-so-distant future.

#### Acknowledgments

This work is financially supported by the Natural Science Foundation of Henan Department of Science & Technology (no. 112300410224 and no. 13A150813) and the Natural Science Foundation of Nanyang Normal University (no. 2X2010014).

#### References

- [1] J. Geng, D. Lu, J. Zhu, and H. Chen, "Antimony(III)-doped  $\text{PbWO}_4$  crystals with enhanced photoluminescence via a shape-controlled sonochemical route," *The Journal of Physical Chemistry B*, vol. 110, no. 28, pp. 13777–13785, 2006.
- [2] J. M. Honig and J. Spalek, "Electronic properties of  $\text{NiS}_{2-x}\text{Se}_x$  single crystals: from magnetic mott–hubbard insulators to normal metals," *Chemistry of Materials*, vol. 10, no. 10, pp. 2910–2929, 1998.
- [3] C. N. R. Rao, S. R. C. Vivekchand, K. Biswasa, and A. Govindaraja, "Synthesis of inorganic nanomaterials," *Dalton Transactions*, no. 34, pp. 3728–3749, 2007.
- [4] M. Zhu and G. Diao, "Synthesis of porous  $\text{Fe}_3\text{O}_4$  nanospheres and its application for the catalytic degradation of xylene orange," *The Journal of Physical Chemistry C*, vol. 115, no. 39, pp. 18923–18934, 2011.
- [5] Y. L. Hou, J. F. Yu, and S. Gao, "Solvothermal reduction synthesis and characterization of superparamagnetic magnetite nanoparticles," *Journal of Materials Chemistry*, vol. 13, no. 8, pp. 1983–1987, 2003.
- [6] X. Li, D. Liu, S. Song, X. Wang, X. Ge, and H. Zhang, "Rhombic dodecahedral  $\text{Fe}_3\text{O}_4$ : ionic liquid-modulated and microwave-assisted synthesis and their magnetic properties," *CrystEngComm*, vol. 13, no. 20, pp. 6017–6020, 2011.
- [7] S. Barth, S. Estrade, F. Hernandez-Ramirez et al., "Studies on surface facets and chemical composition of vapor grown one-dimensional magnetite nanostructures," *Crystal Growth & Design*, vol. 9, no. 2, pp. 1077–1081, 2009.
- [8] J. Lu, X. L. Jiao, D. R. Chen, and W. Li, "Solvothermal synthesis and characterization of  $\text{Fe}_3\text{O}_4$  and  $\gamma\text{-Fe}_2\text{O}_3$  nanoplates," *The Journal of Physical Chemistry C*, vol. 113, no. 10, pp. 4012–4017, 2009.
- [9] Z. Q. Liu, D. H. Zhang, S. Han et al., "Single crystalline magnetite nanotubes," *Journal of the American Chemical Society*, vol. 127, no. 1, pp. 6–7, 2005.
- [10] J. Gong, S. Li, D. Zhang, X. Zhang, C. Liu, and Z. Tong, "High quality self-assembly magnetite ( $\text{Fe}_3\text{O}_4$ ) chain-like core-shell nanowires with luminescence synthesized by a facile one-pot hydrothermal process," *Chemical Communications*, vol. 46, no. 20, pp. 3514–3516, 2010.
- [11] F. H. Chen, L. M. Zhang, Q. T. Chen, Y. Zhang, and Z. J. Zhang, "Synthesis of a novel magnetic drug delivery system composed of doxorubicin-conjugated  $\text{Fe}_3\text{O}_4$  nanoparticle cores and a PEG-functionalized porous silica shell," *Chemical Communications*, vol. 46, no. 45, pp. 8633–8635, 2010.
- [12] T. Fried, G. Shemer, and G. Markovich, "Ordered two-dimensional arrays of ferrite nanoparticles," *Advanced Materials*, vol. 13, no. 15, p. 1158, 2001.
- [13] Y. Tian, B. Yu, X. Li, and K. Li, "Facile solvothermal synthesis of monodisperse  $\text{Fe}_3\text{O}_4$  nanocrystals with precise size control of one nanometre as potential MRI contrast agents," *Journal of Materials Chemistry*, vol. 21, no. 8, pp. 2476–2481, 2011.
- [14] C. Chen, P. Gunawan, and R. Xu, "Self-assembled  $\text{Fe}_3\text{O}_4$ -layered double hydroxide colloidal nanohybrids with excellent performance for treatment of organic dyes in water," *Journal of Materials Chemistry*, vol. 21, no. 4, pp. 1218–1225, 2011.
- [15] Y. Zeng, R. Hao, B. G. Xing, Y. L. Hou, and Z. C. Xu, "One-pot synthesis of  $\text{Fe}_3\text{O}_4$  nanoprisms with controlled electrochemical properties," *Chemical Communications*, vol. 46, no. 22, pp. 3920–3922, 2010.
- [16] C. Yang, J. Wu, and Y. Hou, " $\text{Fe}_3\text{O}_4$  nanostructures: synthesis, growth mechanism, properties and applications," *Chemical Communications*, vol. 47, no. 18, pp. 5130–5141, 2011.
- [17] S. M. Lee, S. N. Cho, and J. Cheon, "Anisotropic shape control of colloidal inorganic nanocrystals," *Advanced Materials*, vol. 15, no. 5, pp. 441–444, 2003.
- [18] J. Mazo-Zuluaga, J. Restrepo, and J. Mejía-López, "Surface anisotropy of a  $\text{Fe}_3\text{O}_4$  nanoparticle: a simulation approach," *Physica B*, vol. 398, no. 2, pp. 187–190, 2007.
- [19] L. H. Zhang, J. J. Wu, H. B. Liao, Y. L. Hou, and S. Gao, "Octahedral  $\text{Fe}_3\text{O}_4$  nanoparticles and their assembled structures," *Chemical Communications*, no. 29, pp. 4378–4380, 2009.
- [20] J. Huang, W. Chen, W. Zhao, Y. Li, X. Li, and C. Chen, "One-dimensional chainlike arrays of  $\text{Fe}_3\text{O}_4$  hollow nanospheres synthesized by aging iron nanoparticles in aqueous solution," *The Journal of Physical Chemistry C*, vol. 113, no. 28, pp. 12067–12071, 2009.
- [21] Y. Wang, Q. Zhu, and L. Tao, "Fabrication and growth mechanism of hierarchical porous  $\text{Fe}_3\text{O}_4$  hollow sub-microspheres and their magnetic properties," *CrystEngComm*, vol. 13, no. 14, pp. 4652–4657, 2011.
- [22] L. Han, Y. Chen, and Y. Wei, "Hierarchical flower-like  $\text{Fe}_3\text{O}_4$  and  $\gamma\text{-Fe}_2\text{O}_3$  nanostructures: synthesis, growth mechanism and photocatalytic properties," *CrystEngComm*, vol. 14, pp. 4692–4698, 2012.
- [23] W. Zhang, X. Wu, J. Hu, Y. Guo, and L. Wan, "Carbon coated  $\text{Fe}_3\text{O}_4$  nanospindles as a superior anode material for lithium-ion batteries," *Advanced Functional Materials*, vol. 18, no. 24, pp. 3941–3946, 2008.
- [24] Y. Lalatonne, J. Richardi, and M. P. Pileni, "Van der Waals versus dipolar forces controlling mesoscopic organizations of magnetic nanocrystals," *Nature Materials*, vol. 3, no. 2, pp. 121–125, 2004.
- [25] S. Si, A. Kotal, T. K. Mandal, S. Giri, H. Nakamura, and T. Kohara, "Size-controlled synthesis of magnetite nanoparticles in the presence of polyelectrolytes," *Chemistry of Materials*, vol. 16, no. 18, pp. 3489–3496, 2004.

- [26] S. Sun and H. Zeng, "Size-controlled synthesis of magnetite nanoparticles," *Journal of the American Chemical Society*, vol. 124, no. 28, pp. 8204–8205, 2002.
- [27] G. Gao, P. Huang, Y. Zhang, K. Wang, W. Qin, and D. Cui, "Gram scale synthesis of superparamagnetic  $\text{Fe}_3\text{O}_4$  nanoparticles and fluid via a facile solvothermal route," *CrystEngComm*, vol. 13, no. 6, pp. 1782–1785, 2011.
- [28] W. Thiessen, A. Dubavik, V. Lesnyak, N. Gaponik, A. Eychmüller, and T. Wolff, "Amphiphilic and magnetic behavior of  $\text{Fe}_3\text{O}_4$  nanocrystals," *Physical Chemistry Chemical Physics*, vol. 12, no. 9, pp. 2063–2066, 2010.
- [29] R. Ghosh, L. Pradhan, Y. P. Devi et al., "Induction heating studies of  $\text{Fe}_3\text{O}_4$  magnetic nanoparticles capped with oleic acid and polyethylene glycol for hyperthermia," *Journal of Materials Chemistry*, vol. 21, no. 35, pp. 13388–13398, 2011.
- [30] T. Yoon, C. Chae, Y. Sun, X. Zhao, H. H. Kung, and J. K. Lee, "Bottom-up *in situ* formation of  $\text{Fe}_3\text{O}_4$  nanocrystals in a porous carbon foam for lithium-ion battery anodes," *Journal of Materials Chemistry*, vol. 21, no. 43, pp. 17325–17330, 2011.
- [31] J. Park, K. J. An, Y. S. Hwang et al., "Ultra-large-scale syntheses of monodisperse nanocrystals," *Nature Materials*, vol. 3, no. 12, pp. 891–895, 2004.
- [32] Y. Lee, J. Lee, C. J. Bae et al., "Large-scale synthesis of uniform and crystalline magnetite nanoparticles using reverse micelles as nanoreactors under reflux conditions," *Advanced Functional Materials*, vol. 15, no. 3, pp. 503–509, 2005.
- [33] L. J. Zhao, H. J. Zhang, Y. Xing et al., "Morphology-controlled synthesis of magnetites with nanoporous structures and excellent magnetic properties," *Chemistry of Materials*, vol. 20, no. 1, pp. 198–204, 2008.
- [34] H. P. Qi, Q. W. Chen, M. S. Wang, M. H. Wen, and J. Xiong, "Study of self-assembly of octahedral magnetite under an external magnetic field," *The Journal of Physical Chemistry C*, vol. 113, no. 40, pp. 17301–17305, 2009.
- [35] D. Kim, N. Lee, M. Park, B. H. Kim, K. An, and T. Hyeon, "Synthesis of uniform ferrimagnetic magnetite nanocubes," *Journal of the American Chemical Society*, vol. 131, no. 2, pp. 454–455, 2009.
- [36] H. L. Ding, Y. X. Zhang, S. Wang, J. M. Xu, S. C. Xu, and G. H. Li, " $\text{Fe}_3\text{O}_4$ @ $\text{SiO}_2$  core/shell nanoparticles: the silica coating regulations with a single core for different core sizes and shell thicknesses," *Chemistry of Materials*, vol. 24, no. 23, pp. 4572–4580, 2012.
- [37] H. Kind, H. Q. Yan, B. Messer, M. Law, and P. D. Yang, "Nanowire ultraviolet photodetectors and optical switches," *Advanced Materials*, vol. 14, no. 2, pp. 158–160, 2002.
- [38] C. Burda, X. B. Chen, and R. Narayanan, "Chemistry and properties of nanocrystals of different shapes," *Chemical Reviews*, vol. 105, no. 4, pp. 1025–1102, 2005.
- [39] B. Wiley, Y. Sun, B. Mayers, and Y. Xia, "Shape-controlled synthesis of metal nanostructures: the case of silver," *Chemistry*, vol. 11, no. 2, pp. 454–463, 2005.
- [40] X. Liu, J. Ma, P. Peng, and W. Zheng, "Hydrothermal synthesis of cubic  $\text{MnSe}_2$  and octahedral  $\alpha$ - $\text{MnSe}$  microcrystals," *Journal of Crystal Growth*, vol. 311, no. 5, pp. 1359–1363, 2009.
- [41] S. O. Hwang, C. H. Kim, Y. Myung et al., "Synthesis of vertically aligned manganese-doped  $\text{Fe}_3\text{O}_4$  nanowire arrays and their excellent room-temperature gas sensing ability," *The Journal of Physical Chemistry C*, vol. 112, no. 36, pp. 13911–13916, 2008.
- [42] W. Wu, X. Xiao, S. Zhang et al., "Large-scale and controlled synthesis of iron oxide magnetic short nanotubes: shape evolution, growth mechanism, and magnetic properties," *The Journal of Physical Chemistry C*, vol. 114, no. 39, pp. 16092–16103, 2010.
- [43] J. Q. Hu, Y. Bando, Z. W. Liu, D. Golberg, and T. Sekiguchi, "Synthesis of crystalline silicon tubular nanostructures with ZnS nanowires as removable templates," *Angewandte Chemie*, vol. 43, no. 1, pp. 63–66, 2004.
- [44] B. Geng, F. Zhan, H. Jiang, Y. Guo, and Z. Xing, "Egg albumin as a nanoreactor for growing single-crystalline  $\text{Fe}_3\text{O}_4$  nanotubes with high yields," *Chemical Communications*, no. 44, pp. 5773–5775, 2008.
- [45] Z. Huang, Y. Zhang, and F. Tang, "Solution-phase synthesis of single-crystalline magnetic nanowires with high aspect ratio and uniformity," *Chemical Communications*, no. 3, pp. 342–344, 2005.
- [46] Z. Xiao, Y. Xia, Z. Ren et al., "Facile synthesis of single-crystalline mesoporous  $\alpha$ - $\text{Fe}_2\text{O}_3$  and  $\text{Fe}_3\text{O}_4$  nanorods as anode materials for lithium-ion batteries," *Journal of Materials Chemistry*, vol. 22, no. 38, pp. 20566–20573, 2012.
- [47] S. Mathur, S. Barth, U. Werner, F. Hernandez-Ramirez, and A. Romano-Rodriguez, "Chemical vapor growth of one-dimensional magnetite nanostructures," *Advanced Materials*, vol. 20, no. 8, pp. 1550–1554, 2008.
- [48] Y. L. Chueh, M. W. Lai, J. Q. Liang, L. J. Chou, and Z. L. Wang, "Systematic study of the growth of aligned arrays of  $\alpha$ - $\text{Fe}_2\text{O}_3$  and  $\text{Fe}_3\text{O}_4$  nanowires by a vapor-solid process," *Advanced Functional Materials*, vol. 16, no. 17, pp. 2243–2251, 2006.
- [49] C. J. Jia, L. D. Sun, F. Luo et al., "Large-scale synthesis of single-crystalline iron oxide magnetic nanorings," *Journal of the American Chemical Society*, vol. 130, no. 50, pp. 16968–16977, 2008.
- [50] K. C. Chin, G. L. Chong, C. K. Poh et al., "Large-scale synthesis of  $\text{Fe}_3\text{O}_4$  nanosheets at low temperature," *The Journal of Physical Chemistry C*, vol. 111, no. 26, pp. 9136–9141, 2007.
- [51] X. Li, Z. Si, Y. Lei et al., "Direct hydrothermal synthesis of single-crystalline triangular  $\text{Fe}_3\text{O}_4$  nanoprisms," *CrystEngComm*, vol. 12, no. 7, pp. 2060–2063, 2010.
- [52] D. Kim, N. Lee, M. Park, B. H. Kim, K. An, and T. Hyeon, "Synthesis of uniform ferrimagnetic magnetite nanocubes," *Journal of the American Chemical Society*, vol. 131, no. 2, pp. 454–455, 2009.
- [53] V. Polshettiwar, B. Baruwati, and R. S. Varma, "Self-assembly of metal oxides into three-dimensional nanostructures: synthesis and application in catalysis," *ACS Nano*, vol. 3, no. 3, pp. 728–736, 2009.
- [54] Y. Zhang, L. Sun, Y. Fu et al., "The shape anisotropy in the magnetic field-assisted self-assembly chain-like structure of magnetite," *The Journal of Physical Chemistry C*, vol. 113, no. 19, pp. 8152–8157, 2009.
- [55] L. S. Zhong, J. S. Hu, H. P. Liang, A. M. Cao, W. G. Song, and L. J. Wan, "Self-assembled 3D flowerlike iron oxide nanostructures and their application in water treatment," *Advanced Materials*, vol. 18, no. 18, pp. 2426–2431, 2006.
- [56] X. Li, Z. Si, Y. Lei et al., "Hierarchically structured  $\text{Fe}_3\text{O}_4$  microspheres: morphology control and their application in wastewater treatment," *CrystEngComm*, vol. 13, no. 2, pp. 642–648, 2011.
- [57] Q. Gao, A. Zhao, Z. Gan et al., "Facile fabrication and growth mechanism of 3D flower-like  $\text{Fe}_3\text{O}_4$  nanostructures and their application as SERS substrates," *CrystEngComm*, vol. 14, no. 14, pp. 4834–4842, 2012.

- [58] Y. Lv, H. Wang, X. Wang, and J. Bai, "Synthesis, characterization and growing mechanism of monodisperse  $\text{Fe}_3\text{O}_4$  microspheres," *Journal of Crystal Growth*, vol. 311, no. 13, pp. 3445–3450, 2009.
- [59] Y. Chen, H. Xia, L. Lu, and J. Xue, "Synthesis of porous hollow  $\text{Fe}_3\text{O}_4$  beads and their applications in lithium ion batteries," *Journal of Materials Chemistry*, vol. 22, no. 11, pp. 5006–5012, 2012.
- [60] W. Dong, X. Li, L. Shang, Y. Zheng, G. Wang, and C. Li, "Controlled synthesis and self-assembly of dendrite patterns of  $\text{Fe}_3\text{O}_4$  nanoparticles," *Nanotechnology*, vol. 20, no. 3, Article ID 035601, 2009.
- [61] S. Yuan, J. Li, L. Yang, L. Su, L. Liu, and Z. Zhou, "Preparation and lithium storage performances of mesoporous  $\text{Fe}_3\text{O}_4$ @C microcapsules," *ACS Applied Materials & Interfaces*, vol. 3, no. 3, pp. 705–709, 2011.
- [62] O. Delmer, P. Balaya, L. Kienle, and J. Maier, "Enhanced potential of amorphous electrode materials: case study of  $\text{RuO}_2$ ," *Advanced Materials*, vol. 20, no. 3, pp. 501–505, 2008.
- [63] L. Li, T. Wang, L. Zhang, Z. Su, C. Wang, and R. Wang, "Selected-control synthesis of monodisperse  $\text{Fe}_3\text{O}_3$ @C core-shell spheres, chains, and rings as high-performance anode materials for lithium-ion batteries," *Chemistry*, vol. 18, no. 36, pp. 11417–11422, 2012.
- [64] M. Latorre-Sanchez, A. Primo, and H. Garcia, "Green synthesis of  $\text{Fe}_3\text{O}_4$  nanoparticles embedded in a porous carbon matrix and its use as anode material in Li-ion batteries," *Journal of Materials Chemistry*, vol. 22, no. 40, pp. 21373–21375, 2012.
- [65] Y. Piao, H. S. Kim, Y. E. Sung, and T. Hyeon, "Facile scalable synthesis of magnetite nanocrystals embedded in carbon matrix as superior anode materials for lithium-ion batteries," *Chemical Communications*, vol. 46, pp. 118–120, 2010.
- [66] S. K. Behera, "Enhanced rate performance and cyclic stability of  $\text{Fe}_3\text{O}_4$ -graphene nanocomposites for Li ion battery anodes," *Chemical Communications*, vol. 47, no. 37, pp. 10371–10373, 2011.
- [67] G. Liu, Q. Deng, H. Wang et al., "Synthesis and characterization of nanostructured  $\text{Fe}_3\text{O}_4$  micron-spheres and their application in removing toxic Cr ions from polluted water," *Chemistry*, vol. 18, no. 42, pp. 13418–13426, 2012.
- [68] J. Cheng, S. M. Yu, and P. Zuo, "Horseradish peroxidase immobilized on aluminum-pillared interlayered clay for the catalytic oxidation of phenolic wastewater," *Water Research*, vol. 40, no. 2, pp. 283–290, 2006.
- [69] Y. Si, T. Ren, B. Ding, J. Yu, and G. Sun, "Synthesis of mesoporous magnetic  $\text{Fe}_3\text{O}_4$ @carbon nanofibers utilizing *in situ* polymerized polybenzoxazine for water purification," *Journal of Materials Chemistry*, vol. 22, no. 11, pp. 4619–4622, 2012.
- [70] G. Xie, P. Xi, H. Liu et al., "A facile chemical method to produce superparamagnetic graphene oxide- $\text{Fe}_3\text{O}_4$  hybrid superposite and its application in the removal of dyes from aqueous solution," *Journal of Materials Chemistry*, vol. 22, no. 3, pp. 1033–1039, 2012.
- [71] G. Kang, H. Son, J. M. Lim et al., "Functionalized  $\text{Fe}_3\text{O}_4$  nanoparticles for detecting zinc ions in living cells and their cytotoxicity," *Chemistry*, vol. 18, no. 19, pp. 5843–5847, 2012.
- [72] J. L. Mietta, M. M. Ruiz, P. S. Antonel et al., "Anisotropic magnetoresistance and piezoresistivity in structured  $\text{Fe}_3\text{O}_4$ -silver particles in PDMS elastomers at room temperature," *Langmuir*, vol. 28, no. 17, pp. 6985–6996, 2012.
- [73] G. Gao, K. Wang, P. Huang et al., "Superparamagnetic  $\text{Fe}_3\text{O}_4$ -Ag hybrid nanocrystals as a potential contrast agent for CT imaging," *CrystEngComm*, vol. 14, no. 22, pp. 7556–7559, 2012.
- [74] Z. S. Wu, S. Yang, Y. Sun, K. Parvez, X. Feng, and K. Müllen, "3D nitrogen-doped graphene aerogel-supported  $\text{Fe}_3\text{O}_4$  nanoparticles as efficient electrocatalysts for the oxygen reduction reaction," *Journal of the American Chemical Society*, vol. 134, no. 22, pp. 9082–9085, 2012.
- [75] S. Chen, R. Si, E. Taylor, J. Janzen, and J. Chen, "Synthesis of Pd/ $\text{Fe}_3\text{O}_4$  hybrid nanocatalysts with controllable interface and enhanced catalytic activities for CO oxidation," *The Journal of Physical Chemistry C*, vol. 116, no. 23, pp. 12969–12976, 2012.
- [76] J. Xie, K. Chen, H. Y. Lee et al., "Ultrasmall c(RGDyK)-coated  $\text{Fe}_3\text{O}_4$  nanoparticles and their specific targeting to integrin  $\alpha_v\beta_3$ -rich tumor cells," *Journal of the American Chemical Society*, vol. 130, no. 24, pp. 7542–7543, 2008.
- [77] E. Amstad, S. Zurcher, A. Mashaghi, J. Y. Wong, M. Textor, and E. Reimhult, "Surface functionalization of single superparamagnetic iron oxide nanoparticles for targeted magnetic resonance imaging," *Small*, vol. 5, no. 11, pp. 1334–1342, 2009.

## Research Article

# An NMR Investigation of Phase Structure and Chain Dynamics in the Polyethylene/Montmorillonite Nanocomposites

Wei Li, Linxi Hou, and Zhongren Chen

Faculty of Material and Chemical Engineering, Ningbo University, Ningbo 315211, China

Correspondence should be addressed to Wei Li; [liwei@nbu.edu.cn](mailto:liwei@nbu.edu.cn) and Linxi Hou; [houlinxi@nbu.edu.cn](mailto:houlinxi@nbu.edu.cn)

Received 14 December 2012; Accepted 26 December 2012

Academic Editor: Jun Zhang

Copyright © 2013 Wei Li et al. This is an open access article distributed under the Creative Commons Attribution License, which permits unrestricted use, distribution, and reproduction in any medium, provided the original work is properly cited.

Novel exfoliated and interacted polyethylene (PE)/montmorillonite (MMT) nanocomposites prepared by *in situ* polymerization were characterized by solid-state nuclear magnetic resonance (NMR). The phase structure and molecular mobility were investigated by proton and carbon NMR under static and magic-angle spinning (MAS) conditions. The results showed that incorporation of MMT layer enhanced the polyethylene crystallinity behavior. The chain mobility of crystalline phase, interphase and amorphous phase was hindered in the nanocomposites. The phase structure and chain dynamics were also investigated upon changing the temperature. The orthorhombic and monoclinic phases were detected according to the  $^{13}\text{C}$  CP/MAS NMR. Quantitative characterization of the phase structure was also conducted by  $^{13}\text{C}$  DP/MAS upon changing the temperature. Finally, the difference in the phase structure and chain dynamics in each phase of PE/nanocomposites was compared based on the NMR results when fiber filler was introduced.

## 1. Introduction

Polymer nanocomposites are a new class of particle filled polymers in which at least one composite consists of dispersed particles in the nanometer size range [1]. The layered silicate clay, such as montmorillonite (MMT), has been used in polymer composites for quite a long time. The entity of sandwiched layers, with 1 nm thickness and few hundred nanometers size in other two dimensions, is stacked together with van der Waals gap [2]. Depending on the space between clay platelets after incorporation with polymer matrix, the composites are roughly classified as following: firstly, exfoliated layers are fully open; secondly, intercalated layers are partially open [3].

Generally, incorporation of small amounts of filler can result in the exfoliated polymer composites form, which can greatly enhance mechanical antflammable and heat-resistant properties as compared to original polymer matrix and intercalated dispersion form [4, 5]. In order to overcome the interlayer van der Waals bonding barrier to achieve the layer exfoliation, *in situ* polymerization approach and melt intercalation method have been developed [6]. The catalyst for ethylene polymerization is introduced into the gallery of

layered silicates after which polyethylene forms *in situ* and the layer structure delaminates [7]. This method has proved to be quite efficient in preparing exfoliated nanocomposites since the entropy resistance for the intercalation of polymer chains significantly reduces and the heat released by polymerization acts favorably to reduce the process-free energy [8].

The molecular architecture of polymers in the solid state is of fundamental importance to understand various macroscopic properties. Solid-state nuclear magnetic resonance (NMR) is one of the most informative techniques to characterize heterogeneous structures in polymer and polymer/clay nanocomposites [9]. Proton wide-line NMR and relaxation experiments have been widely applied to study the phase structure and chain dynamics. An intermediate component has been inferred from the data by fitting the  $^1\text{H}$  wide-line NMR spectra [10–12]. We [13] used fiber clay, named palygorskite (PLT), so as to immobilize metallocene catalyst. The exfoliated PE/palygorskite can be obtained after ethylene polymerization.  $^1\text{H}$  solid-state NMR was used to quantitatively analyse the macromolecular dynamics and phase structure of the resulting polymer nanocomposites. Vander-Hart et al. [14, 15] used proton longitudinal relaxation time

( $T_1$ ) to estimate the dispersion degree of MMT.  $T_1$  showed a pronounced dependence on the  $\text{Fe}^{3+}$  concentration due to the strong paramagnetic of the  $\text{Fe}^{3+}$ . However, the  $^1\text{H}$  NMR spectrum of solid polymers often exhibits severely broad signals due to the strong  $^1\text{H}$ - $^1\text{H}$  dipolar coupling and random orientation of the molecule. Fast magic-angle spinning (MAS) has been successfully used to average the  $^1\text{H}$ - $^1\text{H}$  dipolar coupling and obtain high resolution spectra for organic solids [16]. Lee et al. [17] used proton MAS technique to study the interaction between proton and phosphoric acid in the poly(vinyl phosphoric acid). The results showed that hydrogen-bonded P-OH could be used as proton conductor. Moreover,  $^{13}\text{C}$  cross-polarization and magic-angle spinning (CP/MAS) NMR [18, 19] has been recognized as a powerful tool for investigating structures and dynamics of polymer composites. The combination of dipolar decoupling (DD), cross-polarization (CP), and MAS techniques permits one to detect chemical shifts and magnetic relaxation parameters that are directly related to the chain conformation and dynamics in each phase structure. Wang et al. [20] used solid-state  $^{13}\text{C}$ -NMR to study the conformational change and structural heterogeneity of surfactant molecules on the montmorillonite layer. Those surfactant molecules had higher chain mobility and disordered conformation. Moreover, the existence of two orthorhombic phases was also reported by Hillebrand et al. using solid-state  $^{13}\text{C}$ -NMR [21]. They found that the chains responsible for the orthorhombic crystalline phase with broad-line width made relative fast  $180^\circ$  chain flips by a traveling chain twist defect already at room temperature. The orthorhombic crystalline phase with narrow-line width may indicate the perfect crystalline phase. Our latest work also used solid-state  $^{13}\text{C}$ -NMR to study the phase structure and chain dynamics of polyethylene/palygorskite obtained by *in situ* polymerization [22]. The results of  $^{13}\text{C}$  CP/MAS showed that the chain mobility of orthorhombic crystalline phase with broad resonance line is obviously hindered compared with the narrow resonance line phase when the filler is introduced.

In this work, the exfoliated and intercalated polyethylene/MMT nanocomposites were obtained according to the ethylene *in situ* polymerization, respectively. Subsequently, the phase structure and chain dynamics of nanocomposites with different dispersion state were investigated by solid-state NMR.  $^1\text{H}$  and  $^{13}\text{C}$  solid-state NMR was used to study phase composition and molecular mobility of the samples under static and MAS states. Finally, the change in phase structure of PE nanocomposites was compared based on the NMR results when MMT and PLT were introduced into PE matrix.

## 2. Experiments

**2.1. Materials.** Bis(cyclopentadienyl)titanium dichloride ( $\text{Cp}_2\text{TiCl}_2$ , ACROS Organics) was purchased from J & K Chemical (Shanghai, China) and used as received. Toluene was purified using Solvent Purification (Invention Tech. USA). Methylaluminoxane (MAO) in toluene (wt%, 10%) was purchased from J & K Chemical (Shanghai, China).

Polymerization grade ethylene was obtained from Ningbo Gas Company (Ningbo, China) and purified through Gas Purification instrument (Shengmai Chemical Company, Dalian, China).  $[(\text{C}_{18}\text{H}_{37})_2\text{N}(\text{CH}_3)_2]^+\text{Cl}^-$  and Ca-based MMT was purchased from J & K Chemical. The content of  $\text{Fe}^{3+}$  of MMT was 3.1 wt% according to the product instrument.

### 2.2. Preparation of Polyethylene and Polyethylene/MMT Nanocomposites

**2.2.1. Preparation of the Modified MMT.** The purification procedure of MMT was obtained as follows: 300 g MMT was dispersed in 5 L water and then stirred for 60 mins. 8.5 g  $\text{Na}_2\text{CO}_3$  was added into the MMT suspension and stirred for 45 mins. The mixture was condensed for 120 mins. The supernatant was further rotated in ultracentrifugal instrument with 2000 rpm. Finally, the supernatant was dried at  $90^\circ\text{C}$  for 12 h. The X-ray diffraction (XRD) results showed that interlayer spacing of purified MMT was 1.3 nm.

50 g purified MMT suspended in 6 L water. Then, 9.4 g  $[(\text{C}_{18}\text{H}_{37})_2\text{N}(\text{CH}_3)_2]^+\text{Cl}^-$  was added into the mixture. The pH value of this mixture was maintained around 8.0 modulated by HCl. Subsequently, the mixture was stirred for 120 min at  $65^\circ\text{C}$ . The abundant  $\text{Cl}^-$  was removed using distilled water. Finally O-MMT can be obtained after the mixture was dried. The XRD results showed that interlayer spacing of O-MMT was greatly increased to 3.8 nm.

**2.2.2. Ethylene Polymerization.** The polyethylene bulk was prepared as follows. Ethylene polymerization was conducted in a 300 mL autoclave stainless steel reactor. The reactor was set to  $80^\circ\text{C}$  and purged five times by nitrogen and one time by ethylene before polymerization. Then the reactor temperature was set to  $40^\circ\text{C}$ , and 200 mL toluene was poured into the reactor with cocatalyst 5 mmol MAO. Ethylene pressure was fixed at 0.1 MPa. Polymerization started by introducing 50  $\mu\text{mol}$   $\text{Cp}_2\text{TiCl}_2$  into the reactor. Polymerization was then quenched by adding 20 mL acidified ethanol. Polymers are dried at  $60^\circ\text{C}$  under vacuum for 6 h after filtering. Polyethylene/MMT nanocomposites were prepared following the same method with pure polyethylene except that O-MMT was firstly introduced and stirred for 15 min under ultrasonic; then catalyst was introduced. The content of MMT in the polyethylene matrix was modulated according to the polymerization time.

**2.2.3. Characterization of the PE and PE/MMT Samples.** Molecular weight (MW) and MW distribution (MWD) were determined by gel permeation chromatography (GPC) method at  $150^\circ\text{C}$  using a PL-GPC-220 (Polymer Laboratories, Darmstadt, Germany) instrument and 1,2,5-trichlorobenzene as solvents. Transmission electron micrographs (TEM) were obtained using a Phillips CM100 apparatus at an acceleration voltage of 100 kV. Each sample was prepared using an ultracryomicrotome cutting apparatus at  $-130^\circ\text{C}$ , yielding samples 80 nm in thickness. A thermogravimetric analysis was carried out on a TGA/SDTA851 instrument

(Me\ETTER Corp., Switzerland). The  $N_2$  flow rate was fixed at  $20 \text{ mL} \cdot \text{min}^{-1}$ . Heating took place from 30 to  $1000^\circ\text{C}$  at  $10^\circ\text{C} \cdot \text{min}^{-1}$  heating rate. X-ray diffraction spectra of clay samples were recorded on a Rigaku D/Max-RA diffractometer (Japan) with Cu K $\alpha$  radiation (40 KV, 80 mA). Scanning was done in  $0.02^\circ$  steps at a speed of  $2^\circ \cdot \text{min}^{-1}$ .

**2.3. NMR Measurements.**  $^1\text{H}$  solid-state NMR spectra, longitudinal magnetization relaxation ( $T_1$ ), and DQ build-up curves were obtained using a Bruker DSX-200 spectrometer at a proton frequency of 200.02 MHz. The data were collected for nonspinning samples. A  $1.5 \mu\text{s}$   $90^\circ$  pulse and a 5 s recycle delay were used for all experiments. The detailed experiment followed the same method with the former study [22].  $^{13}\text{C}$  solid-state NMR was carried out on Bruker DSX-500 spectrometer. The magic-angle spinning speed was 5 kHz in all  $^{13}\text{C}$  CP/MAS (cross-polarization and magic-angle spinning) and  $^{13}\text{C}$  DP/MAS (direct-polarization and magic-angle spinning) NMR measurements using 2.5 mm MAS probe.  $^{13}\text{C}$  CP/MAS were recorded using 5 s recycle time with changing the contact time.

### 3. Results and Discussion

**3.1. Basic Information of the Polyethylene and Polyethylene/MMT Nanocomposites.** The results of ethylene polymerization are shown in Table 1. Catalyst activity obviously decreases when more O-MMT is introduced. Particularly, catalyst activity reaches to almost 25% of that in homogeneous catalyst when the loading of O-MMT is 7.2%. It indicates that the electronegativity of the MMT greatly influences the catalyst activity although it is covered by  $[(\text{C}_{18}\text{H}_{37})_2\text{N}(\text{CH}_3)_2]^+\text{Cl}^-$  layer. The defect of the  $[(\text{C}_{18}\text{H}_{37})_2\text{N}(\text{CH}_3)_2]^+\text{Cl}^-$  cover layer, particularly on the side of MMT, causes the uncovered acid MMT layers contacting with catalyst active sites and thus decreases the activity [23].

Figures 1(a) and 1(b) compare the XRD results of PE and PE/MMT nanocomposites. The diffraction peak 001 of O-MMT disappears in the PEMT18, which indicates that the ordered structure of MMT is destroyed after ethylene polymerization. The distance between MMT layers is larger than 8 nm in the PEMT18 matrix. However, two diffraction peaks can be found in the small angle range of XRD spectra of PEMT71. The layer distance can be calculated as 5.07 nm and 1 nm, respectively. This indicates that the MMT layer distance is smaller than PEMT18 and part of MMT layer may aggregate. The dispersion state of MMT in the polyethylene matrix is further investigated by TEM (Figures 1(c) and 1(d)). TEM morphology shows that the distance of MMT layer in PEMT18 is large and exfoliated nanocomposite is obtained. Moreover, MMT layer shows obviously aggregation behavior in PEMT71, and the intercalated dispersion is finally achieved.

#### 3.2. Solid-State NMR Experiments

**3.2.1. Phase Composition and Chain Dynamics by Proton NMR Spectra.** Wide-line proton NMR bases its analysis on

the extent of constrained molecular motions in the different domains [12]. The experimental wide-line spectra are deconvoluted into three components using the WinFit program. The broad component of the spectrum is approximated by a Gaussian function. This is a rough approximation of the actual line shape as shown in the following. The shape parameter ( $\alpha = 0.5$ ) of the line with intermediate width (i.e., the interface) is between that of a Gaussian ( $\alpha = 1$ ) and a Lorentzian ( $\alpha = 0$ ) [22]. The differences in the three component line shapes are expected to arise from differences in polymer chain motilities. The crystalline chains will result in the broad line due to only a partial motional averaging of the dipole-dipole interaction between the protons along the chains.

Figure 2 shows the fitting results of proton wide-line NMR spectra measured at different temperature. Figure 2(a) shows large changes in phase composition when the MMT clay is introduced. As compared to the content of crystalline phase (crystallinity) in the bulk PE, the introduction of MMT into the PE matrix greatly increases the crystallinity in a range of temperature from 300 to 360 K. It suggests that MMT clay layers interfere with the chain folding process leading to an increased content of well-ordered structures. Higher MMT amount in the polymer matrix also shows higher crystallinity. Interestingly, this is an opposite result compared with our former studies where the crystallinity was decreased as the palygorskite (PLT) loading increases in the PE/PLT nanocomposites [22]. In our opinion, the opposite dependence of crystallinity on filler loading may be attributed to the different structure of filler. MMT filler is the layer structure, while PLT filler presents the fiber style. Layer structure of MMT is able to adsorb more molecular chains on the surface compared with the fiber structure [22, 24]. Moreover, these adsorbed chains contribute to more mobility confined chains which can result in higher crystallinity. This can also be inferred from the results of chain mobility in Figure 2(b). All the widths of three phases in the nanocomposites are larger than PE matrix at all measured temperatures which indicates that the chain mobility of nanocomposites is hindered.

**3.2.2. Chain Dynamics by Proton Double-Quantum Dipolar Filter ( $^1\text{H}$  DQ NMR).** The magnetization from the more rigid part of a heterogeneous polymer can be selected using a dipolar filter based on the excitation of the double-quantum coherences [25]. The efficiency of the DQ filter is measured for PE and PE/MMT samples in Figure 3. At small excitation times, the filter selects the magnetisation mainly from the crystalline regions (rigid part). At longer excitation times, the filter starts to act like a transverse relaxation time ( $T_2$ ) filter, and the magnetisation from the less-mobile and mobile amorphous regions can be selected. The faster chain motions in the intermediate and amorphous phases reduce the effectiveness of proton dipole-dipole interactions through motional averaging [11]. Thus, the absence of DQ signal indicates that the dipole-dipole coupling between protons is weak due to either large distance between proton pairs or fast molecular motion on an NMR time scale (10–100  $\mu\text{s}$ ).

TABLE 1: Ethylene polymerization in the presence of O-MMT and the characterization results of PE/MMT hybrid materials<sup>a</sup>.

Run	MMT Conc. in feed $\text{g} \cdot \text{L}^{-1}$	Polymer yield g	Activity $\text{Kg PE/mol}_{\text{Cat}} \cdot \text{h}$	Mw $10^5 \text{g} \cdot \text{mol}^{-1}$	Mw/Mn	MMT in PE <sup>b</sup> wt. %	Sample notation
1 #	0	22.0	2200	4.81	3.3	0	PE
2 #	0.50	10.9	1090	2.19	3.5	1.8	PEMT18
3 #	0.45	5.9	590	1.37	2.9	7.1	PEMT71

<sup>a</sup> Polymerization conditions: solvent 400 mL toluene. Ethylene pressure 0.1 MPa. Cat. conc. In the feed  $25 \mu\text{mol Ti} \cdot \text{L}^{-1}$ . Polymerization time 60 mins.

<sup>b</sup> MMT content in the polyethylene matrix was measured by TGA.

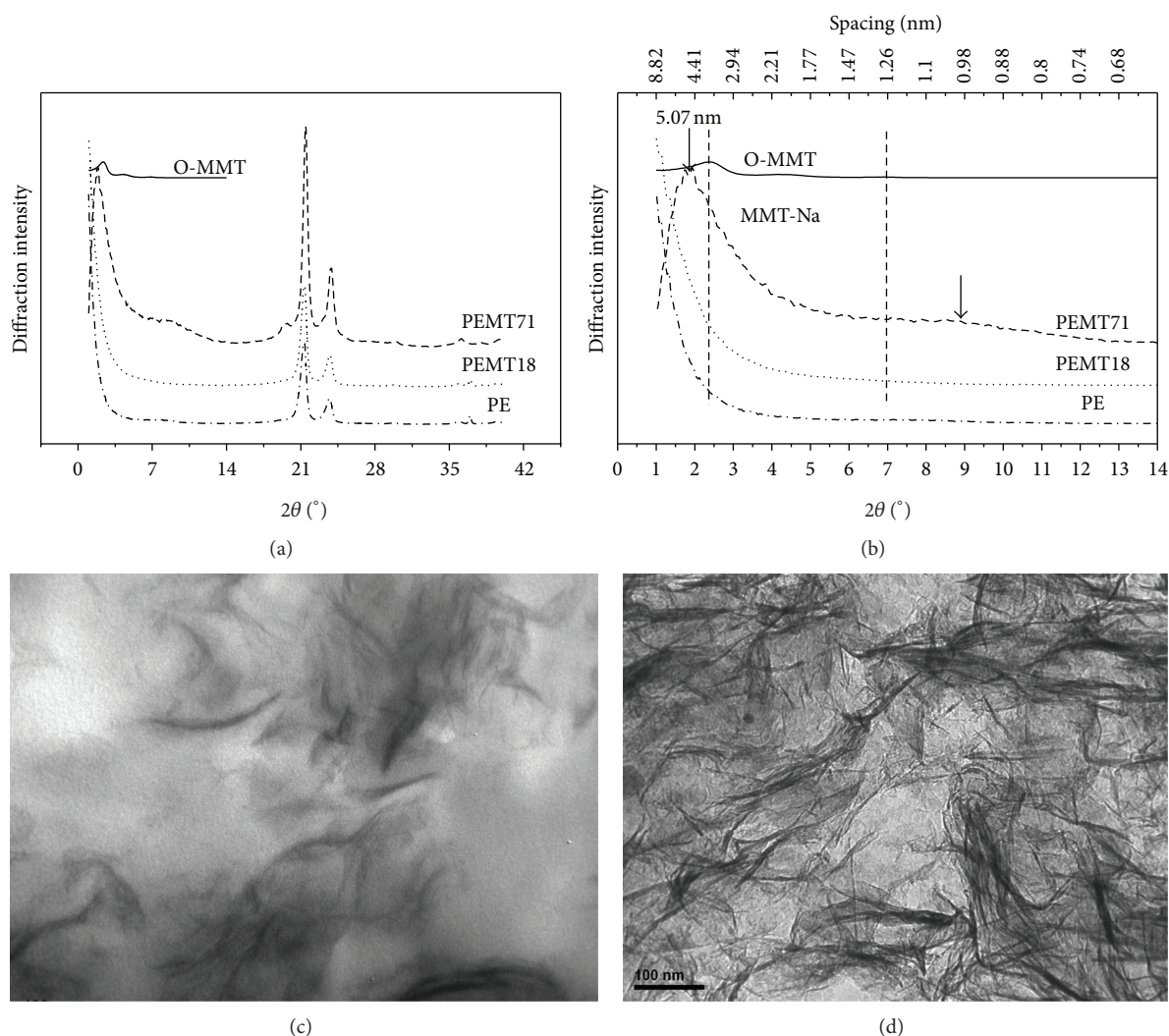


FIGURE 1: X-ray diffraction spectra (a, b) and TEM morphology (c, d) of PE and PE/MMT nanocomposites: (a) spectra in the full diffraction angle; (b) spectra in the small angle range; (c) TEM morphology of PEMT18,  $\times 200000$ ; (d) TEM morphology of PEMT71,  $\times 200000$ .

Figure 3(a) shows the normalized DQ build-up curves of samples measured at room temperature. The intensity of polyethylene matrix DQ spectrum is obviously lower than that of nanocomposites, suggesting that the nanocomposites are more rigid than the bulk PE. Moreover, the maxima of the curves appear at very short excitation time, in the range from 8 to 15  $\mu\text{s}$ , indicating the presence of strong  $^1\text{H}$  dipolar interaction. This interaction represents the feature of crystalline phase in the PE samples. In our case, this

interaction in nanocomposites is higher than that in the PE bulk and is enhanced in higher filler loading samples. It indicates that the chains of crystalline phase are more rigid in polymer nanocomposites, and the rigid degree increases when the filler loading goes up. Moreover, the initial stage of DQ build-up curves without normalization always presents linear shape. The slope of the initial curves can reflect the position of first maximum on the DQ curves. The maximum position will be delayed with a low slope indicating a more

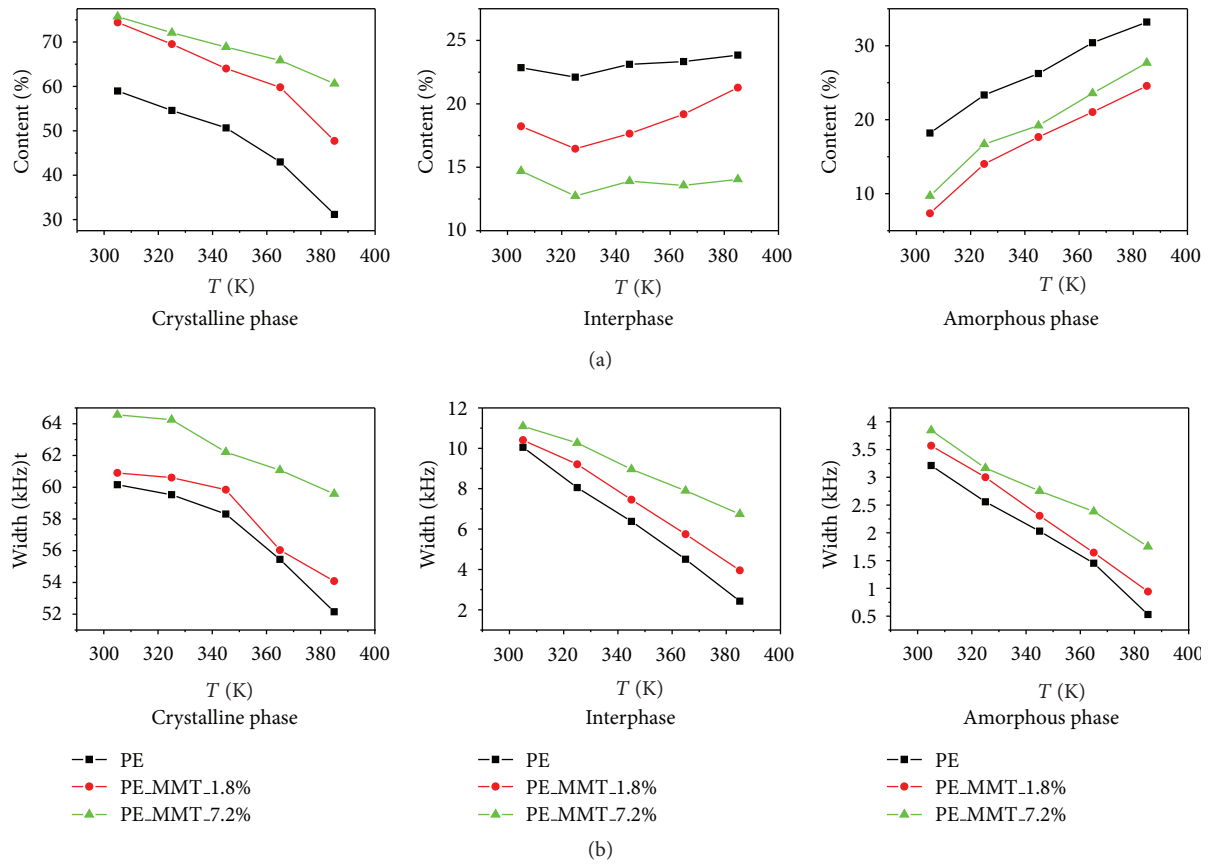


FIGURE 2: Fitting results of <sup>1</sup>H wide-line NMR spectra. (a) Phase composition and (b) line width.

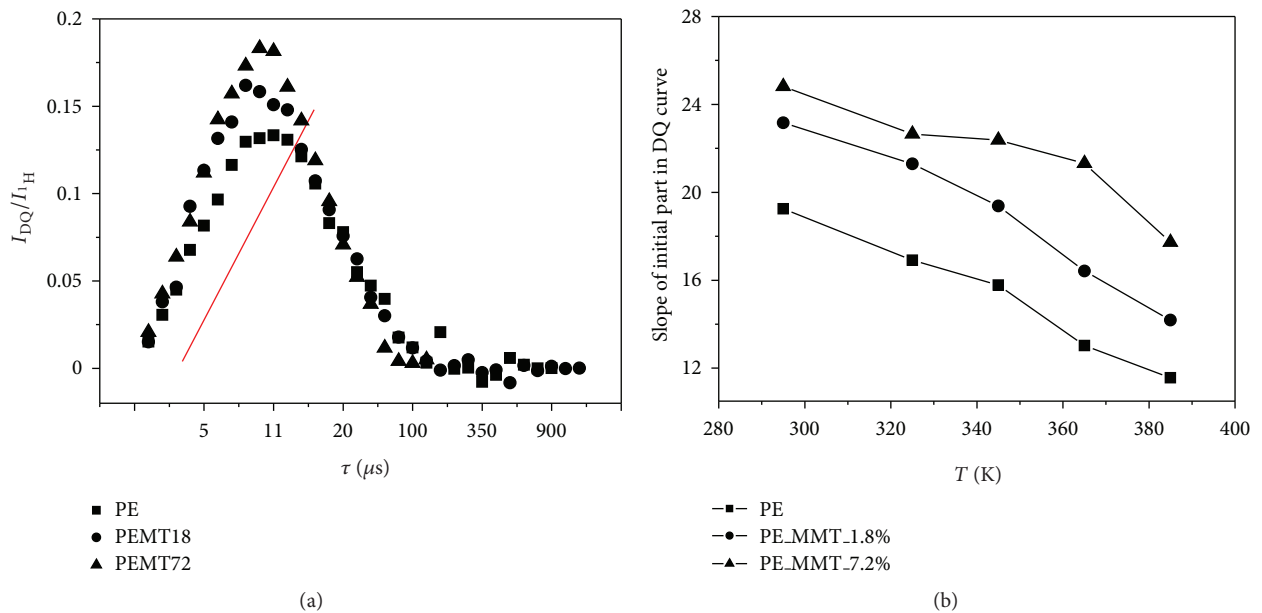


FIGURE 3: The DQ built-up curves of PE and PE nanocomposites measured at room temperature. (a) DQ built-up curves and (b) the slope of initial part in DQ curve.

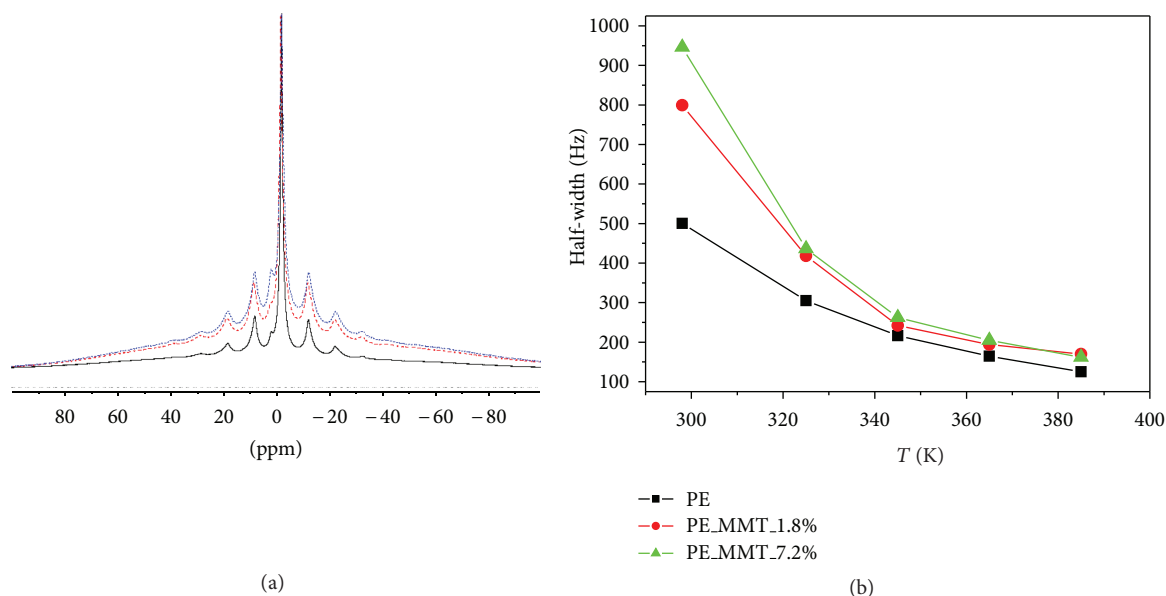


FIGURE 4:  $^1\text{H}/\text{MAS}$  spectrum of PE and PE nanocomposites. (a) A typical  $^1\text{H}/\text{MAS}$  spectrum measured at room temperature; (b) half width of the  $^1\text{H}$  MAS spectra dependence on the temperature.

mobile phase [26]. Temperature-dependent measurements of the DQ build-up curves show some interesting features. The slope of initial stage of DQ curves measured at different temperature is shown in Figure 3(b). The slope decreases upon increasing the temperature. It indicates that the chain mobility of crystalline phase is enhanced. At all temperatures, the slope of nanocomposites is obviously higher than that of polyethylene bulk and also increases as the MMT loading increased. It suggests that the chains become more rigid in crystalline phase when the MMT load is increased. Thus, the results of DQ build-up curves show good correspondence with those of wide-line proton NMR.

**3.2.3. Chain Dynamics by  $^1\text{H}$  MAS Spectrum.** Solid-state variable-temperature/magic-angle spinning (MAS)  $^1\text{H}$  NMR measurements are carried out. The results are shown in Figure 4. For semicrystalline polyethylene, the line width of the  $^1\text{H}$  signal is dominated by the dipolar interactions between protons. The magnitude of such interaction is usually several tens of kHz, and it is possible to achieve high resolution in the  $^1\text{H}$  spectrum by MAS at a speed of 5 kHz in our experiments. During MAS process, strong dipolar couplings from the restricted motions of molecules can be removed. Thus, the soft phase information where the chains mobility has more freedom can be reflected from the proton MAS spectrum [16]. In our results, the half width of PE nanocomposites spectrum is higher than that of PE bulk at all measurements, which indicates that the chains in soft phases are more rigid due to the addition of MMT filler.

Moreover, the difference of line width in PEMT18 and PEMT71 gradually disappears upon increasing the temperature (Figure 4(b)), while the line width of these samples are almost the same at 365 K and 385 K where the temperature

is near to the melting point. This may indicate that the MMT loading plays little effect on the chain dynamics to the chains in soft phases when the chain crystallinity reaches to melting state. However, it needs to be further proved.

**3.2.4. Chain Dynamics by  $^1\text{H}$  Longitudinal Magnetization Relaxation ( $T_1$ ).** Less numerous paramagnetic  $\text{Fe}^{3+}$  ions exist in the MMT with a concentration of 3.1 wt%. However, these ions are strongly paramagnetic and can exert an influence on the nuclear spins near the clay surface. Zhang et al. [27] described the impact of  $\text{Fe}^{3+}$  ions on  $\text{Li}^+$  spins in intercalated MMT clays. The paramagnetic impurities had a great influence on the spin-lattice relaxation time of the protons. The longitudinal magnetization relaxation ( $T_1$ ) decreased when the paramagnetic influence occurred.

The recovery of the magnetization is well fitted with a sum of two components, and the results are shown in Figure 5. Higher values of relaxation times are observed when 1.8 wt% MMT introduces into the bulk polyethylene. It suggests that the presence of the filler leads to an immobilization of the chain in rigid phase (Figure 5(a)) and soft phase (Figure 5(b)). This effect is in agreement with the findings from the wide-line NMR. However, the relaxation time is obviously decreased when the filler loading increases to 7.1 wt%. The influence of paramagnetic of  $\text{Fe}^{3+}$  ions occurs due to the intercalated dispersion state of PEMT71. It is believed that the  $\text{Fe}^{3+}$  mainly resides in the octahedral sites of MMT and can be enriched on the outside of the clay layers [2]. The protons of the organic modifier ( $[(\text{C}_{18}\text{H}_{37})_2\text{N}(\text{CH}_3)_2]^+\text{Cl}^-$ ) on the clay can become as close as 0.5-0.6 nm from the  $\text{Fe}^{3+}$  ions. Such protons, as well as certain PE protons that are very proximate to the surface, will experience both a direct line broadening and a shortening of  $T_1$  [14, 15]. The layers between MMT are closer in the intercalated dispersion state. The influence

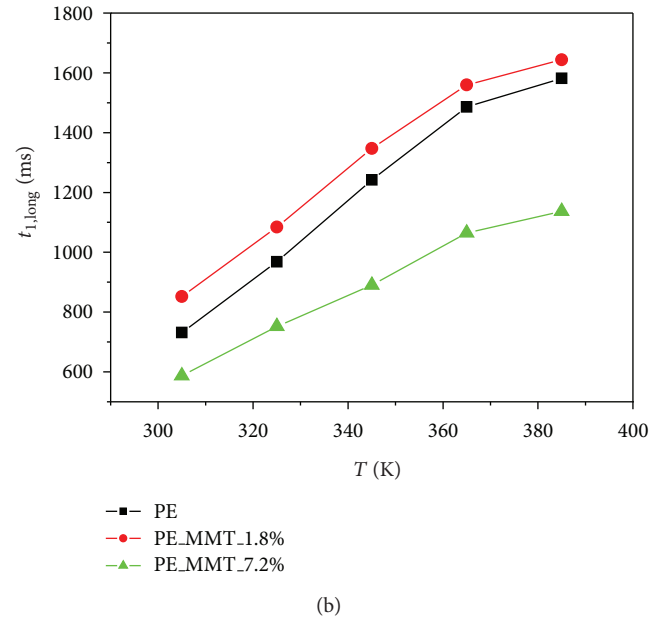
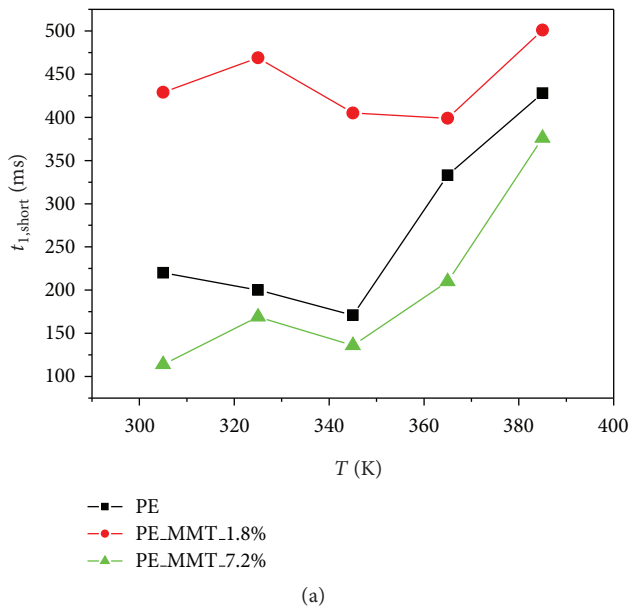


FIGURE 5: Longitudinal magnetization relaxation  $T_1$  value dependence on the temperature.

of  $\text{Fe}^{3+}$  on the relaxation time will be enhanced compared with a relative larger distance of MMT in exfoliated PE/MMT nanocomposites.

**3.2.5. Phase Composition and Chain Dynamics by  $^{13}\text{C}$  Solid-State NMR.** A typical  $^{13}\text{C}$  CP/MAS NMR spectrum is shown in Figure 6. The spectrum is fully deconvoluted by Lorentzian line shapes. A combination of four components fitting leads to the best fitting results for the spectrum measured at RT. The four components correspond to the different phases: amorphous phase (30.82 ppm), intermediate phase (31.64 ppm), orthorhombic crystalline phase (32.67 ppm), and monoclinic phase (33.74 ppm). Based on the gauche effect,  $^{13}\text{C}$  NMR can distinguish between orthorhombic and amorphous phases. For the former, segments are in all-trans conformation, and  $^{13}\text{C}$  NMR resonance appears at 32.9 ppm. For the latter, the 30.8 ppm line is from gauche containing conformation [27]. Moreover, polyethylene usually takes two types of crystal forms: the stable orthorhombic and metastable monoclinic phases. The orthorhombic phase occurs under normal conditions, and the latter appears after straining the PE [20]. The chains in these two phases take all zig-zag conformation but pack in different ways. The planes of the all-trans chains in the monoclinic phase are parallel to one another. However, they are perpendicular to each other in the orthorhombic phase.

Recently, much attention has been paid to deal with the existence of the third crystalline phase [21]. Our latest publication also detected out two orthorhombic crystalline phase in the PE/PLT nanocomposites by  $^{13}\text{C}$  CP/MAS NMR [22]. The chains responsible for the Cr-b carbon resonance, which can form the main fraction of the crystalline domains, make relatively fast  $180^\circ$  chain flips by a traveling chain twist defect already at room temperature. Thus, this resonance is

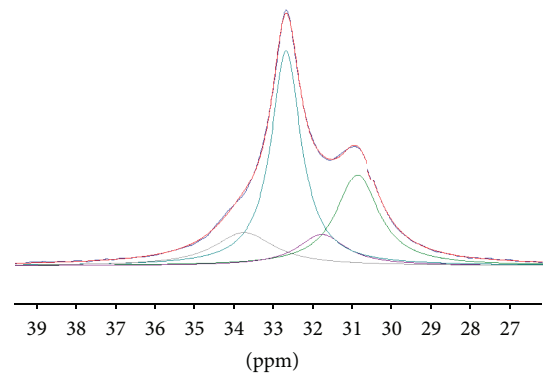


FIGURE 6: Fitting results of  $^{13}\text{C}$  CP/MAS of PE spectra when the CP time is 1 ms at RT.

associated with the defective crystalline phase. The chains responsible for the Cr-n carbon resonance do not show these motions and probably are found in more perfect crystalline structures. However, only one orthorhombic phase with narrow-line width is found in PE/MMT nanocomposites, indicating that more perfect crystalline phase is obtained in PE/MMT nanocomposites.

The crystallinity cannot be calculated directly from the  $^{13}\text{C}$  CP/MAS spectrum, because of the different cross-polarization efficiency of crystalline and amorphous phase. DP/MAS  $^{13}\text{C}$  spectrum is required to measure the crystallinity [20]. The results are listed in Table 2. The contents of orthorhombic phase and monoclinic phase in PE/MMT nanocomposites are both higher than those in polyethylene bulk at room temperature. This shows good correspondence with the results obtained by proton NMR. The line widths of amorphous phase and interphase in nanocomposites

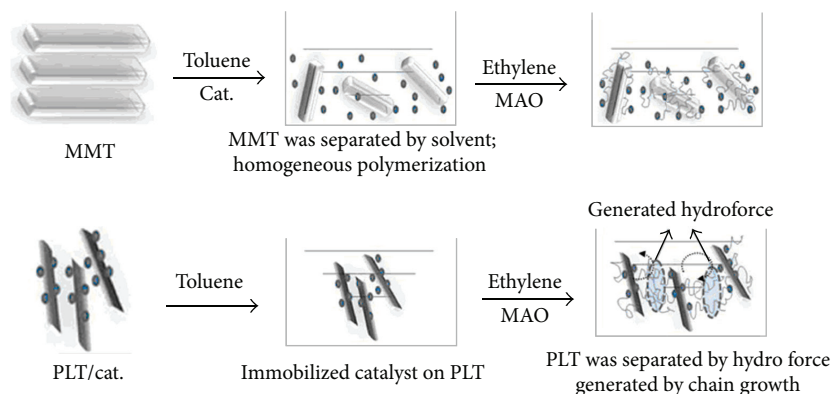


FIGURE 7: Proposed scheme of different polymerization methods for preparing nanocomposites.

TABLE 2: Results of  $^{13}\text{C}$  DP/MAS experiment.

		Phase Composition %					Half-width Hz			
RT	CS (ppm)	$30.82 \pm 0.01$	$31.64 \pm 0.01$	$32.67 \pm 0.01$	$33.74 \pm 0.01$	$30.82 \pm 0.01$	$31.64 \pm 0.01$	$32.67 \pm 0.01$	$33.74 \pm 0.01$	
	0%	59.83	4.45	29.35	6.37	145.9	104.6	119.4	174.4	
	1.8%	40.66	11.42	38.3	9.62	151.4	138.5	110.2	172.4	
	7.2%	38.34	11.13	34.53	15.97	173.5	198.8	98.1	280.9	
385 K	CS (ppm)	$29.77 \pm 0.01$	$30.44 \pm 0.01$	$32.25 \pm 0.01$	$33.76 \pm 0.01$	$29.77 \pm 0.01$	$30.44 \pm 0.01$	$32.25 \pm 0.01$	$33.76 \pm 0.01$	
	0%	77.99	3.63	14.25	4.13	45.7	162.2	153.3	327.5	
	1.8%	75.24	6.55	16.41	0.9	60.2	178.1	139.3	127.2	
	7.2%	71.99	10.81	17.16	—	51.5	326.5	136.3	—	

are both higher than those of polyethylene bulk. The line width also broadens as increasing the filler loading, which means that the chain mobility in these two phases is more rigid. Furthermore, the line width of orthorhombic phase in nanocomposite gradually decreases compared with polyethylene bulk, while the line width of monoclinic phase obviously increases. It indicates that the introduction of MMT has more influences on monoclinic crystalline phase. The proton dipolar-dipolar interaction from monoclinic crystalline phase may contribute more in broadening the proton wide-line NMR spectrum. The monoclinic phase of PE/MMT nanocomposites almost disappears when the temperature reaches to the melting point. It suggests that the monoclinic phase is more sensitive to the temperature compared to the orthorhombic phase due to its metastable state.

**3.2.6. The Influence of Filler Style on the Crystalline Behaviors of Nanocomposites.** In summary, chain dynamics and phase composition investigated by solid-state NMR show that MMTs with layer structure have obviously different influence on polyethylene crystalline behaviors compared with the PLT with fiber style, especially in crystalline phase. The reasons may be concluded as follows. first, the surface area of MMT is larger than fiber PLT filler due to the 2D layer structure of MMT [20]. Larger surface area can adsorb more polymer chains during the polymerization. This can result in much interaction between the polymer chains; thus more rigid chains will be obtained. Secondly, the polymerization method of PE/PLT and PE/MMT is a bit different which is shown in Figure 7.  $\text{Cp}_2\text{TiCl}_2$  was firstly supported on the

outer surface of PLT fibers during the preparation of PE/PLT nanocomposites. Polymerization directly occurred on the surface of PLT. The crystalline behavior of those growing chains was influenced as soon as the chain growth starts [28, 29]. The physical structure and surface chemistry of PLT could both influence the nascent growing chains. Thus, this results in more defective crystalline phase. However, the chain growing process of PE/MMT is different. MMT filler is a multilayer structure. The distance between each layer is about 1.24 nm in the original MMT. This distance mainly increases to 3.68 nm after being modified by  $[(\text{C}_{18}\text{H}_{37})_2\text{N}(\text{CH}_3)_2]^+\text{Cl}^-$ . The modified MMT (O-MMT) can achieve best dispersion in toluene after ultrasonic 15 mins. Polymerization was conducted by  $\text{Cp}_2\text{TiCl}_2$ /toluene solution after the best dispersion state was obtained. Here, the polymerization was actually conducted by homogeneous  $\text{Cp}_2\text{TiCl}_2$ . The tensile force coming from the chain growth could easily separate MMT layers without conquering the layer force between them (support fragmentation). Thus, the effect of support fragmentation to the chain folder process was less [28]. MMT can mainly act as the nucleator when the growing chain reaches to a relative large scale. The great influence on crystalline behavior of the growing chains may arrive from the solution. As a result, more confined molecular chains can be obtained.

## 4. Conclusion

In this work, solid-state NMR is used to study the phase structure and chain dynamics in the exfoliated and intercalated

PE/MMT nanocomposites prepared by *in situ* polymerization. A combination of proton and carbon methods under static and MAS conditions are used for the detailed study of phase structure. The results show that the incorporation of MMT with layer structure causes a large change in the phase structure. This structure also shows great difference from that of PE/PLT nanocomposites. The incorporated MMT enhances the crystallization process which results in higher crystallinity in PE/MMT nanocomposites. The polyethylene chains in the crystalline phase, interphase, and amorphous phase are also hindered due to the addition of MMT.  $^{13}\text{C}$  CP/MAS NMR shows that only one orthorhombic crystalline phase with narrow-line width can be detected.  $^{13}\text{C}$  DP/MAS NMR are quantitatively used to measure the phase structure and chain dynamics. The results show that the introduction of MMT has more influences on monoclinic crystalline phase. The proton dipolar-dipolar interaction from monoclinic crystalline phase may contribute more in broadening the proton wide-line NMR spectrum. The monoclinic phase of PE/MMT nanocomposites almost disappears when the temperature reaches to the melting point due to its metastable state.

## Conflict of Interests

The authors declare that there is no conflict of interests. They have bought the materials from a company that has no relationship with this paper. This paper was only attributed to our research group.

## Acknowledgments

Funding from the Project of Natural Science Foundation of China (no. 21206078), the Natural Science Foundation of Zhejiang Province (LQ12B06003), Zhejiang Province Department of Education Fund (Y201223797, Y201223742), K. C. Wong Education Foundation, and K. C. Wong Magna Fund, Hong Kong, are gratefully acknowledged. Professor Zhongren Chen's group is also acknowledged.

## References

- [1] M. Alexandre and P. Dubois, "Polymer-layered silicate nanocomposites: preparation, properties and uses of a new class of materials," *Materials Science and Engineering R*, vol. 28, no. 1-2, pp. 1-63, 2000.
- [2] S. S. Ray and M. Okamoto, "Polymer/layered silicate nanocomposites: a review from preparation to processing," *Progress in Polymer Science*, vol. 28, no. 11, pp. 1539-1641, 2003.
- [3] A. B. Morgan and J. W. Gilman, "Characterization of polymer-layered silicate (clay) nanocomposites by transmission electron microscopy and X-ray diffraction: a comparative study," *Journal of Applied Polymer Science*, vol. 87, no. 8, pp. 1329-1338, 2002.
- [4] M. Tanniru, Q. Yuan, and R. D. K. Misra, "On significant retention of impact strength in clay-reinforced high-density polyethylene (HDPE) nanocomposites," *Polymer*, vol. 47, no. 6, pp. 2133-2146, 2006.
- [5] J. Zhang and C. A. Wilkie, "Polyethylene and polypropylene nanocomposites based on polymerically-modified clay containing alkylstyrene units," *Polymer*, vol. 47, no. 16, pp. 5736-5743, 2006.
- [6] Q. H. Zeng, D. Z. Wang, A. B. Yu, and G. Q. Lu, "Synthesis of polymer-montmorillonite nanocomposites by *in situ* intercalative polymerization," *Nanotechnology*, vol. 13, no. 5, pp. 549-553, 2002.
- [7] S. Ray, G. Galgali, A. Lele, and S. Sivaram, "In situ polymerization of ethylene with bis(imino)pyridine iron(II) catalysts supported on clay: the synthesis and characterization of polyethylene-clay nanocomposites," *Journal of Polymer Science A*, vol. 43, no. 2, pp. 304-318, 2005.
- [8] M. Kawasumi, "The discovery of polymer-clay hybrids," *Journal of Polymer Science A*, vol. 42, no. 4, pp. 819-824, 2004.
- [9] B. Blümich, *NMR Imaging of Materials*, Clarendon Press, Oxford, UK, 2000.
- [10] D. E. Demco, G. Rata, R. Fechete, and B. Blümich, "Self-diffusion anisotropy of small penetrant molecules in deformed elastomers," *Macromolecules*, vol. 38, no. 13, pp. 5647-5653, 2005.
- [11] A. Buda, D. E. Demco, M. Bertmer et al., "Domain sizes in heterogeneous polymers by spin diffusion using single-quantum and double-quantum dipolar filters," *Solid State Nuclear Magnetic Resonance*, vol. 24, no. 1, pp. 39-67, 2003.
- [12] C. Hedesiu, D. E. Demco, R. Kleppinger et al., "The effect of temperature and annealing on the phase composition, molecular mobility and the thickness of domains in high-density polyethylene," *Polymer*, vol. 48, no. 3, pp. 763-777, 2007.
- [13] W. Li, A. Adams, J. D. Wang, B. Blümich, and Y. R. Yang, "Polyethylene/palygorskite nanocomposites: preparation by *in situ* polymerization and their characterization," *Polymer*, vol. 51, no. 21, pp. 4686-4697, 2010.
- [14] D. L. VanderHart, A. Asano, and J. W. Gilman, "Solid-state NMR investigation of paramagnetic nylon-6 clay nanocomposites. 1. Crystallinity, morphology, and the direct influence of  $\text{Fe}^{3+}$  on nuclear spins," *Chemistry of Materials*, vol. 13, no. 10, pp. 3781-3795, 2001.
- [15] D. L. VanderHart, A. Asano, and J. W. Gilman, "Solid-state NMR investigation of paramagnetic nylon-6 clay nanocomposites. 2. Measurement of clay dispersion, crystal stratification, and stability of organic modifiers," *Chemistry of Materials*, vol. 13, no. 10, pp. 3796-3809, 2001.
- [16] Q. Chen, H. Hurosu, I. Ando, and X. Wu, "Solid-state variable-temperature  $^1\text{H}$  MAS NMR studies on deuterated polyethylene," *Solid State Nuclear Magnetic Resonance*, vol. 7, no. 4, pp. 319-325, 1997.
- [17] Y. J. Lee, B. Bingöl, T. Murakhtina et al., "High-resolution solid-state NMR studies of poly(vinyl phosphonic acid) proton-conducting polymer: molecular structure and proton dynamics," *Journal of Physical Chemistry B*, vol. 111, no. 33, pp. 9711-9721, 2007.
- [18] F. A. Bovey and P. A. Mirau, *NMR of Polymers*, Academic Press, New York, NY, USA, 1996.
- [19] K. Schmidt and H. W. Spiess, *Multidimensional Solid-State NMR and Polymers*, Academic Press, London, UK, 1994.
- [20] L. Y. Wang, P. F. Fang, C. H. Ye, and J. W. Feng, "Solid-state NMR characterizations on phase structures and molecular dynamics of poly(ethylene-co-vinyl acetate)," *Journal of Polymer Science B*, vol. 44, no. 19, pp. 2864-2879, 2006.

- [21] L. Hillebrand, A. Schmidt, A. Bolz et al., "Nuclear magnetic resonance detection of two distinctly different chains in the orthorhombic crystalline phase of polyethylenes," *Macromolecules*, vol. 31, no. 15, pp. 5010–5021, 1998.
- [22] W. Li, B. Jiang, A. Buda et al., "An NMR investigation on the phase structure and molecular mobility of the novel exfoliated polyethylene/palygorskite nanocomposites," *Journal of Polymer Science B*, vol. 48, no. 12, pp. 1363–1371, 2010.
- [23] J. Heinemann, P. Reichert, R. Thomann, and R. Mülhaupt, "Polyolefin nanocomposites formed by melt compounding and transition metal catalyzed ethene homo- and copolymerization in the presence of layered silicates," *Macromolecular Rapid Communications*, vol. 20, no. 8, pp. 423–430, 1999.
- [24] H. Sertchook, H. Elimelech, C. Makarov et al., "Composite particles of polyethylene @ silica," *Journal of the American Chemical Society*, vol. 129, no. 1, pp. 98–108, 2007.
- [25] M. Bertmer, L. Gasper, D. E. Demco, B. Blümich, and V. M. Litvinov, "Investigation of soft component mobility in thermoplastic elastomers using homo- and heteronuclear dipolar filtered  $^1\text{H}$  double quantum NMR experiments," *Macromolecular Chemistry and Physics*, vol. 205, no. 1, pp. 83–94, 2004.
- [26] M. Bertmer, M. Wang, D. E. Demco, and B. Blümich, "Segmental mobility in short-chain grafted-PDMS by homo- and heteronuclear residual dipolar couplings," *Solid State Nuclear Magnetic Resonance*, vol. 30, no. 1, pp. 45–54, 2006.
- [27] Q. J. Zhang, W. X. Lin, G. Yang, and Q. Chen, "Studies on the phase structure of ethylene-vinyl acetate copolymers by solid-state  $^1\text{H}$  and  $^{13}\text{C}$  NMR," *Journal of Polymer Science B*, vol. 40, no. 19, pp. 2199–2207, 2002.
- [28] T. F. L. Mckenna, A. D. Martino, G. Weickert, and J. B. P. Soares, "Particle growth during the polymerization of olefins on supported catalysts, 1—nascent polymer structures," *Macromolecular Reaction Engineering*, vol. 4, no. 1, pp. 40–64, 2010.
- [29] D. Jauffrès, O. Lame, G. Vigier, and F. Doré, "How nascent structure of semicrystalline polymer powders enhances bulk mechanical properties," *Macromolecules*, vol. 41, no. 24, pp. 9793–9801, 2008.

## Review Article

# 3D Self-Supported Nanoarchitected Arrays Electrodes for Lithium-Ion Batteries

Xin Chen,<sup>1</sup> Ying Du,<sup>1,2</sup> Nai Qing Zhang,<sup>2,3</sup> and Ke Ning Sun<sup>2,3</sup>

<sup>1</sup>Department of Chemistry, Harbin Institute of Technology, Harbin, Heilongjiang 150001, China

<sup>2</sup>Academy of Fundamental and Interdisciplinary Sciences, Harbin Institute of Technology, Harbin, Heilongjiang 150001, China

<sup>3</sup>State Key Laboratory of Urban Water Resource and Environment, Harbin Institute of Technology, Harbin, Heilongjiang 150001, China

Correspondence should be addressed to Ke Ning Sun, keningsun@yahoo.com.cn

Received 17 October 2012; Accepted 3 December 2012

Academic Editor: Jianmin Ma

Copyright © 2012 Xin Chen et al. This is an open access article distributed under the Creative Commons Attribution License, which permits unrestricted use, distribution, and reproduction in any medium, provided the original work is properly cited.

Three-dimensional self-supported nanoarchitected arrays electrodes (3DSNAEs) consisting of a direct growth of nanoarchitected arrays on the conductive current collector, including homogeneous and heterogeneous nanoarchitected arrays structures, have been currently studied as the most promising electrodes owing to their synergies resulting from the multistructure hybrid and integrating heterocomponents to address the requirements (high energy and power density) of superperformance lithium ion batteries (LIBs) applied in portable electronic consumer devices, electric vehicles, large-scale electricity storage, and so on. In the paper, recent advances in the strategies for the fabrication, selection of the different current collector substrates, and structural configuration of 3DSNAEs with different cathode and anode materials are investigated in detail. The intrinsic relationship of the unique structural characters, the conductive substrates, and electrochemical kinetic properties of 3DSNAEs is minutely analyzed. Finally, the future design trends and directions of 3DSNAEs are highlighted, which may open a new avenue of developing ideal multifunctional 3DSNAEs for further advanced LIBs.

## 1. Introduction

Currently, extensive concern about the increasingly worsened environmental pollution and impending exhaustion of limited energy resources has brought about the ever-going demand for seeking renewable and clean energy sources to cope with these serious energy and environmental issues [1–3]. As a suitable energy source, lithium ion batteries (LIBs) are being exploited for the widespread applications [4–7] in portable electronic consumer devices, electric vehicles, and large-scale electricity storage in intelligent grids, due to the multiple superiorities such as high energy density, safety, long life, low cost, and environmental benignity.

A typical commercial LIB consists of a positive electrode (cathode) formed from layered  $\text{LiCoO}_2$ , a nonaqueous liquid electrolyte, and a graphite negative electrode (anode) in Figure 1(a). During the charging process, lithium ion ( $\text{Li}^+$ ) is deintercalated from the layered  $\text{LiCoO}_2$  host, passes through the electrolyte, and is intercalated between the graphite

layers. Vice versa, discharge reverses this process. The electrons, of course, pass across the external circuit [8]. To realize the charge and discharge, the commercial LIBs are commonly constructed by electrodes and the electrolyte trapped within a polypropylene separator, in which electrodes are fabricated by the slurry procedure involved in mixing active electrodes materials with conducting carbon and polymeric binders and then casting them onto the current collector in Figure 1(b).

The electrodes materials are rated on the basis of their specific (gravimetric) capacity ( $\text{mAh g}^{-1}$ ), determined by their charge/discharge graphs, and the degree of capacity change upon cycling at different demands. Intense scrutinized cathode materials, mainly including  $\text{LiCoO}_2$ ,  $\text{LiMn}_2\text{O}_4$ ,  $\text{LiNi}_x\text{Mn}_y\text{Co}_z\text{O}_2$ ,  $\text{LiFePO}_4$ , and  $\text{V}_2\text{O}_5$  [9–13], have their own unique structured merits, offering highly accessible  $\text{Li}^+$  diffusion pathways and demerits like limited specific capacities as well as poor capacity retention [14, 15]. Anode materials, such as carbon, silicon, alloy, metal oxides,

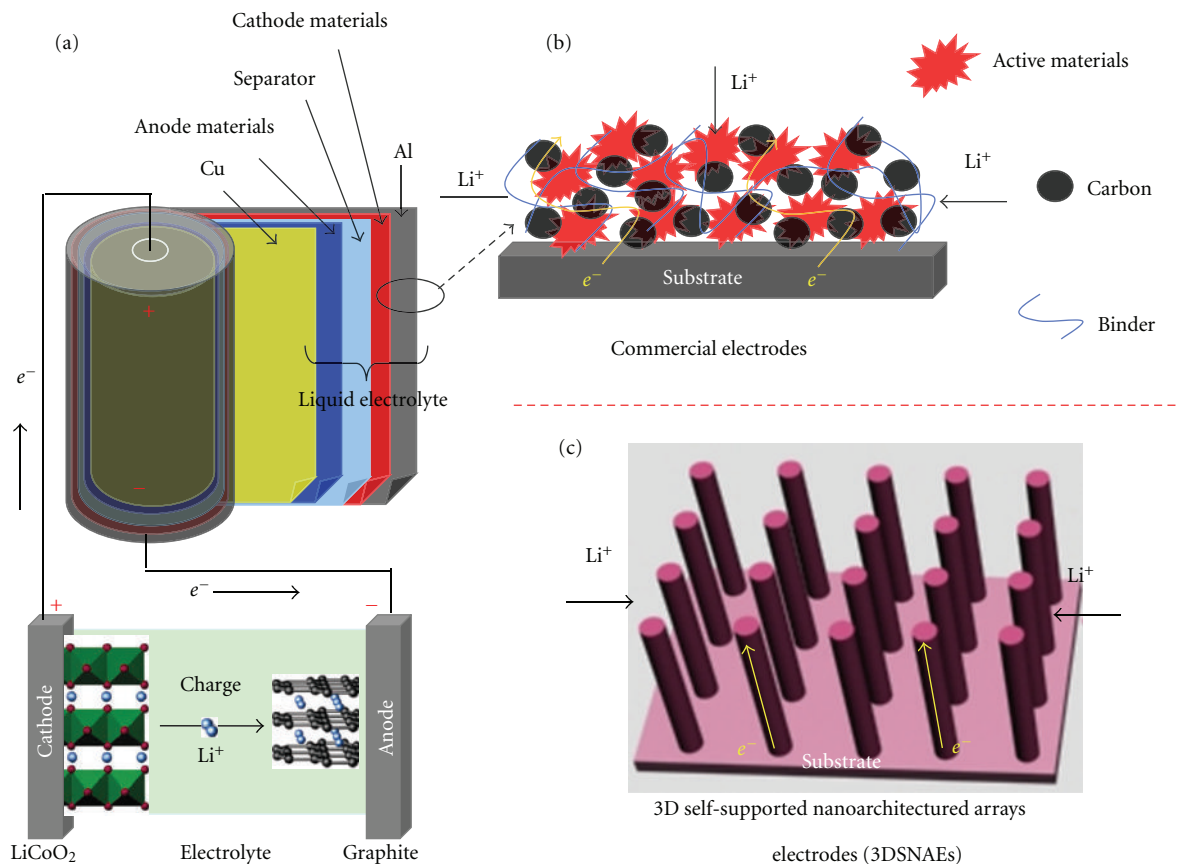


FIGURE 1: Schematic showing (a) operating principles and components of the typical commercial cylindrical lithium ion batteries (LIBs), (b) the slurry procedure of fabricating commercial electrodes, and (c) the configuration of novel 3D self-supported nanoarchitected arrays electrodes (3DSNAEs).

and metal sulfides/phosphides, exhibit high capacities and couple to the poorly structured stability and volume variation issues [16–24]. No matter how creative researchers design new lithium intercalation materials, one drawback exists due to the intrinsic diffusivity of  $Li^+$  in the solid state (ca.  $10^{-8} \text{ cm}^2 \text{ s}^{-1}$ ), which unavoidably limits the charge/discharge performance [25]. In this regard, many efforts have been devoted to devise a variety of nanomaterials with unique structures from zero-dimensional nanoparticles and one-dimensional (1D) nanowires to three-dimensional (3D) micro-/nanostructures and hollow- and core-shell structures, resulting in improved electrochemical performance to satisfy the demands of industrial applications [25–31].

These nanomaterials aforementioned have great superiorities [1, 32, 33] over their bulk counterparts. The reduced dimensions of materials shorten the  $Li^+$  and electron transport length, leading to higher capacity at high rates. Meanwhile, a high surface area allows a large contact interface between the electrode material and electrolyte and enhances the  $Li^+$  flux across the interface, resulting in a higher capacity. In addition, the small size could accommodate the strain associated with intercalation, reducing the capacity losses. However, nanomaterials are not a panacea to a certain extent and have some disadvantages [34, 35]

such as more side reactions with the electrolyte due to the high electrolyte/electrode surface area, weak structure stabilities induced by aggregations, and lower volumetric energy density compared with microscale materials.

To transcend the above limitations of nanomaterials, selecting a proper approach, a proper structure, and a proper combination of various materials to assemble the active materials into the desired structures is indispensable. Recently, a novel configuration of 3D self-supported nanoarchitected arrays electrodes (3DSNAEs) in Figure 1(c) has attracted much attention owing to the combination of diversified nanostructures' merits, including high surface in favor of high capacity, ordered and stable structures to the benefit of buffering for the volume change and improving the electric conductivity of electrodes, and lower aggregation and collapse in comparison to nanoparticles [36–38]. This kind of 3DSNAEs consists of a direct growth of nanoarchitected arrays on the conductive current collector, providing a direct pathway for efficient charge transport along the arrays axis and forming a 3D conductive network among active materials, nanoarchitected arrays pathways, and the conductive current collector. Differencing from the traditional slurry procedure, each nanoarchitected array of 3DSNAEs is directly connected to the current-carrying substrate without any conductive and binder agents and allows for all

structures' contribution to the capacity and efficient charge transport, leading to the excellent electrochemical properties [37, 39, 40].

In this paper, detailed investigations are focused on strategies for the fabrication, selection of the different current collector substrates, and structural configuration of 3DSNAEs with different cathode and anode materials for LIBs. The intrinsic relationship of the unique structural characters, the conductive substrates, and electrochemical kinetic properties of 3DSNAEs is minutely analyzed, and recent work by our group is also summarized. Finally, the problems and prospects are highlighted on this kind of 3DSNAEs.

## 2. Strategies for Fabrication

Nanoarchitected arrays of 3DSNAEs, including 1D nanowires (NWs), and nanotubes (NTs), nanorods (NRs), are apparently influenced by their properties of the conductive substrates, owing to the unique structures that nanoarchitected arrays are directly grown on the current collector substrates. Different strategies, therefore, should be made to fabricate the 3DSNAEs grown on the different substrates. To the best of our knowledge, the conductive substrates applied in the 3DSNAEs principally contain Al, Cu, Ti, Ni, Au, Si, stainless steel (SS), Fe-based alloy, Sn-doped  $\text{In}_2\text{O}_3$  (ITO), and so on. And the strategies to fabricate 3DSNAEs may be classified into 3 categories in Figure 2, namely, self-growing, wet-etching, and template-based growth.

Self-growing in Figure 2(a) is the one for fabricating the nanoarchitected arrays directly grown on the substrates by using a variety of techniques such as vapor phase growth, hydro-/solvothermal growth, and solution-based growth. Vapor phase growth including thermal chemical vapor deposition (CVD), direct thermal evaporation [41], and pulsed-laser deposition (PLD) is a straightforward way that controls the reaction between oxygen gas and metal vapor source in the light of vapor-liquid-solid and vapor-solid mechanisms [42, 43]. CVD involves the process of growing the nanoarchitected arrays on the substrate surface via the chemical reaction in the gas phase, which is resulted from the vapor with the element of nanoarchitected arrays and other indispensable gases in the reactive chamber. By using the CVD approach, Si NWs [37] and  $\text{V}_2\text{O}_5/\text{SnO}_2$  NWs [44] could be directly grown on the SS substrate, and  $\text{V}_2\text{O}_5$  nanoribbons [45] would be also done on the Si substrate. Whilst employing the thermal evaporation technique, Si nanopillars [46] and  $\text{SnO}_2$  NWs [47] could be orderly grown on the SS substrate. Besides, hydro-/solvothermal growth is a common method of preparing nanoarchitected arrays grown on the metal or alloy substrate. The process involves the aqueous mixture of soluble metal salt (metal and/or metal-organic) of the precursor material and the treatment of the mixed solution in an autoclave filled under elevated temperature from  $100^\circ\text{C}$  to  $300^\circ\text{C}$  and relatively high pressure conditions  $>1$  atm. Recently,  $\text{MoO}_x$  NRs on the Cu substrate [48], single-crystal mesoporous  $\text{Co}_3\text{O}_4$

nanobelts [49] and  $\alpha\text{-Fe}_2\text{O}_3$  NRs [50] were prepared via the hydro-/solvothermal method. These approaches aforementioned, however, ordinarily require high temperature or high pressure. By comparison, the solution-based method based on a liquid-solid growth mechanism has been extensively exploited for preparing the free-standing nanoarchitected arrays at the low temperature, which could reduce considerably the complexity and cost of fabrication [51, 52]. The process is that a piece of substrate immersed in reaction solutions generates a thin film with nanoarchitected arrays at a low temperature  $<100^\circ\text{C}$  for a while. For instance, the homogeneous and dense arrays of ZnO NWs grown on arbitrary substrates were produced by Greene et al. via the liquid-solid growth [53], and Li et al. prepared mesoporous  $\text{Co}_3\text{O}_4$  NWs arrays on the Ti substrate by the ammonia-induced solution growth [54].

Self-etching in Figure 2(b) involves a pure chemical or electrochemical reaction process, in which the surface layer of the conductive substrates is corroded and converted immediately to nanoarchitected arrays by using the reactions between solutions and the etching materials. Lately, some considerable efforts have been devoted to fabricate ordered 1D Si nanostructured arrays via a metal-assisted chemical etching approach [55, 56]. The etching process included the following aspects: (a) the oxidant was preferentially reduced on the surface of the noble metal; (b) the holes resulted from the reduction of the oxidant on the noble metal surface and were injected into the Si that was in contact with the noble metal; (c) the Si was oxidized and dissolved at the Si/metal interface by HF. Different from the Si etching, a solution-based corrosion is also to prepare nanoarchitected arrays [57]. Immersed in alkaline solutions, the surface layers of Cu foil and Ni grid were corroded into 1D CuO arrays [58, 59] and  $\text{Ni}_3\text{S}_2$  NW arrays [60], respectively. In addition, self-organized  $\text{TiO}_2$  NTs arrays [61, 62] had been prepared via electrochemical anodization of Ti foils by controlling the electrolyte composition as well as the rate at which the resultant oxide was dissolved. To be excited, a novel vapor-phase corrosion strategy had been developed by our group to fabricate CuO hierarchically mesoporous nanosheet-assembled gearlike pillar arrays (HMNGPAs) and mesoporous nanosheet cluster arrays (MNCAs) [63, 64]. This strategy involved the oxidation, complexation, and thermal decomposition processes and was simple, low-cost, and broadly applicable, providing a new avenue for large-scale configuration of nanoarchitected arrays with unique multifunctional properties.

Template-based growth, just as its name implies, is that the employed materials deposited in the template decorated on the substrate surface via a certain chemical or physical approach are transformed to nanoarchitected arrays by removing the template membrane, as shown in Figure 2(c). The AAO membrane is the most widely used template, because of its facile preparation and the controllable uniformity pore distribution with lower ohmic drop, validating the homogeneous electrolyte flow. For example, arrays of perpendicular Cu nanopillars on the Cu foil substrate were fabricated by Taberna et al. via cathodic electrodepositing of the electrolyte with  $\text{Cu}^{2+}$  ion into the pores of AAO

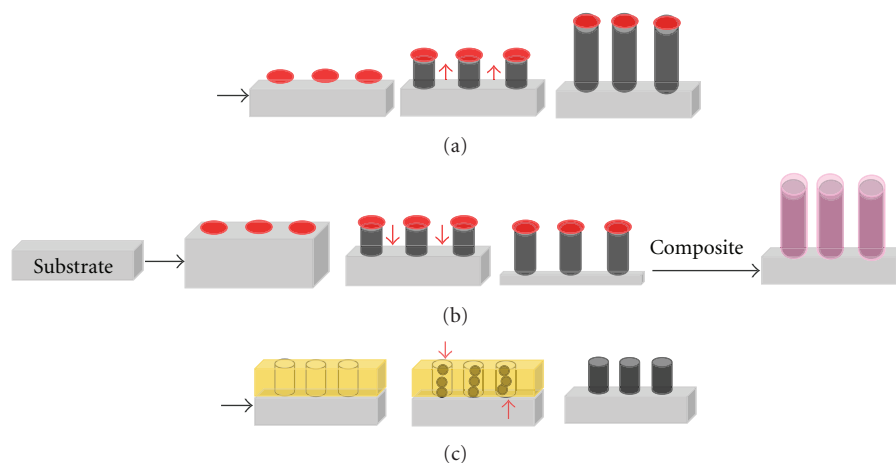


FIGURE 2: Schematic for the fabrication principle of 3DSNAEs by self-growing (a), self-etching (b), and template-based growth (c).

membrane [65]. Kim et al. [66] prepared vertical arrays of  $\text{MnO}_2$  NWs on the Si substrate by the following steps: (a) sputtering a thick aluminum layer on silicon chips, (b) anodizing the aluminum layer, (c) anodic electrodepositing of  $\text{MnO}_2$  NWs in the alumina pores, and (d) removing the AAO layer. Besides, by employing the CVD and AAO templates technique, the vertically aligned core-shell Au/CNT- $\text{V}_2\text{O}_5$  NRs arrays on the Al substrate had been synthesized by Kim et al. shown in Figure 3 [67]. Coupled with the previous irrigation from the top of templates,  $\text{V}_2\text{O}_5$ - $\text{TiO}_2$  NRs arrays were prepared by a capillary-enforced template-based method, filling into the pores of a polycarbonate membrane (PC) from the bottom with  $\text{VOSO}_4$  and  $\text{TiOSO}_4$  solutions [68].

### 3. Selecting Substrate

The current collector substrate, as a main component of 3DSNAEs, plays a significant role in the configuration and electrochemical performance of 3DSNAEs. The substrate could be classified into three major categories shown in Table 1: cathode substrate with high oxidation voltage (Al), anodic substrate with high electrochemical stability in a low voltage window (Cu), and multifunctional substrate, on the basis of functions of 3DSNAEs for LIBs.

**3.1. Cathode Substrate.** Generally, cathode substrate used to load cathode materials ( $\text{LiCoO}_2$ ,  $\text{LiMn}_2\text{O}_4$ , and  $\text{LiFePO}_4$ ) requires high oxidation voltage and high electrochemical stability in a wide voltage window. Al with multiple superiorities, such as high oxidation voltage (5 V versus  $\text{Li/Li}^+$ ), good electric conductivity, and low price, could be protected by a thin and dense  $\text{Al}_2\text{O}_3$  layer. However, in a low voltage close to 0 V (versus  $\text{Li/Li}^+$ ), an Li-Al alloying process would happen because of the deposition of dissolved  $\text{Al}^{3+}$  from the  $\text{Al}_2\text{O}_3$  layer of the Al foil [114, 115]. Therefore, Al is mainly used as the current collector of cathode materials for LIBs. The single-crystal  $\text{V}_2\text{O}_5$  NRs and NTs arrays directly connected to the planar Al substrate were fabricated by

Wang et al. via template-based electrodeposition and delivered 5 and 1.3 times higher capacity than sol-gel-derived films at the same current density, respectively [69, 116, 117]. Despite the improved electrochemical performance of  $\text{V}_2\text{O}_5$  nanoarchitected arrays, the planar Al substrate has limited surface area to provide the limited contact between active materials and substrate. In this regard, Ni NRs arrays were firstly grown on the planar Al substrate and then coated with  $\text{V}_2\text{O}_5$  to synthesize  $\text{Ni-V}_2\text{O}_5 \cdot n\text{H}_2\text{O}$  nanocable arrays, which delivered approximately 10 times higher capacities single-crystal  $\text{V}_2\text{O}_5$  NRs and 20 times higher than sol-gel-derived  $\text{V}_2\text{O}_5$  films, due to the large surface and short diffusion path offered by the  $\text{Ni-V}_2\text{O}_5 \cdot n\text{H}_2\text{O}$  nanocable arrays [118]. Afterwards, Al NRs arrays directly grown on the Al foil to construct 3D current collectors for LIBs offered high surface area and facilitated the contribution to the capacity of active materials [119, 120]. For example, a vertically aligned Au/CNT- $\text{V}_2\text{O}_5$  core-shell NRs electrode developed by Kim et al. demonstrated high capacity ( $473.7 \text{ mAh g}^{-1}$  at 1C rate) and excellent rate performance ( $379.2 \text{ mAh g}^{-1}$  at 10C rate) owing to the aligned nanostructures with increased reaction sites, facilitated charge transport, and improved mechanical stability [67].

**3.2. Anode Substrate.** Cu foil has been extensively used as the current collector of anode materials, because metal Cu with good conductivity hardly forms the Li-Cu alloy at a low voltage and could be oxidized and dissolved at the high voltage ( $>3.6 \text{ V}$  versus  $\text{Li/Li}^+$ ) [115]. Nickel nanocones arrays (NCAs) which supported Si anode was firstly constructed by Zhang et al. via the electrodeposition and sputtering techniques and delivered a high capacity of  $2400 \text{ mAh g}^{-1}$  at 0.2C rate over 100 cycles, because Ni NCAs facilitated charge collection and transport, supported the electrode structure, and acted as inactive confining buffers [121]. Thanks to factors that the chemical property of metal Cu is considerably brisk and easy to be corroded by acid or alkali solutions. The template-based growth is an effective strategy to construct 3DSNAEs on the Cu substrate.

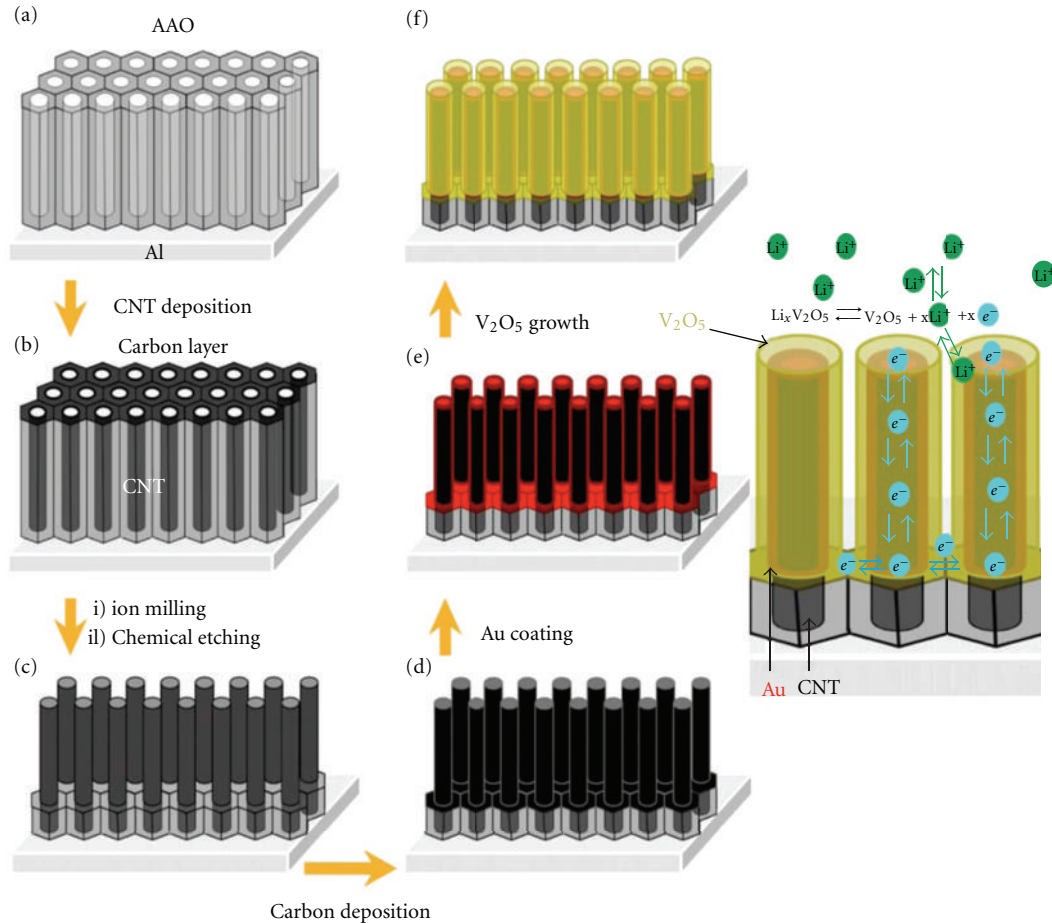


FIGURE 3: Schematic of the fabrication process of Au/CNT-V<sub>2</sub>O<sub>5</sub> core-shell nanorod arrays with the schematized electrochemical reaction involving the nanostructured Li battery electrode [67].

Since Taberna et al. prepared Cu NRs arrays on the Cu substrate to construct Cu NRs arrays supported Fe<sub>3</sub>O<sub>4</sub> via AAO template-based electrodeposition [65], many anode materials such as Cu-Fe<sub>3</sub>O<sub>4</sub> [122, 123], Cu-Sn [74, 124], Cu-Bi [75], Cu-Cu<sub>3</sub>P [84], and Cu-Ni<sub>3</sub>Sn<sub>4</sub> [18] have been developed by the template-based growth. For example, as the anode materials, Cu-Ni<sub>3</sub>Sn<sub>4</sub> delivered a capacity of 500 mAh g<sup>-1</sup> with no decay over 200 cycles at 0.8C rate. In addition, solution-based growth is also an efficient way to large-scale fabricate 3DSNAEs on the Cu substrate, due to the easy realization of the preparation conditions. By varying these parameters including the ratio of reaction precursor ions, temperature, and immersing time, CuO NTs [58], nanobelts [59], NRs [76], ZnO NRs [77], and Cu<sub>2</sub>S NWs [83] could be directly grown on the Cu substrate. At 0.5C rate, CuO NRs delivered a high capacity of 650 mAh g<sup>-1</sup> with no capacity decay even after 100 cycles. Even at a high rate as high as 20C, Cu<sub>2</sub>S NWs were capable of delivering a reversible capacity of 145 mAh g<sup>-1</sup>.

Metal Ni is widely available in many forms, such as foil, grid, and felts, and is stable up to 4.5 V (versus Li/Li<sup>+</sup>), after which the electrodisolution of Ni begins [125]. Ni is commonly used as the current collector of anode materials. Fan et al. reported that freestanding Co<sub>3</sub>O<sub>4</sub> nanosheets on the Ni

foil substrate delivered a reversible capacity of 631 mAh g<sup>-1</sup> after 50 cycles at a constant current of 150 mA g<sup>-1</sup> in a fixed voltage window from 2.5 V to 0.01 V [87]. Wu et al. prepared interconnected MnO<sub>2</sub> NWs on the Ni foil substrate by electrodeposition, which delivered reversible capacity of 800 mAh g<sup>-1</sup> and with low capacity decay after 100 cycles [86]. Additionally, the oriented Ni<sub>3</sub>S<sub>2</sub> NWs arrays on the Ni grid substrate fabricated via the solution-based growth showed a reversible capacity of 430 mAh g<sup>-1</sup> with the capacity retention 80% over 100 cycles [60].

Fe is an inexpensive metal and cannot generate Li-Fe alloy at 0 V (versus Li/Li<sup>+</sup>) during polarization in the cathodic direction; thus, Fe-based alloy substrate could be exploited for loading the metal oxide anode materials to construct 3DSNAEs via the hydro-/solvothormal growth. By controlling the conditions of the hydro-/solvothormal growth, Liu and coworkers have prepared SnO<sub>2</sub> NRs [88], C/α-Fe<sub>2</sub>O<sub>3</sub> NTs [89], ZnO/C NRs [90], and SnO<sub>2</sub>/C NRs [126] directly grown on the Fe-base alloy substrate. The C/α-Fe<sub>2</sub>O<sub>3</sub> NTs retained a reversible capacity of as high as 659 mAh g<sup>-1</sup> at 0.2C rate after 150 cycles, and the pristine α-Fe<sub>2</sub>O<sub>3</sub> NTs maintained only 384 mAh g<sup>-1</sup> at the same conditions. Such good electrochemical performance may be attributed to the nanoscale intimate contact of α-Fe<sub>2</sub>O<sub>3</sub> with

TABLE 1: A summary of optimizing various electrode materials and suitable strategies to construct 3DSNAEs on various current collector substrates.

3DSANEs	Collector	Materials	Growth method	Remark
Cathode	Al	V <sub>2</sub> O <sub>5</sub> [69], LiCoO <sub>2</sub> [70]	Template-based chemical or physical deposition	Needing complicated synthesis techniques
	Sn-doped In <sub>2</sub> O <sub>3</sub> (ITO)	V <sub>2</sub> O <sub>5</sub> -TiO <sub>2</sub> [68], InVO <sub>4</sub> [71]	Chemical or physical deposition	
Anode	Cu	CNTs [72], Si [73], metal (Sn, Bi) [74, 75], MO (M = Fe, Cu, Zn, Ni) [65, 76–78], alloy (SnCo [79], NiSn [18, 80, 81], SiGe [82]), Cu <sub>2</sub> S [83], Cu <sub>3</sub> P [84], Sn/graphene [85]	Template-based chemical or physical deposition	It is a technique for large scale preparation
	Ni	Ni <sub>3</sub> S <sub>2</sub> [60], MnO <sub>2</sub> [86], Co <sub>3</sub> O <sub>4</sub> [87]	Solution-based growth	
	Fe-based alloy	MO (M = Sn, Fe, Zn) [88–90]	Electrodeposition, solution-based growth	
	Gold	SnO <sub>2</sub> [91], CNT-MnO <sub>2</sub> [92], SnCo [93]	Hydrothermal, solution-based growth	Needing complicated synthesis techniques
Cathode or anode	The stainless steel	CNTs [94], Ge [95], Si [37, 96–99], CNT-Si [100], Si/Cu [101], SnO <sub>2</sub> [47], ITO/TiO <sub>2</sub> [102], Ni/MnO <sub>2</sub> [103], Fe <sub>2</sub> O <sub>3</sub> /SnO <sub>2</sub> [104], V <sub>2</sub> O <sub>5</sub> /SnO <sub>2</sub> [44], CNTs-LiCoO <sub>2</sub> (LiMn <sub>2</sub> O <sub>4</sub> ) [105], CNTs-LiCoPO <sub>4</sub> [106, 107]	Template-based chemical or physical deposition	Needing high temperature
	Ti	V <sub>2</sub> O <sub>5</sub> [108], MO (M = Ti, Co, Fe, Sn) [49, 50, 62, 109]	Chemical/physical vapor deposition	
	Si	V <sub>2</sub> O <sub>5</sub> [45], Si [56], Si/NiO [110], MnO <sub>2</sub> [111], Cu <sub>2</sub> O [112], Sn [113]	Anodization, hydro/solvothermal, Solution-based growth	It is a hope for large scale preparation
			Chemical/physical deposition, etching	Needing complicated synthesis techniques

conductive carbon framework and the unique porous tubular nanostructures readily derived from sacrificial template-accelerated hydrolysis.

**3.3. Dual Functional Substrate.** Dual functional substrate, including SS, Ti, Ni, and Si, could act as cathode or anode substrate, owing to the superiorities such as a high oxidation voltage and non-Li-metal alloying process in a low voltage.

As an inert substrate, SS with a high oxidation voltage (5 V versus Li/Li<sup>+</sup>) has been widely used as the current collector for LIBs, because the Cr and Fe oxides on the surface protect the metal bulk from general corrosion. To the best of our knowledge, CVD and physical vapor deposition (PVD) are usually developed to construct 3DSNAEs on the SS substrate. Masarapu et al. found that aligned multiwall carbon nanotubes (MWNTs) on the SS substrate obtained by CVD technique delivered an initial capacity of 132 mAh g<sup>-1</sup> at 1C rate and a reversible capacity of 460 mAh g<sup>-1</sup> after 1200 cycles, attributing to the morphology of the MWNTs with structural and surface defects and the SS substrate's contribution to capacity [94]. Chan and coworkers prepared a series of Si-based nanoarchitected arrays on the SS substrate by using CVD [37, 72, 95, 97] and found that Si NWs exhibited a stable capacity ~3500 mAh g<sup>-1</sup> for 20 cycles. Besides, Yan et al. used multistep CVD to construct V<sub>2</sub>O<sub>5</sub>/SnO<sub>2</sub> NWs with high power density of 60 kW kg<sup>-1</sup> and energy density of as high as 282 Wh kg<sup>-1</sup> [44]. Such excellent performance might be ascribed to the unique

core/shell structure that the thin V<sub>2</sub>O<sub>5</sub> layer was in favor of the fast Li<sup>+</sup> lithiation/delithiation, and the SnO<sub>2</sub> core offered a fast path for electron transportation and also increased the utilization of V<sub>2</sub>O<sub>5</sub>. By employing PVD technique, the vertical Si nanopillars arrays and single-crystal SnO<sub>2</sub> NWs on the SS substrate were also fabricated by Fleischauer et al. [46] and Ko et al. [47]. The SnO<sub>2</sub> NWs delivered a high discharge capacity of 510 mAh g<sup>-1</sup> after 50 cycles at 1C rate and displayed superior rate capability of 440 mAh g<sup>-1</sup> at 10C rate.

Metal Ti is very resistive to the alkaline ammonia solution and oxidation, does not alloy with lithium at low voltage, and therefore is a good current collector material for LIBs [127]. V<sub>2</sub>O<sub>5</sub> nanobelt arrays on the Ti substrate prepared via hydrothermal growth could deliver a reversible capacity of 240 mAh g<sup>-1</sup> stably after 50 cycles at the current density of 400 mA g<sup>-1</sup>, and a high rate capacity of 150 mAh g<sup>-1</sup> at 4000 mA g<sup>-1</sup> [108]. And the mesoporous Co<sub>3</sub>O<sub>4</sub> NWs arrays on the Ti substrate via solution-based growth exhibited a high reversible capacity of 859 mAh g<sup>-1</sup> at the current density of 111 mA g<sup>-1</sup> and high rate capacities of 450 mAh g<sup>-1</sup> at 2220 mA g<sup>-1</sup> and 240 mAh g<sup>-1</sup> at 5550 mA g<sup>-1</sup> [54]. Whilst directly anodizing and annealing Ti foil, the self-organized TiO<sub>2</sub> NTs on the Ti substrate could be obtained. Ortiz et al. found that the amorphous TiO<sub>2</sub> NTs delivered a highest capacity of 77 μAh cm<sup>-2</sup>, and crystalline TiO<sub>2</sub> NTs had the best capacity retention up to 90% over 50 cycles [62]. Wei et al. reported that the TiO<sub>2</sub> NTs with 50 nm pore size and 20 nm thickness showed the highest reversible capacity of

180 mAh g<sup>-1</sup> over 140 cycles [128]. Liu and coworkers found that TiO<sub>2</sub> NTs annealed at N<sub>2</sub> possessed an initial discharge capacity of 163 mAh g<sup>-1</sup> and maintained 145 mAh g<sup>-1</sup> over 50 cycles and that TiO<sub>2</sub> NTs annealed at CO exhibited an initial capacity of 223 mAh g<sup>-1</sup> with the reversible capacity of 179 mAh g<sup>-1</sup> at the 50th cycle [129, 130]. The results might be attributed to the presence of surface defects like Ti-C species and Ti<sup>3+</sup> groups with oxygen vacancies, improving the charge-transfer conductivity of the arrays and promoting phase transition.

Although Si could form Li-Si alloy at ca. 0.12 V (versus Li/Li<sup>+</sup>), crystalline Si cores of core-shell crystal-amorphous Si NWs functioned as not active material store but a stable mechanical support [97]. Therefore, the Si substrate can act as a dual functional substrate for loading cathode or anode materials to construct 3DSNAEs. Chan et al. prepared single-crystal V<sub>2</sub>O<sub>5</sub> nanoribbons via thermal vapor deposition and found that transformation of V<sub>2</sub>O<sub>5</sub> into the ω-Li<sub>3</sub>V<sub>2</sub>O<sub>5</sub> phase could take place within 10 s in thin nanoribbons, suggesting a significant increase in battery power density [45]. Liu and coworkers found that MnO<sub>2</sub>·0.5H<sub>2</sub>O nanowall arrays electrodeposited on the Si substrate exhibited a reversible capacity of 220 mAh g<sup>-1</sup> over 50 cycles at 0.5C rate and mesoporous MnO<sub>2</sub>·0.5H<sub>2</sub>O nanowall arrays with 500 nm thickness delivered a stable capacity of 256 mAh g<sup>-1</sup> [111, 131]. Such excellent electrochemical performance might be ascribed to the hierarchically structured macro- and mesoporosity of MnO<sub>2</sub>·0.5H<sub>2</sub>O, which offered a large surface area to volume ratio of favoring interface faradic reactions and shortened solid-state diffusion paths. Moreover, Kim et al. prepared vertical arrays of Sn NWs on the Si substrate via AAO template-based electrodeposition [113], which showed the discharge capacity of 400 mAh g<sup>-1</sup> after 15 cycles at the current density of 4200 mA g<sup>-1</sup>.

## 4. Structural Configuration

As electrodes materials of LIBs, nanomaterials could enhance charge/discharge kinetics and improve high Li storage capacity, despite of suffering from low thermodynamic stability and surface side-reactions. Optimizing and designing proper nanoarchitected arrays to take advantages and restrain disadvantages of electrodes materials are, therefore, of particular importance to the electrochemical properties of 3DSNAEs. Types of the 3DSNAEs structure reviewed here contain homogeneous nanoarchitected arrays and heterogeneous nanoarchitected arrays (Figure 4).

**4.1. Homogenous Nanoarchitected Arrays.** Homogenous nanoarchitected arrays, namely, single-component nanostructure arrays, mainly include simple nanostructure arrays, nanostructure cluster arrays, and nanostructure gearlike arrays on the basis of the structure characteristic of nanoarchitected arrays. For this category, nanostructure arrays directly connected to the conductive substrate are used as both the structural support and electroactive materials to alleviate large strain without pulverization and provide good electronic contact and conduction. Electroactive materials

of nanoarchitected arrays, therefore, are considerably rigorous and should possess the merits including a degree of conductivity and easy growth controll.

Simple nanostructure arrays are commonly composed of single-phase 1D NWs, NTs, and NRs arrays directly connected to the conductive substrate. Up to now, the 1D array materials such as V<sub>2</sub>O<sub>5</sub> nanobelts [108], multiwall carbon nanotubes (MWCNTs) [72, 94], Si NWs [132], Ge NWs [95], Sn NWs [113], SnO<sub>2</sub> NRs [88], and MnO<sub>2</sub> NWs [86] have been developed to act as the 3DSNAEs with rate capability and cycling stability. V<sub>2</sub>O<sub>5</sub> nanobelts directly grown on a Ti substrate based on the hydrogen bonding action delivered high reversible capacity of 650 and 520 mAh g<sup>-1</sup> after 50 cycles at the current density of 1.2 and 3 A g<sup>-1</sup>, respectively. MWCNTs directly grown on a Cu current collector (MWCNT-on-Cu) in Figure 5 were synthesized by a two-step process of catalyst deposition and CVD and showed a high reversible capacity of 900 mAh g<sup>-1</sup> after 50 cycles at 1C rate. Excellent electrochemical properties of MWCNT-on-Cu structure could be ascribed to high Li ion intercalation on the carbon nanotube walls, strongly bonding with the Cu substrate and good conductivity.

Nanostructure cluster arrays, generally, consist of clusters of assembled NWs, NRs, and nanosheets. Because NWs, NRs and nanosheets are usually inclined to aggregate and form the nanostructure clusters due to their structural instability. Some nanostructure cluster arrays, recently, including network-like and flower-like CuO [133, 134], CuO MNCAs [64], and CuO pine-needle-like (PNL) arrays (see Figure 6) [135], have been used as the 3DSNAEs with enhanced lithium storage properties. CuO MNCAs synthesized by our group exhibited a high reversible capacity of 639.8 mAh g<sup>-1</sup> after 100 cycles at 1C rate and a high-rate capability of 548.8 mAh g<sup>-1</sup> at 10C rate. CuO PNL arrays fabricated by our group via an anodic route delivered high rate capacity of 545.9 and 492.2 mAh g<sup>-1</sup> at 15C and 20C rates and exhibited excellent cyclability of 583.1 mAh g<sup>-1</sup> after 100 cycles at 2C rate. The enhanced lithium storage properties could be ascribed to the unique nanostructure cluster arrays, which provide suitable branches for lithium storage and suitable free space to facilitate Li<sup>+</sup> flux across the interface as well as accommodating the large volume variation.

Nanostructure gearlike arrays. In this respect, the size of arrays directly connect to the substrate is mainly microscale, which is stable and easy to controlled synthesis by a simple approach. Furthermore, microarrays are ordinarily assembled by a mass of nanosheets, NWs, or NBs with the same component, in favor of enlarging the contact areas between active materials and electrolyte. The microscale coglike CuO fabricated by the microemulsion-mediated method exhibited a high reversible capacity of 583 mAh g<sup>-1</sup> at a rate of 4C [136]. In our work, CuO HMNGPAs [63] shown in Figure 7 have been synthesized via a novel vapor-phase corrosion strategy and exhibited excellent cycling stability of 651.6 mAh g<sup>-1</sup> after 100 cycles at 0.5C rate and high-rate capability of 561.6 mAh g<sup>-1</sup> at 10C rate, because the unique HMNGPAs consisting of numerous gearlike pillars assembled by nanosheets could take full advantage of both micro and nano, namely, micropillars with structural

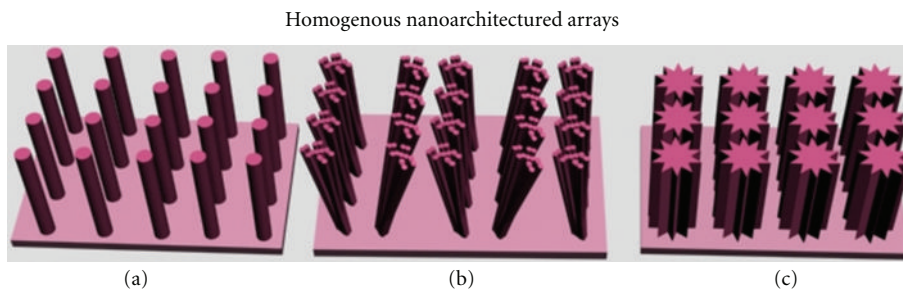


FIGURE 4: Schematic of homogenous nanoarchitected arrays. (a) Simple nanostructure arrays, (b) nanostructure cluster arrays, and (c) nanostructure gearlike arrays.

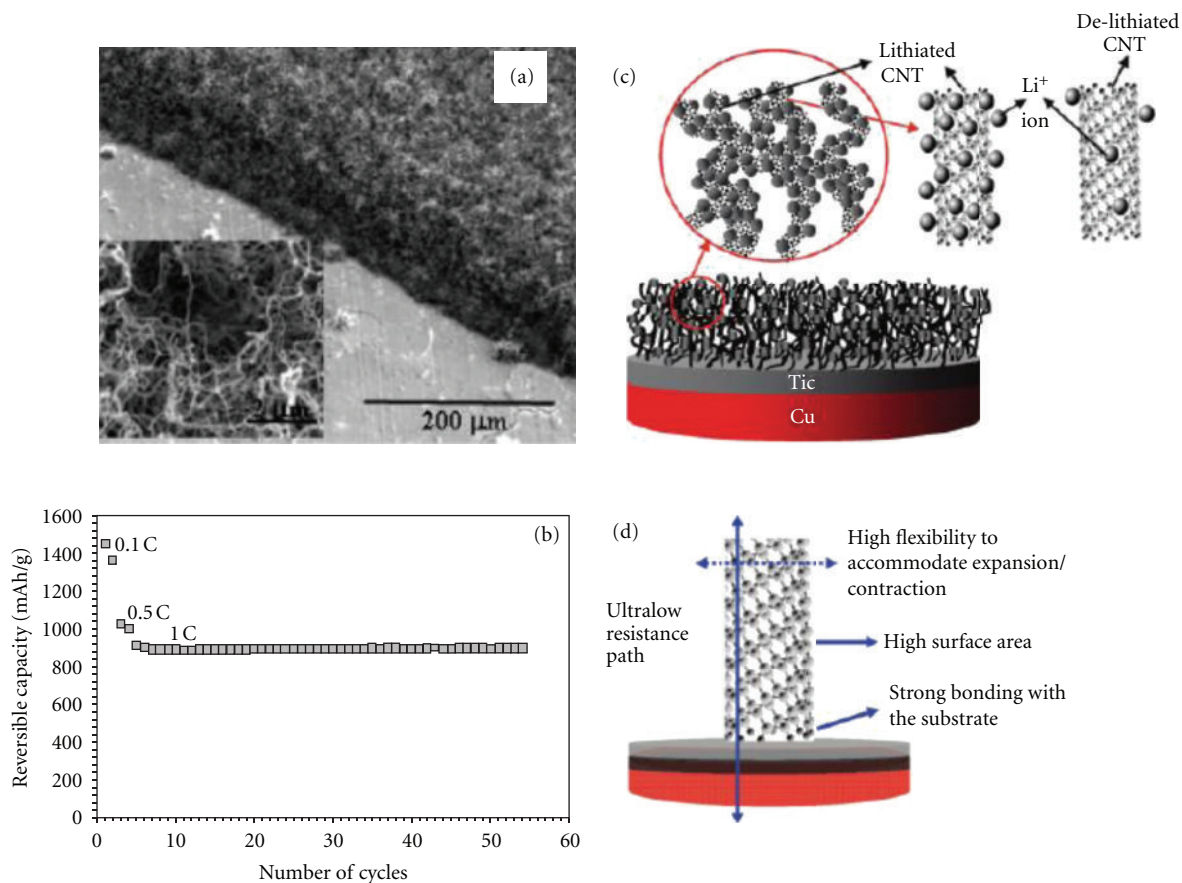


FIGURE 5: (a) SEM images of the as-grown MWCNT-on-Cu structure. (b) Exceptional stability of the reversible capacity of the MWCNT-on-Cu anode in long-run, at 1C rate. (c) A schematic of the proposed lithiation/delithiation mechanism. (d) A schematic of the proposed anode structure [72].

stability and mesoporous nanosheets with high lithium-storage sites.

**4.2. Heterogeneous Nanoarchitected Arrays.** Heterogeneous nanoarchitected array are hybrid nanostructure arrays with multicomponents each tailored to satisfy different demands such as high energy density, high conductivity, and excellent mechanical stability. On the basis of the structural characteristic, heterogeneous nanoarchitected arrays could be classified to six types, including (a) simple heterogeneous nanostructure arrays, (b) coaxial or core/shell heterogeneous

nanostructure arrays, (c) semicoated grenadelike heterogeneous nanostructure arrays, (d) dispersed heterogeneous nanostructure arrays, (e) branched heterogeneous nanostructure arrays, and (h) folded heterogeneous nanostructure arrays (Figure 8).

**4.2.1. Simple Heterogeneous Nanostructure Arrays.** Generally, this kind of structure is composed of 1D array structures with two or more components used as active materials, on the basis of the dual lithium insertion/desertion mechanism.  $\text{V}_2\text{O}_5\text{-TiO}_2$  NRs arrays with molar ratio

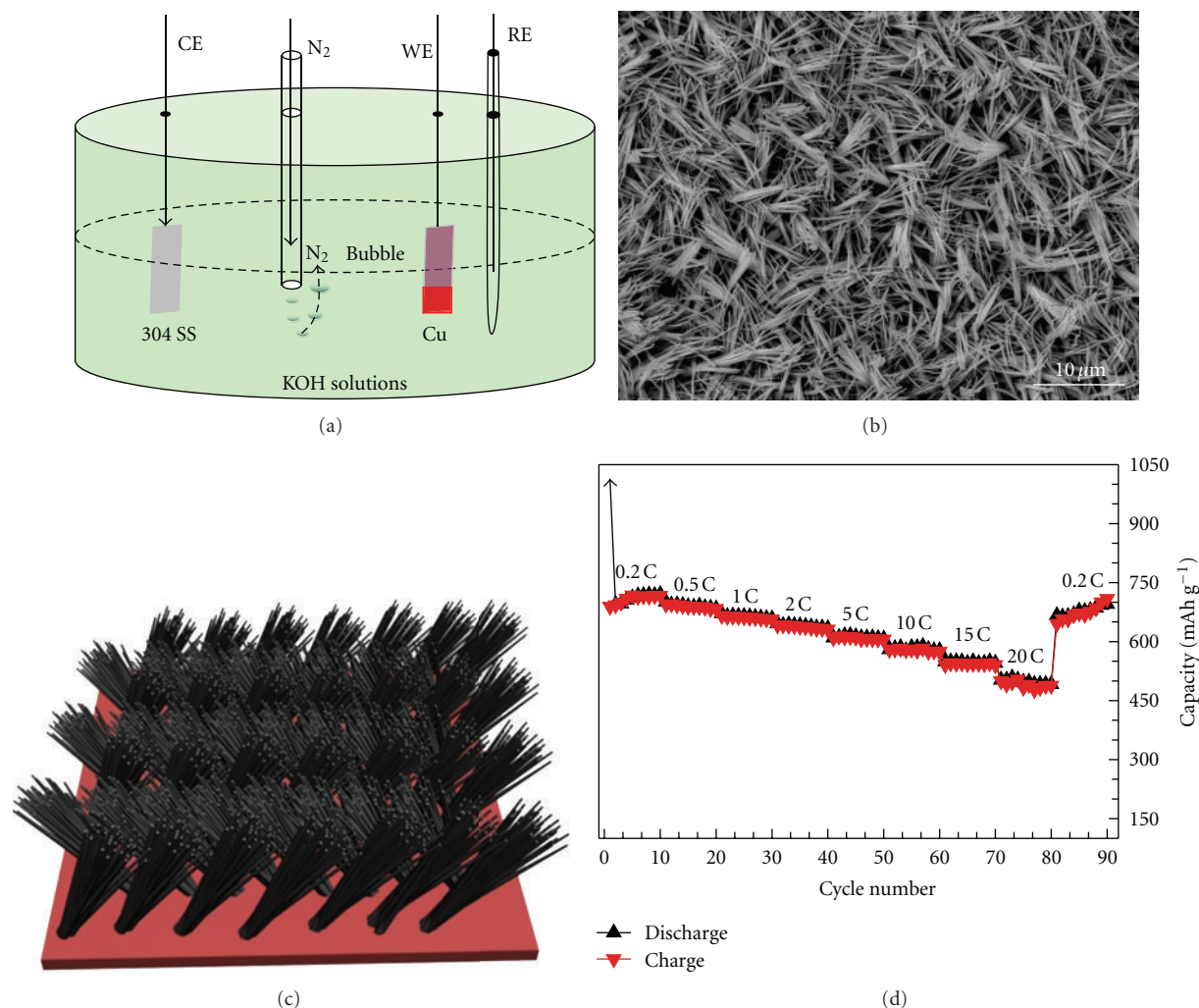


FIGURE 6: (a) A schematic of the cell used for the preparation of  $\text{Cu}(\text{OH})_2$  PNL arrays, wherein CE, WE, and RE represent the counter, working, and reference electrode, respectively. SEM image (b), structural schematic (c), and rate cyclability (d) of  $\text{CuO}$  PNL arrays gained by annealing  $\text{Cu}(\text{OH})_2$  PNL arrays [135].

V/Ti = 75/25 prepared by Takahashi et al. could deliver 1.5 times discharge capacity of  $\text{V}_2\text{O}_5$  NRs at the current density of  $92 \text{ mA g}^{-1}$ , resulting from the change of crystallinity and interaction forces between adjacent layers in  $\text{V}_2\text{O}_5$  [68].  $\text{SnO}_2/\alpha\text{-Fe}_2\text{O}_3$  NTs arrays fabricated by Zeng et al. showed high areal capacities of  $1.289 \text{ mAh cm}^{-2}$  at a current rate of  $0.1 \text{ mA cm}^{-2}$ , possibly due to the synergistic lithium storage of  $\text{SnO}_2$  and  $\alpha\text{-Fe}_2\text{O}_3$  electroactive materials [137].

**4.2.2. Coaxial or Core/Shell Heterogeneous Nanostructure Arrays.** In this case, the coaxial or core/shell structures refer to 1D array inner cores coated completely by other materials as shells. The functions of 1D array inner cores and shells can be both the structural support and electroactive materials on the basis of the particularity of 1D array directly connected to the conductive substrate.

While the 1D array inner cores are only used as the structural support, the outer shells are used as the electroactive materials, and the unique structured materials containing

Al NRs- $\text{LiCoO}_2$  (see Figure 9) [70], Cu NRs- $\text{Fe}_3\text{O}_4$  [65], Cu-Si nanocable [138], Cu- $\text{Si}_{1-x}\text{Ge}_x$  NWs [82], hybrid ITO/ $\text{TiO}_2$  [102], and Ni/Si NWs [139] exhibit a super high-rate performance. For example, the Cu-Si nanocable exhibited a specific capacity as high as  $1890 \text{ mAh g}^{-1}$  under a current density of  $0.3 \text{ A g}^{-1}$  and  $1660 \text{ mAh g}^{-1}$  under a current density of  $1.4 \text{ A g}^{-1}$ . Hybrid ITO/ $\text{TiO}_2$  demonstrated an extremely low average capacity fading  $\sim 0.1\%$  per cycle for 1000 cycles at a current density of 60C. The previous excellent lithium storage properties could be related to the unique Al, Cu, ITO, and Ni 1D nanostructures directly connected to the conductive substrate, which act as inner cores of electroactive materials and form the 3D conductive network of the current collectors, providing both efficient pathways for ion and electron transport, improving the energy density per unit area.

The other strategy is that the 1D array inner cores act as the active materials and the shell as conductive agents (amorphous carbon). The semiconductor metal oxides have been usually constructed to the core/shell  $\text{Fe}_2\text{O}_3/\text{C}$  NTs and

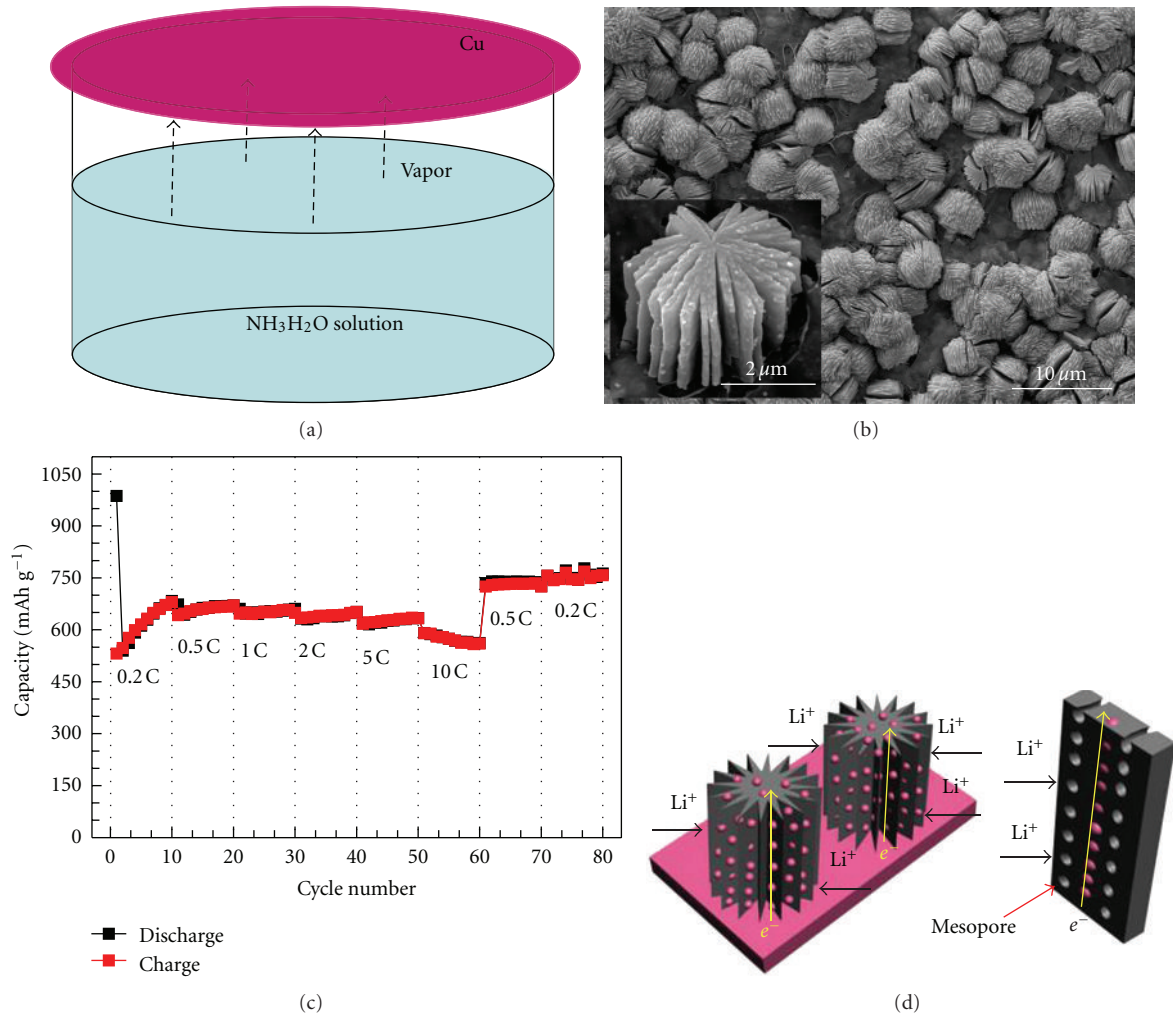


FIGURE 7: (a) Schematic device of the ammonia vapor-phase corrosion route. SEM images (b), rate cyclability (c), and a schematic diagram of discharge-charge (d) of CuO HMNGPAs [63].

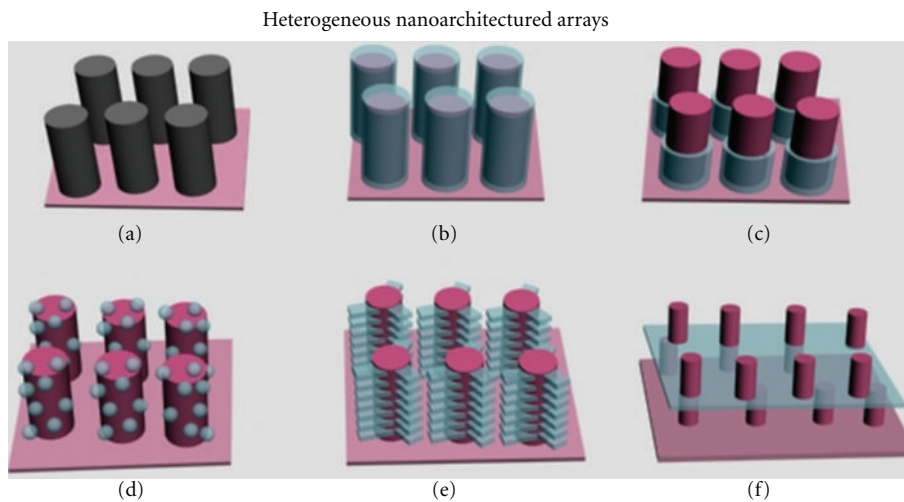


FIGURE 8: Schematic of heterogeneous nanoarchitected arrays based on structural complexity. (a) Simple heterogeneous nanostructure arrays, (b) coaxial or core/shell heterogeneous nanostructure arrays, (c) semicoated grenadelike heterogeneous nanostructure arrays, (d) dispersed heterogeneous nanostructure arrays, (e) branched heterogeneous nanostructure arrays, and (f) folded heterogeneous nanostructure arrays.

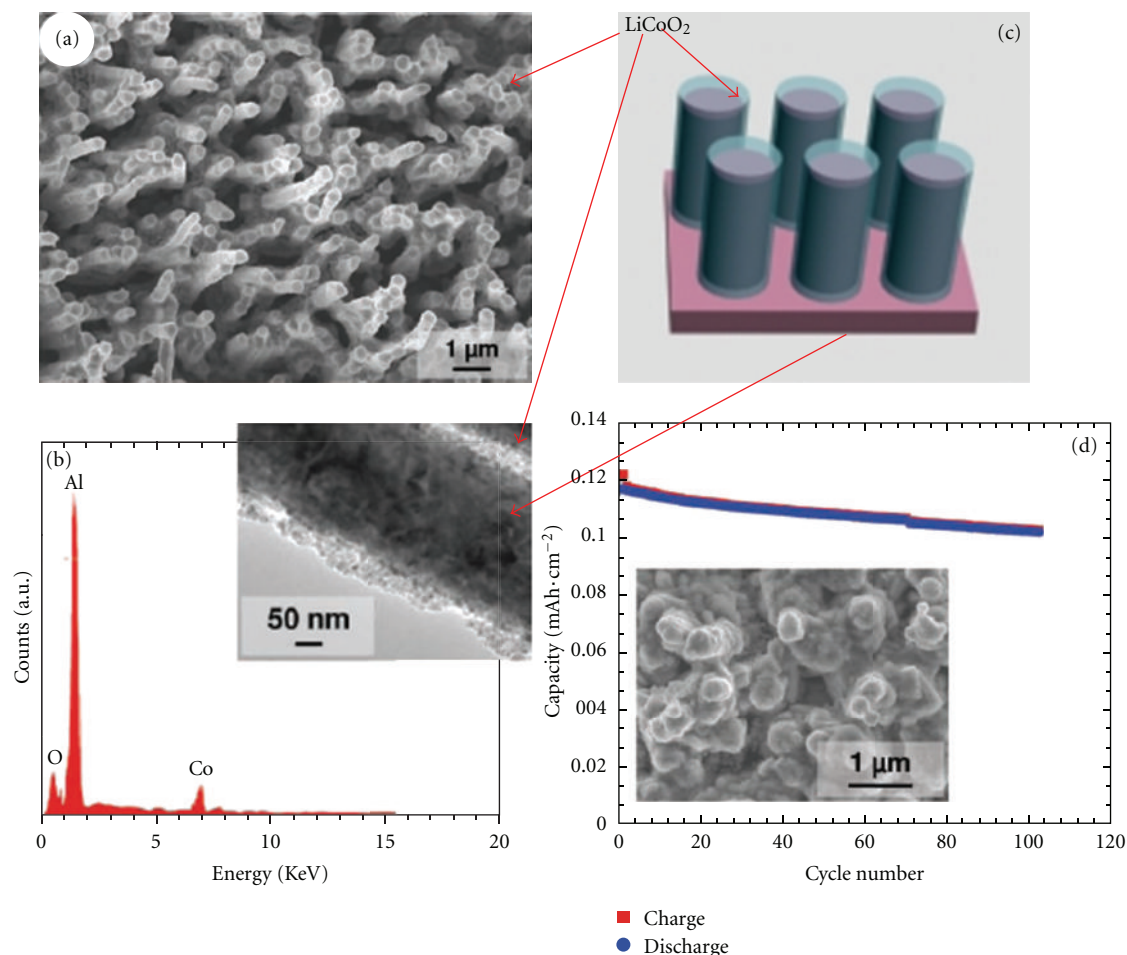


FIGURE 9: SEM images (a), EDX pattern (b), structural schematic (c), and cycling performance (d) of Al NRs-LiCoO<sub>2</sub>. Insert of (b) shows a TEM image of Al NRs-LiCoO<sub>2</sub>, and insert of (d) shows an SEM image of Al NRs-LiCoO<sub>2</sub> 3D electrode cycled 50 times at 0.2C rate [70].

NRs [50, 89], ZnO/C [90], and SnO<sub>2</sub>/C NRs [126] arrays, wherein metal oxides functioned as both the active core and the structural skeleton, and the carbon shells (nano-Cu) are used to improve the conductivity of materials and suppress the volume expansion. SnO<sub>2</sub>/C NRs prepared by a two-step hydrothermal method exhibited a high reversible capacity of 585 mAh g<sup>-1</sup> after 50 cycles at 500 mA g<sup>-1</sup>. Furthermore, a new copper-coating layer has better conductivity than carbon and can suppress electrolyte decomposition on the surface of 1D array. Chen et al. found the copper-coated Si NWs showed an initial Coulombic efficiency of 90.3% at a current density of 210 mA g<sup>-1</sup> [101].

The third way is that the inner cores and shells are both the active materials to construct the coaxial SnO<sub>2</sub> NWs/CNTs [91], hybrid MnO<sub>2</sub>/CNTs [92], and C-Si NTs sponge [140]. Hybrid MnO<sub>2</sub>/CNTs delivered the first discharge capacity of 2170 mAh g<sup>-1</sup> and a reversible capacity of ~500 mAh g<sup>-1</sup> after 15 cycles. This kind of material showed the good charge/discharge performance, due to the dual lithium storage mechanism of insertion/desertion, in which CNTs acted as a highly conductive backbone to accommodate the volume expansion and avoid agglomeration.

**4.2.3. Semicoated Grenadelike Heterogeneous Nanostructure Arrays.** The grenadelike structure is analogous to the core/shell structure and composed of inner cores and outer shells. The difference, however, is that the outer shell of grenadelike structures is semicoated. Generally, the inner core is the major component with functional properties, while the outer shell acts as the structural support. Ortiz et al. prepared NWs SnO/NTs TiO<sub>2</sub> [141] and NWs Fe<sub>2</sub>O<sub>3</sub>/NTs TiO<sub>2</sub> (see Figure 10) [142] in the matrix of TiO<sub>2</sub> NTs by anodization and electrodeposition. At the current density of 50 μA cm<sup>-2</sup>, NWs SnO/NTs TiO<sub>2</sub> exhibited a remarkable reversible capacity of about 140 μAh cm<sup>-2</sup> with the capacity retention of ca. 85% over 50 cycles. The enhanced electrochemical performance could be ascribed to the TiO<sub>2</sub> NTs matrix that allows the volume expansion during the Li<sup>+</sup> insertion and desertion process.

**4.2.4. Dispersed Heterogeneous Nanostructure Arrays.** In this dispersed structure, nanomaterials are commonly anchored on the surface of 1D array to be used as the electroactive components or the conductive network for facile electrons transport. While the 1D array (CNTs and Si NWs)

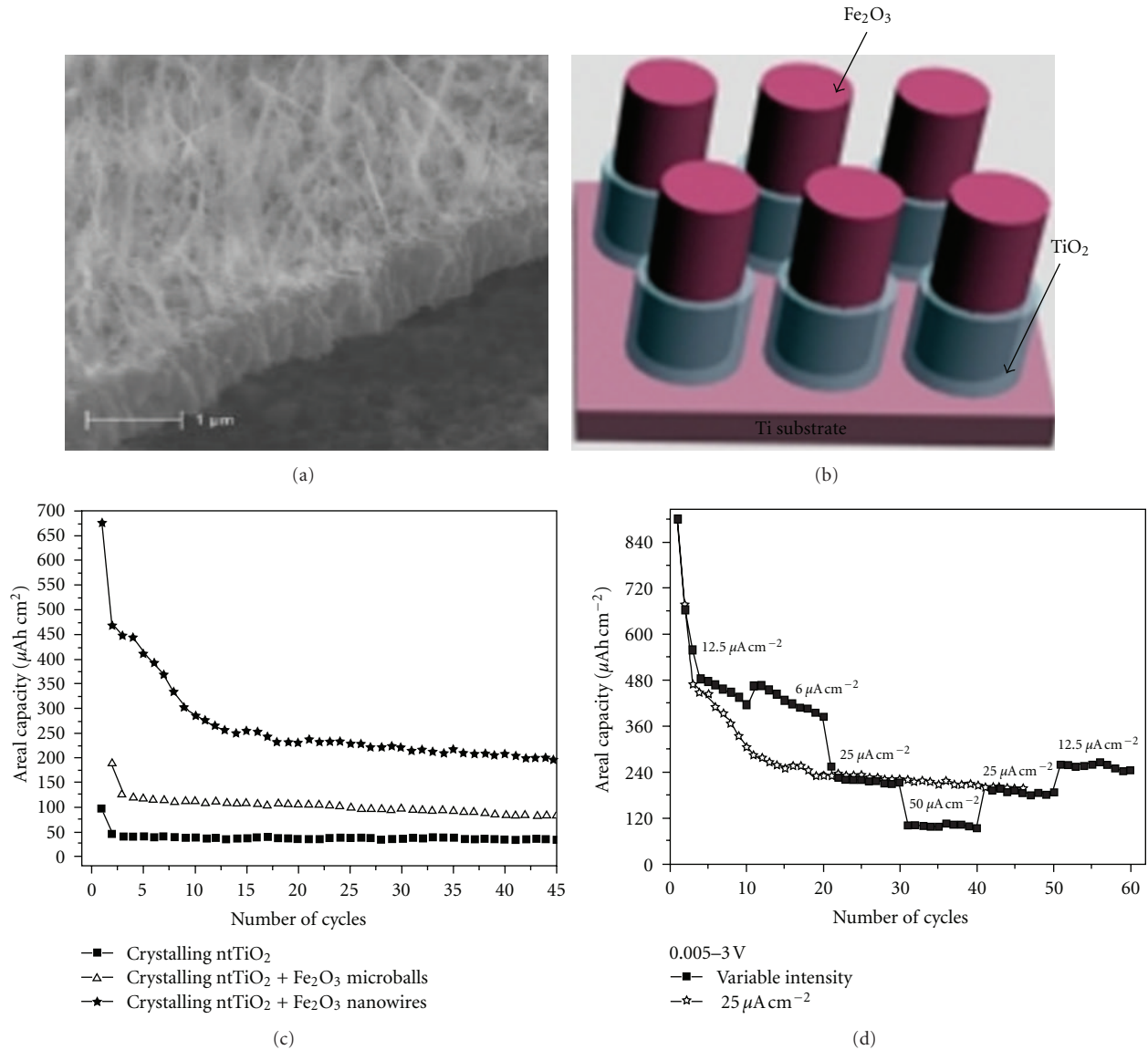


FIGURE 10: SEM images (a) and structural schematic (b) of nanocomposite NWs Fe<sub>2</sub>O<sub>3</sub>/NTs TiO<sub>2</sub>, cycling life (c), and rate performance (d) of nanocomposite electrodes [142].

functioned as the electrical conducting pathway and the stable mechanical support for strain release, the anchored nanomaterials including LiCoO<sub>2</sub> (LiMn<sub>2</sub>O<sub>4</sub>) [105], LiCoPO<sub>4</sub> [106, 107], and NiO NWs [110] acted as the electroactive components. The binder-free LiCoO<sub>2</sub>-3 wt% SAC-NTs composites could deliver high reversible capacities of 145.7 mAh g<sup>-1</sup> at 0.1C rate and 130.4 mAh g<sup>-1</sup> at 2C rate. The ordered NiO-coated Si NWs arrays showed a reversible capacity of 606.13 mAh g<sup>-1</sup> at the rate of 50 mA g<sup>-1</sup> after 30 cycles. While the dispersed nanomaterials (Ag nanoparticles) are mainly applied to improve the conductive and utilization of the active materials, the Co<sub>3</sub>O<sub>4</sub>-Ag NWs arrays exhibited more than 82% capacity retention at the current density of 2000 mA g<sup>-1</sup> after 20 cycles, in comparison with 74% capacity retention of the pristine Co<sub>3</sub>O<sub>4</sub> arrays [143]. When 1D array and dispersed nanomaterials are both used as

electroactive materials, these structural materials of VA CNTs-Si [100, 144–146] showed high rate capacities of lithium storage. For instance, VA-CNTs/Si arrays shown in Figure 11 via a two-step CVD technique exhibited high discharge capacities of 2980, 1890, and 765 mAh g<sup>-1</sup> at 1.3C, 5C and 15C rate, respectively.

**4.2.5. Branched Heterogeneous Nanostructure Arrays.** Being similar to core-shell structure, branched heterogeneous nanostructure arrays, generally, consist of an inner core and outer shell with a branched structure and possess both all desired functions of each component and a strong synergistic enhancement. More specifically, the inner core provides a direct pathway for electron transport, while the outer shell maintains the structural stability of the inner core during the discharge-charge process. The core-shell Ni/MnO<sub>2</sub> hybrid

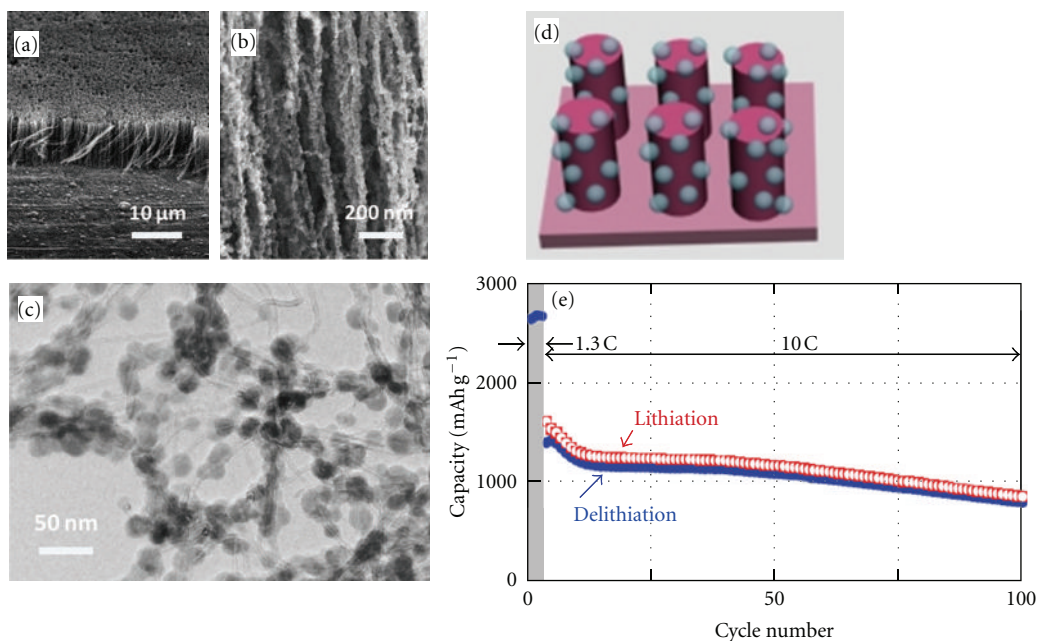


FIGURE 11: SEM (a, b), TEM (c) images, structural schematic (d), and cycling performance (e) of the as-prepared VA-CNTs/Si arrays on the Si substrate [146].

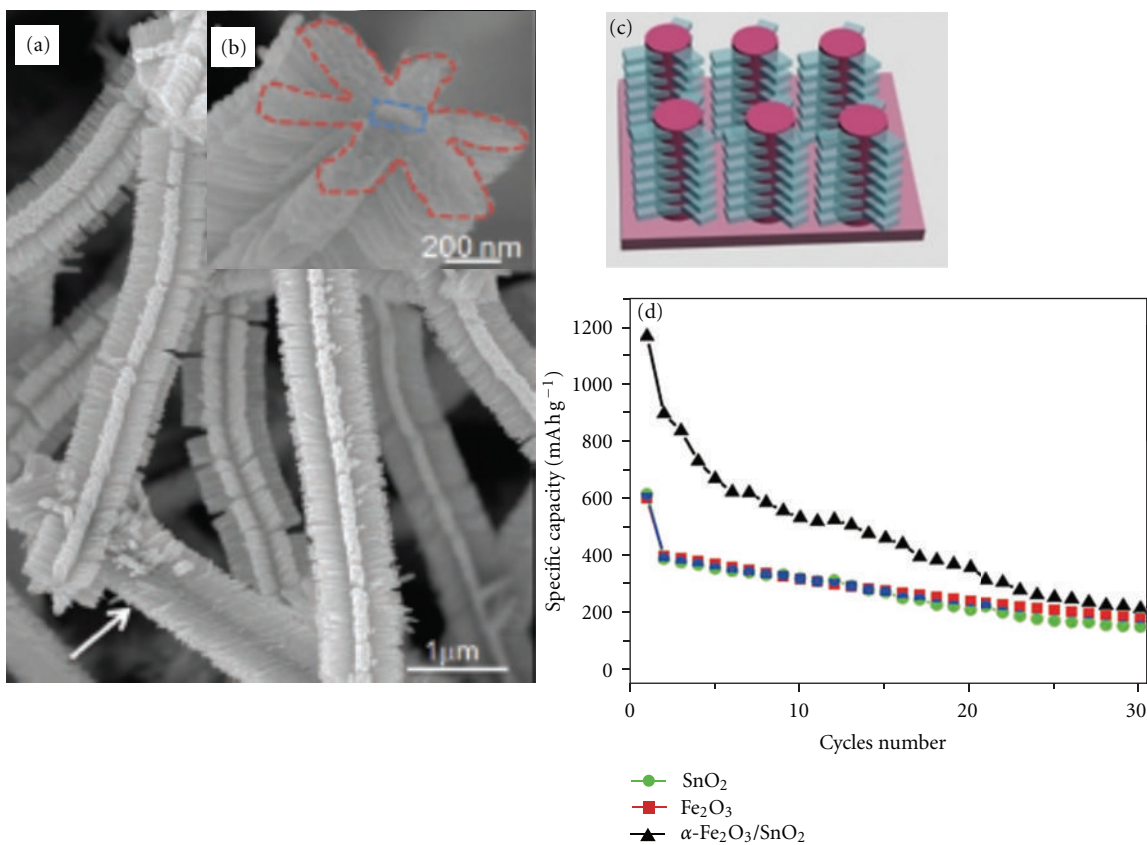


FIGURE 12: SEM images (a, b) and structural schematic (c) of branched  $\alpha$ -Fe<sub>2</sub>O<sub>3</sub>/SnO<sub>2</sub> nanostructures, (d) cycling performance of  $\alpha$ -Fe<sub>2</sub>O<sub>3</sub>/NRs arrays, pristine SnO<sub>2</sub> NWs, and  $\alpha$ -Fe<sub>2</sub>O<sub>3</sub>/SnO<sub>2</sub> nanostructures at a rate of 1 A g<sup>-1</sup> [104].

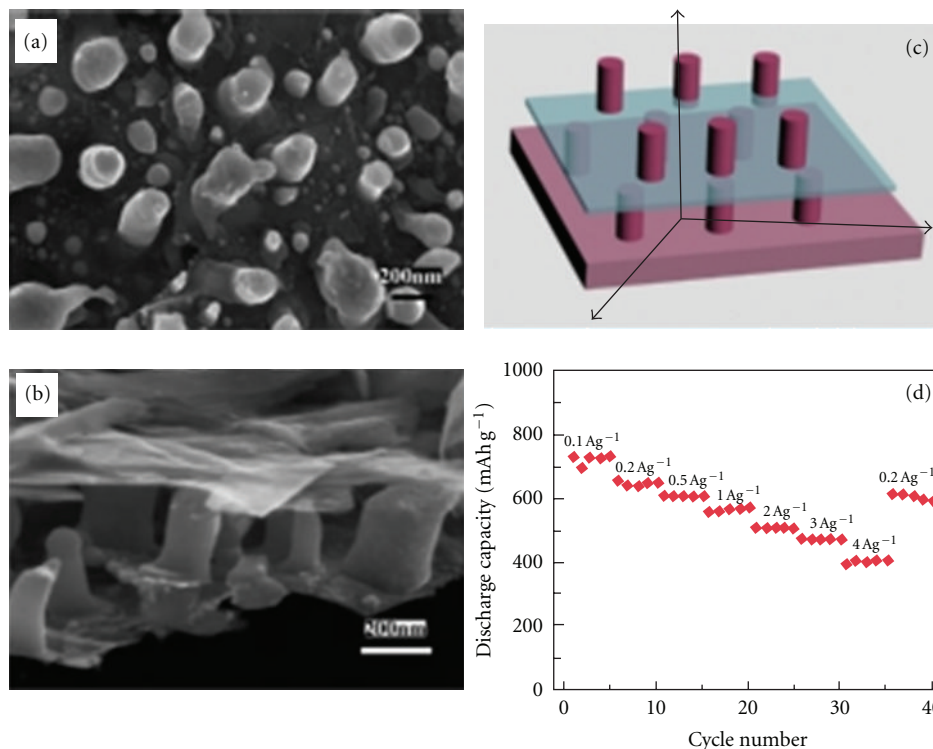


FIGURE 13: SEM images (a, b), structural schematic (c), and rate cyclability (d) of the graphene/Sn-nanopillar nanostructures [85].

[103] fabricated by Jiang et al. via a hydrothermal method delivered reversible capacities of 690, 572, and 445 mAh g<sup>-1</sup> at the current density of 1478, 2958, and 5804 mA g<sup>-1</sup>, respectively. Zhou et al. reported that the branched  $\alpha$ -Fe<sub>2</sub>O<sub>3</sub>/SnO<sub>2</sub> [104] (see Figure 12) prepared by combining a vapor transport deposition and a facile hydrothermal method showed a remarkably improved initial discharge capacity of 1167 mAh g<sup>-1</sup>, which was about twice the SnO<sub>2</sub> NWs (612 mAh g<sup>-1</sup>), and  $\alpha$ -Fe<sub>2</sub>O<sub>3</sub> NRs (598 mAh g<sup>-1</sup>). The higher capacity of the branched  $\alpha$ -Fe<sub>2</sub>O<sub>3</sub>/SnO<sub>2</sub> is due to that  $\alpha$ -Fe<sub>2</sub>O<sub>3</sub> branches provide new Li<sup>+</sup> hosts, increase the reversible capacity, and suppress the degradation of the core SnO<sub>2</sub>.

**4.2.6. Folded Heterogeneous Nanostructure Arrays.** Even though complicated, the folded heterogeneous nanostructure arrays are ordinarily composed of multilayered 1D nanostructure arrays embedded between 2D sheets, offering the morphological flexibility to hamper the structural collapse and efficient transport of both Li<sup>+</sup> and electrons and leading to the excellent electrochemical performance [147]. Ji et al. reported that a multilayered graphene/Sn-nanopillar nanostructure (Figure 13), by using the self-assembly and annealing processes, retained a reversible capacity of 501 and 408 mAh g<sup>-1</sup> at a current density of 1 and 5 A g<sup>-1</sup> after 35 cycles, respectively, which could be attributed to that both graphene and Sn served as electroactive materials, electronic conductive materials, and mechanically supporting materials [85].

## 5. Conclusions and Outlook

In conclusion, the recent advances in the design, fabrication, and properties of 3DSNAEs with homogeneous or heterogeneous nanoarchitected structures for LIBs have been reviewed in detail here. Table 1 illustrates an evaluation of optimizing various electrode materials and suitable strategies to construct 3DSNAEs on various current collector substrates. From an industrial perspective, solution-based growth at low temperature and hydrothermal methods are considered to be most promising for constructing 3DSNAEs with proper electrode materials and proper electrode structures.

Evidently, the nanostructure arrays of 3DSNAEs connected to the conductive collector substrate become mechanically unstable when they are grown excessively long in the axial direction. Besides, the electrochemical performance of 3DSNAEs strongly depends on the physical/chemical properties of interface within the heterogeneous nanoarchitected structures. Systematic/synergetic combining of the mechanical integrity and electrochemical kinetic properties of 3DSNAEs, therefore, will be required to the development of high-performance LIBs.

It can be seen that a large amount of research has been made in designing homogeneous or heterogeneous nanoarchitected arrays in 3DSNAEs. On one hand, the hybrid structures among 1D NWs, NRs, and 2D nanosheets increase the specific energy density (especially the area and volumetric energy densities) of electrodes, by making full use of voids within the electrodes, and function simultaneously

as “stabilizers” and “buffers” to the 3DSNAEs with excellent cycling stability. On the other, the heterogeneous components concept opens a promising avenue for designing multifunctional 3DSNAEs by integrating the superiorities of each constituent. Therefore, designing the multifunctional 3DSNAEs with synergic properties by selecting suitable electrode materials and suitable structures is a bright way to address different requirements (high energy density, high conductivity, good mechanical stability, etc.) of superperformance LIBs applied in portable electronic consumer devices, electric vehicles, and large-scale electricity storage.

## References

- [1] A. S. Aricò, P. Bruce, B. Scrosati, J. M. Tarascon, and W. Van Schalkwijk, “Nanostructured materials for advanced energy conversion and storage devices,” *Nature Materials*, vol. 4, no. 5, pp. 366–377, 2005.
- [2] M. Armand and J. M. Tarascon, “Building better batteries,” *Nature*, vol. 451, no. 7179, pp. 652–657, 2008.
- [3] J. B. Goodenough and Y. Kim, “Challenges for rechargeable Li batteries,” *Chemistry of Materials*, vol. 22, pp. 587–603, 2009.
- [4] J. M. Tarascon and M. Armand, “Issues and challenges facing rechargeable lithium batteries,” *Nature*, vol. 414, no. 6861, pp. 359–367, 2001.
- [5] Annual Energy Outlook, 2010, <http://www.eia.gov/ieo>.
- [6] F. Cheng, J. Liang, Z. Tao, and J. Chen, “Functional materials for rechargeable batteries,” *Advanced Materials*, vol. 23, no. 15, pp. 1695–1715, 2011.
- [7] G. Jeong, Y. U. Kim, H. Kim, Y. J. Kim, and H. J. Sohn, “Prospective materials and applications for Li secondary batteries,” *Energy and Environmental Science*, vol. 4, no. 6, pp. 1986–2002, 2011.
- [8] M. S. Whittingham, “Lithium batteries and cathode materials,” *Chemical Reviews*, vol. 104, no. 10, pp. 4271–4301, 2004.
- [9] M. Okubo, E. Hosono, J. Kim et al., “Nanosize effect on high-rate Li-ion intercalation in  $\text{LiCoO}_2$  electrode,” *Journal of the American Chemical Society*, vol. 129, no. 23, pp. 7444–7452, 2007.
- [10] E. Hosono, T. Kudo, I. Honma, H. Matsuda, and H. Zhou, “Synthesis of single crystalline spinel  $\text{LiMn}_2\text{O}_4$  nanowires for a lithium ion battery with high power density,” *Nano Letters*, vol. 9, no. 3, pp. 1045–1051, 2009.
- [11] C. S. Johnson, N. Li, C. Lefief, J. T. Vaughey, and M. M. Thackeray, “Synthesis, characterization and electrochemistry of lithium battery electrodes:  $\text{XLi}_2\text{MnO}_{3-(1-x)}\text{LiMn}_{0.333}\text{Ni}_{0.333}\text{Co}_{0.333}\text{O}_2$  ( $0 \leq x \leq 0.7$ ),” *Chemistry of Materials*, vol. 20, no. 19, pp. 6095–6106, 2008.
- [12] S. Yang, X. Zhou, J. Zhang, and Z. Liu, “Morphology-controlled solvothermal synthesis of  $\text{LiFePO}_4$  as a cathode material for lithium-ion batteries,” *Journal of Materials Chemistry*, vol. 20, no. 37, pp. 8086–8091, 2010.
- [13] G. Li, S. Pang, L. Jiang, Z. Guo, and Z. Zhang, “Environmentally friendly chemical route to vanadium oxide single-crystalline nanobelts as a cathode material for lithium-ion batteries,” *Journal of Physical Chemistry B*, vol. 110, no. 19, pp. 9383–9386, 2006.
- [14] H. K. Song, K. T. Lee, M. G. Kim, L. F. Nazar, and J. Cho, “Recent progress in nanostructured cathode materials for lithium secondary batteries,” *Advanced Functional Materials*, vol. 20, no. 22, pp. 3818–3834, 2010.
- [15] B. L. Ellis, K. T. Lee, and L. F. Nazar, “Positive electrode materials for Li-Ion and Li-batteries,” *Chemistry of Materials*, vol. 22, no. 3, pp. 691–714, 2010.
- [16] N. A. Kaskhedikar and J. Maier, “Lithium storage in carbon nanostructures,” *Advanced Materials*, vol. 21, no. 25–26, pp. 2664–2680, 2009.
- [17] H. Kim, M. Seo, M. H. Park, and J. Cho, “A critical size of silicon nano-anodes for lithium rechargeable batteries,” *Angewandte Chemie*, vol. 49, no. 12, pp. 2146–2149, 2010.
- [18] J. Hassoun, S. Panero, P. Simon, P. L. Taberna, and B. Scrosati, “High-rate, long-life Ni-Sn nanostructured electrodes for lithium-ion batteries,” *Advanced Materials*, vol. 19, no. 12, pp. 1632–1635, 2007.
- [19] C. M. Park, J. H. Kim, H. Kim, and H. J. Sohn, “Li-alloy based anode materials for Li secondary batteries,” *Chemical Society Reviews*, vol. 39, no. 8, pp. 3115–3141, 2010.
- [20] P. Poizot, S. Laruelle, S. Grugeon, L. Dupont, and J. M. Tarascon, “Nano-sized transition-metal oxides as negative-electrode materials for lithium-ion batteries,” *Nature*, vol. 407, no. 6803, pp. 496–499, 2000.
- [21] I. A. Courtney and J. R. Dahn, “Electrochemical and in situ X-ray diffraction studies of the reaction of lithium with tin oxide composites,” *Journal of the Electrochemical Society*, vol. 144, no. 6, pp. 2045–2052, 1997.
- [22] I. Exnar, L. Kavan, S. Y. Huang, and M. Grätzel, “Novel 2V rocking-chair lithium battery based on nano-crystalline titanium dioxide,” *Journal of Power Sources*, vol. 68, no. 2, pp. 720–722, 1997.
- [23] J. Cabana, L. Monconduit, D. Larcher, and M. R. Palacín, “Beyond intercalation-based Li-ion batteries: the state of the art and challenges of electrode materials reacting through conversion reactions,” *Advanced Materials*, vol. 22, no. 35, pp. E170–E192, 2010.
- [24] L. Ji, Z. Lin, M. Alcoutlabi, and X. Zhang, “Recent developments in nanostructured anode materials for rechargeable lithium-ion batteries,” *Energy and Environmental Science*, vol. 4, no. 8, pp. 2682–2689, 2011.
- [25] P. G. Bruce, B. Scrosati, and J. M. Tarascon, “Nanomaterials for rechargeable lithium batteries,” *Angewandte Chemie*, vol. 47, no. 16, pp. 2930–2946, 2008.
- [26] F. Cheng, Z. Tao, J. Liang, and J. Chen, “Template-directed materials for rechargeable lithium-ion batteries,” *Chemistry of Materials*, vol. 20, no. 3, pp. 667–681, 2008.
- [27] J. W. Long, B. Dunn, D. R. Rolison, and H. S. White, “Three-dimensional battery architectures,” *Chemical Reviews*, vol. 104, no. 10, pp. 4463–4492, 2004.
- [28] X. W. Lou, L. A. Archer, and Z. Yang, “Hollow micro-/nanostructures: synthesis and applications,” *Advanced Materials*, vol. 20, no. 21, pp. 3987–4019, 2008.
- [29] Y. K. Sun, S. T. Myung, H. S. Shin, Y. C. Bae, and C. S. Yoon, “Novel core-shell-structured  $\text{Li}[(\text{Ni}_{0.8}\text{Co}_{0.2})_{0.8}(\text{Ni}_{0.5}\text{Mn}_{0.5})_{0.2}]\text{O}_2$  via coprecipitation as positive electrode material for lithium secondary batteries,” *Journal of Physical Chemistry B*, vol. 110, no. 13, pp. 6810–6815, 2006.
- [30] L. W. Su, Y. Jing, and Z. Zhou, “Li ion battery materials with core-shell nanostructures,” *Nanoscale*, vol. 3, no. 10, pp. 3967–3983, 2011.
- [31] R. Liu, J. Duay, and S. B. Lee, “Heterogeneous nanostructured electrode materials for electrochemical energy storage,” *Chemical Communications*, vol. 47, no. 5, pp. 1384–1404, 2011.
- [32] D. R. Rolison, J. W. Long, J. C. Lytle et al., “Multifunctional 3D nanoarchitectures for energy storage and conversion,” *Chemical Society Reviews*, vol. 38, no. 1, pp. 226–252, 2009.

- [33] N. Meethong, H. Y. S. Huang, W. C. Carter, and Y. M. Chiang, "Size-dependent lithium miscibility gap in nanoscale Li  $1-x$ FePO $_4$ ," *Electrochemical and Solid-State Letters*, vol. 10, no. 5, pp. 134–138, 2007.
- [34] L. J. Fu, H. Liu, C. Li et al., "Surface modifications of electrode materials for lithium ion batteries," *Solid State Sciences*, vol. 8, no. 2, pp. 113–128, 2006.
- [35] T. Fang, J. G. Duh, and S. R. Sheen, "Improving the electrochemical performance of LiCoO $_2$  cathode by nanocrystalline ZnO coating," *Journal of the Electrochemical Society*, vol. 152, no. 9, pp. A1701–A1706, 2005.
- [36] A. I. Hochbaum and P. Yang, "Semiconductor nanowires for energy conversion," *Chemical Reviews*, vol. 110, no. 1, pp. 527–546, 2010.
- [37] C. K. Chan, H. Peng, G. Liu et al., "High-performance lithium battery anodes using silicon nanowires," *Nature Nanotechnology*, vol. 3, no. 1, pp. 31–35, 2008.
- [38] J. Liu, G. Cao, Z. Yang et al., "Oriented nanostructures for energy conversion and storage," *ChemSusChem*, vol. 1, no. 8–9, pp. 676–697, 2008.
- [39] C. Liu, F. Li, M. Lai-Peng, and H. M. Cheng, "Advanced materials for energy storage," *Advanced Materials*, vol. 22, no. 8, pp. E28–E62, 2010.
- [40] J. Jiang, Y. Li, J. Liu, and X. Huang, "Building one-dimensional oxide nanostructure arrays on conductive metal substrates for lithium-ion battery anodes," *Nanoscale*, vol. 3, no. 1, pp. 45–58, 2011.
- [41] Z. R. Dai, Z. W. Pan, and Z. L. Wang, "Novel nanostructures of functional oxides synthesized by thermal evaporation," *Advanced Functional Materials*, vol. 13, no. 1, pp. 9–24, 2003.
- [42] R. S. Wagner, W. C. Ellis, K. A. Jackson, and S. M. Arnold, "Study of the filamentary growth of silicon crystals from the vapor," *Journal of Applied Physics*, vol. 35, no. 10, pp. 2993–3000, 1964.
- [43] A. Sekar, S. H. Kim, A. Umar, and Y. B. Hahn, "Catalyst-free synthesis of ZnO nanowires on Si by oxidation of Zn powders," *Journal of Crystal Growth*, vol. 277, no. 1–4, pp. 471–478, 2005.
- [44] J. Yan, A. Sumboja, E. Khoo, and P. S. Lee, "V $_2$ O $_5$  loaded on SnO $_2$  nanowires for high rate Li ion batteries," *Advanced Materials*, vol. 23, no. 6, pp. 746–750, 2010.
- [45] C. K. Chan, H. Peng, R. D. Twisten, K. Jarausch, X. F. Zhang, and Y. Cui, "Fast, completely reversible Li insertion in vanadium pentoxide nanoribbons," *Nano Letters*, vol. 7, no. 2, pp. 490–495, 2007.
- [46] M. D. Fleischauer, J. Li, and M. J. Brett, "Columnar thin films for three-dimensional microbatteries," *Journal of the Electrochemical Society*, vol. 156, no. 1, pp. A33–A36, 2009.
- [47] Y. D. Ko, J. G. Kang, J. G. Park, S. Lee, and D. W. Kim, "Self-supported SnO $_2$  nanowire electrodes for high-power lithium-ion batteries," *Nanotechnology*, vol. 20, no. 45, Article ID 455701, 2009.
- [48] L. Zheng, Y. Xu, D. Jin, and Y. Xie, "Well-aligned molybdenum oxide nanorods on metal substrates: solution-based synthesis and their electrochemical capacitor application," *Journal of Materials Chemistry*, vol. 20, no. 34, pp. 7135–7143, 2010.
- [49] Y. Wang, H. Xia, L. Lu, and J. Lin, "Excellent performance in lithium-ion battery anodes: rational synthesis of Co(CO $_3$ ) $_{0.5}$ (OH) $_{0.11}$ H $_2$ O nanobelt array and its conversion into mesoporous and single-crystal Co $_3$ O $_4$ ," *ACS Nano*, vol. 4, no. 3, pp. 1425–1432, 2010.
- [50] Y. Song, S. Qin, Y. Zhang, W. Gao, and J. Liu, "Large-scale porous hematite nanorod arrays: direct growth on titanium foil and reversible lithium storage," *Journal of Physical Chemistry C*, vol. 114, no. 49, pp. 21158–21164, 2010.
- [51] L. E. Greene, M. Law, D. H. Tan et al., "General route to vertical ZnO nanowire arrays using textured ZnO seeds," *Nano Letters*, vol. 5, no. 7, pp. 1231–1236, 2005.
- [52] H. Yu, Z. Zhang, M. Han, X. Hao, and F. Zhu, "A general low-temperature route for large-scale fabrication of highly oriented ZnO nanorod/nanotube arrays," *Journal of the American Chemical Society*, vol. 127, no. 8, pp. 2378–2379, 2005.
- [53] L. E. Greene, M. Law, J. Goldberger et al., "Low-temperature wafer-scale production of ZnO nanowire arrays," *Angewandte Chemie*, vol. 42, no. 26, pp. 3031–3034, 2003.
- [54] Y. Li, B. Tan, and Y. Wu, "Mesoporous Co $_3$ O $_4$  nanowire arrays for lithium ion batteries with high capacity and rate capability," *Nano Letters*, vol. 8, no. 1, pp. 265–270, 2008.
- [55] Z. Huang, N. Geyer, P. Werner, J. De Boor, and U. Gösele, "Metal-assisted chemical etching of silicon: a review," *Advanced Materials*, vol. 23, no. 2, pp. 285–308, 2011.
- [56] C. M. Hsu, S. T. Connor, M. X. Tang, and Y. Cui, "Wafer-scale silicon nanopillars and nanocones by Langmuir-Blodgett assembly and etching," *Applied Physics Letters*, vol. 93, no. 13, Article ID 133109, 2008.
- [57] W. Zhang, X. Wen, and S. Yang, "Controlled reactions on a copper surface: synthesis and characterization of nanostructured copper compound films," *Inorganic Chemistry*, vol. 42, no. 16, pp. 5005–5014, 2003.
- [58] J. Y. Xiang, J. P. Tu, X. H. Huang, and Y. Z. Yang, "A comparison of anodically grown CuO nanotube film and Cu $_2$ O film as anodes for lithium ion batteries," *Journal of Solid State Electrochemistry*, vol. 12, no. 7–8, pp. 941–945, 2008.
- [59] F. S. Ke, L. Huang, G. Z. Wei et al., "One-step fabrication of CuO nanoribbons array electrode and its excellent lithium storage performance," *Electrochimica Acta*, vol. 54, no. 24, pp. 5825–5829, 2009.
- [60] C. H. Lai, K. W. Huang, J. H. Cheng et al., "Oriented growth of large-scale nickel sulfide nanowire arrays via a general solution route for lithium-ion battery cathode applications," *Journal of Materials Chemistry*, vol. 19, no. 39, pp. 7277–7283, 2009.
- [61] F. Fabregat-Santiago, E. M. Barea, J. Bisquert, G. K. Mor, K. Shankar, and C. A. Grimes, "High carrier density and capacitance in TiO $_2$  nanotube arrays induced by electrochemical doping," *Journal of the American Chemical Society*, vol. 130, no. 34, pp. 11312–11316, 2008.
- [62] G. F. Ortiz, I. Hanzu, T. Djenizian, P. Lavela, J. L. Tirado, and P. Knauth, "Alternative Li-ion battery electrode based on self-organized titania nanotubes," *Chemistry of Materials*, vol. 21, no. 1, pp. 63–67, 2009.
- [63] X. Chen, N. Q. Zhang, and K. N. Sun, "A vapor-phase corrosion strategy to hierarchically mesoporous nanosheet-assembled gearlike pillar arrays for super-performance lithium storage," *The Journal of Physical Chemistry C*, vol. 116, no. 40, pp. 21224–21231.
- [64] X. Chen, N. Q. Zhang, and K. N. Sun, "Facile fabrication of CuO mesoporous nanosheet cluster array electrodes with super lithium-storage properties," *Journal of Materials Chemistry*, vol. 22, no. 27, pp. 13637–13642, 2012.
- [65] P. L. Taberna, S. Mitra, P. Poizot, P. Simon, and J. M. Tarascon, "High rate capabilities Fe $_3$ O $_4$ -based Cu nano-architected electrodes for lithium-ion battery applications," *Nature Materials*, vol. 5, no. 7, pp. 567–573, 2006.

- [66] J. H. Kim, T. Ayalasomayajula, V. Gona, and D. Choi, "Fabrication and electrochemical characterization of a vertical array of  $\text{MnO}_2$  nanowires grown on silicon substrates as a cathode material for lithium rechargeable batteries," *Journal of Power Sources*, vol. 183, no. 1, pp. 366–369, 2008.
- [67] Y. S. Kim, H. J. Ahn, S. H. Nam, S. H. Lee, H. S. Shim, and W. B. Kim, "Honeycomb pattern array of vertically standing core-shell nanorods: its application to Li energy electrodes," *Applied Physics Letters*, vol. 93, no. 10, Article ID 103104, 2008.
- [68] K. Takahashi, Y. Wang, K. Lee, and G. Cao, "Fabrication and  $\text{Li}^+$ -intercalation properties of  $\text{V}_2\text{O}_5$ - $\text{TiO}_2$  composite nanorod arrays," *Applied Physics A*, vol. 82, no. 1, pp. 27–31, 2006.
- [69] Y. Wang, K. Takahashi, H. Shang, and G. Cao, "Synthesis and electrochemical properties of vanadium pentoxide nanotube arrays," *Journal of Physical Chemistry B*, vol. 109, no. 8, pp. 3085–3088, 2005.
- [70] M. M. Shaijumon, E. Perre, B. Daffos, P. L. Taberna, J. M. Tarascon, and P. Simon, "Nanoarchitected 3D cathodes for Li-ion microbatteries," *Advanced Materials*, vol. 22, no. 44, pp. 4978–4981, 2010.
- [71] Y. Wang and G. Cao, "Synthesis and electrochemical properties of  $\text{InVO}_4$  nanotube arrays," *Journal of Materials Chemistry*, vol. 17, no. 9, pp. 894–899, 2007.
- [72] I. Lahiri, S. W. Oh, J. Y. Hwang et al., "High capacity and excellent stability of lithium ion battery anode using interface-controlled binder-free multiwall carbon nanotubes grown on copper," *ACS Nano*, vol. 4, no. 6, pp. 3440–3446, 2010.
- [73] R. Teki, R. Krishnan, T. C. Parker, T. M. Lu, P. N. Kumta, and N. Koratkar, "Nanostructured silicon anodes for lithium ion rechargeable batteries," *Small*, vol. 5, no. 20, pp. 2236–2242, 2009.
- [74] L. Bazin, S. Mitra, P. L. Taberna et al., "High rate capability pure Sn-based nano-architected electrode assembly for rechargeable lithium batteries," *Journal of Power Sources*, vol. 188, no. 2, pp. 578–582, 2009.
- [75] A. Finke, P. Poizot, C. Guéry et al., "Electrochemical method for direct deposition of nanometric bismuth and its electrochemical properties vs Li," *Electrochemical and Solid-State Letters*, vol. 11, no. 3, pp. E5–E9, 2008.
- [76] Z. Wang, F. Su, S. Madhavi, and X. W. Lou, "CuO nanostructures supported on Cu substrate as integrated electrodes for highly reversible lithium storage," *Nanoscale*, vol. 3, no. 4, pp. 1618–1623, 2011.
- [77] H. Wang, Q. Pan, Y. Cheng, J. Zhao, and G. Yin, "Evaluation of ZnO nanorod arrays with dandelion-like morphology as negative electrodes for lithium-ion batteries," *Electrochimica Acta*, vol. 54, no. 10, pp. 2851–2855, 2009.
- [78] Q. Pan, L. Qin, J. Liu, and H. Wang, "Flower-like ZnO-NiO-C films with high reversible capacity and rate capability for lithium-ion batteries," *Electrochimica Acta*, vol. 55, no. 20, pp. 5780–5785, 2010.
- [79] G. Ferrara, L. Damen, C. Arbizzani et al., "SnCo nanowire array as negative electrode for lithium-ion batteries," *Journal of Power Sources*, vol. 196, no. 3, pp. 1469–1473, 2011.
- [80] M. Tian, W. Wang, S. H. Lee et al., "Enhancing Ni-Sn nanowire lithium-ion anode performance by tailoring active/inactive material interfaces," *Journal of Power Sources*, vol. 196, no. 23, pp. 10207–10212, 2011.
- [81] M. Tian, W. Wang, Y. J. Wei, and R. G. Yang, "Stable high areal capacity lithium-ion battery anodes based on three-dimensional Ni-Sn nanowire networks," *Journal of Power Sources*, vol. 211, no. 23, pp. 46–51, 2012.
- [82] J. Z. Wang, N. Du, H. Zhang et al., "Cu-Si<sub>1-x</sub>Ge<sub>x</sub>Core-Shell nanowire arrays as three-dimensional electrodes for high-rate capability lithium-ion batteries," *Journal of Power Sources*, vol. 208, no. 15, pp. 434–439, 2012.
- [83] C. H. Lai, K. W. Huang, J. H. Cheng, C. Y. Lee, B. J. Hwang, and L. J. Chen, "Direct growth of high-rate capability and high capacity copper sulfide nanowire array cathodes for lithium-ion batteries," *Journal of Materials Chemistry*, vol. 20, no. 32, pp. 6638–6645, 2010.
- [84] C. Villevieille, F. Robert, P. L. Taberna, L. Bazin, P. Simon, and L. Monconduit, "The good reactivity of lithium with nanostructured copper phosphide," *Journal of Materials Chemistry*, vol. 18, no. 48, pp. 5956–5960, 2008.
- [85] L. W. Ji, Z. K. Tan, T. Kuykendall et al., "Multilayer nanoassembly of Sn-nanopillar arrays sandwiched between graphene layers for high-capacity lithium storage," *Energy & Environmental Science*, vol. 4, no. 9, pp. 3611–3616, 2011.
- [86] M. S. Wu, P. C. J. Chiang, J. T. Lee, and J. C. Lin, "Synthesis of manganese oxide electrodes with interconnected nanowire structure as an anode material for rechargeable lithium ion batteries," *Journal of Physical Chemistry B*, vol. 109, no. 49, pp. 23279–23284, 2005.
- [87] Y. Fan, H. Shao, J. Wang, L. Liu, J. Zhang, and C. Cao, "Synthesis of foam-like freestanding  $\text{Co}_3\text{O}_4$  nanosheets with enhanced electrochemical activities," *Chemical Communications*, vol. 47, no. 12, pp. 3469–3471, 2011.
- [88] J. Liu, Y. Li, X. Huang et al., "Direct growth of  $\text{SnO}_2$  nanorod array electrodes for lithium-ion batteries," *Journal of Materials Chemistry*, vol. 19, no. 13, pp. 1859–1864, 2009.
- [89] J. Liu, Y. Li, H. Fan et al., "Iron oxide-based nanotube arrays derived from sacrificial template-accelerated hydrolysis: large-area design and reversible lithium storage," *Chemistry of Materials*, vol. 22, no. 1, pp. 212–217, 2010.
- [90] J. Liu, Y. Li, R. Ding et al., "Carbon/ZnO nanorod array electrode with significantly improved lithium storage capability," *Journal of Physical Chemistry C*, vol. 113, no. 13, pp. 5336–5339, 2009.
- [91] N. Zhao, G. Wang, Y. Huang, B. Wang, B. Yao, and Y. Wu, "Preparation of nanowire arrays of amorphous carbon nanotube-coated single crystal  $\text{SnO}_2$ ," *Chemistry of Materials*, vol. 20, no. 8, pp. 2612–2614, 2008.
- [92] A. L. M. Reddy, M. M. Shaijumon, S. R. Gowda, and P. M. Ajayan, "Coaxial  $\text{MnO}_2$ /carbon nanotube array electrodes for high-performance lithium batteries," *Nano Letters*, vol. 9, no. 3, pp. 1002–1006, 2009.
- [93] G. Ferrara, C. Arbizzani, and L. Damen, "High-performing SnCo nanowire electrodes as anodes for lithium-ion batteries," *Journal of Power Sources*, vol. 211, pp. 103–107, 2012.
- [94] C. Masarapu, V. Subramanian, H. Zhu, and B. Wei, "Long-cycle electrochemical behavior of multiwall carbon nanotubes synthesized on stainless steel in Li ion batteries," *Advanced Functional Materials*, vol. 19, no. 7, pp. 1008–1014, 2009.
- [95] C. K. Chan, X. F. Zhang, and Y. Cui, "High capacity Li ion battery anodes using Ge nanowires," *Nano Letters*, vol. 8, no. 1, pp. 307–309, 2008.
- [96] L. Hu, H. Wu, S. S. Hong et al., "Si nanoparticle-decorated Si nanowire networks for Li-ion battery anodes," *Chemical Communications*, vol. 47, no. 1, pp. 367–369, 2011.
- [97] L. F. Cui, R. Ruffo, C. K. Chan, H. Peng, and Y. Cui, "Crystalline-amorphous core-shell silicon nanowires for high capacity and high current battery electrodes," *Nano Letters*, vol. 9, no. 1, pp. 491–495, 2009.

- [98] A. Gohier, B. Laïk, J. P. Pereira-Ramos et al., "Influence of the diameter distribution on the rate capability of silicon nanowires for lithium-ion batteries," *Journal of Power Sources*, vol. 203, pp. 135–139, 2012.
- [99] N. Liu, L. B. Hu, M. T. McDowell et al., "Pre-lithiated silicon nanowires as an anode for lithium ion batteries," *ACS Nano*, vol. 5, no. 8, pp. 6487–6493, 2011.
- [100] L. F. Cui, L. Hu, J. W. Choi, and Y. Cui, "Light-weight free-standing carbon nanotube-silicon films for anodes of lithium ion batteries," *ACS Nano*, vol. 4, no. 7, pp. 3671–3678, 2010.
- [101] H. Chen, Y. Xiao, L. Wang, and Y. Yang, "Silicon nanowires coated with copper layer as anode materials for lithium-ion batteries," *Journal of Power Sources*, vol. 196, no. 16, pp. 6657–6662, 2011.
- [102] K. S. Park, J. G. Kang, Y. J. Choi, S. Lee, D. W. Kim, and J. G. Park, "Long-term, high-rate lithium storage capabilities of TiO<sub>2</sub> nanostructured electrodes using 3D self-supported indium tin oxide conducting nanowire arrays," *Energy and Environmental Science*, vol. 4, no. 5, pp. 1796–1801, 2011.
- [103] J. Jiang, J. H. Zhu, Y. M. Feng et al., "A novel evolution strategy to fabricate a 3D hierarchical interconnected core-shell Ni/MnO<sub>2</sub> hybrid for Li-ion batteries," *Chemical Communications*, vol. 48, no. 60, pp. 7471–7473, 2012.
- [104] W. Zhou, C. Cheng, J. Liu et al., "Epitaxial growth of branched  $\alpha$ -Fe<sub>2</sub>O<sub>3</sub>/SnO<sub>2</sub> nano-heterostructures with improved lithium-ion battery performance," *Advanced Functional Materials*, vol. 21, no. 13, pp. 2439–2445, 2011.
- [105] S. Luo, K. Wang, J. P. Wang et al., "Binder-free LiCoO<sub>2</sub>/carbon nanotube cathodes for high-performance lithium ion batteries," *Advanced Materials*, vol. 24, no. 17, pp. 2294–2298, 2012.
- [106] J. J. Schneider, J. Khanderi, A. Popp et al., "Hybrid architectures from 3D aligned arrays of multiwall carbon nanotubes and nanoparticulate LiCoPO<sub>4</sub>: synthesis, properties and evaluation of their electrochemical performance as cathode materials in lithium ion batteries," *European Journal of Inorganic Chemistry*, vol. 211, no. 28, pp. 4349–4359, 2011.
- [107] L. Dimesso, C. Förster, W. Jaegermann et al., "Developments in nanostructured LiMPO<sub>4</sub> (M= Fe, Co, Ni, Mn) composites based on three dimensional carbon architecture," *Chemical Society Reviews*, vol. 41, no. 15, pp. 5068–5080, 2012.
- [108] Y. Wang, H. J. Zhang, W. X. Lim, J. Y. Lin, and C. C. Wong, "Designed strategy to fabricate a patterned V<sub>2</sub>O<sub>5</sub> nanobelt array as a superior electrode for Li-ion batteries," *Journal of Materials Chemistry*, vol. 21, no. 7, pp. 2362–2368, 2011.
- [109] G. Du, Z. Guo, P. Zhang et al., "SnO<sub>2</sub> nanocrystals on self-organized TiO<sub>2</sub> nanotube array as three-dimensional electrode for lithium ion microbatteries," *Journal of Materials Chemistry*, vol. 20, no. 27, pp. 5689–5694, 2010.
- [110] M. C. Qiu, L. W. Yang, X. Qi, J. Li, and J. X. Zhong, "Fabrication of ordered NiO coated Si nanowire array films as electrodes for a high performance lithium ion battery," *ACS Applied Materials and Interfaces*, vol. 2, no. 12, pp. 3614–3618, 2010.
- [111] D. Liu, Q. Zhang, P. Xiao et al., "Hydrous manganese dioxide nanowall arrays growth and their Li<sup>+</sup> ions intercalation electrochemical properties," *Chemistry of Materials*, vol. 20, no. 4, pp. 1376–1380, 2008.
- [112] Y. H. Lee, I. C. Leu, C. L. Liao et al., "Fabrication and characterization of Cu<sub>2</sub>O nanorod arrays and their electrochemical performance in Li-ion batteries," *Electrochemical and Solid-State Letters*, vol. 9, no. 4, pp. A207–A210, 2006.
- [113] J. H. Kim, S. Khanal, M. Islam, A. Khatiri, and D. Choi, "Electrochemical characterization of vertical arrays of tin nanowires grown on silicon substrates as anode materials for lithium rechargeable microbatteries," *Electrochemistry Communications*, vol. 10, no. 11, pp. 1688–1690, 2008.
- [114] S. S. Zhang and T. R. Jow, "Aluminum corrosion in electrolyte of Li-ion battery," *Journal of Power Sources*, vol. 109, no. 2, pp. 458–464, 2002.
- [115] S. T. Myung, Y. Hitoshi, and Y. K. Sun, "Electrochemical behavior and passivation of current collectors in lithium-ion batteries," *Journal of Materials Chemistry*, vol. 21, no. 27, pp. 9891–9911, 2011.
- [116] K. Takahashi, S. J. Limmer, Y. Wang, and G. Cao, "Synthesis and electrochemical properties of single-crystal V<sub>2</sub>O<sub>5</sub> nanorod arrays by template-based electrodeposition," *Journal of Physical Chemistry B*, vol. 108, no. 28, pp. 9795–9800, 2004.
- [117] K. Takahashi, S. J. Limmer, Y. Wang, and G. Cao, "Growth and electrochemical properties of single-crystalline V<sub>2</sub>O<sub>5</sub> nanorod arrays," *Japanese Journal of Applied Physics Part 1*, vol. 44, no. 1 B, pp. 662–668, 2005.
- [118] K. Takahashi, Y. Wang, and G. Z. Cao, "Ni-V<sub>2</sub>O<sub>5</sub>·nH<sub>2</sub>O core-shell nanocable arrays for enhanced electrochemical intercalation," *The Journal of Physical Chemistry B*, vol. 109, no. 1, pp. 48–51, 2005.
- [119] E. Perre, L. Nyholm, T. Gustafsson, P. L. Taberna, P. Simon, and K. Edström, "Direct electrodeposition of aluminium nano-rods," *Electrochemistry Communications*, vol. 10, no. 10, pp. 1467–1470, 2008.
- [120] G. Oltean, L. Nyholm, and K. Edström, "Galvanostatic electrodeposition of aluminium nano-rods for Li-ion three-dimensional micro-battery current collectors," *Electrochimica Acta*, vol. 56, no. 9, pp. 3203–3208, 2011.
- [121] S. Zhang, Z. Du, R. Lin et al., "Nickel nanocone-array supported silicon anode for high-performance lithium-ion batteries," *Advanced Materials*, vol. 22, no. 47, pp. 5378–5382, 2010.
- [122] H. Duan, J. Gnanaraj, X. Chen, B. Li, and J. Liang, "Fabrication and characterization of Fe<sub>3</sub>O<sub>4</sub>-based Cu nanostructured electrode for Li-ion battery," *Journal of Power Sources*, vol. 185, no. 1, pp. 512–518, 2008.
- [123] H. Duan, J. Gnanaraj, and J. Liang, "Synthesis and rate performance of Fe<sub>3</sub>O<sub>4</sub>-based Cu nanostructured electrodes for Li ion batteries," *Journal of Power Sources*, vol. 196, no. 10, pp. 4779–4784, 2011.
- [124] D. D. Jiang, H. Y. Tian, C. C. Qiu et al., "Electrodeposition and characterization of assembly of Sn on Cu nanorods for Li-ion microbattery application," *Journal of Solid State Electrochemistry*, vol. 15, no. 11–12, pp. 2639–2644, 2011.
- [125] H. Lee, J. J. Cho, J. Kim, and H. J. Kim, "Comparison of voltammetric responses over the cathodic region in LiPF<sub>6</sub> and LiBETI with and without HF," *Journal of the Electrochemical Society*, vol. 152, no. 6, pp. A1193–A1198, 2005.
- [126] X. Ji, X. Huang, J. Liu et al., "Carbon-coated SnO<sub>2</sub> nanorod array for lithium-ion battery anode material," *Nanoscale Research Letters*, vol. 5, no. 3, pp. 649–653, 2010.
- [127] C. Iwakura, Y. Fukumoto, H. Inoue et al., "Electrochemical characterization of various metal foils as a current collector of positive electrode for rechargeable lithium batteries," *Journal of Power Sources*, vol. 68, no. 2, pp. 301–303, 1997.
- [128] Z. Wei, Z. Liu, R. Jiang, C. Bian, T. Huang, and A. Yu, "TiO<sub>2</sub> nanotube array film prepared by anodization as anode material for lithium ion batteries," *Journal of Solid State Electrochemistry*, vol. 14, no. 6, pp. 1045–1050, 2010.

- [129] D. Liu, P. Xiao, Y. Zhang et al., "TiO<sub>2</sub> nanotube arrays annealed in N<sub>2</sub> for efficient lithium-ion intercalation," *Journal of Physical Chemistry C*, vol. 112, no. 30, pp. 11175–11180, 2008.
- [130] D. Liu, Y. Zhang, P. Xiao et al., "TiO<sub>2</sub> nanotube arrays annealed in CO exhibiting high performance for lithium ion intercalation," *Electrochimica Acta*, vol. 54, no. 27, pp. 6816–6820, 2009.
- [131] D. Liu, B. B. Garcia, Q. Zhang et al., "Mesoporous hydrous manganese dioxide nanowall arrays with large lithium ion energy storage capacities," *Advanced Functional Materials*, vol. 19, no. 7, pp. 1015–1023, 2009.
- [132] K. Kang, H. S. Lee, D. W. Han et al., "Maximum Li storage in Si nanowires for the high capacity three-dimensional Li-ion battery," *Applied Physics Letters*, vol. 96, no. 5, Article ID 053110, 2010.
- [133] H. Wang, Q. Pan, J. Zhao, G. Yin, and P. Zuo, "Fabrication of CuO film with network-like architectures through solution-immersion and their application in lithium ion batteries," *Journal of Power Sources*, vol. 167, no. 1, pp. 206–211, 2007.
- [134] Q. Pan, H. Jin, H. Wang, and G. Yin, "Flower-like CuO film-electrode for lithium ion batteries and the effect of surface morphology on electrochemical performance," *Electrochimica Acta*, vol. 53, no. 2, pp. 951–956, 2007.
- [135] X. Chen, N. Q. Zhang, and K. N. Sun, "Facile fabrication of CuO 1D pine-needle-like arrays for super-rate lithium storage," *Journal of Materials Chemistry*, vol. 22, no. 30, pp. 15080–15084, 2012.
- [136] W. X. Zhang, M. Li, Q. Wang et al., "Hierarchical self-assembly of microscale cog-like superstructures for enhanced performance in lithium-ion batteries," *Advanced Functional Materials*, vol. 21, no. 8, pp. 3516–3523, 2011.
- [137] W. Q. Zeng, F. P. Zheng, R. Z. Li et al., "Template synthesis of SnO<sub>2</sub>/α-Fe<sub>2</sub>O<sub>3</sub> nanotube array for 3D lithium ion battery anode with large areal capacity," *Nanoscale*, vol. 4, no. 8, pp. 2760–2765, 2012.
- [138] F. F. Cao, J. W. Deng, S. Xin et al., "Cu-Si nanocable arrays as high-rate anode materials for lithium-ion batteries," *Advanced Materials*, vol. 23, no. 38, pp. 4415–4420, 2011.
- [139] X. Chen, K. Gerasopoulos, J. Guo et al., "A patterned 3D silicon anode fabricated by electrodeposition on a virus-structured current collector," *Advanced Functional Materials*, vol. 21, no. 2, pp. 380–387, 2011.
- [140] L. B. Hu, H. Wu, Y. F. Gao et al., "Silicon-carbon nanotube coaxial sponge as Li-ion anodes with high areal Capacity," *Advanced Energy Materials*, vol. 1, no. 4, pp. 523–527, 2011.
- [141] G. F. Ortiz, I. Hanzu, P. Lavela, P. Knauth, J. L. Tirado, and T. Djenizian, "Nanoarchitected TiO<sub>2</sub>/SnO: a future negative electrode for high power density Li-Ion microbatteries," *Chemistry of Materials*, vol. 22, no. 5, pp. 1926–1932, 2010.
- [142] G. F. Ortiz, I. Hanzu, P. Lavela, J. L. Tirado, P. Knauth, and T. Djenizian, "A novel architected negative electrode based on titania nanotube and iron oxide nanowire composites for Li-ion microbatteries," *Journal of Materials Chemistry*, vol. 20, no. 20, pp. 4041–4046, 2010.
- [143] H. Cheng, Z. G. Lu, J. Q. Deng, C. Y. Chung, K. Zhang, and Y. Y. Li, "A facile method to improve the high rate capability of Co<sub>3</sub>O<sub>4</sub> nanowire array electrodes," *Nano Research*, vol. 3, no. 12, pp. 895–901, 2010.
- [144] W. Wang, R. Epur, and P. N. Kumta, "Vertically aligned silicon/carbon nanotube (VASCNT) arrays: hierarchical anodes for lithium-ion battery," *Electrochemistry Communications*, vol. 13, no. 5, pp. 429–432, 2011.
- [145] W. Wang and P. N. Kumta, "Nanostructured hybrid silicon/carbon nanotube heterostructures: reversible high-capacity lithium-ion anodes," *ACS Nano*, vol. 4, no. 4, pp. 2233–2241, 2010.
- [146] A. Gohier, B. Laik, K. H. Kim et al., "High rate capacity silicon decorated vertically aligned carbon nanotubes for Li-ion batteries," *Advanced Materials*, vol. 24, no. 19, pp. 2592–2597, 2012.
- [147] T. I. Lee, J. P. Jeagal, J. H. Choi et al., "Binder-free and full electrical-addressing free-standing nanosheets with carbon nanotube fabrics for electrochemical applications," *Advanced Materials*, vol. 23, no. 40, pp. 4711–4715, 2011.